

# The Dugganites: A New Potentially Multiferroic $\text{Te}^{6+}$ -containing Subclass of the Langasites

by

Harlyn Jacob SILVERSTEIN

A thesis submitted to the Faculty of Graduate Studies of

The University of Manitoba

in partial fulfillment of the requirements of the degree of

Doctor of Philosophy

Department of Chemistry

University of Manitoba

Winnipeg

Copyright © 2015 by Harlyn J. Silverstein

# *Abstract*

The langasites are a diverse group of materials with the  $\text{Ca}_3\text{Ga}_2\text{Ge}_4\text{O}_{14}$  structure that contains four cationic sites that vary in both size and coordination possessing  $P321$  symmetry. Paramagnetic transition metal ions can be placed onto the  $3f$  site such that they form planar isolated equilateral trimers that stack normal to the plane. The geometrically frustrated nature of the trimer sublattice prevents the system from simultaneously satisfying all of its energetic obligations at low temperatures. Consequently, nature attempts to make energetic compromises that result in complex magnetism. The objective of this thesis is to explore these magnetic states such that they can be understood, and perhaps, even taken advantage of for future engineering applications.

Four different langasites are presented in this work.  $\text{Ba}_3\text{NbFe}_3\text{Si}_2\text{O}_{14}$  has  $\text{Fe}^{3+}$  ions occupying the trimer site. Below 26 K, the magnetic moments in this material order into a unique doubly chiral magnetic structure. The coupling of the magnetic structure to the lattice also results in ferroelectric polarization in this material.  $\text{Pb}_3\text{TeMn}_3\text{P}_2\text{O}_{14}$ ,  $\text{Pb}_3\text{TeCo}_3\text{P}_2\text{O}_{14}$ , and  $\text{Pb}_3\text{TeCo}_3\text{V}_2\text{O}_{14}$  have all been prepared phase pure and studied using x-ray diffraction, magnetization in fields up to 35 T, heat capacity, dielectric measurements, neutron diffraction, and inelastic neutron spectroscopy. All three  $\text{Te}^{6+}$ -containing materials, known as the dugganite subclass of the langasite series, distort into large supercells away from  $P321$  symmetry. Magnetic phase diagrams were constructed for each of these new systems using multiple experimental probes.  $\text{Pb}_3\text{TeMn}_3\text{P}_2\text{O}_{14}$  has a complex magnetic structure believed to be quite similar to  $\text{Ba}_3\text{NbFe}_3\text{Si}_2\text{O}_{14}$ . On the other hand,  $\text{Pb}_3\text{TeCo}_3\text{P}_2\text{O}_{14}$  shows very different magnetism: a unique two-tiered magnetic structure was solved using neutron scattering, Rietveld refinement, and representational analysis.  $\text{Pb}_3\text{TeCo}_3\text{V}_2\text{O}_{14}$  behaves quite like  $\text{Pb}_3\text{TeCo}_3\text{P}_2\text{O}_{14}$ , except a second zero-field magnetic transition is observed, implying that orbital hybridization with diamagnetic  $\text{P}^{5+}$  or  $\text{V}^{5+}$  is very important in these materials.

## *Acknowledgements*

Firstly, I have to begin with my friends: I could fill this whole thesis thanking each and every one of you individually. Since high school, I always had a fascination with science, particularly biology. But it wasn't until I took that first class with Professor Brian Pettitt that I found my love for chemistry and physics. Professor Doug Craig then showed me how exciting experimental research actually is. I have them to thank for making me second guess my career trajectory, which turned out to be the second best decision that I've ever made. My committee members, Professors Mario Bieringer, Johan van Lierop, Scott Kroeker, and Peter Budzelaar, have been the most supportive group of academics that I could have possibly asked for.

I need to acknowledge every organization who has contributed to my funding over the years, particularly the National Sciences and Engineering Research Council of Canada (NSERC) and the University of Manitoba. I also have to thank my group members: Alannah, Arzoo, Paul, Brenden, Kanisha, Alison, Avichai, Micaela, Cole and Chris K. I don't really know what to say except that I am going to miss all of you so much. You are all wonderful and amazing people.

Chris, words can't describe how you've impacted me over the years. Your love for all things science is what drove me to your lab in the first place. The enthusiasm you showed for PhysChem, the kindness you gave me even though I bugged you way too often, and your constant never-waiving support have literally shaped me into the person that I am today. My success is a direct product of the environment that you have provided for your students. When it's time for me to lead the next generation, I could only hope to be even half the mentor you are.

My final thanks go to my parents, my sisters, my aunts, uncles, cousins, and my zaida. You guys mean everything to me. Thank you for raising me, for encouraging me to take risks, for listening to me rant, for putting me up in school, for bragging about my successes, but most importantly, for your love. I couldn't have asked for anything better. To Jenny, my baby, I love you so much! You have truly made me the luckiest man alive. You and your family have welcomed me as if I was one of your own. Asking you to marry me was the first best decision that I've ever made in my life. Thank you for finding the strength to put up with me for the past eight years. If they have been any indication of things to come, then I can't wait to spend the rest of our lives together.

*For Jenny...*

# Contents

<b>Abstract</b>	<b>i</b>
<b>Acknowledgements</b>	<b>ii</b>
<b>Dedication</b>	<b>iii</b>
<b>Contents</b>	<b>iv</b>
<b>List of Figures</b>	<b>vii</b>
<b>List of Tables</b>	<b>x</b>
<b>1 Introduction</b>	<b>1</b>
1.1 Introduction . . . . .	1
1.2 Magnetism . . . . .	3
1.3 Magnetic ground states and geometric frustration . . . . .	11
1.4 Final notes . . . . .	16
<b>2 Experimental Techniques</b>	<b>17</b>
2.1 The Ceramic method . . . . .	17
2.2 Diffraction . . . . .	19
2.2.1 Introduction . . . . .	19
2.2.2 Formalism . . . . .	21
2.2.3 Bragg peak intensity . . . . .	28
2.2.4 X-ray diffraction . . . . .	30
2.2.5 Neutron diffraction . . . . .	33
2.3 Rietveld refinement . . . . .	39
2.3.1 Mathematical procedure . . . . .	40
2.3.2 Magnetic structure refinements: Representational analysis . . . . .	43
2.3.3 Bond valence sums . . . . .	47
2.4 Direct Current (DC) magnetometry . . . . .	48
2.5 Heat capacity . . . . .	54
2.6 Dielectric constant . . . . .	59

2.7	Inelastic neutron scattering	61
<b>3</b>	<b>Nuclear and Magnetic Structures of the Multiferroic Langasite, <math>\text{Ba}_3\text{NbFe}_3\text{Si}_2\text{O}_{14}</math></b>	<b>63</b>
3.1	Preamble	63
3.2	Introduction	64
3.3	Methods	67
3.3.1	Preparation	67
3.3.2	Diffraction	69
3.4	Refinement	71
3.4.1	Room-Temperature Refinement ( $T > T_N$ )	71
3.4.2	Low-Temperature Refinement ( $T < T_N$ )	74
3.5	Discussion and Current Literature Review	76
3.5.1	Magnetic Structure	76
3.5.2	Moment Dynamics	80
3.5.3	Multiferroic Behaviour	84
3.6	Conclusion	87
<b>4</b>	<b>Complex nuclear and magnetic superstructures in the <math>S=5/2</math> multiferroic candidate <math>\text{Pb}_3\text{TeMn}_3\text{P}_2\text{O}_{14}</math></b>	<b>89</b>
4.1	Introduction	89
4.2	Methods	92
4.2.1	Preparation	92
4.2.2	Diffraction	97
4.2.3	Physical property measurements	100
4.3	Refinement	101
4.3.1	Initial refinement	101
4.3.2	Supercell refinement	105
4.4	Results and Discussion	111
4.4.1	Crystal structure	111
4.4.2	Physical property measurements	114
4.4.3	Magnetic structure	120
4.4.4	Discussion	125
4.5	Conclusion	129
<b>5</b>	<b>Magnetic phase diagram and spin dynamics in <math>\text{Pb}_3\text{TeCo}_3\text{P}_2\text{O}_{14}</math></b>	<b>131</b>
5.1	Introduction	131
5.2	Methods	132
5.2.1	Preparation	132
5.2.2	Diffraction	134
5.2.3	Physical property measurements	134
5.2.4	Refinement	135
5.2.5	Inelastic neutron scattering	142
5.3	Results and Discussion	143
5.3.1	Crystal structure	143
5.3.2	Physical property measurements	147

---

5.3.3	Magnetic phases	152
5.3.4	Inelastic excitations	161
5.4	Conclusion	169
<b>6</b>	<b>Two magnetic transitions in the multiferroic candidate <math>\text{Pb}_3\text{TeCo}_3\text{V}_2\text{O}_{14}</math></b>	<b>170</b>
6.1	Preamble	170
6.2	Introduction	171
6.3	Methods	171
6.3.1	Preparation	171
6.3.2	Diffraction	172
6.3.3	Physical property measurements	173
6.3.4	Refinement	174
6.3.5	Inelastic neutron scattering	178
6.4	Results and Discussion	178
6.4.1	Crystal structure	178
6.4.2	Physical property measurements	189
6.4.3	Magnetic structures	191
6.4.4	Inelastic excitations	205
6.5	Conclusion	209
<b>7</b>	<b>Conclusions and Future Directions</b>	<b>210</b>

# List of Figures

1.1	Electron angular momentum	5
1.2	Dipolar interaction	7
1.3	Dzyaloshinskii-Moriya interaction	9
1.4	Populations of magnetic states with temperature	11
1.5	Magnetic ground states	12
1.6	Geometric frustration	13
1.7	Multiferroics and symmetry	15
2.1	The ceramic method	18
2.2	Neutron scattering cross sections	22
2.3	Construction of a crystal lattice	23
2.4	Bragg's law derivation	24
2.5	von Laue scattering	25
2.6	Bragg's law from the von Laue condition	28
2.7	Powder averaging	29
2.8	Absorption effect	32
2.9	Differential scattering cross section	34
2.10	Powder averaging and magnetic structures	39
2.11	Polar and axial vectors	45
2.12	Magnetic susceptibility	50
2.13	Magnetometer Brass holder	51
2.14	Magnetometer rod	52
2.15	Physical Property Measurement System	53
2.16	Heat capacity puck	58
3.1	Langasite kagomé sublattice	64
3.2	Langasite trimer sublattice	65
3.3	Triangular chirality and helicity	66
3.4	Langasite stability field	68
3.5	Preparation of $\text{Ba}_3\text{NbFe}_3\text{Si}_2\text{O}_{14}$	70
3.6	Refinement of $\text{Ba}_3\text{NbFe}_3\text{Si}_2\text{O}_{14}$	72
3.7	$\text{Ba}_3\text{NbFe}_3\text{Si}_2\text{O}_{14}$ crystal structure	73
3.8	Structural holes in $\text{Ba}_3\text{NbFe}_3\text{Si}_2\text{O}_{14}$	74
3.9	$\text{Ba}_3\text{NbFe}_3\text{Si}_2\text{O}_{14}$ magnetic structure	75
3.10	Exchange pathways in $\text{Ba}_3\text{NbFe}_3\text{Si}_2\text{O}_{14}$	77



4.1	Cation $1a$ and $3f$ occupation	90
4.2	$\text{Pb}_3\text{TeMn}_3\text{P}_2\text{O}_{14}$ intermediate	94
4.3	Common symmetry of intermediates	96
4.4	$\text{Pb}_3(\text{PO}_4)_2$ /langasite similarities	98
4.5	Mn and Cu langasite mechanism	99
4.6	X-ray refinement of $\text{Pb}_3\text{TeMn}_3\text{P}_2\text{O}_{14}$	101
4.7	Synchrotron x-ray diffraction of $\text{Pb}_3\text{TeMn}_3\text{P}_2\text{O}_{14}$	103
4.8	Rigid body definition	106
4.9	Final refinement of $\text{Pb}_3\text{TeMn}_3\text{P}_2\text{O}_{14}$	110
4.10	$\text{Pb}_3\text{TeMn}_3\text{P}_2\text{O}_{14}$ supercell	112
4.11	Supercell trimers	113
4.12	DC susceptibility	115
4.13	Field-dependence of $T_N$	116
4.14	Possible phase diagram of $\text{Pb}_3\text{TeMn}_3\text{P}_2\text{O}_{14}$	117
4.15	DC-susceptibility in high fields	118
4.16	Heat capacity	118
4.17	Microscopy on $\text{Pb}_3\text{TeMn}_{1.5}\text{Zn}_{1.5}\text{P}_2\text{O}_{14}$	119
4.18	Dielectric measurements	120
4.19	Frequency dependence of the dielectric constant	121
4.20	Low temperature refinement using C2 diffractometer	123
4.21	Low temperature refinement using POWGEN diffractometer	124
4.22	Final low temperature refinement of $\text{Pb}_3\text{TeMn}_3\text{P}_2\text{O}_{14}$	126
4.23	Magnetic unit cell $\text{Pb}_3\text{TeMn}_3\text{P}_2\text{O}_{14}$	127
4.24	Possible mechanism for multiferroicity	128
5.1	$3d$ electronic environments	133
5.2	$\text{Pb}_3\text{TeCo}_3\text{P}_2\text{O}_{14}$ $\vec{k}$ search	136
5.3	Space group choice	137
5.4	Final refinement of $\text{Pb}_3\text{TeCo}_3\text{P}_2\text{O}_{14}$	138
5.5	Crystal structure comparison with the literature	143
5.6	Crystal structure $\text{Pb}_3\text{TeMn}_3\text{P}_2\text{O}_{14}$	145
5.7	Isosceles trimers	146
5.8	DC susceptibility of $\text{Pb}_3\text{TeCo}_3\text{P}_2\text{O}_{14}$	148
5.9	Field-dependence of $T_N$ in $\text{Pb}_3\text{TeCo}_3\text{P}_2\text{O}_{14}$	149
5.10	Magnetization vs field	150
5.11	High-field phase transition	151
5.12	High-field magnetization	152
5.13	Heat capacity and magnetic entropy	153
5.14	Heat capacity in fields	154
5.15	Phase diagram of $\text{Pb}_3\text{TeCo}_3\text{P}_2\text{O}_{14}$	155
5.16	Net trimer moment	157
5.17	Full magnetic unit cells	158
5.18	Magnetic cell refinements	159
5.19	Evolution of a magnetic reflection with temperature	160

---

5.20	Excitation contour map	163
5.21	Excitation fits	164
5.22	Susceptibility trimer fit	167
5.23	Triangular lattice of trimer clusters	168
6.1	Subcell refinement of $\text{Pb}_3\text{TeCo}_3\text{V}_2\text{O}_{14}$	175
6.2	Supercell refinement of $\text{Pb}_3\text{TeCo}_3\text{V}_2\text{O}_{14}$	177
6.3	$\text{Pb}_3\text{TeCo}_3\text{V}_2\text{O}_{14}$ final structure	183
6.4	Pb-decahedra	186
6.5	Comparison with other structure models	188
6.6	Magnetic susceptibility	191
6.7	Magnetic phase diagram of $\text{Pb}_3\text{TeCo}_3\text{V}_2\text{O}_{14}$	192
6.8	High-field magnetic susceptibility	193
6.9	Heat capacity	194
6.10	Dielectric constant	195
6.11	Neutron diffraction contour plot	196
6.12	Subcell magnetic unit cells	197
6.13	Supercell $T_{N1}\Gamma(1)$ refinement	198
6.14	Supercell $T_{N1}\Gamma(2)$ refinement	199
6.15	Magnetic structure at $T_{N1}$	200
6.16	Variation of moment at $T_{N1}$	201
6.17	Supercell $T_{N2}\Gamma(1)$ refinement	202
6.18	Supercell $T_{N2}\Gamma(2)$ refinement	203
6.19	Magnetic structure at $T_{N2}$	204
6.20	Possible first order transition	205
6.21	Inelastic excitations at $T_{N1}$	207
6.22	Inelastic excitations at $T_{N2}$	208

# List of Tables

3.1	Refined parameters for $\text{Ba}_3\text{NbFe}_3\text{Si}_2\text{O}_{14}$ . . . . .	71
4.1	Initial refinement of the $\text{Pb}_3\text{TeMn}_3\text{P}_2\text{O}_{14}$ subcell . . . . .	102
4.2	Joint refinement of the $\text{Pb}_3\text{TeMn}_3\text{P}_2\text{O}_{14}$ subcell . . . . .	104
4.3	$\text{Pb}_3\text{TeMn}_3\text{P}_2\text{O}_{14}$ subcell bond lengths . . . . .	104
4.4	Supercell refinement of $\text{Pb}_3\text{TeMn}_3\text{P}_2\text{O}_{14}$ (Part 1) . . . . .	107
4.5	Supercell refinement of $\text{Pb}_3\text{TeMn}_3\text{P}_2\text{O}_{14}$ (Part 2) . . . . .	108
4.6	Supercell refinement of $\text{Pb}_3\text{TeMn}_3\text{P}_2\text{O}_{14}$ (Part 3) . . . . .	109
5.1	Supercell refinement of $\text{Pb}_3\text{TeCo}_3\text{P}_2\text{O}_{14}$ (Part 1) . . . . .	139
5.2	Supercell refinement of $\text{Pb}_3\text{TeCo}_3\text{P}_2\text{O}_{14}$ (Part 2) . . . . .	140
5.3	Supercell refinement of $\text{Pb}_3\text{TeCo}_3\text{P}_2\text{O}_{14}$ (Part 3) . . . . .	141
5.4	Magnetic structure of $\text{Pb}_3\text{TeCo}_3\text{P}_2\text{O}_{14}$ . . . . .	144
6.1	Initial refinement of $\text{Pb}_3\text{TeCo}_3\text{V}_2\text{O}_{14}$ . . . . .	175
6.2	Supercell refinement of $\text{Pb}_3\text{TeCo}_3\text{V}_2\text{O}_{14}$ (Part 1) . . . . .	179
6.3	Supercell refinement of $\text{Pb}_3\text{TeCo}_3\text{V}_2\text{O}_{14}$ (Part 2) . . . . .	180
6.4	Supercell refinement of $\text{Pb}_3\text{TeCo}_3\text{V}_2\text{O}_{14}$ (Part 3) . . . . .	181
6.5	Bond lengths and bond valence sums (Part 1) . . . . .	184
6.6	Bond lengths and bond valence sums (Part 2) . . . . .	185

# Chapter 1

## Introduction

### 1.1 Introduction

What is materials science? The nature of this question is so broad that no single answer would be satisfying. Yes, materials science is the study of materials, but what is a material? Materials are everywhere and everything; they are composed of many atoms from elements on the periodic table, but the material as a whole is so much greater than the sum of its parts. Chemistry, Biology, Physics, and Engineering are all required to discover, create, understand, and use materials. Economics largely governs the types of problems materials scientists aim to solve. A beautiful symmetry is observed in materials science: every student of the discipline contributes a small part to the larger whole, and just like materials, the entire body of knowledge is greater than the sum of its parts.

This aim of this thesis is to keep with that tradition. Although historically more of a curiosity than a practicality [1], magnetic materials are used ubiquitously in society today for purposes such as information storage [2], quantum computing [3], or even as common fridge magnets. Transition metal oxides dominate this field, exhibiting further useful properties such as high-temperature superconductivity [4] and ferroelectricity [5]. This is largely due to the tunability of transition metal oxides through chemical substitution, their low toxicity, and their low cost of the starting reagents. Large families containing

many materials with similar structural motifs, but with vastly different properties such as the perovskites can be made by substituting various transition metal cations throughout the many atomic environments in the unit cell.

Langasites are typically materials with rare-earth atoms rather than transition metal ions. They are often used as piezoelectric materials, outperforming quartz (the industry standard) by a factor of three [6]. High quality single crystals can also be used as optical filters and polarizers [7]. While rare-earth ions have interesting properties of their own, they are a lot more difficult to locate and isolate from natural sources. Consequently, they are quite a lot more expensive. However, with some careful chemistry, it is possible to substitute rare-earth ions for cheaper transition metal ions that may impart new properties to members of the langasite family. It is these transition metal langasite materials and their associated magnetic properties that will be explored in this work.

The outline of this thesis begins with an introduction to magnetism, magnetic transitions, various magnetic interactions, ground states, and the consequences of crystal symmetry on magnetic transitions. Chapter Two describes the various experimental and computational techniques used in this thesis. I have attempted to mirror the level of detail within each experimental description to the amount of time spent using that particular technique, and its relative importance to my conclusions. Only one transition metal paramagnetic langasite has been studied in great detail previously:  $\text{Ba}_3\text{NbFe}_3\text{Si}_2\text{O}_{14}$ . Chapter Three is both a presentation of my results on this material and a literature review to set the rest of the results into proper context. Chapters Four, Five, and Six contain the bulk of my work on  $\text{Pb}_3\text{TeMn}_3\text{P}_2\text{O}_{14}$ ,  $\text{Pb}_3\text{TeCo}_3\text{P}_2\text{O}_{14}$ , and  $\text{Pb}_3\text{TeCo}_3\text{V}_2\text{O}_{14}$  respectively, including their preparation, detailed structural studies of the crystal and magnetic unit cells, magnetic properties and phase diagrams, heat capacities, dielectric and magnetic excitation spectra. Overall conclusions are presented in Chapter Seven.

## 1.2 Magnetism

The magnetic sources associated with an atom can be broadly classified as being either diamagnetic or paramagnetic. Diamagnetism arises from the bound charges in atom acting to shield the interior from an external magnetic field [8]. Classically, this effect is described by Lenz's law that states that when the flux through an electrical circuit is changed, an current will be induced that opposes that change. When considering an atom with spherical charge density, it is assumed that the motion of the electrons about the nucleus remains unchanged in upon the application of a magnetic field, except that the electrons precess with an angular frequency proportional to the field. Then the diamagnetic susceptibility is given as

$$\chi_{diamagnetic} = -\frac{\mu_0 N Z e^2}{6m} \langle r^2 \rangle \quad (1.1)$$

where  $N$ ,  $Z$ ,  $e$ ,  $m$ , and  $\langle r^2 \rangle$  are the number of atoms per unit volume, number of electrons, electronic charge, electronic mass, and radial distribution respectively. This result can also be derived using a quantum mechanical treatment of the atom and first-order perturbation theory.

Paramagnetism is responsible for the familiar magnetic phenomenon. A paramagnetic material is simply one that contains unpaired electrons that, when placed in an external magnetic field, work to internally augment the magnetic field rather than oppose it [1, 8]. In the early 20<sup>th</sup> century, quantum mechanics was being developed as a means of understanding the electronic configuration of an atom. Pauli discovered a principle that states that no two electrons can have the same set of quantum numbers that dictate the electron's energy, orbital angular momentum, and orientations of the orbital and spin angular momenta. The latter two properties are directly responsible for the atomic magnetic moment. Electrons have negative charge and orbit the nucleus with angular moment  $\vec{L}$ . The orbital magnetic moment  $\vec{\mu}_L$  is given as

$$\vec{\mu}_L = -\frac{e}{2m_e}\vec{L} \quad (1.2)$$

where  $e$  is the elementary charge of an electron and  $m_e$  is its mass. However, the angular momentum is peculiar here due to Heisenberg's Uncertainty Principle that states that the absolute direction of  $\vec{L}$  cannot be precisely known (Figure 1.1). Only the magnitude of  $\vec{L}$  is known and is quantized according to  $\hbar\sqrt{L(L+1)}$ , where  $L$  is the azimuthal quantum number and  $\hbar$  is defined as Planck's constant divided by  $2\pi$ . The spin angular momentum gives rise to the spin magnetic moment  $\vec{\mu}_S$ , given as

$$\vec{\mu}_S = -\frac{e}{2m_e}\vec{S} \quad (1.3)$$

where  $\vec{S}$  is an intrinsic angular momentum. It takes on a value of  $\hbar\sqrt{S(S+1)}$ , where  $S$  is only 1/2 for electrons. There is no classical analogue to the intrinsic angular momentum, but one could envision an electron spinning on its own axis with a fixed value either clockwise or anticlockwise as a rough approximation [8–10]. According to the Pauli principle, electrons are added one-by-one first to unoccupied orbitals followed by singly occupied orbitals. Only two electrons can have the same orbital angular momentum, but they must have opposite spin. Because of the spatial symmetry of the atom, positive orbital angular momentum is equally as likely as negative orbital angular momentum. If all electrons in an atom are paired, then the addition of all the orbital and spin angular momentum vectors sum to zero and produce no net magnetic moment. That is, due to *the way* that the electrons fill atomic orbitals, only unpaired spins can result in an atomic moment. Nuclear magnetism exists as well, but its effects are orders of magnitude weaker than the electrons because of the differences in masses [11].

The total atomic magnetic moment is found by combining both the orbital and spin angular momenta of all of the unpaired electrons. From a classical perspective, when the exact orientations of the momentum vectors are not known a distribution of values is found through vector addition of  $\vec{L}$  and  $\vec{S}$

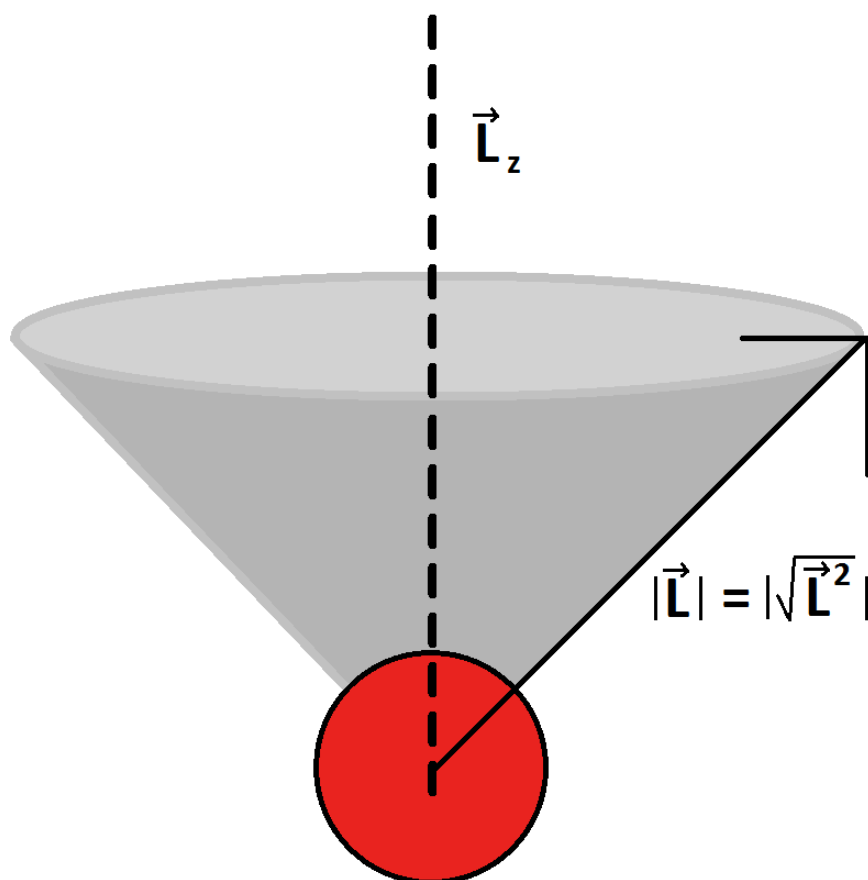


FIGURE 1.1: Only one directional component (usually defined as the  $z$ -component) of the angular momentum can be known precisely. The total angular momentum squared can also be known precisely, from which the magnitude of the total angular momentum can be derived.

$$\vec{J} = \vec{L} + \vec{S} \quad (1.4)$$

where  $L$  is the sum over all  $z$ -components of the orbital angular momenta of the electrons and  $s$  is the sum over all of the spin components of the electrons. In reality,  $J$ ,  $L$ , and  $S$  are operators; whenever a measurement is performed via these operators, the collapse of the wavefunction of the system will result in a moment consistent with the probability distribution. All three components of the moment cannot be precisely known because no



two operators describing the measurements of two moment components commute with each other. Inner electron shells will always sum to zero such that only the valence shell needs to be considered. For valence shells less than half full,  $J = L - S$ . For valence shells more than half full,  $J = L + S$ . Valence shells that are exactly half filled have  $L = 0$ . The total atomic magnetic moment is then [8]

$$\vec{\mu} = \gamma \hbar \vec{J} = -\frac{ge\hbar}{2m_e} \vec{J} = -g\mu_B \vec{J} \quad (1.5)$$

where  $\gamma$  is the gyromagnetic ratio, the ratio of the magnetic moment to the angular momentum, composed of the g-factor and the Bohr Magneton,  $\mu_B$ , which is the spin magnetic dipole moment of a free electron. The g-factor for an electron spin is 2.0023, while for an atom, it is given by

$$g = 1 + \frac{J(J+1) + S(S+1) - L(L+1)}{2J(J+1)}. \quad (1.6)$$

What is perhaps more important than the atomic magnetic moment is how the moments interact with each other. Magnetic moments are dipoles that weakly interact according to an inverse cubic relationship (Figure 1.2)

$$U \propto \frac{1}{r^3} (\vec{m}_i \cdot \vec{m}_j - 3(\vec{m}_i \cdot \hat{r}_{ij})(\vec{m}_j \cdot \hat{r}_{ij})) \quad (1.7)$$

where  $\vec{m}_{i,j}$  are the dipole vectors and  $\hat{r}_{ij}$  is the vector defining the closest  $r$  distance between the two atoms.

This is a classical relationship with a maximum value occurring when the moments are antiparallel to each other and parallel to  $\hat{r}_{ij}$ . The energy scale for these dipolar interactions is on the order of a milli-electron-volt (meV) and cannot explain magnetism observed at higher energy scales, such as that found at room temperature [8]. For quantum systems, the exchange interaction between electronic orbitals is responsible for magnetic correlations

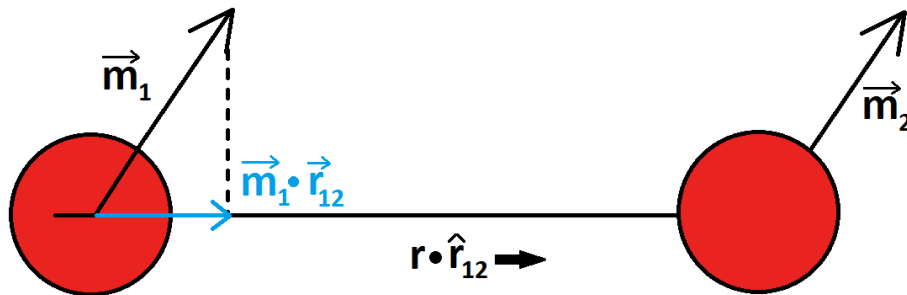


FIGURE 1.2: Magnetic moments are dipoles that interact according to equation 1.7.  $\hat{r}_{12}$  is the unit vector in the direction of the bond length and is depicted by the black arrow.

$$H = -J_{ex} \sum_{i,j} \vec{s}_i \cdot \vec{s}_j \quad (1.8)$$

where  $H$  is the Hamiltonian from the interaction,  $J_{ex}$  is the exchange integral (not to be confused with the total angular momentum quantum number  $J$ ), and  $\vec{s}_{i,j}$  are the spin vectors for the electrons. Like the spin angular momentum, there is no classical analogue of the exchange integral; it arises from the antisymmetry requirement of the wave function of a multi-electron system (the Pauli principle is also a direct consequence of this requirement) [10]. When  $J_{ex} > 0$ , the system prefers a ferromagnetic interaction where moments tend to align parallel to each other. Alternatively when  $J_{ex} < 0$ ,  $H$  is minimized when moments align antiparallel to each other. Direct exchange is rare in transition metal oxide insulators. Instead, exchange is usually mediated through an oxygen ligand atom since most transition metal cations occupy the centres of coordination polyhedra. This is called superexchange. The Goodenough-Kanamori rules [12, 13] are used to predict if the exchange interaction should be positive or negative and depends on the metal-oxygen-metal bond angle, the  $d$ -orbitals involved, and the level of hybridization with oxygen  $2p$  orbitals. Of course, more complexity in the system will result in a strong deviation from these rules [14].

Another type of interaction involves coupling of the magnetic moments to the lattice itself. This type of interaction is called antisymmetric exchange, or the Dzyaloshinskii-Moriya interaction after Dzyaloshinskii, who first observed the phenomenon [15], and Moriya, who first deduced the microscopic mechanism from spin-orbit coupling: the coupling of an electron's spin with its orbital motion [16]. This interaction is quantified by

$$H_{\text{DM}} = \vec{D}_{ij} \cdot (\vec{s}_i \times \vec{s}_j) \quad (1.9)$$

where the orientation of  $\vec{D}_{ij}$  is constrained by the geometry of the metal-ligand-metal bond (Figure 1.3). This interaction is responsible for magnetic moment canting due to small shifts in the position of the ligand, but the inverse effect is commonly observed as well, where moment canting results in small ligand shifts. Especially in chiral materials, shifts in the same direction can result in a net electric polarization in some materials [17].

Now that some basic types of magnetic interactions in metal oxide insulators has been discussed, the question regarding how one measures these interactions must be answered. The magnetic susceptibility, which measures how a material behaves in a magnetic field, is used as a quick probe of the interactions. The orbital and spin angular momenta both give rise to a magnetic field,  $\vec{B}$ . Orbital motions of the electrons adjust to create an internal magnetic field that opposes the external one (Lenz's law), while the coupling of the intrinsic spin moment with the field creates a torque that tends to align the moment with the field [1]. All materials exhibit the opposing internal field due to orbital motion. This is the diamagnetic contribution to the susceptibility and is typically very weak (in fact, it is ignored for the materials studied in this thesis) [8]. The latter property due to the intrinsic spin motion only manifests in a net moment if there are unpaired electrons; this effect can be quite strong for these materials. The magnetization  $\vec{M}$  of a material is defined as the magnetic dipole density within the material: the total magnetic field can then be divided into the component that is bound to the system and that from free electric currents,  $\mu_0 \vec{H}$  (often thought of as the external field). The

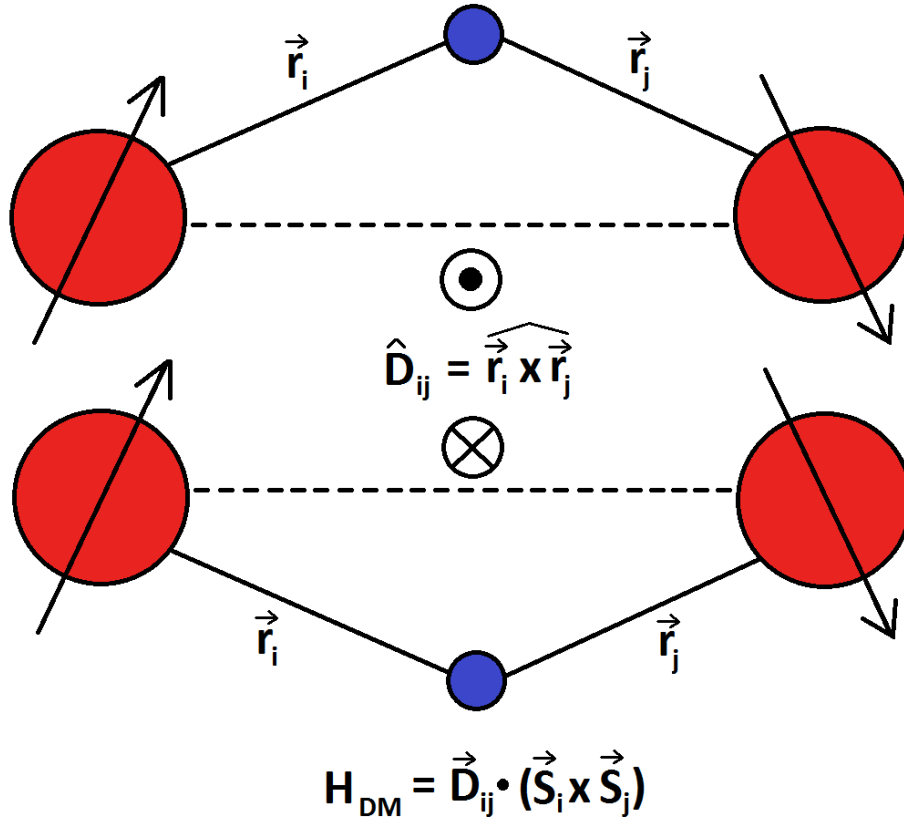


FIGURE 1.3: The Dzyaloshinskii-Moriya interaction is also known as the antisymmetric interaction due to the orientation of  $\hat{D}_{ij}$ . Two separate cases are shown in this figure. Metal centres are depicted as large red circles while the ligand is a small dark blue circle. The orientation of  $\hat{D}_{ij}$  is shown coming out of the page (dotted circle) or going into the page (crossed circle) dependent on the ligand shifting direction.

magnetic susceptibility  $\chi$  is defined as [8, 18, 19]

$$\chi = \frac{\vec{M}}{\mu_0 \vec{H}}. \quad (1.10)$$

Given that  $\mu_0 \vec{H} > 0$ , if  $\chi < 0$ , then  $\vec{M} < 0$  and the material is diamagnetic (similarly,  $\chi > 0$  for paramagnetic materials).

For paramagnetic materials, the Curie-Weiss law can be used to describe the temperature dependence of the susceptibility of the material. If the interactions between the unpaired

magnetic moments are much smaller than the energy scale set by  $k_B T$ , then the Curie-Weiss law is

$$\chi = \frac{C}{T - \theta_{\text{CW}}} \quad (1.11)$$

where  $C$  is the Curie constant given by  $C = \mu_0 N g^2 \mu_B^2 J(J+1)/(3k_B)$  and  $\theta_{\text{CW}}$  is the Weiss temperature, which is a measure of the average interaction energy between moments. Calculated values of  $C$  typically compare very well to experiment, especially for rare-earth magnetic materials. However, they fail for  $3d$  transition metal magnetism. This is because the orbital component of the magnetism is quenched due to the highly extending outermost  $3d$  orbitals participating in bonding. Crystal fields give a large non-uniform potential that can quench the contribution of  $\vec{L}$  to  $\vec{J}$ . By contrast, the unpaired electrons in rare-earth ions are in the  $4f$  orbitals that are located much closer to the nucleus where a more uniform potential exists. At temperatures above  $\theta_{\text{CW}}$ , a material is expected to behave like a typical paramagnet, but as the temperature is lowered,  $k_B T$  becomes comparable to the exchange energy. This results in a divergence of the susceptibility away from the Curie-Weiss law. For most systems that can be described this way, when  $T < \theta_{\text{CW}}$  the system transitions into a magnetically ordered state, where thermal effects are no longer strong enough to overcome the orienting internal exchange field: a ferromagnet if  $\theta_{\text{CW}}$  is positive where moments order parallel with respect to each other or an antiferromagnet if  $\theta_{\text{CW}}$  is negative and the moments are oriented antiparallel to each other. Before concluding this section it is worth pointing out that the atomic moment  $\vec{\mu}$  is both temperature and field dependent. This is because in a field, the different angular momentum quantized states become non-degenerate, splitting by a factor of  $g\mu_B m_J \mu_0 |\vec{H}|$ , where  $m_J$  are integers equal to  $-J, -J+1, \dots, J-1, J$ . These states will be populated differently at different temperatures (Figure 1.4) [20]. It is convenient to define a temperature-independent effective moment from the Curie constant [8]

$$\mu_{\text{eff}} = g\sqrt{J(J+1)}\mu_B \approx 2.82\sqrt{C}. \quad (1.12)$$

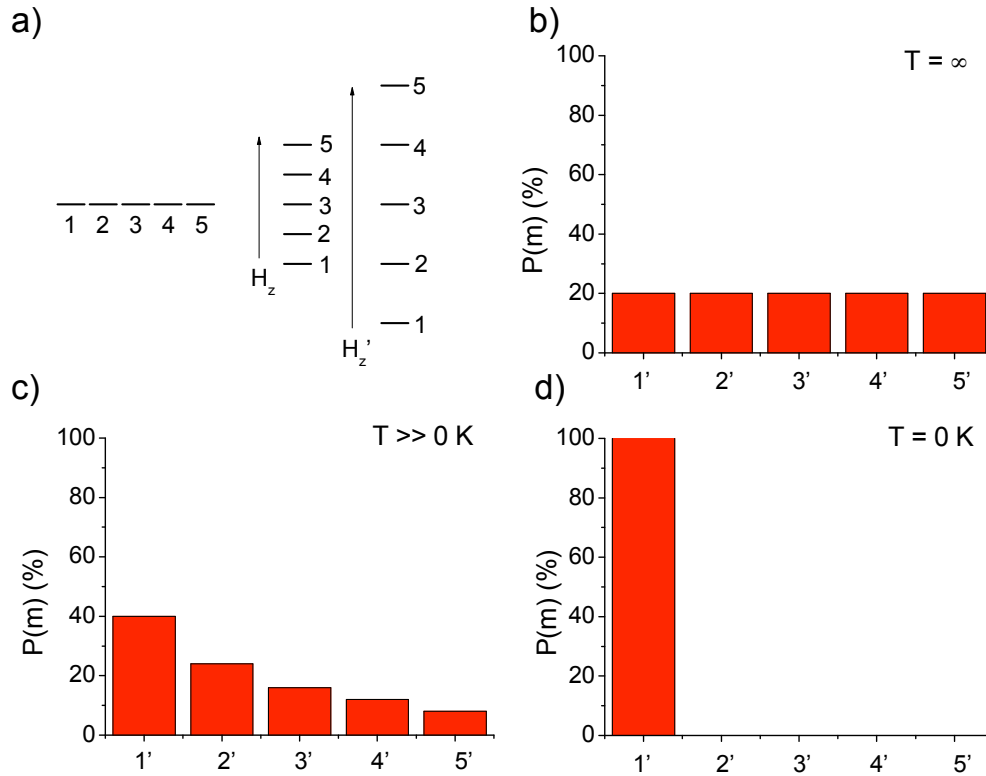


FIGURE 1.4: **a)** Five magnetic states labelled 1 through 5 are degenerate in the absence of a magnetic field  $\vec{H}_z$ . The application of a field splits these states into different energy levels, the splitting being dependent on the strength of the field. For the purposes of this figure, the state with the lowest energy level in a field is renamed 1' while the state with the highest energy level is renamed 5'. At  $T = \infty$  all states are populated equally by the magnetic dipoles in the solid (**b**). As the temperature is lowered towards 0 K, the population distribution becomes more favoured towards the lower energy states (**c**) until only the ground state is populated in the limit of 0 K (**d**).

### 1.3 Magnetic ground states and geometric frustration

Due to the particular way that transition metal oxides tend to bond, most are insulators and most have antiferromagnetic interactions between the moments due to super exchange. When the temperature is lowered such the interaction energy is much larger than  $k_B T$ , the magnetic moments no longer find it energetically favourable to constantly fluctuate in random orientations as they would for a typical paramagnet. Instead the moments prefer to behave more statically and align themselves in antiparallel arrangement.

However, this is only the simplest case of magnetic order. In addition to antiferromagnetism, there are many types of ground states that have been observed in transition metal oxides including ferromagnetism [21], ferrimagnetism [22], spin density waves [23], helical ordering [24], and cycloidal ordering [25] (Figure 1.5). The search for the lowest energy configuration (ground state) of the moments in materials at low temperatures is a huge branch of materials science, particularly when lattice geometry plays a role.

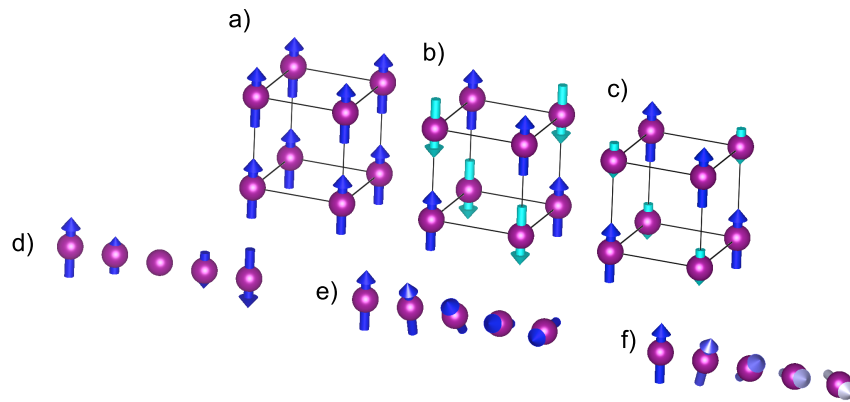


FIGURE 1.5: A survey of different magnetic ground states. These are **a)** ferromagnetism, **b)** antiferromagnetism, **c)** ferrimagnetism, **d)** spin density waves, **e)** helical ordering, and **f)** cycloidal ordering. Some antiparallel moments are coloured light blue as a guide to the eye. Ferromagnetism and ferrimagnetism both have net moments oriented in the direction of the dark blue moments. Spin density waves have real basis vectors with a non-zero sine component to the propagation vector. Helical and cycloidal order are similar to spin density waves except that the basis vectors are now complex. The difference between helical and cycloidal order lies in how the basis vectors are oriented: If the basis vectors lie in a plane perpendicular to the propagation vector, then a helix results. If there is some basis vector component parallel to the propagation vector (coloured white as a guide to the eye), cycloidal order results. This is explained in more detail in Chapter 2.

It has been shown in the previous section that magnetic moment interactions can be coupled to the crystal lattice. The mere geometry of the lattice can heavily influence the magnetic ground states of an antiferromagnet. For example, if antiferromagnetic moments constrained to point along one axis were arranged in triangular fashion, the magnetic system is unable to minimize the interaction energies between all moments

simultaneously, even at 0 K [26–28] (Figure 1.6). Geometrically frustrated materials typically do not order at the temperature defined by  $\theta_{\text{CW}}$ ; in fact, some show no signs of ordering at all despite strong interactions [29–32]. How does a system overcome the effects of geometric frustration? This is generally achieved through an energetic compromise. A “normally” higher energy ground state will be adopted by the system such as a state with mixed ferromagnetic and antiferromagnetic interactions. These energetic compromises frequently lead to unique ground states, which may, and often do, lead to exotic physical properties that could one day be manipulated for practical applications. Researchers are constantly trying to find materials with geometrically frustrated lattices such as the triangular lattice [33], the kagomé lattice [34], and the pyrochlore lattice [35] in an effort to study the consequences imposed by these energetic compromises.

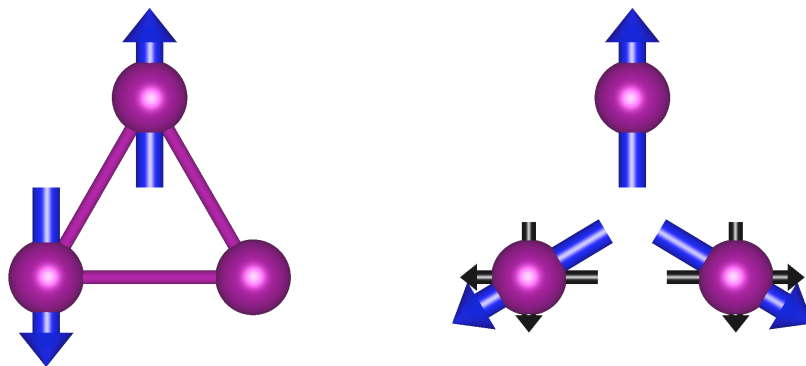


FIGURE 1.6: A triangular lattice geometry prevents the system from simultaneously satisfying all of the antiferromagnetic interactions. The third will always be parallel to a neighbouring moment regardless of its orientation. Instead, the system tends to reach an energetic compromise, such as that shown on the right. Note that the horizontal components of the bottom moment vectors are antiparallel while the vertical components are parallel.

One example of a unique magnetic ground state relevant to the studies presented here is a special case of multiferroic behaviour. Multiferroics are materials that traditionally exhibit at least two or more of the following primary ferroic orders: ferromagnetism,



ferroelectricity, ferroelasticity, and ferrotoroidicity [36, 37]. Most are familiar with ferromagnetism as being the spontaneous appearance of sample magnetization even in the absence of an external magnetic field. Likewise, ferroelectricity and ferroelasticity are the spontaneous appearance of an electric dipole moment and strain in the absence of an electric field and stress respectively. Ferrotoroidicity has only recently been observed experimentally and is the spontaneous formation of long-range ordered toroid moments arising from spin vortices. More generally these properties share the feature that their “order” remains even in the absence of the disturbing force. This is because ferroic materials form ordered domains separated by domain walls that form as a result of the system lowering its overall energy. For example, ferromagnetic domains form where within each domain moments are aligned parallel to each other but the domains are not necessarily aligned with respect to each other. In a ferromagnet with a single domain, a large dipole over the entire system would lead to a high magnetic energy; the formation of unaligned domains results in a small dipole and lowers the overall magnetic energy. In any ferroic material, these domains will align in the presence of some disturbing field [8]. Order alone due to geometric frustration is not enough for practical applications; domains are necessary and control over these domain walls lies at the crux of many technologies, not the least of which include data storage. These ferroic orders can be beautifully classified based on how they behave when space or time symmetry is broken [37] (Figure 1.7). However, a broader definition of the term “multiferroic” is now used to describe a magnetically ordered material that is also ferroelectric, ferroelastic, or ferrotoroidic. The definition includes those materials with complex magnetic structures that can exhibit a ferromagnetic component and lead to the formation of domains. While each of these ferroic properties are worthy of study individually, it is the coupling *between* these properties in multiferroics that is most exciting for technological applications, such as being able to control the electron’s spin using an electric field and vice versa [17].

Because these ferroic orders depend on different symmetry requirements, combining them into a single material has proven quite difficult. Furthermore, the microscopic

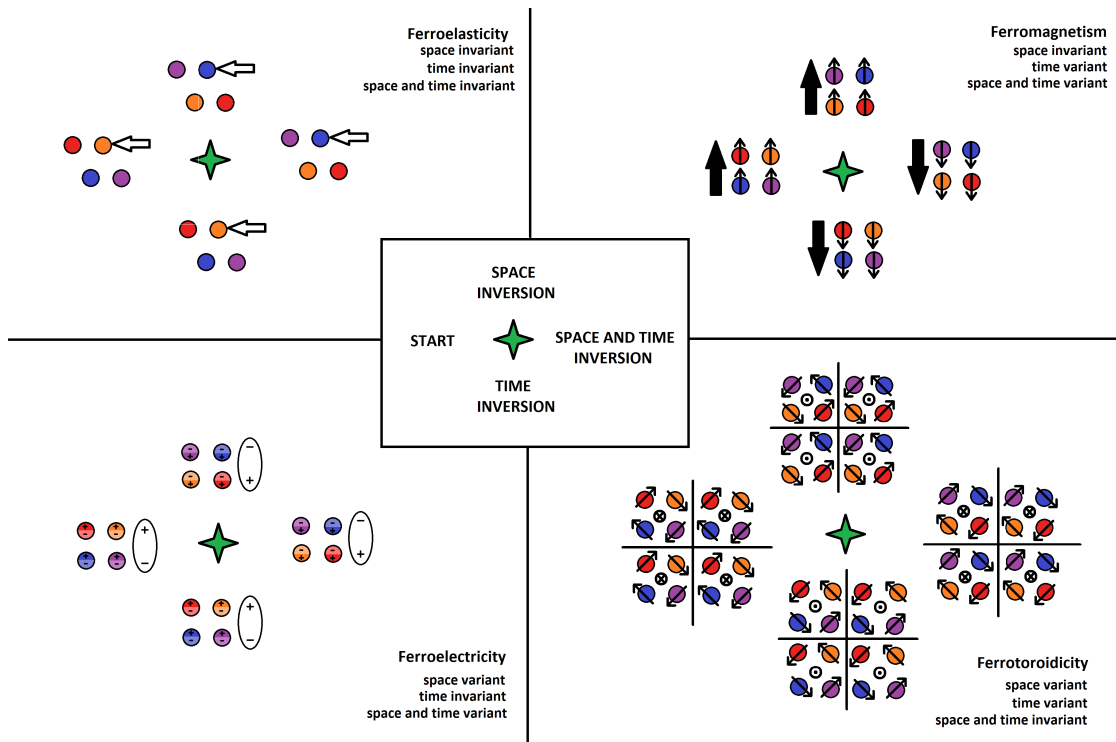


FIGURE 1.7: The primary ferroic orders all behave differently under space or time inversion. Ferroelasticity is invariant under both space and time, ferromagnetism is invariant under space only, ferroelectricity is invariant under time only, and ferrotoroidicity is invariant under none alone.

mechanisms behind the ferroic properties tend to differ between materials. As a result, multiferroics are often discovered by accident. Multiferroics can be classified according to the mechanism for ferroelectricity. Proper multiferroics exhibit strong ferroelectricity either via electron hopping through hybridized empty  $3d^0$  to oxygen  $2p$  orbitals or via electronic lone pair polarization [36]. Obviously the former mechanism excludes the possibility of ferromagnetism, which requires partially filled orbitals. The latter mechanism has yielded room temperature multiferroics such as  $\text{BiFeO}_3$  [38], but the electronic and magnetic properties are decoupled. Improper multiferroics are those where electric polarization comes as a secondary effect through a structural or magnetic phase transition, or through charge ordering. In these cases, the electric polarization is usually much weaker but tends to be coupled to the other ferroic orders. Geometric frustration is an avenue for discovering new multiferroics where the orders are coupled due to the complexity of the magnetic states that often result.

## 1.4 Final notes

This chapter has introduced the concepts behind magnetism, magnetic transitions, magnetic ground states and the influence that geometric frustration can have on those states. Multiferroic behaviour with strong magnetoelectric coupling was highlighted as an example of some of the exotic states that can arise from geometrically frustrated sublattices. In 2008,  $\text{Ba}_3\text{NbFe}_3\text{Si}_2\text{O}_{14}$  (one of the first discovered paramagnetic langasites) was shown to exhibit a fascinating, unique single-domain doubly chiral magnetic structure predicted to give rise to ferroelectric polarization. This was the first langasite to show multiferroic properties, even using the broadest definition of the word. The work presented in this thesis starts there, in Chapter Three, and works to explore the rich variety of magnetic ground states in new transition metal oxide langasites.

## Chapter 2

# Experimental Techniques

In examining the structures and magnetic ground states of various langasites, a variety of experimental techniques will be mentioned. This chapter provides an overview of each of these techniques.

### 2.1 The Ceramic method

Throughout history there have been many methods that have been used to create bulk materials in the solid state including, but not limited to, the use of melts [39], precipitation [40], evaporation [41], chemical vapour transport [42], and electrochemical synthesis [43]. The preparation of solid-state materials and development of these techniques has traditionally depended on the demands of industry at the time [44, 45]. Currently, one of the most popular methods to prepare metal-oxide materials is the ceramic method. Commonly referred to as “shake-and-bake” chemistry, the ceramic method is so wide spread due to its ease of use and relatively low overhead costs.

The theory behind the ceramic method is simple: given enough energy, two materials in contact in the right orientation with each other will react to form products at the interface (Figure 2.1) [44]. There are many ways to induce this type of reaction, but all of them are based on increasing the kinetic energy of the system, increasing contact between the materials, or placing the reactant molecules in a more favourable orientation. In a

typical reaction, solid oxide powders will be combined in stoichiometric amounts and finely ground together. Grinding serves as a means of maximizing the surface area of the reactant powders. Often, the ground-up reactant particles are pelleted to maximize the contact between reactant particles. Next, the reactants are heated to increase the kinetic energy of the system. Reactant particles must diffuse to the interface in order to react. Increasing the kinetic energy also increases the rate of diffusion, but heating is not the only way to do this. Reactants that degrade when heated introduce defects into the system that increase the overall diffusion rate by increasing the amount of local “diffusive sites”. The orientations of the reactants matter as well; the rate of reaction is commonly increased when reactants with similar crystal structures to each other, and to the product, are used. Reactions of this type are called topotactic (or epitactic for a two-dimensional surface).

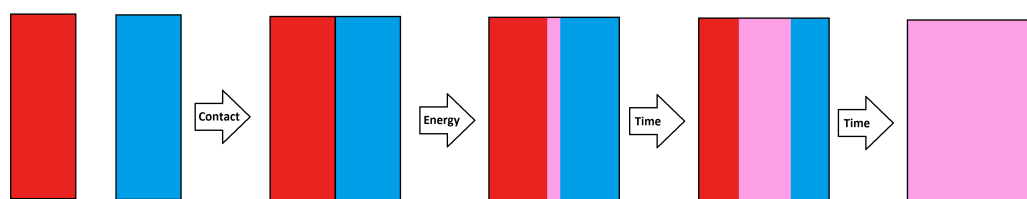


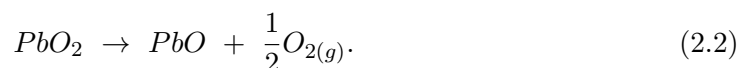
FIGURE 2.1: Two materials in contact with the right orientation and enough energy will react at the interface.

Despite its ease, there are many drawbacks of the ceramic method. The primary disadvantage is that the use of high temperatures makes it all but impossible to isolate kinetically metastable products that may form at lower temperatures. High temperatures also make it difficult to work with volatile reactants such as  $\text{SnO}_2$ . Additionally, the thermodynamics of high temperature reactions tend to favour products with greater entropy

$$dG = dH - TdS \quad (2.1)$$

where  $G$  is the Gibbs free energy,  $H$  is the enthalpy,  $T$  is the temperature, and  $S$  is the entropy (note that constant pressure is assumed here). This means that reactants with

multiple oxidation states will tend to favour lower ones due to the degradation of the initial product, as in  $PbO_2$  for example [46, 47]:



There are methods to deal with many of these issues including adding additional volatile reactants as a compensation mechanism, pre-reaction at lower temperatures, working with different atmospheres (oxidizing, reducing, inert, or vacuum), different crucibles ( $Al_2O_3$ , Pt, etc.), and working under different pressures.

## 2.2 Diffraction

### 2.2.1 Introduction

The Nobel Prize in physics was awarded to Max von Laue in 1914 for his discovery of the diffraction of x-rays by crystals, and again in 1915 to William Henry and William Lawrence Bragg for their services in the analysis of crystal structures by means of x-rays. The discovery by von Laue not only shed light on the nature of the x-ray, but also showed that solids were composed of atoms arranged on a lattice. The Braggs' discovery made simple the connection between the x-ray wavelength and the arrangement of the atoms within the lattice. Additionally, they built a device that could be used to analyze the structure of solids, called a diffractometer.

Diffraction is a property of wave-like entities wherein waves will bend around an obstacle or opening. The effect is most pronounced when the “slit-width” is of a similar size to the wavelength. Light and matter both have wave-particle duality and are both able to diffract. Electromagnetic radiation (EMR) has the energy-momentum relationship defined in the following equation:

$$E_{\text{EMR}} = |\vec{p}|c = \frac{hc}{\lambda} \quad (2.3)$$

where  $\vec{p}$  is the photon momentum,  $c$  is the speed of light,  $h$  is Planck's constant, and  $\lambda$  is the wavelength. Alternatively, the energy-momentum relationship for matter is found to be

$$E_{\text{matter}} = \frac{|\vec{p}|^2}{2M} = \frac{h^2}{2M\lambda^2} \quad (2.4)$$

where  $M$  is the mass of the unit matter. Due to the differences between light-matter and matter-matter interactions, structure determination by light or matter diffraction will yield differing results: each type of diffraction is complimentary to the other.

X-rays interact with the electron cloud of an atom. As a result, the more electrons an atom has, the higher the degree of interaction between the atom and the x-ray. Heavy elements such as Pb are quite “visible” using x-ray diffraction. When heavy elements exist in extended solids, the interaction of the material with x-rays is such that it becomes quite difficult to detect lighter elements such as O. Due to both the wavelength of the x-rays used and the presence of absorbing elements, the penetration depth of x-rays is only a few microns in the diffraction experiments described in this work [18, 48]. X-rays have a wavelength on the order of Ångstroms (Å), which gives them an energy on the order of kilo-electron-volts (keV). This energy is well beyond the average energy of excitations in solids, but is typical of the energy of inner-electron transitions of the atoms composing the solids (the treatment of inelastic x-ray scattering is beyond the scope of this work). The advantage with using x-rays is that it is easy to produce them in a laboratory setting with a high photon flux (photons/sec/unit area). In fact, x-ray diffraction is routinely and ubiquitously used in the study of new materials.

On the other hand neutrons interact with the nuclei of atoms, allowing them to penetrate far deeper into the material on the order of centimetres (cm). This also allows neutrons to interact with elements without any clear dependence on an atomic property such as the number of electrons it has (this makes elements like O quite visible with neutrons where they are virtually invisible with x-rays) (Figure 2.2). Neutrons are able

to discern between different elemental isotopes: H and D (Deuterium) scatter neutrons very differently. Because neutrons are matter and have mass, a wavelength on the order of Ångstroms imparts an energy on the order of milli-electron-volts (a factor of one million smaller than x-rays), which is also on the order of  $k_B T$  excitations observable in solids (inelastic neutron scattering will be discussed in another section). Furthermore, neutrons have a magnetic moment that allows for an additional interaction with the moments from unpaired electrons, giving rise to magnetic diffraction. However, neutrons are much harder to produce in the flux required for scattering experiments. In this thesis, a common theme will be structure determination using data obtained with both x-rays and neutrons.

### 2.2.2 Formalism

A lattice is a mathematical array of points that infinitely and periodically repeat in space with some dimension [19, 50]. For three dimensions, any lattice point  $W$  can be found by

$$\vec{W} = m\vec{a}_1 + n\vec{a}_2 + o\vec{a}_3 \quad (2.5)$$

where  $m$ ,  $n$ , and  $o$  are integers and  $\vec{a}_i$  are vectors defining the space, the lengths of which are called lattice parameters. A unit cell is a volume of space that, when translated, can completely fill space without overlap. A primitive unit cell contain only one lattice point (Figure 2.3). To describe a crystal, a basis is required. This basis is composed of the atoms of the unit cell. A basis is convoluted with the lattice to create a crystal structure.

When x-rays are made incident upon a crystalline solid, the parallel planes of atoms in the solid behave as a diffraction grating for the x-rays (Figure 2.4). X-rays constructively interfere with each other to give rise to a diffraction pattern that uniquely identifies the type of structure being studied. The Braggs found that this characteristic pattern of diffracted x-rays also heavily depends on the wavelength of the x-rays. For single crystals, the diffracted x-rays form point-like regions of high intensity, while they form



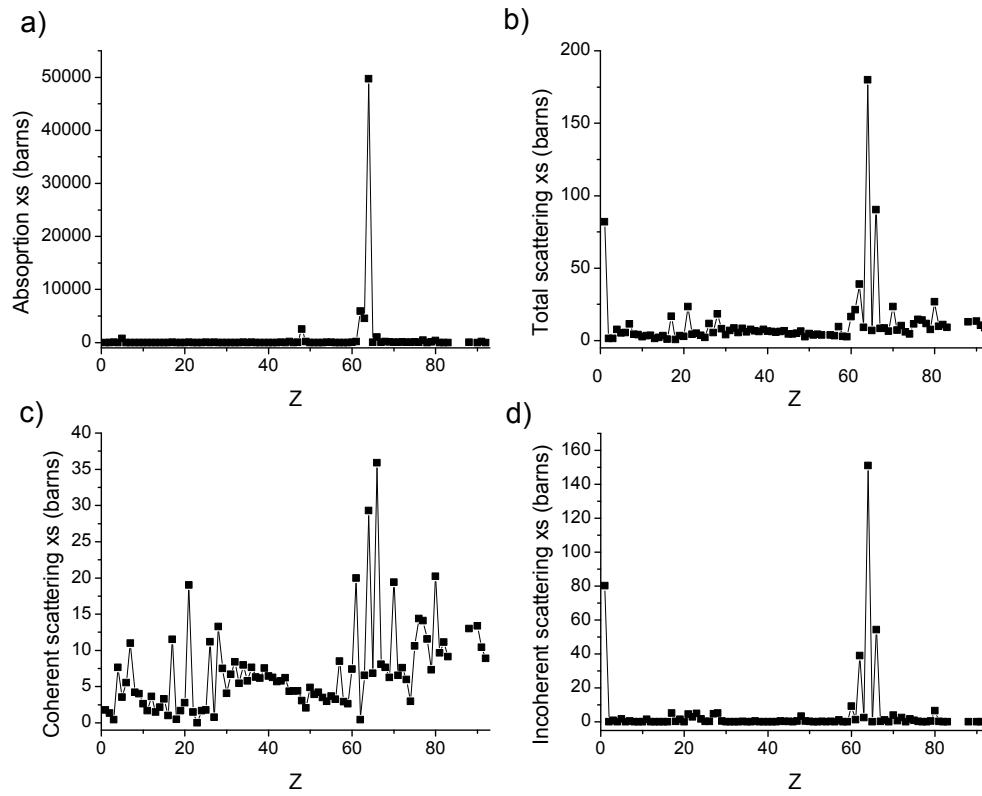


FIGURE 2.2: While the scattering length describes the potential felt by the neutron by the nucleus, the scattering cross section is the effective area that the neutron scatters off of. The absorption (a), total (b), coherent (c), and incoherent (d) scattering cross sections are shown. Strong absorbers should be avoided. While it may be tempting to look at the total scattering cross section to determine how an element might behave during the experiment, it is important to look at both the coherent and incoherent cross sections separately. For example, hydrogen has a low absorption cross section and a strong total scattering cross section, but the bulk of that is incoherent scattering that only contributes to the background noise rather than Bragg scattering [49].

high intensity cones for powder samples. Integrating over the intensity radially outward from the incident beam through these cones gives rise to the familiar Bragg peaks found in a typical powder diffractogram. The Braggs put together their findings into a single elegant equation used to describe the constructive interference condition of the diffracted x-rays:

$$2d\sin\theta = n\lambda \quad (2.6)$$

where  $d$  is the spacing between planes,  $\theta$  is the incident angle of the x-ray beam to the

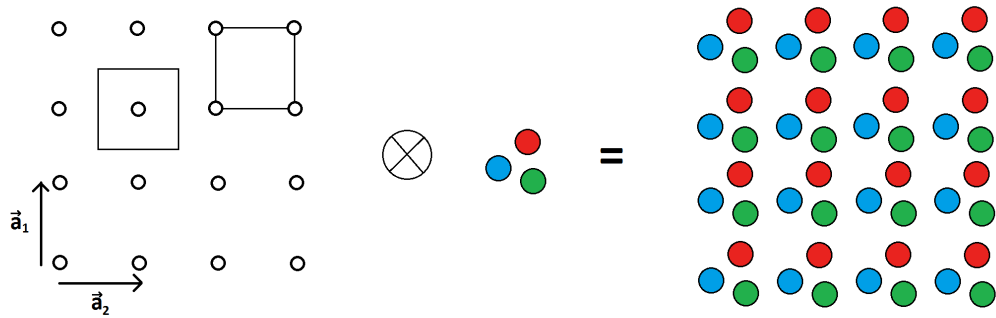


FIGURE 2.3: The primitive cell of a lattice contains one lattice point and can be translated anywhere repeatedly to fill space without overlap. Although the lattice is merely a mathematical construct, if a basis consisting of a set of atoms is convoluted with the lattice, one obtains a crystal structure.

plane of atoms,  $\lambda$  is the x-ray wavelength, and  $n$  is an integer. One can imagine that if the diffraction pattern and x-ray wavelengths are known, then it should be possible to work backwards to draw a map of the spaces between atoms in the structure. The Bragg problem approximates diffraction as x-ray reflection from flat planes of atoms. However, this interpretation is somewhat simplistic for two reasons. Firstly, diffraction can occur in other scattering geometries such as transmission. Secondly, no information regarding the identities of the atoms composing planes can be extracted using their equation: the Bragg equation can only identify the positions of the peaks.

The oscillating electromagnetic field of x-rays forces the electrons to oscillate with the same frequency, causing the electrons to emit new x-rays responsible for the observed constructive interference [48, 51, 52]. In the following discussion of the von Laue treatment, the magnetic component of the electromagnetic field is ignored since it is quite weak compared to the electric component. The electric field at point  $\vec{r}$  and time  $t$ ,  $\vec{E}(\vec{r}, t)$ , can be written as a wave equation:

$$\vec{E}(\vec{r}, t) = E_0 e^{i(\vec{k} \cdot \vec{r}) - i\omega t} \quad (2.7)$$

where  $E_0$  is the wave amplitude,  $\vec{k}$  is the wave vector defined as having magnitude  $\frac{2\pi}{\lambda}$

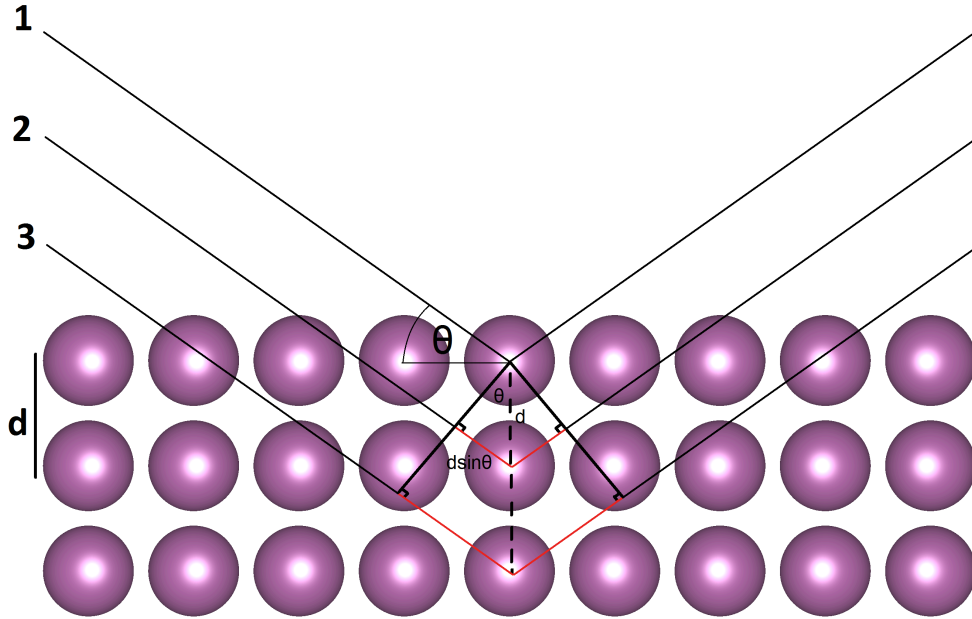


FIGURE 2.4: In order to get constructive interference of waves 1, 2, and 3, the extra path travelled by wave 2 must equal the wavelength. Similarly, wave 3 must travel “two wavelengths” to remain in phase with wave 1. This is generalized in Bragg’s law (equation 2.6).

and pointing in the direction of the wave propagation,  $\omega$  is the angular frequency of the field oscillation, and  $t$  is the time. Only the real part of the wave can be observed as the intensity,  $I$ :

$$I = |E_0 e^{i(\vec{k} \cdot \vec{r}) - i\omega t}|^2 = |E_0|^2. \quad (2.8)$$

If the x-ray source and detector are held at position  $\vec{R}$  and  $\vec{R}'$  respectively, and are located far from the point of scatter  $\vec{r}$ , then one can approximate the x-rays as plane waves (Figure 2.5). The relative electric field at point  $\vec{r}$  is then given as

$$\vec{E}(\vec{r}, t) \propto e^{i(\vec{k} \cdot (\vec{r} - \vec{R})) - i\omega t} \quad (2.9)$$

that will give rise to scattered x-rays in all directions, although only the direction towards the detector is of interest right now.

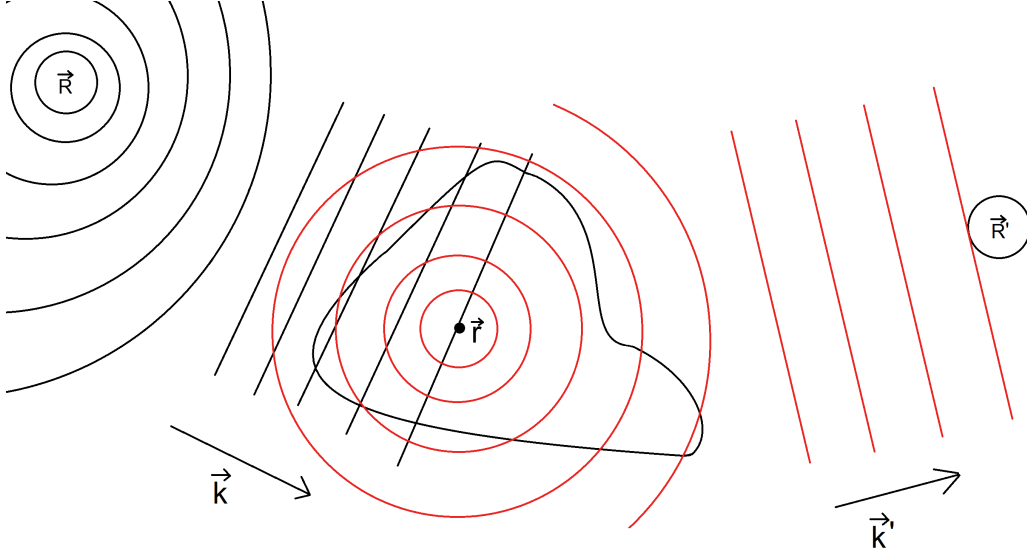


FIGURE 2.5: The von Laue treatment does not assume reflection geometry like the Bragg treatment. It is more general.  $\vec{R}$  and  $\vec{R}'$  denote the positions of the source and detector respectively,  $\vec{k}$  and  $\vec{k}'$  are the wave vectors of the incident and scattered x-rays respectively, and  $\vec{r}$  is the position of the point scatterer.

Similarly, the relative electric field at the detector arising from the scattering event at point  $\vec{r}$  can be written as

$$\vec{E}(\vec{R}', t) \propto \vec{E}(\vec{r}, t) \rho(\vec{r}) e^{i(\vec{k}' \cdot (\vec{R}' - \vec{r}))} \quad (2.10)$$

where it is assumed that the scattered wave with wave vector  $\vec{k}'$  depends not only on the incoming electric field, but also on the electron density at  $\rho(\vec{r})$ . Only the direction of  $\vec{k}'$  differs from  $\vec{k}$  (the magnitude is the same) since diffraction is elastic. Substituting 2.9 into 2.10 yields

$$\begin{aligned} \vec{E}(\vec{R}', t) &\propto e^{i(\vec{k} \cdot (\vec{r} - \vec{R}))} \rho(\vec{r}) e^{i(\vec{k}' \cdot (\vec{R}' - \vec{r}))} e^{-i\omega t} \\ &= e^{i(\vec{k}' \cdot \vec{R}' - \vec{k} \cdot \vec{R})} \rho(\vec{r}) e^{i(\vec{k} - \vec{k}') \cdot \vec{r}} e^{-i\omega t} \propto \rho(\vec{r}) e^{i(\vec{k} - \vec{k}') \cdot \vec{r}} e^{-i\omega t}. \end{aligned} \quad (2.11)$$

After summing over all points throughout the entire volume of the crystal one obtains

$$\vec{E}(\vec{R}', t) \propto e^{-i\omega t} \int_V \rho(\vec{r}) e^{i(\vec{k}-\vec{k}')\cdot\vec{r}} dV \quad (2.12)$$

assuming that  $\vec{k}'$  does not change much with each point in the crystal, since  $\vec{R}'$  is sufficiently far away. Only the intensity is detected (that is, phase information is lost):

$$\vec{I}(\vec{K}) \propto \left| \int_V \rho(\vec{r}) e^{i\vec{K}\cdot\vec{r}} dV \right|^2 \quad (2.13)$$

where the substitution  $\vec{K} = \vec{k} - \vec{k}'$  has been made.  $\vec{K}$  is called the scattering vector. Equation 2.13 relates the intensity to the scattering vector, and therefore, the atomic structure since the electrons are generally held in relative close proximity to the nucleus and are indicative of the atomic positions.

It is extremely difficult to use the intensity and work backwards to figure out the structure of a solid. Instead, the reciprocal lattice is used to immensely simplify the task. The reciprocal lattice vector,  $\vec{G}$ , is defined as

$$\vec{W} \cdot \vec{G} = 2\pi n \quad \text{and} \quad \vec{G} = h\vec{b}_1 + k\vec{b}_2 + l\vec{b}_3 \quad (2.14)$$

where  $n$ ,  $h$ ,  $k$ , and  $l$  are integers and  $\vec{b}_1$ ,  $\vec{b}_2$ , and  $\vec{b}_3$  are reciprocal lattice vectors. From the definition of a reciprocal lattice, the relationship between real and reciprocal lattice vectors is found to be

$$\vec{b}_1 = \frac{2\pi}{V}(\vec{a}_2 \times \vec{a}_3); \quad \vec{b}_2 = \frac{2\pi}{V}(\vec{a}_3 \times \vec{a}_1); \quad \vec{b}_3 = \frac{2\pi}{V}(\vec{a}_1 \times \vec{a}_2) \quad (2.15)$$

where  $V = \vec{a}_1 \cdot (\vec{a}_2 \times \vec{a}_3)$  is the volume of the cell. For any real and reciprocal lattice vectors  $\vec{a}_i$  and  $\vec{b}_j$ , the following relation holds:

$$\vec{a}_i \cdot \vec{b}_j = 2\pi\delta_{ij} \quad (2.16)$$

where  $\delta_{ij}$  is the Kronecker delta function. If one were to consider any function  $\rho(\vec{r}) =$

$\rho(\vec{r} + \vec{W})$  that has the periodicity of the lattice (such as the electron density), then one can write the function as a Fourier series with complex coefficients  $\rho_n$

$$\rho(\vec{r}) = \sum_{-\infty}^{\infty} \rho_n e^{i\vec{r} \cdot \frac{2\pi m}{\vec{W}}} = \sum_{-\infty}^{\infty} \rho_n e^{i\vec{r} \cdot \vec{G}} \quad (2.17)$$

where  $\rho_n = \rho_{-n}^*$  to ensure a real function and  $m$  is an integer. The reciprocal lattice is therefore a Fourier transform of the real lattice. The advantage of using the reciprocal lattice is that instead of having to give the function  $\rho$  for each  $\vec{r}$ , one need only find the coefficients of the Fourier series. This turns equation 2.13 into

$$I(\vec{K}) \propto \left| \sum_{\vec{G}} \rho_{\vec{G}} \int_V e^{i(\vec{G} - \vec{K}) \cdot \vec{r}} dV \right|^2. \quad (2.18)$$

The key here is the integrand. Assuming a very large crystal, the integrand will always average over all of the constructive and destructive interference of the waves. The only time this will not occur is when  $\vec{G} = \vec{K}$  (called the Laue condition), in which case the intensity will be proportional to the square of the Fourier coefficient of the charge density. If one were to measure all diffraction spots for all possible  $\vec{G} = \vec{K}$ , then one can extract all of the Fourier coefficients and reconstruct the electron density, and therefore the structure. Unfortunately this is not possible because the Fourier coefficients are complex: only the magnitudes of the coefficients are known, not their phase. Because of this phase problem, a crystal structure cannot directly be obtained from a regular diffraction pattern. Instead, one can use methods such as Rietveld refinement to help solve the structure (discussed later). In concluding this section it is noted that the Bragg condition is derived from von Laue's conditions (Figure 2.6), since  $|\vec{k}| = |\vec{k}'|$  and  $|\vec{G}| = 2\pi/d_{hkl}$  and  $\vec{G}$  is normal to the  $(hkl)$  plane. Although specific references were made to the mechanism of interaction between x-rays and atoms, these same principles can be extended to neutron diffraction as well, treating the incoming neutron beam as plane waves.

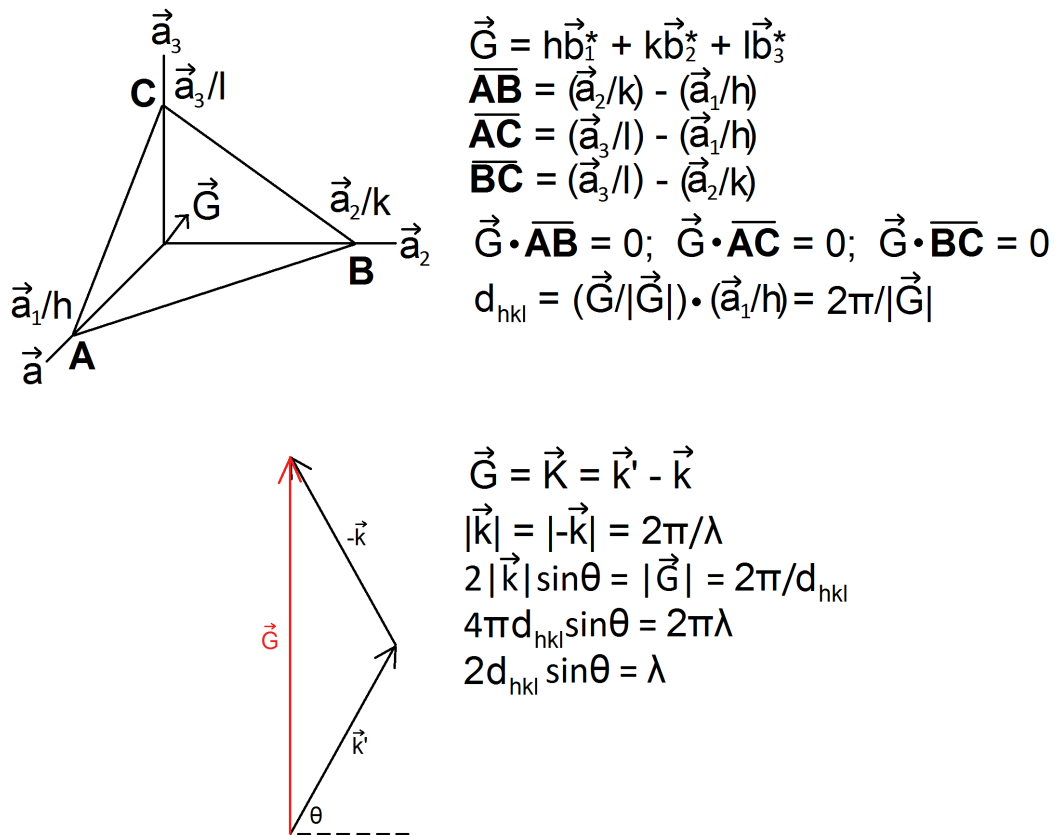


FIGURE 2.6: The reciprocal lattice vector is always perpendicular to the plane defined by integers  $h$ ,  $k$ , and  $l$ , regardless of the type of Bravais lattice that is used. Bragg's is derived from the von Laue condition.

### 2.2.3 Bragg peak intensity

Solving a crystal structure from powder diffraction data can be quite challenging because all of the peaks in reciprocal space collapse onto a single one dimensional axis (Figure 2.7). The Bragg equation only gives information regarding the spaces between planes of atoms, but says nothing about the contents of those planes such as where the atoms are within the plane or what their identities are. Further complicating matters is the loss of phase information. In formulating the Bragg and von Laue approaches, it was assumed that atoms are point scatterers. While this assumption may be valid for neutron diffraction (more on this later), x-rays interact with the electron cloud of an atom which is a distance away from the atomic nucleus of similar magnitude to the x-ray wavelength.

Because the atoms are not point scatterers, atoms displaced slightly out of the Bragg plane can also contribute to the observed intensity. Summed over the entire crystal, all of these contributions are manifested in the atomic form factor,  $f_i(\theta)$ , which is generally calculated from first principles and is normalized to the number of electrons to atom  $i$  at  $\theta = 0$  [19, 50].

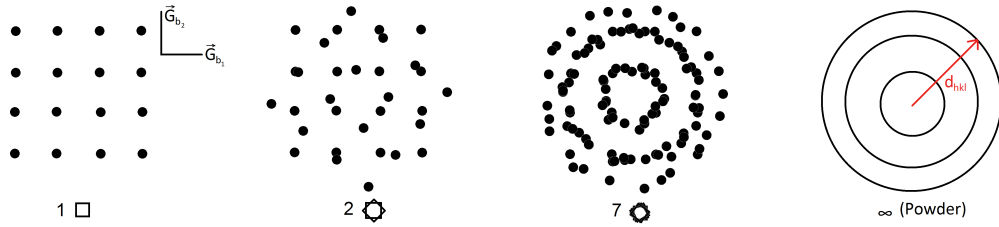


FIGURE 2.7: A powder is a collection of small single crystals in random orientations. The effects of powder averaging result in a collapse of the three dimensional reciprocal space onto a one dimensional axis. This can make it quite difficult to solve a complex structure. The numbers and shapes at the bottom represent the number and orientations of the crystal grains used in each instance respectively.

Atoms were also assumed to be static on the planes. In reality, the atoms are moving since a non-zero temperature imparts the atoms with some kinetic energy. The interaction between the x-ray or neutron with the atom is much faster than the thermal motion. As such, the position of an atom is an average of all scattering events at a single position over time:

$$f'_i(\theta) = f_i(\theta)e^{-2\pi^2 \frac{\langle u^2 \rangle}{d^2}} = f_i(\theta)e^{-B \frac{\sin^2(\theta)}{\lambda^2}} \quad (2.19)$$

where  $f$  is the atomic form factor of atom  $i$ ,  $\langle u^2 \rangle$  is the mean square of the displacement, and  $B$  is the Debye-Waller factor defined as  $8\pi^2 \langle u^2 \rangle$ , where isotropic vibrations are assumed.

Before discussing the final intensity of a Bragg peak, one last consideration should be mentioned. The periodic repetition of all of the atoms in a crystal introduces translational symmetry in addition to the atomic point symmetry. This causes a phase shift relative to the unit cell origin when considering unit cells with more than one atom.



When summed over the contents of the unit cell, the scattered wave obtained for every  $(hkl)$  plane of atoms is called the structure factor:

$$S_{hkl} = \sum_{i=1}^N f'_i(\theta) e^{i2\pi(hx_i + ky_i + lz_i)} \quad (2.20)$$

where  $x$ ,  $y$ , and  $z$  are the real space coordinates of the atom in the  $i^{th}$  unit cell and  $h$ ,  $k$ , and  $l$ , are the integers composing the reciprocal lattice vector. If the positions of the atoms are known, then the scattered waves from each atom can be combined to give  $S_{hkl}$  and calculate the diffraction pattern intensity  $I$ . However, only the intensity is recorded using a detector, so this phase information is lost:

$$I = S_{hkl} S_{hkl}^* e^{-2B \frac{\sin^2(\theta)}{\lambda^2}}. \quad (2.21)$$

The structure factor contains important information about the symmetry of the unit cell. For example, if the basis of every point in a cubic lattice contains an atom at  $(0, 0, 0)$  and an atom at  $(\frac{1}{2}, \frac{1}{2}, \frac{1}{2})$ , then each plane of atoms will create patterns of constructive interference that are directly out of phase and cancel with each other for every  $h+k+l =$  odd integer (that is,  $S_{hkl} = 0$ ). Absences of intensity for planes with certain values of  $h$ ,  $k$ , and  $l$  are called systematic absences, and can be used to help identify the symmetry of the unit cell.

#### 2.2.4 X-ray diffraction

The history of the diffraction instrumentation is quite lengthy considering that x-rays were only discovered 120 years ago [52]. While the development of diffraction instrumentation is beyond the scope of this thesis, a general overview of the instrumentation used here is presented.

To produce x-rays in the laboratory, a cathode is first heated beyond its work function such that electrons are ejected. These electrons are then accelerated in a high-voltage vacuum tube towards a metal target. During the collision with the target, the electrons

are quickly decelerated and a photon is released within the x-ray range. This creates a broad continuous spectrum of x-ray radiation termed Bremsstrahlung (“braking radiation”). However, if the incoming accelerated electron has enough energy it can cause an inner shell (usually  $1s$ ) electron from a target atom to eject. The excited target atom will then release a photon of characteristic wavelength upon returning to its ground state. Electrons from higher shells will move to fill in the hole in the inner shell: those moving from a  $p$ -shell will release  $K\alpha$  radiation. For Cu, the target used in the x-ray diffractometers mentioned here, these photons have wavelengths of 1.54056 and 1.54439 Å. These slight differences occur due to splitting of the  $p$ -orbitals from the spin-orbit coupling interaction; the energies average out to 1.5418 Å.

In practice, many instrumental features can contribute to the quality of the data obtained. A monochromator can be used before the sample to isolate a particular wavelength, or after the sample to minimize contributions from fluorescence. Filters are much more cost effective but less efficient than monochromators and are used to eliminate unwanted  $K\beta$  ( $d$  to  $s$ -shell transition) and  $\lambda/2$  radiation. Slits are typically used to shape the beam to improve the peak shape and resolution at the expense of flux. X-rays are often absorbed by samples with heavy elements with both a dependence on sample thickness and diffraction angle. The geometry of a diffractometer can be used to offset the absorption. Bragg-Brentano geometry aligns the sample such that x-rays appear to reflect from the sample surface in much the same manner as the Bragg configuration. This nullifies the angular dependence of the absorption by taking advantage of the angular dependence of the penetration depth (Figure 2.8) [51, 52]. However, effects from preferred orientation of the powder grains and large sample sizes are known disadvantages to using Bragg-Brentano geometry as opposed to some sort of transmission geometry set up. There are many types of x-ray detectors but the most popular is the scintillation counter, which converts an x-ray to a visible photon that can be detected by a photomultiplier tube.

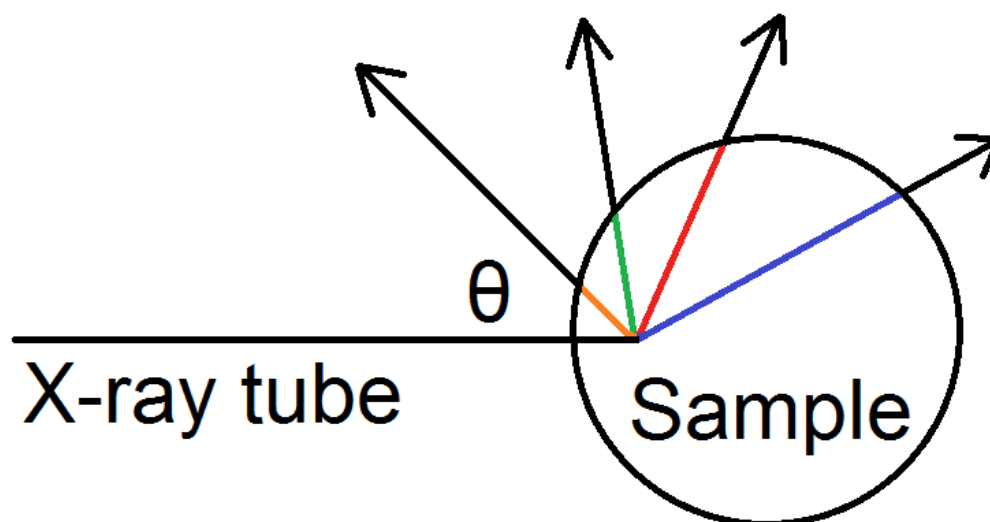


FIGURE 2.8: Materials absorb x-rays according to an exponential relationship. This means that in transmission geometry, the path-length of the incident and scattered x-ray in the material will change with the detector angle and penetration depth. This is not the case with reflection geometry where the penetration depth makes up for the change in detector angle. The absorption correction behaves more like a constant.

However, synchrotron x-ray diffraction is the current state-of-the-art, producing x-ray intensities many orders of magnitude above common laboratory instruments. Here, x-rays are produced by accelerating electrons to speeds close to the speed of light. Accelerating charges always emit radiation as a consequence of conserving their energy and momentum. The use of synchrotron x-rays results in extremely high-resolution diffraction patterns, stemming from the brightness of the x-ray source, the precise tunability of the x-ray wavelengths, and the intrinsic collimation of the beam [51]. Large scale facilities are required to produce x-rays in this manner, and as such, synchrotrons are generally nationally or internationally funded. A crystal monochromator is always used to select for specific wavelengths. However, the basic principles behind the operation of diffractometers found at a synchrotron are the same as those found in the laboratory. The 11-BM line at the Advanced Photon Source (Argonne, IL) [53–55] is one example of a synchrotron instrument; it has been used extensively in these experiments.

### 2.2.5 Neutron diffraction

Although the principles of x-ray diffraction extend to neutron diffraction, additional subtleties must be introduced due to the differing manner in which neutrons interact with matter. Neutrons interact primarily with the nucleus via short-range (femtometre) forces, although they can also interact with unpaired electrons via a magnetic-dipole interaction (addressed later). Let  $\Phi$  be the neutron flux (number of incident neutrons/unit area/second). Then  $\sigma$  is defined as the total scattering cross section, which is the total number of neutrons scattered/second, normalized by the flux. All nuclei can be approximated as point scatterers because of their size relative to the atomic area;  $\sigma$  is the effective area of the nucleus to the incident neutron. In polar spherical coordinates, the detector is held at a fixed distance  $\vec{r}$  from the sample at angles  $\theta$  and  $\phi$ . The measured quantity of interest is the number of neutrons scattered in the direction of the detector (Figure 2.9), called the differential scattering cross section [11, 18, 56]:

$$\frac{d\sigma}{d\Omega} = \frac{\text{number of neutrons scattered into the solid angle } d\Omega \text{ in the direction } \theta, \phi \text{ per second}}{\Phi d\Omega} \quad (2.22)$$

$$\sigma = \int_0^{2\pi} \int_0^{\pi} \left( \frac{d\sigma}{d\Omega} \right) \sin(\theta) d\theta d\phi. \quad (2.23)$$

Consider elastic scattering from a single nucleus located at the origin. Just as with the von Laue treatment of x-ray scattering from a single point in the sample specimen, the wave function of a scattered neutron from the nucleus is spherically symmetric and is given by  $\psi = -(b/\vec{r})e^{i\vec{k}' \cdot \vec{r}}$ , where  $\vec{k}'$  is the wave vector with magnitude equivalent to that of the incident neutron and  $b$  is the scattering length (the negative sign correlates a positive  $b$  with a repulsive potential). When a neutron encounters some types of nuclei such as  $^{113}\text{Cd}$ , the neutron-nucleus compound energy lies close to an excited state; these nuclei tend to strongly absorb neutrons and have a large complex scattering length ill-suited for neutron scattering experiments. However, most nuclei do not behave this way

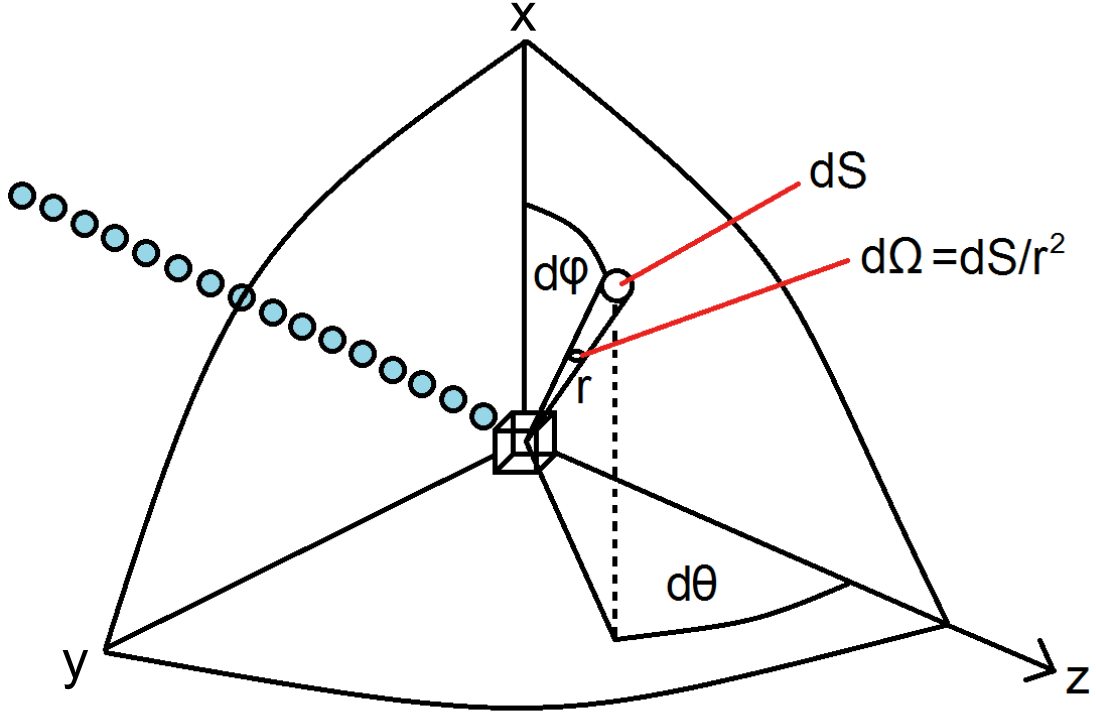


FIGURE 2.9: Schematic of the differential scattering cross section. Incident neutrons travel from the source along the  $z$ -axis and scatter off the sample in all directions. The number of neutrons to hit the detector area  $dS$  per second is the measured quantity of interest. Naturally, this is the fraction of the number of total neutrons scatter  $d\sigma$  into the solid angle  $d\Omega$  defined by angles  $\theta$  and  $\phi$ . The detector is located at a distance  $r$  from the sample.

and have scattering lengths with a small imaginary component. If  $dS$  is taken as the area of the detector (Figure 2.9), the number of neutrons passing through  $dS$  per second after scattering is:

$$vdS|\psi|^2 = vb^2\left(\frac{dS}{r^2}\right) = vb^2d\Omega \quad (2.24)$$

where  $v$  is the velocity of the neutron. Substituting 2.24 into 2.22 gives

$$\frac{d\sigma}{d\Omega} = \frac{vb^2d\Omega}{\Phi d\Omega} = b^2; \quad \sigma = 4\pi b^2 \quad (2.25)$$

since  $\Phi = v|\psi_{\text{incident}}|^2 = v$ . If one were to now sum up the neutrons scattered by many nuclei located at  $\vec{R}_i$ , then the scattered neutron wavelength becomes

$$\psi_{\text{scattered}} = \sum_{i=1}^N e^{i\vec{k}\cdot\vec{R}_i} \left( -\frac{b_i e^{i\vec{k}'\cdot(\vec{r}-\vec{R}_i)}}{|\vec{r}-\vec{R}_i|} \right) \quad (2.26)$$

$$\frac{d\sigma}{d\Omega} = \frac{v dS |\psi_{\text{scattered}}|^2}{v d\Omega} = \frac{dS}{d\Omega} \left| e^{-i\vec{k}\cdot\vec{r}} \sum_{i=1}^N b_i \left( \frac{1}{|\vec{r}-\vec{R}_i|} \right) e^{-i\vec{K}\cdot\vec{R}_i} \right|^2 \quad (2.27)$$

$$\frac{d\sigma}{d\Omega} = \sum_{i,j} b_i b_j e^{-i\vec{K}\cdot(\vec{R}_i-\vec{R}_j)} \quad (2.28)$$

where the last equation was found summing over pairs of atoms using the relationship  $d\Omega = dS/|\vec{r}|^2$ , assuming  $|\vec{r}| \gg |\vec{R}_i|$ . Before proceeding, it is noted that there are two types of scattering that compose the total scattering cross section, which is caused because of the isotope effect. Coherent scattering gives information about the solid structure. It is caused by correlations between atoms located at different positions at different times and results in Bragg peaks or broad diffuse scattering for short range order. On the other hand, incoherent scattering does not give rise to Bragg peaks and is mainly isotropic. It arises from an atom's self-correlation over time (see the definition of the dynamic structure factor in section 2.7). Because neutrons have a spin of  $1/2$  and nuclei have a spin of  $I$ , each nuclei will have two scattering lengths because the neutron-nucleus compound will either have a spin of  $I + 1/2$  or  $I - 1/2$  (the exception is when  $I = 0$ , where only one scattering length is observed). The number of states for each nuclear spin type differs, but the probabilities for observing each state are the same. Furthermore, the location of each isotope within the crystal structure is completely random. These effects must be averaged out of the partial differential scattering cross section.

Neutrons can be produced via two primary methods for use in diffraction: through fission or through spallation. At a fission source, a neutron will be absorbed by  $^{235}\text{U}$ , exciting it to  $^{236}\text{U}$ , which will then decay into gamma rays, elemental isotope products (predominantly  $^{89}\text{Kr}$  and  $^{144}\text{Ba}$ ), and three more neutrons. Neutrons liberated this way

can be used to continue the reaction or can be used for neutron scattering. A moderator is used to control the speed of the released neutrons; moderated neutrons have a Maxwellian distribution of velocities (wavelengths) that are tightly controlled by the moderator temperature. The colder the temperature of the moderator, the slower the most probable speed of the neutron, the longer the wavelength used, and the better sensitivity one will have to larger interplane spacings (where, for example, the magnetic form factor is greatest). Powder diffraction experiments using neutrons produced in this way are called constant wavelength; a monochromator is used to select the desired wavelength in conjunction with various filters and collimators. The setup is quite comparable to laboratory x-ray diffraction.

Alternatively, neutrons can be produced at a spallation source. Here, protons are accelerated and stored in a synchrotron ring. At fixed intervals, a burst of protons are made to collide with a heavy metal target. Many neutrons are released with each pulse. The neutrons travel through a moderator that decelerate the neutrons, and then the neutrons travel towards the beam lines. Each pulse consists of a white beam of neutrons. As the pulse of neutrons makes its way towards the instrument, the neutron pulse begins to broaden (neutrons with shorter wavelengths have faster speeds than neutrons of longer wavelengths). Rather than isolating neutrons of a constant wavelength, all of the neutrons hit the sample and travel to fixed banks housing detectors ( $\theta$  is fixed). The time it takes for each pulse of neutrons to scatter from the sample and hit the detector is known, and the d spacing can be calculated

$$\lambda = \frac{hm_nL}{t}; \quad d = \left(\frac{nhm_nL}{2\sin(\theta)}\right)\frac{1}{t} \quad (2.29)$$

where  $h$  is Planck's constant,  $m_n$  is the mass of the neutron,  $L$  is the pathlength and  $t$  is the time it takes for the neutron to reach the detector. Diffraction done in this manner is called time-of-flight. Each detector pixel receives a full diffraction pattern, the resolution of which not only depends on the position of the detector bank, but the length of the path that the pulse of neutrons takes before reaching the detector: a longer

path will provide better time resolution. Spallation sources are far more efficient with neutron use than constant wavelength sources. However, there are many disadvantages to time-of-flight neutron diffraction, the primary one being issues with the peak shape due to instrumental features. POWGEN (Spallation Neutron Source, Oak Ridge, TN) and WISH (ISIS, Didcot, Oxford) are both time-of-flight diffractometers that were used for the experiments described in this work.

Neutrons have a magnetic moment that allows them to interact with unpaired electrons via a dipole interaction. The interaction energy  $U$  between the magnetic moment of the neutron and the electrons in the solid is given as

$$U = \vec{\mu} \cdot \vec{B} = -\gamma \vec{\mu}_n \sigma \cdot \vec{B} \quad (2.30)$$

where  $\vec{\mu}_n$  is the nuclear magneton (about  $5.501 \times 10^{-27}$  J/T),  $\gamma$  is the neutron gyromagnetic ratio (1.913),  $\sigma$  is the Pauli spin operator ( $\pm 1$ ) and  $\vec{B}$  is the magnetic field produced by the electrons in the material.

Using a quantum mechanical derivation, the partial differential scattering cross section is found by summing through all of the state changes in the detector area  $dS$  [56]

$$\frac{d\sigma}{d\Omega} = \left(\frac{\vec{k}}{k'}\right) \left(\frac{m}{2\pi\hbar^2}\right)^2 | \langle \vec{k}' \lambda' | V(\vec{r}) | \vec{k} \lambda \rangle |^2 \quad (2.31)$$

where  $| \langle \vec{k}' \lambda' | V(\vec{r}) | \vec{k} \lambda \rangle |^2$  is the probability of a neutron with wave vector  $\vec{k}$  changing from state  $\lambda$  to  $\lambda'$  with final vector  $\vec{k}'$  through the Fermi pseudopotential  $V(\vec{r})$ . The Fermi pseudopotential is used to simplify the complex interaction between the neutron and nucleus; the scattering process is assumed to be spherically symmetric occurring from a point in space,  $V(\vec{r}) = (2\pi\hbar^2/m)b\delta(\vec{r})$  where  $\delta(\vec{r})$  is the Dirac delta function and  $b$  is the scattering length. For the magnetic case, one must replace  $V(\vec{r})$  with  $U$  (equation 2.30), which will also include a magnetic form factor completely analogous to the x-ray atomic form factor. Solving this equation is a formidable task, the result of



which is presented here [56]:

$$\frac{d\sigma}{d\Omega} = \left(\frac{\vec{k}}{k'}\right) \left(\frac{1}{h}\right) (\gamma r_0)^2 |F(\vec{k})|^2 \sum_{\alpha,\beta} (\delta_{\alpha\beta} - \hat{K}_\alpha \hat{K}_\beta). \quad (2.32)$$

The scattering length of a magnetic moment is  $\gamma r_0$ , which is comparable to the nuclear scattering length of most isotopes (this means that the integrated intensities of magnetic Bragg peaks should be comparable to nuclear Bragg peaks).  $F(\vec{K})$  is the magnetic form factor and  $(\delta_{\alpha\beta} - \hat{K}_\alpha \hat{K}_\beta)$  is called the polarization factor where  $\alpha$  and  $\beta$  are spin components of the tensor [18, 56]. This term signifies that neutrons can only couple to the component of the moment perpendicular to  $\vec{K}$ , which results in a “spin-flip” event; the interaction between the neutron magnetic moment vector and the atomic magnetic moment vector is much more complex than simple atomic scattering.

The same rules that govern the structure factor – which defines the conditions for constructive interference for a scattering event for a given material – for nuclear diffraction also apply to magnetic diffraction, such as systematic absences. However, instead of scattering from points, neutrons are scattered from vectors. For example, it is possible to determine body-centered cubic ordering of the moments, but much more difficult to determine the absolute orientation of the moments. If a single crystal were to order as depicted in Figure 2.10, the average direction of the moments can be found via different crystal alignments since only the moment component perpendicular to  $\vec{K}$  will yield intensity. In powders however, it is assumed that there are grains in every orientation, so a direct solution is not possible. The orientation of the moments can be found relative to each other, but not relative to the positions of the nuclei (the nuclear unit cell). For materials with sufficiently low symmetry, a unique solution can be obtained using powders, in principle.

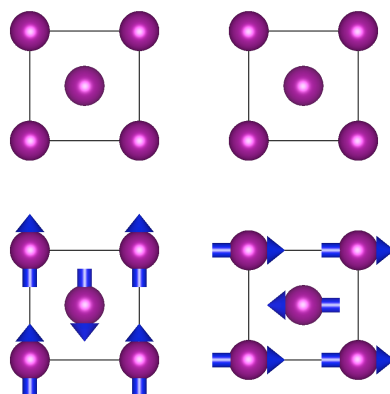


FIGURE 2.10: Here, moments are aligned parallel or antiparallel to the  $c$ -axis. Using a single crystal, it would be quite easy to determine the orientations of the moments; one need only align the crystal such that the  $c$ -axis is perpendicular to the scattering vector  $\vec{K}$ . However if powders are used, both of the directions shown are equivalent. Only the antiferromagnetic character of the moments could be determined, not their absolute orientations. This is because new reflections would arise since the magnetic unit cell is primitive while the nuclear unit cell is body-centred.

## 2.3 Rietveld refinement

In diffraction experiments, one loses all phase information about the scattered wave rather than the amplitude. Unfortunately, the phase of the scattered wave is far more important than the amplitude in determining the location of the atoms within the unit cell. For simple highly symmetric structures, one is able to solve them *ab initio* from powder diffraction data by analyzing each of the observed reflections. But for more complicated structures, it becomes increasingly more difficult to grow single crystals, and reflections that are found using powder diffraction tend to overlap, quickly complicating the analysis. The Rietveld refinement method was developed in the late 1960s to deal with this issue using computers to handle large data throughput. In other words, a computer matches the entire diffraction pattern calculated from a user-defined structural model to the entire observed diffraction pattern using least squares fitting. The computer then changes the model and fits it to the observed pattern in the next cycle, always comparing the fit to the previous one using a feedback mechanism. The process is

complete when a minimum is reached.

### 2.3.1 Mathematical procedure

Powder diffraction data is first read in to a computer program such that the intensity of each point,  $y_i$ , is recorded. Regardless of the method in which the data is collected (x-ray, neutron, constant wavelength, time-of-flight), the Rietveld refinement method is the same. The objective is to minimize

$$S = \sum_{i=1}^N \frac{(y_i - y_{ci})^2}{y_i} \quad (2.33)$$

where  $y_{ci}$  is the calculated data point and  $S$  is summed over all data points (the term “point”, rather than “reflection”, is key). A powder diffraction pattern is composed of many typically overlapping peaks that each have their own height, position, shape, and integrated intensity proportional to the structure factor squared [18, 57]. No attempts are made at resolving these peaks or assigning intensity to any one particular peak before the procedure begins. This limits Rietveld refinement as a method to solve new structures in and by itself; instead Rietveld refinement is best used when one has a good structural model to begin with. The calculated intensity at any given point is given by [57]

$$y_{ci} = s \sum_K L_K |F_K|^2 \phi(2\theta_i - 2\theta_K) P_K A + y_{bi} \quad (2.34)$$

where  $s$  is the scale factor and  $K$  are the Miller Indices  $h$ ,  $k$ , and  $l$  defining the plane of atoms responsible for the given reflection.  $L_K$  is a term containing the Lorentz, polarization, and multiplicity factors. The Lorentz factor comes from the fact that the lattice points and scattering vector  $K$  are not infinitesimal: they have width and  $K$  need not strictly equal  $G$  to observe some intensity. The polarization factor is a correction required for laboratory x-ray scattering because, depending on the initial individual photon polarization, the scattered photon can change polarization dependent on the scattering angle (laboratory x-ray tubes will produce photons of every polarization).

The multiplicity factor strictly depends on the  $h, k, l$  values in relation to the symmetry of the unit cell. For example, for a unit cell with cubic symmetry, all reflections of the form  $(h00)$  will be equivalent to reflections of the form  $(0h0)$  and  $(00h)$ . All of those reflections will contribute to the intensity at  $y_i$  for a cubic cell, whereas they would not for a system that is not metrically cubic.  $F_K$  is the structure factor equivalent to  $S_{hkl}$  from equation 2.20.  $\phi$  is the profile function that is typically some mixture of Gaussian and Lorentzian functions, but can be much more complicated in synchrotron and spallation source diffraction [57].  $(2\theta_i - 2\theta_K)$  is a term to account for the displacement between an observed and calculated reflection.  $P_K$  is a preferred orientation function that is included when powder grains prefer to form along certain planes and are not randomly distributed within the sample (this is more of an issue for reflection geometry).  $A$  is an absorption correction assumed to be constant for reflection geometry, but can have angular dependence with transmission geometry. Finally,  $y_{bi}$  is the background intensity at point  $i$  typically calculated using some polynomial function. Other contributions to the intensity may be included in the calculation of  $y_{ci}$  such as particle size, microstrain, and even an addition of a second phase, but these are beyond the scope of this discussion.

In order to carry out the refinement, the fit between the calculated pattern and the observed pattern is evaluated at every cycle with respect to each point for each adjustable parameter

$$M_{jk} = - \sum_i 2 \left( \frac{1}{y_i} \right) [(y_i - y_{ci}) \left( \frac{\partial^2 y_{ci}}{\partial x_j \partial x_k} \right) - \left( \frac{\partial y_{ci}}{\partial x_j} \right) \left( \frac{\partial y_{ci}}{\partial x_k} \right)] \quad (2.35)$$

where  $i$  is the index for each point and  $j$  and  $k$  are the same set of adjustable parameters at different cycles. This set of non-linear equations are solved in matrix form computationally, although the solutions must be solved iteratively. The shift in any adjustable parameter is calculated as

$$\Delta x_k = \sum_j M_{jk}^{-1} \frac{\partial S}{\partial x_k}. \quad (2.36)$$

where  $M_{jk}^{-1}$  is the inverse matrix with elements  $M_{jk}$ .

There are a number of ways that the quality of fit can be judged: No single numerical method by itself is sufficient. Before continuing it is noted that each of these numerical methods rests on the fact that there are statistical errors in every measurement. The goodness-of-fit parameter, often denoted as  $\chi^2$ , is defined as

$$\chi^2 = \frac{1}{N} \sum_{i=1}^N \frac{(y_{ci} - y_i)^2}{\sigma^2(y_i)} \quad (2.37)$$

where  $\sigma^2(y_i)$  is the uncertainty in the observed intensity and  $\chi^2$  is normalized over all  $N$  points. This means that the ideal model will yield a  $\chi^2$  of exactly 1, since the average of  $(y_{ci} - y_i)^2$  over all points cannot be better than  $\sigma^2(y_i)$ . Another set of useful indices are the profile R-factor,  $R_p$ , the weighted profile R-factor,  $R_{wp}$ , and the expected R factor,  $R_e$ , defined as

$$R_p = \frac{\sum |y_{ci} - y_i|}{\sum y_i} \quad (2.38)$$

$$R_{wp} = \sqrt{\frac{\sum \frac{(y_i - y_{ci})^2}{y_i}}{\sum \frac{y_i^2}{y_i}}} \quad (2.39)$$

$$R_e = \sqrt{\frac{N}{\sum \frac{y_i^2}{y_i}}} \quad (2.40)$$

It is noted that  $\chi^2 = R_{wp}/R_e$ , which makes it somewhat clearer why  $\chi^2$  should never be less than 1. Other convergence statistics have been used such as the Bragg R-factor and structure R-factor, but these are biased towards the model being used, since they incorporate the calculated intensities of specific reflections rather than each data point [57, 58].

If it were solely up to statistical analysis to determine the correct crystal structure, then computers could do it without human aid. The problem with numerical analysis is

that it cannot distinguish between a good model and a bad one: that is, two different models may fit the data such that the same convergence criteria are reached. Because Rietveld refinement fits the entire diffraction pattern as opposed to specific reflections, statistical measures are very dependent on a variety of factors. As an example, consider  $\chi^2$ . In addition to having a good model,  $\chi^2$  can also be lowered using poorer quality data because 1) it is easier to fit a large background in data with a poor signal-to-noise ratio than it is to fit a diffraction pattern, and 2) high values of  $\sigma^2(y_i)$  will allow a greater distribution of  $(y_{ci} - y_i)^2$  values to yield a low  $\chi^2$  [57, 58]. Conversely, it is possible to “overfit” the data and achieve a  $\chi^2 < 1$ , either by fitting to instrumental noise or adjusting too many parameters. Rietveld refinement also allows one to extract standard uncertainties for calculated values, but these are only minimum statistical uncertainties due to random noise in the data and do not reflect uncertainties due to systematic errors with the model that may not be properly accounted for [58], such as preferred orientation, background, peak shape, graininess etc. These numerical methods must always be taken with a grain of salt, so to speak. However, they are useful while the refinement is being performed more as a measure of how well a refinement is proceeding: that is they better measure *how bad* a bad model is than *how good* a good model is. With all of these statistical measures it becomes quite easy to get lost in the calculation and to forget what all of these numbers represent. Quite often, it is necessary to introduce constraints in the model to represent the physical world. In the end, a visual representation of a chemically reasonable calculated model against the observed pattern is always the best way to determine the quality of a refinement.

### 2.3.2 Magnetic structure refinements: Representational analysis

Using group theory, mathematicians long ago realized that combining the 32 point groups with the translational symmetry of the 7 Bravais lattices leaves 230 possible space groups to completely describe the symmetry of any crystallographic system that completely fills space [50]. The symmetry of the nuclear arrangement of a crystal governs most of the observables of that system, including the diffraction pattern. However, magnetic structures

are different since the “nuclear points” describing their position in space become axial vectors. While the standard rules of diffraction equally apply to magnetic diffraction, one cannot determine the directions of the magnetic moments solely from the positions of the paramagnetic ions (the space group). However, there are tools extending from group theory that can help describe magnetic structures. A full treatment of magnetic structure refinements is beyond the scope of this discussion. Some common strategies are only briefly introduced.

An axial vector, also called a pseudovector, is unlike a familiar polar vector due to the different ways that certain symmetry operations act on them. The orientation of a polar vector is invariant under translation, rotation, and mirror operations, but flips with inversion. In addition to remaining invariant under translation and rotation, axial vectors are also invariant under inversion but flip under a mirror operation (Figure 2.11). In three dimensions, axial vectors are derived from the cross product of two polar vectors. Because axial vectors have both magnitude and direction, additional symmetry operators (for example, anti-reflection, which does not invert an axial vector for a mirror operation) need to be combined within the 230 space group to completely describe magnetic symmetry. All of these additional symmetry operations are derived from the time-reversal operator, named after the physical basis from which the cross product of two vectors  $\vec{v}_1 \times \vec{v}_2$  can be converted to  $\vec{v}_2 \times \vec{v}_1 = -(\vec{v}_1 \times \vec{v}_2)$ . This creates a total of 1651 magnetic space groups that considerably complicates the refinement procedure [59]. Representational analysis is a compact way to represent the magnetic structure of a crystal by taking advantage of the symmetry of the unit cell and an additional translation vector called the propagation vector.

A Bloch wave (a wave in a periodic potential such as a crystal lattice used to describe the motion of a particle) can be used to describe the moments on atoms that differ by an integer multiple of a lattice vector. Then the moment on atom  $j$  can be described by a plane wave using the moment on atom  $i$  in the zeroth unit cell [60–66]:

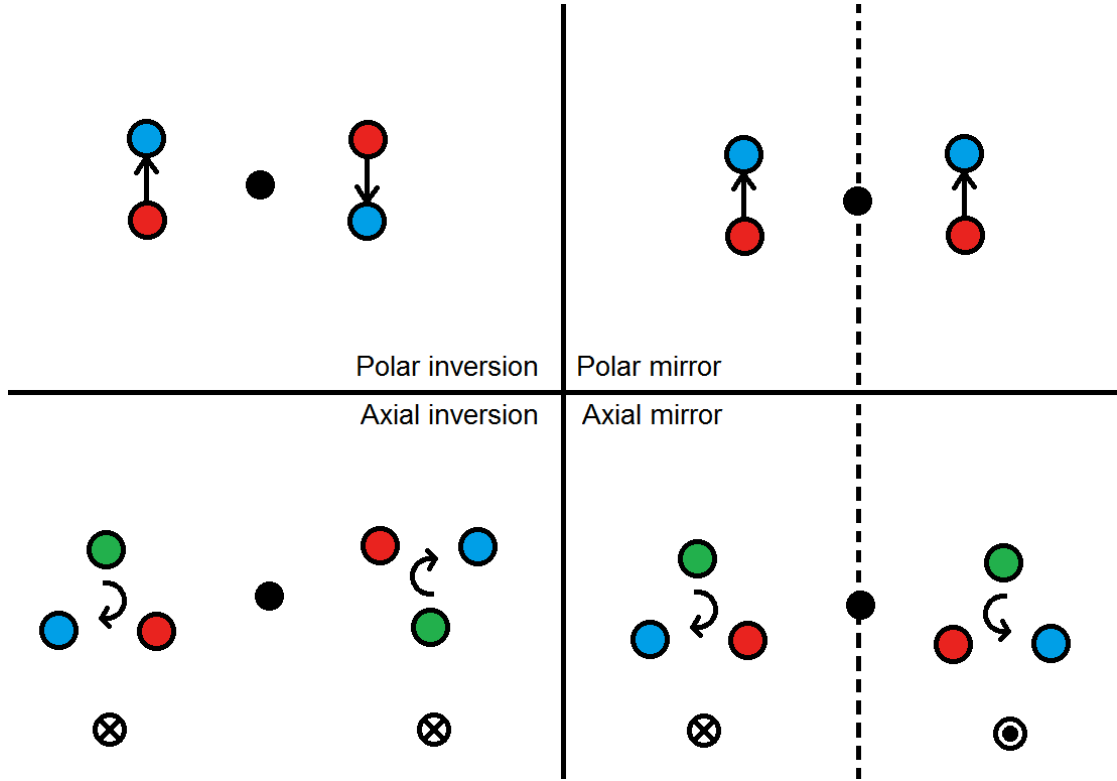


FIGURE 2.11: The behavioural differences under various symmetry operations between polar and axial vectors.

$$\vec{M}_j = \vec{M}_i e^{-2\pi i \vec{k} \cdot \vec{W}} \quad (2.41)$$

where  $\vec{W}$  is the lattice vector relating atom  $i$  to atom  $j$  and  $\vec{k}$  is called the propagation vector that need not necessarily be commensurate with the crystal lattice, though both vectors are defined using the lattice parameters as coordinate axes (that is, the propagation vector  $\vec{k}$  should not be confused with the scattering vector  $\vec{K}$ ). The propagation vector describes how a magnetic moment transforms under translation.

The symmetry operations belonging to a space group are also able to transform  $\vec{k}$ . Since  $\vec{k}$  itself is a translation vector, only the rotational parts of the space group are considered here. The rotational operations of a space group that leave  $\vec{k}$  invariant form a special subgroup called the little group,  $G_k$ . In effect,  $G_k$  describes all possible symmetries of the space group that are compatible with the positions of the observed reflections, severely



limiting the possible choice of magnetic orientations. The magnetic representation is a matrix that represents all the possible ways that the symmetry of the space group will affect the positions of all magnetic ions in the unit cell and the directions of their moment axial vectors, which are independent of each other. However, there are infinite ways that a magnetic representation can be constructed: they can all be broken up into a series of orthogonal irreducible representations from which all other representations can be built [60, 61]. These have been tabulated previously in ref. [67].

A magnetic moment can be decomposed into basis vector components:

$$\vec{M}_j = \sum_{\vec{k}} \Psi_j^{\vec{k}} e^{-2\pi i \vec{k} \cdot \vec{G}} \quad (2.42)$$

$$\Psi_j = \sum_{\nu} C_{\nu} \psi_{\nu} \quad (2.43)$$

where  $\vec{G}$  is the reciprocal lattice vector, and  $C_{\nu}$  and  $\psi_{\nu}$  are the coefficients and basis vectors composing  $\Psi_j$ . Basis vectors can then be constructed by projecting test functions into components that transform according to the irreducible representations. A moment is a linear combination of those basis vectors. Quite generally, more than one propagation vector can be present in a single magnetic structure, but these examples are rare. Only systems with a single propagation vector will be included in the discussion.

If one expands equation 2.41, then certain values of  $\vec{k}$  may leave the imaginary component zero. These cases simply flip the orientation of the moment from one unit cell to the next, or leave them invariant (that is, these are ferromagnetic and antiferromagnetic structures). However if  $\vec{k}$  takes on a values such that the sine component is not zero, then an issue regarding complex moments is encountered: magnetic moments are real entities, so this needs to be remedied. The moments are made real by considering basis vectors from more than one propagation vector, in particular from  $-\vec{k}$  (this makes basis vectors  $\psi_{-\vec{k}} = \psi_{\vec{k}}^*$ ). For commensurate structures,  $\vec{k}$  and  $-\vec{k}$  are equivalent, but this is

not the case for incommensurate magnetic structures. Real basis vectors with a non-zero sine component result in spin density waves where the magnitude of the moment varies from site to site. Complex basis vectors for a propagation vector that has a non-zero sine component result in a structure that modulates according to a cosine function in one direction and modulates according to a sine function in a transverse direction. If the basis vectors are oriented in a plane perpendicular to the propagation vector, then this type of structure is a helix and can be circular or elliptical dependent on the relative magnitudes of the cosine and sine components. If there is a component of the basis vectors parallel to the propagation vector, then the result is a cycloidal moment structure.

Representational analysis immensely simplifies the refinement of magnetic structures: the only prior information needed before the refinement are the atomic space group, the coordinates of the magnetic ion(s) in the unit cell, and the propagation vector, which is found by indexing the extra reflections. Algorithms have been developed to search for the most probable propagation vectors by taking the symmetry of the reciprocal lattice into account [68]. SARAh (Simulated Annealing and Representational Analysis) is a suite of programs with an algorithm used to calculate the basis vectors of all the different irreducible representations by deconstructing a magnetic representation defined by the parameters input by the user [69, 70]. Other programs are available to do the same thing [71]. The refinement proceeds by varying only the coefficients of the basis vectors for the chosen irreducible representation until a satisfactory result is observed. However, one must be careful with powder diffraction data; powder averaging and overlapping reflections can lead to a considerable number of equivalent solutions that may need to be selected against either through single crystal diffraction or by other methods.

### 2.3.3 Bond valence sums

Once the bond distances have been determined from diffraction and Rietveld refinement, the oxidation state of an atomic species can be calculated strictly on the basis of Bond Valence Theory [72–74]. There is an empirical relationship between the bond distances

of an atom and its oxidation state, although the exact relationship has been refined over the years based on newer and better diffraction data [18, 73, 75]. The relationship is found to be

$$V_i = \sum_{j=1}^N e^{\frac{(R_o - R_{ij})}{b}} \quad (2.44)$$

where  $R_o$  is the tabulated expected bond distance between atoms  $i$  and  $j$  based on empirical evidence,  $R_{ij}$  is the observed bond distance found through refinement, and  $b$  is an empirical constant normally taken to be 0.37 Å.  $V_i$  is known as the bond valence sum, a sum of contributions from the  $N$  bonds of atom  $i$  to the valence state of atom  $i$ . For example, by analyzing the bond distances around a Ti ion in six-fold coordination with O, one can calculate the valence state of Ti by summing the contributions from each of the six Ti-O bond lengths using equation 2.44; this would add up to 4 if Ti were in its 4+ valence state. Because the relationship is empirical, the accuracy of this approach is dependent on how frequently materials involving an ion are typically studied. For example, the tabulated bond distance between  $\text{Te}^{6+}$  and  $\text{O}^{2-}$  is probably less accurate than  $\text{Ti}^{4+}$  and  $\text{O}^{2-}$  owing to the many more materials studied with  $\text{Ti}^{4+}$  than  $\text{Te}^{6+}$ . Furthermore, bond valence sums are also dependent on the precision of bond distances reported using refinements, which are frequently overestimated for reasons mentioned in section 2.3.1. Typically the errors associated with bond valence sum analysis are around 10 - 15%.

## 2.4 Direct Current (DC) magnetometry

DC magnetometry is used as a means to gain insight into the magnetic interactions and as a tool to observe magnetic phase transitions within a sample. Figure 2.12 shows how the susceptibility of paramagnets, diamagnets, ferromagnets and antiferromagnets behave as a function of temperature. Because the susceptibility describes how materials behave upon the application of a magnetic field, it can be used to classify materials as either paramagnets and diamagnets. Paramagnets and diamagnets should have zero

magnetization in the absence of a field, since the magnetic moments are dynamic. Ferromagnets spontaneously order as the temperature is lowered beneath a critical threshold called the Curie Temperature,  $T_c$ , such that a finite magnetization is observed even in the absence of an external field. This is caused because of a slowing of the moments such that their orientations are no longer random, but average out so that they are aligned parallel to each other. The susceptibility diverges as  $T_c$  is approached followed by a strong increase in the magnetization below  $T_c$ . Cooling the sample in a field (field-cooling) as opposed to cooling in the absence of a field (zero-field cooling) will result in different magnetization values in the sample due to the preferred orientations of the magnetic domains towards the field direction. When the magnetic behaviour of a material is dependent on not only its current, but its previous exposure to a magnetic field, it is said to exhibit field-dependent hysteresis. On the other hand, the magnetization in antiferromagnets also diverges as the critical temperature, called the Néel temperature  $T_N$ , is approached from above. However, below  $T_N$  the moments slow and align antiparallel to each other such that there is no net magnetization in the absence of a field. A cusp is observed in the susceptibility and the magnetization tends towards zero [18].

In this work, a vibrating sample magnetometer is used to measure the magnetic susceptibility. A sample is connected to a long rod which is attached to a linear driving motor that vibrates the sample inside a chamber surrounded by a pickup coil. The entire apparatus is placed inside a magnetic field (Figures 2.13 through 2.15). The magnetic field induces a finite magnetization within the sample. Vibrating the sample inside the pickup coil chamber creates a magnetic flux that induces a voltage within the pickup coil

$$V_{\text{coil}} = \frac{d\phi}{dt} = \frac{d\phi}{dz} \frac{dz}{dt} \quad (2.45)$$

where  $\phi$  is the magnetic flux within the pickup coil chamber,  $z$  is the position of the sample with respect to the coil chamber, and  $t$  is the time [76]. The position of the sample oscillates according to a sine curve, which makes the voltage equate to

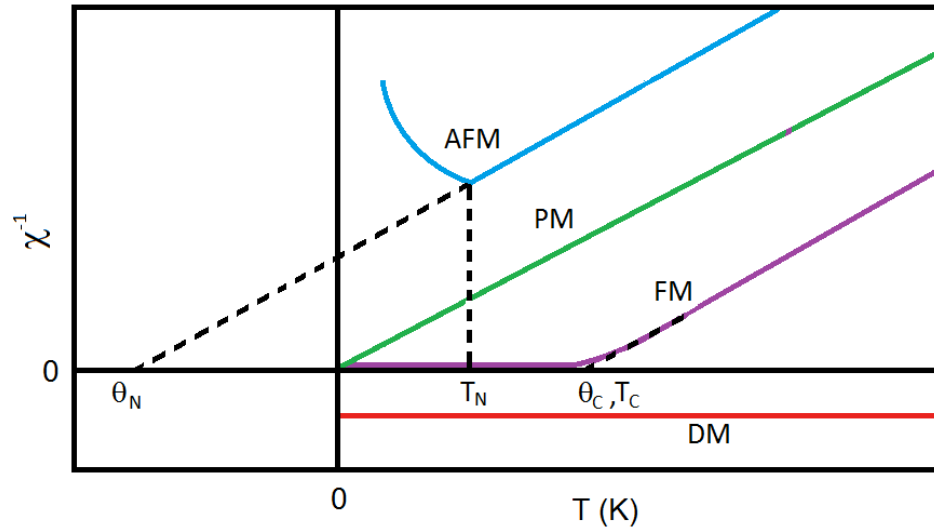


FIGURE 2.12: The temperature dependence of the magnetic susceptibility for antiferromagnets (AFM), paramagnets (PM), ferromagnets (FM), and diamagnets (DM).

$$V_{\text{coil}} = 2\pi f C m A \sin(2\pi f t) \quad (2.46)$$

Where  $f$  is the oscillation frequency,  $C$  is a coupling constant,  $m$  is the magnetization of the sample, and  $A$  is the oscillation amplitude. In order to calculate the moment, the motor centres the sample to the vertical centre of the pickup coil. It then not only oscillates the sample sinusoidally, but communicates the position of the sample with the computer. Simultaneously, the voltage induced by the pickup coil is amplified and relayed to the computer as well.



FIGURE 2.13: The material with known mass is placed inside a plastic holder and held at a fixed position in a brass clasp. The susceptibility of the holder and clasp are measured prior to measurement of the sample.



FIGURE 2.14: The brass holder is placed at the end of a long rod. This rod is vibrated inside a coil pickup at the bottom of the Physical Property Measurement System. The motor can be seen at the top right corner of the figure.



FIGURE 2.15: A superconducting ring can produce fields of up to 9 T at the base of the instrument. The sample rod is inserted through the top of the PPMS all the way to the base where the coil pickup sits.



## 2.5 Heat capacity

The heat capacity of a system,  $C$ , is defined as the amount of heat,  $q$ , it takes to change the temperature of a system,  $T$  [9, 19]

$$C = \frac{dq}{dT} \quad (2.47)$$

Heat capacity measurements can provide an enormous amount of information about the sample. Measurements can be performed under conditions of constant volume, where the heat capacity is directly related to the change in internal energy of a system through the first law of thermodynamics:

$$dU = \delta q + \delta w \quad (2.48)$$

Here,  $dU$  is the change in internal energy (exact differential) and  $\delta q$  and  $\delta w$  are the changes in the heat and work respectively (inexact differentials). However, an experiment under constant volume is quite difficult to achieve in the laboratory. In practice, heat capacity experiments are frequently performed under constant pressure, where the heat capacity is instead related to the enthalpy of system defined as

$$dH = dU + d(PV) = \delta q_p \quad (2.49)$$

where  $dH$  is the change in enthalpy and  $d(PV)$  is the change in the pressure-volume product. For solids that are relatively incompressible, the constant volume and constant pressure heat capacities are similar. For the purposes of discussing the theory, it is assumed that the heat capacity is measured at constant volume.

At high temperatures, the heat capacities of all solids are roughly equivalent according to the Dulong-Petit Law:

$$C = 3Nk_B \quad (2.50)$$

where  $N$  is the number of atoms and  $k_B$  is the Boltzmann constant. At low temperatures, the heat capacities of solids can generally be described by the empirical relationship

$$C = \gamma T + \beta T^3 \quad (2.51)$$

where  $\gamma T$  is the electronic portion of the heat capacity with linear temperature dependence and  $\beta T^3$  is the lattice contribution to the heat capacity with a cubic temperature dependence. Since most langasites are insulators, the electronic portion of the heat capacity is negligible. The lattice portion of the heat capacity can be derived using Debye's approach. A sample consisting of  $N$  atoms, each with mass  $m$ , with cubic symmetry is said to have  $N$  harmonic oscillators each having  $3N$  degrees of freedom of vibration in the lattice. In previous treatments of the heat capacity such as those by Einstein, each of these harmonic oscillators is treated as essentially independent vibrations having a certain frequency. Debye began his approach by treating these vibrations as quasi-particles: they are able to interact with each other, their individual frequencies being dependent on their wave vector, behaving within the periodic potential of the lattice. The Debye heat capacity is given by

$$C = 9Nk_B \left(\frac{T}{\theta_D}\right)^3 \int_0^{\frac{\theta_D}{T}} \frac{e^x x^4 dx}{(e^x - 1)^2} \quad (2.52)$$

which assumes a frequency of the of the modes that is linearly dependent on the wave vector. Here,  $\theta_D$  is a relative temperature called the Debye temperature describing the energy at which the phonon modes begin freezing out as the temperature is lowered. The integral is solved numerically, but it is useful to look at the limiting cases. At high temperatures,  $x$  becomes quite small such that  $e^x$  can be approximated to be  $1 + x$ . This reduces the integral to  $\theta_D^3/T^3$  making  $C$  the value of the Dulong-Petit law. At low temperatures,  $\theta_D/T$  becomes very large reducing the integral to a constant. The heat capacity at low temperatures becomes

$$C = \left(\frac{12\pi^4 N k_B}{5\theta_D^3}\right)T^3 = \beta T^3. \quad (2.53)$$

For more complicated materials, the equation becomes considerably more complex and begins to break down. Langanites do not have cubic symmetry so equation 2.52 is not so useful.

Most observable changes to the internal energy should manifest in the heat capacity. Phase transitions to a long-range ordered state show up in the heat capacity as sharp asymmetric spikes in the heat capacity. Magnetic transitions are also observable in the heat capacity. The heat capacity is related to the entropy by the following relation

$$S = \int_0^T \frac{C_v dT}{T}. \quad (2.54)$$

If one were to subtract off the phonon contribution of the heat capacity either by fitting the experimental heat capacity to the Debye function (if appropriate) or through using an appropriate lattice standard (isostructural diamagnetic analogue), it is possible to obtain the magnetic entropy by integrating under the curve of  $C_V/T$  as a function of  $T$ . According to Boltzmann's definition of the entropy  $S = k_B \ln W$  where  $W$  is the number of states in the system, integrating the curve under a magnetic lambda anomaly should approximately equal  $S = N k_B \ln(2J + 1)$  or  $S = N k_B \ln(2S + 1)$  where the orbital component of the magnetism is quenched [9].

The heat capacity at low temperatures for small sample sizes is usually measured through a relaxation method: a fixed amount of heat is delivered to the sample followed by a measurement of the change in temperature of the sample. Here, a Quantum Design Physical Property Measurement System was used for all heat capacity measurements. The relaxation method is a dynamic technique that places special importance on the geometry and thermal diffusivity of the sample (it cannot be longer than the relaxation time). This makes the relaxation method prohibitively long for large samples or those

with poor thermal diffusivity.

A sample is placed on top of a sample stage connected with thermal links to a puck frame that acts as a temperature bath (Figure 2.16). The sample is held onto the stage via Apiezon N-grease that also provides thermal contact to the platform heater. It is important to subtract the contribution of the puck chamber, sample stage, and N-grease from the contribution of the sample: this is called the addenda measurement. The chamber must be evacuated such that the only source of thermal contact is through the heater on the sample stage. In addition to the high vacuum environment, a charcoal puck is often used to absorb any remaining gas. The puck chamber contains a puck thermometer, which measures the temperature of the bath. Eight wires suspend the sample stage platform, which contains its own thermometer and its own heater. A thermal radiation shield surrounds the entire apparatus while in use.

Assuming that the sample and platform have good thermal contact, the temperature of the sample platform (including the sample) as a function of time can be described by

$$C \frac{dT}{dt} = P(t) - K_W(T(t) - T_b) \quad (2.55)$$

where  $K_W$  is the thermal conductance of the wires,  $T_b$  is the temperature of the thermal bath, and  $P(t)$  is the heater power delivered to the sample platform, which is a constant on heating or zero upon measurement [76]. The solution is an exponential equation with a time constant,  $\tau$  that equates to  $C/K_W$ . A more sophisticated two- $\tau$  model is sometimes used for sample with poorer thermal contact with the platform:

$$C_{\text{platform}} \frac{dT_P}{dt} = P(t) - K_W(T_P(t) - T_b) + K_g(T_s(t) - T_P(t)) \quad (2.56)$$

$$C_{\text{sample}} \frac{dT_s}{dt} = -K_g(T_s(t) - T_P(t)) \quad (2.57)$$

where  $K_g$  is the thermal conductance between the platform and the sample due to the

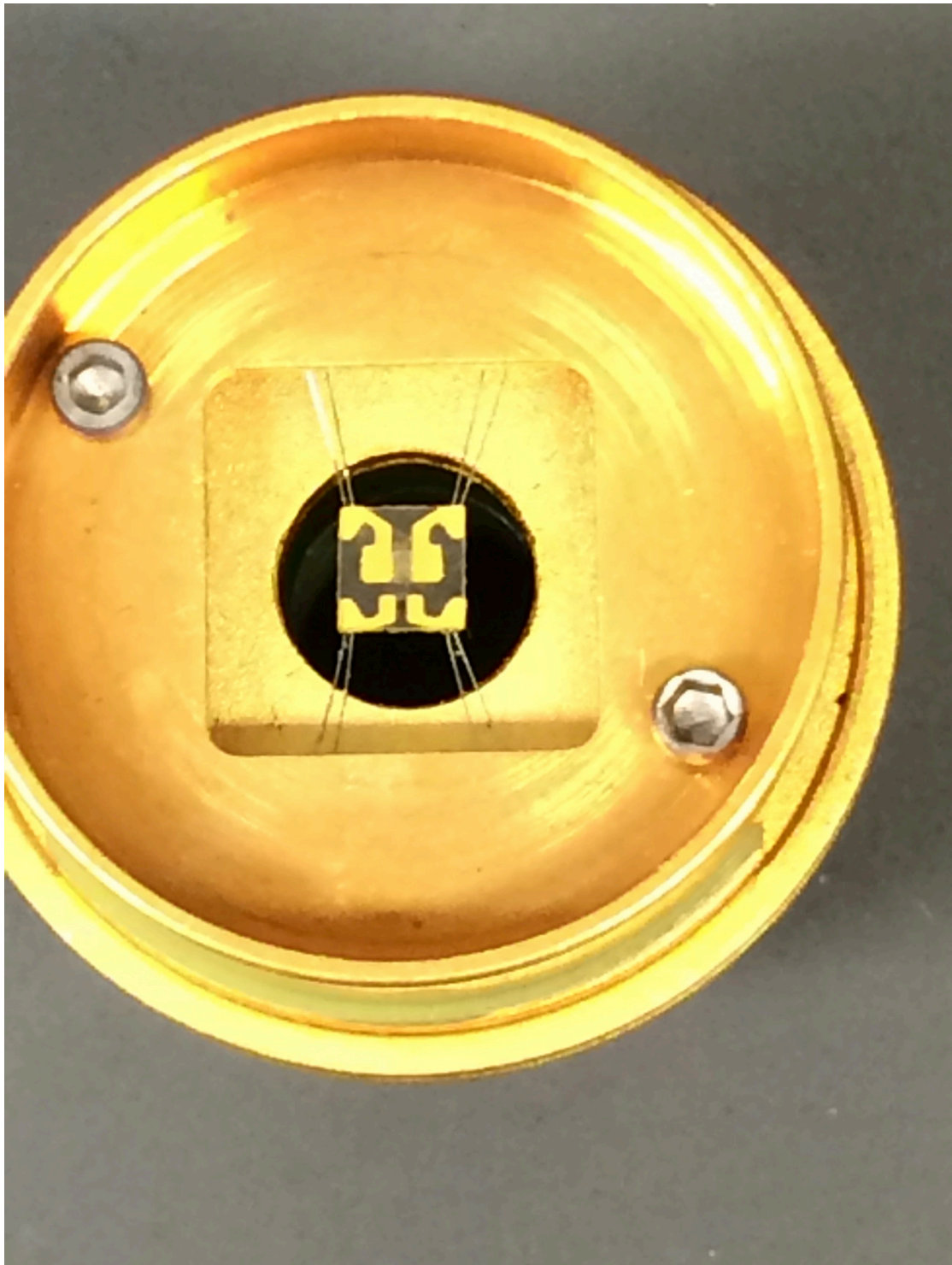


FIGURE 2.16: The sample stage is shown connected by the eight wires to the gold-plated puck frame. A small heater and thermometer are located on the back of the sample stage (not visible). This puck is inserted inside the Physical Property Measurement System (Figure 2.15) where the coil pickup for the magnetometer option would normally sit.

grease. Both models assume that the heat capacity is constant before and after heat is delivered to the sample. A nonlinear least-square fitting algorithm is used to fit the model to the data to derive the relevant parameters. For the addenda measurement, the simple one- $\tau$  model is used to extract the addenda heat capacity and the time constant. For the sample measurement, the two- $\tau$  model is used that calculates the total heat capacity composed of the sample and previously measured addenda heat capacities, the time constants  $\tau_1 = 1/(\alpha - \beta)$  and  $\tau_2 = 1/(\alpha + \beta)$ , and the sample coupling  $100 \times K_g/(K_g + K_W)$ , where  $K_g$  is also found from the addenda measurement. Here,  $\alpha$  and  $\beta$  are

$$\alpha = \frac{K_W}{2C_{\text{platform}}} + \frac{K_g}{2C_{\text{platform}}} + \frac{K_g}{2C_{\text{sample}}} \quad (2.58)$$

$$\beta = \frac{\sqrt{K_g^2 C_{\text{sample}}^2 + 2K_g^2 C_{\text{sample}} C_{\text{platform}} + K_g^2 C_{\text{sample}}^2 + K_W^2 C_{\text{sample}} K_g - 2K_W C_{\text{sample}} K_g C_{\text{platform}}}}{2C_{\text{sample}} C_{\text{platform}}} \quad (2.59)$$

## 2.6 Dielectric constant

Analogous to the magnetic susceptibility is the dielectric susceptibility, which measures the response of a material under an electric field. Just as diamagnetic materials are magnetically polarized such the internally induced field opposes the external field direction, dielectric materials are electrically polarized such that the internally induced field opposes the external electric field direction. The dielectric constant,  $\epsilon$ , is related to the capacitance of a material through

$$\epsilon = \frac{dC}{A\epsilon_0} \quad (2.60)$$

where  $d$  is the distance between parallel plates,  $A$  is the area of the parallel plates,  $C$  is the capacitance, and  $\epsilon_0$  is the constant permittivity of free space ( $8.854 \times 10^{-12}$  F/m) [77]. The dielectric constant is measured for the material placed between the parallel plates.

Measurements can be made in static or alternating electric fields; generally the dielectric constant is a complex number, the imaginary component arising from a phase shift of the internal polarization relative to the external electric field. Using an alternating current, the dependence of the dielectric constant on the frequency of the electric field can be assessed. At low frequencies, the real component should dominate and will mirror results using a static field. At high frequencies, the imaginary component begins to dominate: charges will move in response to the changing frequency that results in a loss of energy through heat. Lossy dielectrics are typically parametrized through the loss tangent,  $\tan(\delta)$

$$\tan(\delta) = \frac{(\omega\epsilon'' + \sigma)}{\omega\epsilon'} \quad (2.61)$$

where  $\omega$  is the angular frequency of the field,  $\epsilon''$  is the imaginary component of the dielectric constant attributed to bound charges, and  $\epsilon'$  is the real component.  $\sigma$  is an important parameter that distinguishes these measurements from magnetic susceptibility measurements. It defines the loss due to free charges. Ideally, magnetic susceptibility measurements have no direct contact between the pickup coils and the sample. On the other hand, measurements of the dielectric constant require physical contacts between the electric field source and the sample. Samples must be cut in the shape of a parallel plate with its dimensions precisely known. Electric contacts are typically made using silver paste. These contacts introduce charge to the material: the movement of these free charges throughout the sample, and the heat generated from them is described by  $\sigma$  and are indistinguishable from  $\epsilon''$  in this type of measurement (free charge carriers also exist in metals that are also described by  $\sigma$ ). Each experimental apparatus must be carefully calibrated and monitored. Because of the electrical contacts, there are many potential sources for anomalous behaviour [78]. The dielectric loss is useful for detecting resonance frequencies associated with polarization behaviour: a sharp increase in the dielectric loss is observed around these frequencies.

## 2.7 Inelastic neutron scattering

Neutron diffraction was covered extensively in section 2.2, culminating in equations 2.27 and 2.28. However, those equations integrated over all possible neutron energies. Neutrons produced through fission or spallation have a wide distribution of energies and it is possible to separate and detect the energies of scattered neutrons. If the initial neutron energy is  $E$  and the final neutron energy is  $E'$ , then the equations are modified as follows [11, 18, 56]:

$$\frac{d^2\sigma}{d\Omega dE'} = \frac{\text{neutrons scattered into } d\Omega(\theta, \phi) \text{ per second with final energy } E' + dE'}{\Phi d\Omega dE'} \quad (2.62)$$

$$\frac{d^2\sigma}{d\Omega dE'} = \left(\frac{\vec{k}}{\vec{k}'}\right) \left(\frac{m}{2\pi\hbar^2}\right)^2 \sum_{\lambda} P_{\lambda} \sum_{\lambda'} |\langle \vec{k}'\lambda' | V(\vec{r}) | \vec{k}\lambda \rangle|^2 \delta(E_{\lambda} - E_{\lambda'} - E_i - E_f) \quad (2.63)$$

$$\frac{d^2\sigma}{d\Omega dE'} = \left(\frac{\vec{k}}{\vec{k}'}\right) N b^2 S(\vec{K}, \omega) \quad (2.64)$$

$$S(\vec{K}, \omega) = \frac{1}{\hbar N} \sum_{i,j} \int_{-\infty}^{\infty} e^{i\omega t} \langle (e^{-i\vec{K}\cdot\vec{R}_i(0)})(e^{-i\vec{K}\cdot\vec{R}_j(t)}) \rangle dt. \quad (2.65)$$

In equation 2.63, the scattering cross section is now summed over not only the initial and final states  $\lambda$  and  $\lambda'$  through the Fermi pseudopotential  $V(\vec{r})$ , but also through the relative populations of those states  $P_{\lambda}$ . The delta function at the end specifies that detection of the neutron can occur through two ways. In the first, the initial and final energies are equivalent, so the initial and final states must also be equivalent: this is standard diffraction. The second way is that any difference in the initial and final states can be compensated through an equivalent difference between the initial and final energy states of the system.  $S(\vec{K}, \omega)$  is called the dynamic structure factor dependent on  $\vec{K}$  and  $\omega$ , the latter defined by  $\omega = \Delta E/\hbar = (E_f - E_i)/\hbar$ . The dynamic structure factor



is derived by evaluating 2.63 followed by a Fourier transform. It is dependent on the position of atom  $j$  at a time  $t$  relative to atom  $i$  at time 0. Note that if atom  $i$  and  $j$  are equal, incoherent diffuse scattering naturally results, which contributes to a small, isotropic, and temperature-independent background signal.

Inelastic neutron scattering can be done through a variety of methods that include the use of a triple-axis spectrometer that won Canadian Professor Bertram Brockhouse half of the Nobel Prize in 1994. Here, inelastic neutron scattering data was performed on the time-of-flight instrument SEQUOIA [79, 80] at the Spallation Neutron Source at Oak Ridge National Laboratory. An incoming white pulse of neutrons is made incident on velocity selecting choppers. The choppers are made of a neutron absorbing material with a small hole cut out from the side. These choppers are spun with a certain angular frequency in opposing fashion such that only a single neutron velocity is selected. The neutrons are then guided towards the sample inside a large evacuated chamber. Detectors almost completely surround the sample. Since the initial velocity of the neutrons is known, the pulse timing is known, and the distance from the sample to each of the detectors is known, both the position and change in neutron velocity are known once the scattered neutron hits the detector. A large multidimensional data set results that relates the number of scattering events to both the position and energy transfer of the event (for single crystals, a four dimensional data set is obtained since  $\vec{K}$  is no longer isotropic). Inelastic neutron scattering is an irreplaceable probe for solid materials: luckily, the energy scale of neutrons with useable wavelengths is of the same order of magnitude as phonons and magnetic excitations in materials [56].

## Chapter 3

# Nuclear and Magnetic Structures of the Multiferroic Languisite, $\text{Ba}_3\text{NbFe}_3\text{Si}_2\text{O}_{14}$

### 3.1 Preamble

When this project started in 2010, the ultimate goal was to understand the magnetism of languisite series members. The first of such languisites to be studied was  $\text{Ba}_3\text{NbFe}_3\text{Si}_2\text{O}_{14}$ . We had made enough of the material so that we could perform inelastic neutron scattering experiments on the new Cold Neutron Chopper Spectrometer (CNCS) and/or SEQUOIA instruments at the Spallation Neutron Source (SNS, Oak Ridge, TN). However after preparing the material, analyzing its crystal and magnetic structures, and submitting a proposal to build on previous experiments from Zhou *et al.* [81], a paper was released detailing the measurements that we had proposed [82].

Despite abandoning this project early on, I have included my structural analysis of  $\text{Ba}_3\text{NbFe}_3\text{Si}_2\text{O}_{14}$  due to the influence that this section had on the development of my thesis as a whole. The discussion will include recent findings using inelastic neutron spectroscopy from other studies.

## 3.2 Introduction

The langasites, characterized and named after  $La_3Ga_5SiO_{14}$ , have long been known for their optical [83] and piezoelectric properties [84] owing to their  $P321$  symmetry. They can be made into single crystals relatively easily and many have no accompanying phase transitions below their respective melting temperatures. As such, nonmagnetic langasites are often found in electronic devices as sensors, filters, and resonators. In 2006, a strong interest in magnetic langasites developed when it was realized that these materials contain geometrically frustrated sublattices. For example,  $Nd_3Ga_5SiO_{14}$  contains rare-earth ions situated on two-dimensional distorted kagomé sublattices that stack along the  $c$ -axis (Figure 3.1), which is still being investigated as a potential spin liquid material. [85–89]

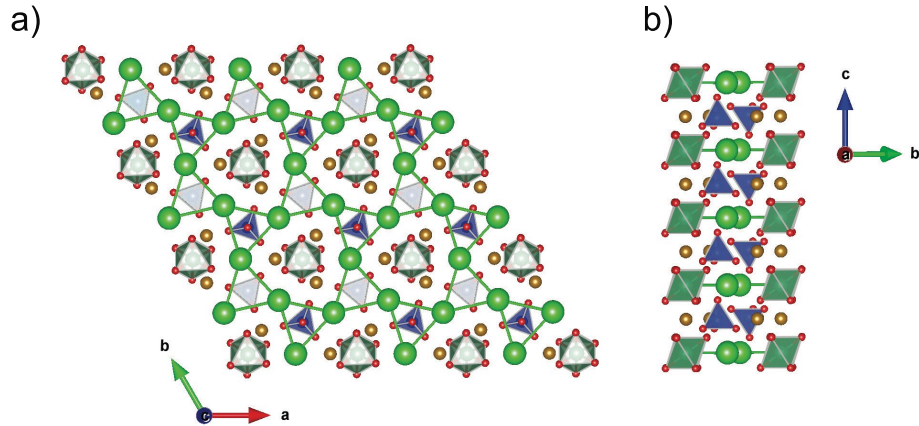


FIGURE 3.1: The kagomé sublattice in  $Nd_3Ga_5SiO_{14}$  as viewed from the **a)**  $ab$ -plane and **b)** stacked along  $c$ .  $Nd^{3+}$  ions are located on the  $3e$  site identified by large green coloured spheres connected by bonds, whereas  $Ga^{3+}$  and  $Si^{4+}$  equally occupy the  $2d$  site that is four-fold coordinated with  $O^{2-}$ , represented as blue tetrahedra. Gold spheres and dark green octahedra denote the  $3f$  and  $1a$  sites respectively and are both occupied by  $Ga^{3+}$ .

However, a second frustrated sublattice exists: isolated equilateral trimers containing tetrahedrally coordinated ions are located in the centre of each kagomé star and spaced directly between kagomé layers (Figure 3.2).

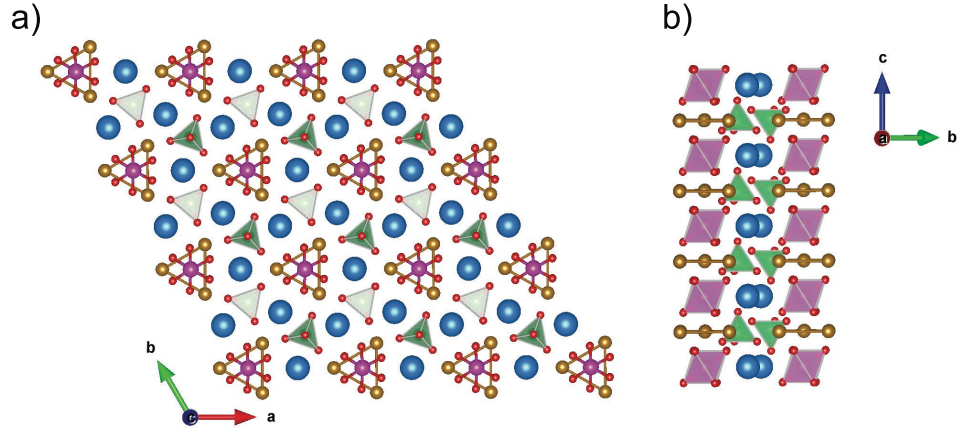


FIGURE 3.2: The langasite trimer sublattice as viewed from the a)  $ab$ -plane and b) stacked along  $c$ . The trimers are composed of the ions that occupy the  $3f$  site coloured by the gold spheres while ions that make up the kagomé sublattice are coloured blue.  $1a$  ions (pink) bonded to  $O^{2-}$  form octahedra (they are shown without polyhedral faces for clarity in a).  $2d$  ions are coloured green and are shown as tetrahedra with oxygen.  $3f$  ions also tetrahedrally coordinate with  $O^{2-}$ , but these tetrahedra are much larger and more distorted than the  $2d$  tetrahedra.

The ions that occupy these trimers are spaced much closer together than the rare-earth ions on the kagomé sublattice making it easier for orbital overlap to occur in the former than the latter.

$Ba_3NbFe_3Si_2O_{14}$  was first reported in 2008 [90] where the  $Fe^{3+}$  ions occupy the vertices of the trimers. This material magnetically orders below the Néel temperature  $T_N = 26$  K into a very complex helical spin structure. Single crystals of this material grown using the optical floating zone method were used to show that the magnetic moments propagate along the  $c$ -axis over approximately seven unit cells. By virtue of the chiral crystal structure found using anomalous x-ray diffraction [90], it was determined that this material simultaneously exhibits single domain moment chirality, not only within each individual trimer, but in the helical propagation as well. Hereafter, the helical propagation will be referred to as “helicity” so as not to confuse it with the triangular chirality (Figure 3.3).

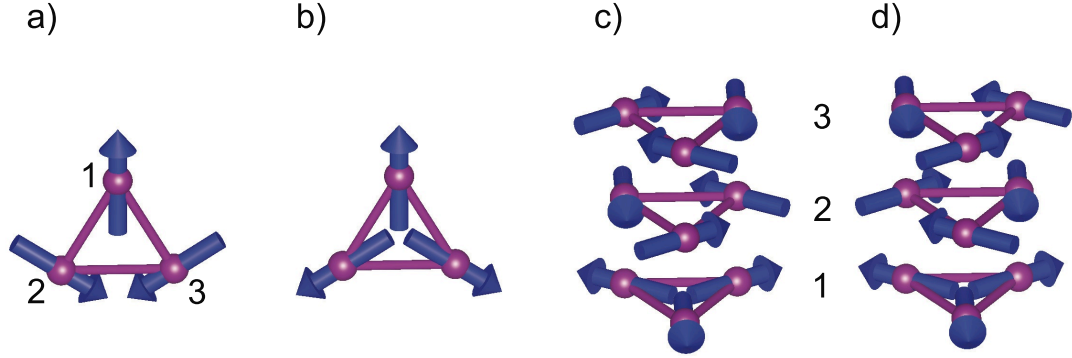


FIGURE 3.3: Clockwise triangular chirality is shown in **a)** as the moment in atom one rotates  $120^\circ$  while counterclockwise chirality is displayed in **b)**. Chirality can also be displayed in the helix, independent of the triangular chirality as shown for the **c)** left-handed and **d)** right-handed helices.

This complex magnetic ordering was hypothesized to induce an electric polarization on the basis of the discovery of this phenomenon in similar materials [17] and earlier theoretical studies [91–93]. One year later, Zhou *et al.* [94] showed that electric polarization could be achieved below  $T_N$  by applying an electric field along the  $c$ -axis.

Due to the complexity of the magnetic structure and multiferroic behaviour in this material, it is of considerable interest to study the magnetic dynamics present in this system. Inelastic neutron spectroscopy has been used on a wide variety of systems including  $Ba_3NbFe_3Si_2O_{14}$ . [81] In that study, Zhou *et al.* used the Disc Chopper Spectrometer (DCS) at the NIST Center for Neutron Research (NCNR, Gaithersburg, MD) on an oriented sample of single crystal  $Ba_3NbFe_3Si_2O_{14}$ . Short-range correlations were found to develop far above  $T_N$  which manifested in well-defined spin-waves, propagating excitations from the magnetic lattice, below  $T_N$ . These spin waves could be modelled using a Heisenberg Hamiltonian with a triangular magnetic structure utilizing nearest and next-nearest neighbour interactions. However a peak in the development of short-range correlations, manifested as diffuse quasi-elastic scattering, was found at 40 K. The

authors attempt to explain this peak as arising from a saturation of elastic diffuse scattering followed by an opening of a spin gap just outside of the resolution of the DCS. A full attempt to incorporate the effects of the Dzyaloshinskii-Moriya interaction into the Hamiltonian would require higher energy resolution scans over the possible gap. Here,  $Ba_3NbFe_3Si_2O_{14}$  is prepared and the crystal and magnetic structures were studied in order to confirm the phase purity and integrity of the sample. The intent was to grow a single crystal using this powder and perform high-resolution inelastic neutron scattering experiments.

## 3.3 Methods

### 3.3.1 Preparation

The successful preparation of a langasite is thought to be highly dependent on the size ratio of the ion [95] that occupies the  $P321$   $3e$  site to the size of the unit cell although this is mostly based on empirical evidence [96] rather than theoretical studies. In surveying 118 different langasite materials, a stability field can be produced built from the crystal radius ratios of the cations (Figure 3.4) [96–112]. However, electronic differences between the various ions used are expected to play a role in the formation of the final phase; the stability field should be used as a guide rather than a rule. These ions are normally eight-fold coordinated with oxygen to form a distorted Thomson cube or decahedron. Langasites using  $La^{3+}$  [84],  $Pr^{3+}$  [113], and  $Nd^{3+}$  [85] have all been prepared, but using smaller ions further down the lanthanide series results in the formation of the competing garnet phase, such as  $Ln_3Ga_5O_{12}$  ( $Ln =$  rare earth ion) with the expulsion of  $SiO_2$  during the reaction. Attempts have been made at expanding the  $3e$  site radius tolerance by making the unit cell smaller either through physical or chemical pressure. The latter has been achieved with mixed results using cation [110, 114] or anion [96] substitution (or sometimes both).

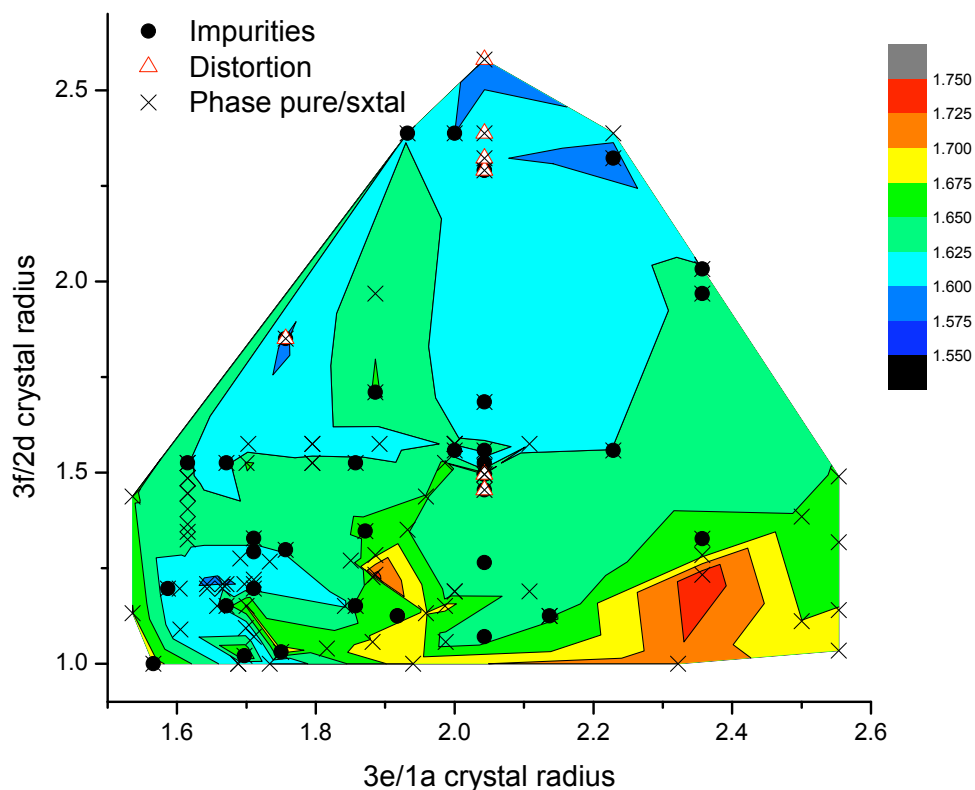
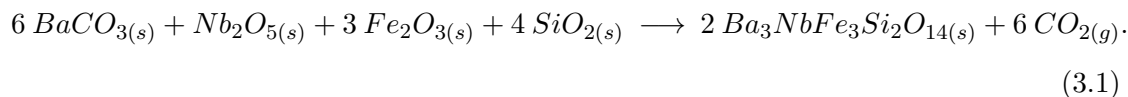


FIGURE 3.4: A proposed langasite stability field based on the crystal radius ratios of the decahedral/octahedral site and large/small tetrahedral site. The colour map depicts the ratio of the  $a/c$  lattice constants and does not appear to correlate with the stability of the langasite. Many different langasites were surveyed including single crystals, powders, dugganites, and langasites with up to 40% vacancies on a single site (called “vacant langasites” here). There are many conflicting studies regarding lattice constants for the same material: they heavily depend on site-stoichiometry and preparative method. The crystal radius of vacant langasite sites were adjusted for the vacancy. Although vacancies are quite clear for the  $3e$  site, they are less so for the other sites and had to be estimated. For langasites that distort, the trigonal subcell lattice constants were used. Some studies report impurities along with the main phase. For materials with greater than 15% impurities, data could not be obtained. Many points overlap due to there being more than one study on the material. Note that this is not an exhaustive data set and further work needs to be done to improve the stability field.

All data was taken from [96–112].

The reaction equation is shown below:



Since  $BaCO_3$  is slightly hygroscopic, this material was dried at 200 °C prior to use. All reactants were purchased from Sigma Aldrich and all have purity of 99.9% or greater. The materials were ground up by hand for 15 minutes per gram of material, pelleted using 25 MPa of pressure, and placed in a tube furnace under oxygen atmosphere. The furnace was ramped to 950 °C in 2.5 hours and kept there for 24 hours followed by cooling to room temperature. The sample was then reground by hand and repelleted under the same conditions and heated to 1200 °C for another 24 hours. Finally, the sample was once again reground and repelleted and annealed at 1000 °C for another 24 hours. Each reagent was tested for phase purity before its first use.

A large impurity was present which was found to be the garnet phase (Figure 3.5) although the exact chemical identity is not known for certain.

Annealing the sample for longer periods of time suppressed the impurities until they were present in about 3-4% excess. This was approximated by comparing x-ray powder peak heights of the impurities and main phases. It is interesting that such a garnet phase would form here since  $Ba^{2+}$  is, at present, the largest ion known to occupy the  $3e$  site of a langasite. The garnets generally form for smaller  $3e$  ions such as for  $Ln^{3+}$ , possibly suggesting the role of the garnet structure in the formation of the main phase (this is addressed further in the next chapter). A phase pure sample within the resolution of our diffractometer was made using a 7 wt% excess  $SiO_2$ . In total, six grams of sample was prepared.

### 3.3.2 Diffraction

All x-ray diffraction measurements were performed on a Siemens D5000 using a Cu anode with the slit configuration 0.4 mm x 0.6 mm x 0.6 mm x 1 mm in Bragg-Brentano



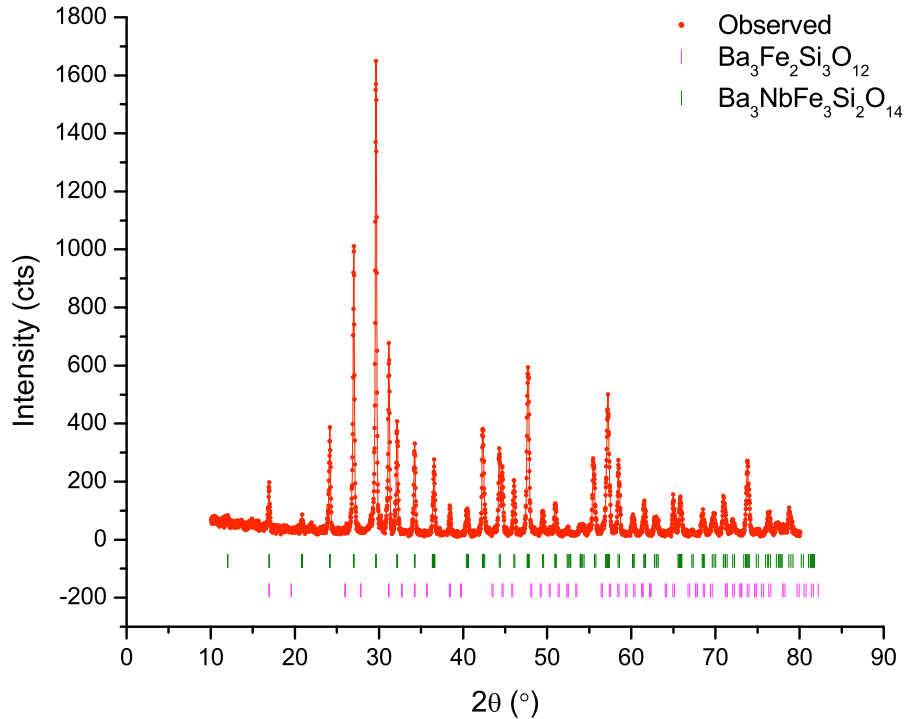


FIGURE 3.5: A large garnet impurity is found to compete with the langasite at reaction temperatures (approximately 1000 to 1200  $^\circ$ C). A third unknown phase is also present with its sole peak at  $55^\circ$   $2\theta$ , estimated to be about 5% based on relative peak intensities between phases.

geometry using a zero-background sample stage and Ni filter. Scans were collected over  $10$ - $80^\circ$   $2\theta$  in  $0.01^\circ$  steps counting for eight seconds per step. Neutron powder diffraction was performed on the POWGEN time-of-flight diffractometer (SNS, Oak Ridge, TN) [115] using banks 3 and 7 (detector banks with centring wavelengths of  $1.066$  and  $4.797$   $\text{\AA}$  respectively), capable of reaching  $d = 0.3$  to  $15.2$   $\text{\AA}$ . Six grams of powder was loaded into a vanadium cylindrical sample can under a  $He_{(g)}$  atmosphere. The sample height and diameter of the can were measured in order to optimize the placement of the can within the neutron beam. Measurements were taken at  $300$  K and  $10$  K so as to observe the low-temperature magnetic unit cell that forms below  $T_N = 26$  K. Refinements were performed first using solely x-ray diffraction data and then jointly with neutron diffraction data taken at  $300$  K using a weighting of 45% x-ray,

45% bank 3, and 10% bank 7 (Figure 3.6). Fe fluorescence and neutron absorption were roughly approximated using background and peak shape parameters since the relative concentration of Fe within this material is low.

## 3.4 Refinement

### 3.4.1 Room-Temperature Refinement ( $T > T_N$ )

The refinement was carried out using the prototypical langasite unit cell (the atomic coordinates and thermal parameters are given in Table 3.1). The structure of  $Ba_3NbFe_3Si_2O_{14}$  is shown in Figure 3.7.

TABLE 3.1: Atomic coordinates and refined thermal parameters at 300 K for  $Ba_3NbFe_3Si_2O_{14}$ . The cell was found to have  $P321$  symmetry with lattice parameters  $a = 8.5031(5)$  Å and  $c = 5.2357(3)$  Å.  $\chi^2 = 4.49, 2.31$ ;  $R_p = 12.4, 17.7$ ;  $R_{wp} = 9.07, 21.2$  for neutron and x-ray data respectively.

Ion	Site	x	y	z	$B_{iso}$ (Å <sup>2</sup> )
Ba <sup>3+</sup>	3e	0.4344(4)	0	0	0.67(2)
Nb <sup>5+</sup>	1a	0	0	0	0.76(3)
Fe <sup>3+</sup>	3f	0.7510(3)	0	$\frac{1}{2}$	0.65(2)
Si <sup>4+</sup>	2d	$\frac{1}{3}$	$\frac{2}{3}$	0.5217(12)	0.39(5)
O1 <sup>2-</sup>	2d	$\frac{2}{3}$	$\frac{1}{3}$	0.780(1)	0.86(4)
O2 <sup>2-</sup>	6g	0.5266(4)	0.8226(4)	0.6424(6)	0.85(2)
O3 <sup>2-</sup>	6g	0.2160(5)	0.1001(5)	0.7746(7)	1.66(2)

The fit converged on a trigonal  $P321$  unit cell with lattice constants equating to  $a = 8.5031(5)$  Å and  $c = 5.2357(3)$  Å. Isolated  $NbO_6$  octahedra are located at the corners of the unit cell sitting on the 3-fold rotation axis, which is oriented along the  $c$ -axis. Each Nb-O bond length is equidistant as a result of the 3- and 2-fold symmetry present in the cell, with a value of  $1.98(8)$  Å, which gives Nb a bond valence sum of 5.02.  $SiO_4$  tetrahedra are also isolated and sit on the inner 3-fold rotation axes with the  $Si-O_{apical}$  bond pointing directly along the  $c$ -axis. There are two Si-O bond lengths with  $Si-O_{apical}$

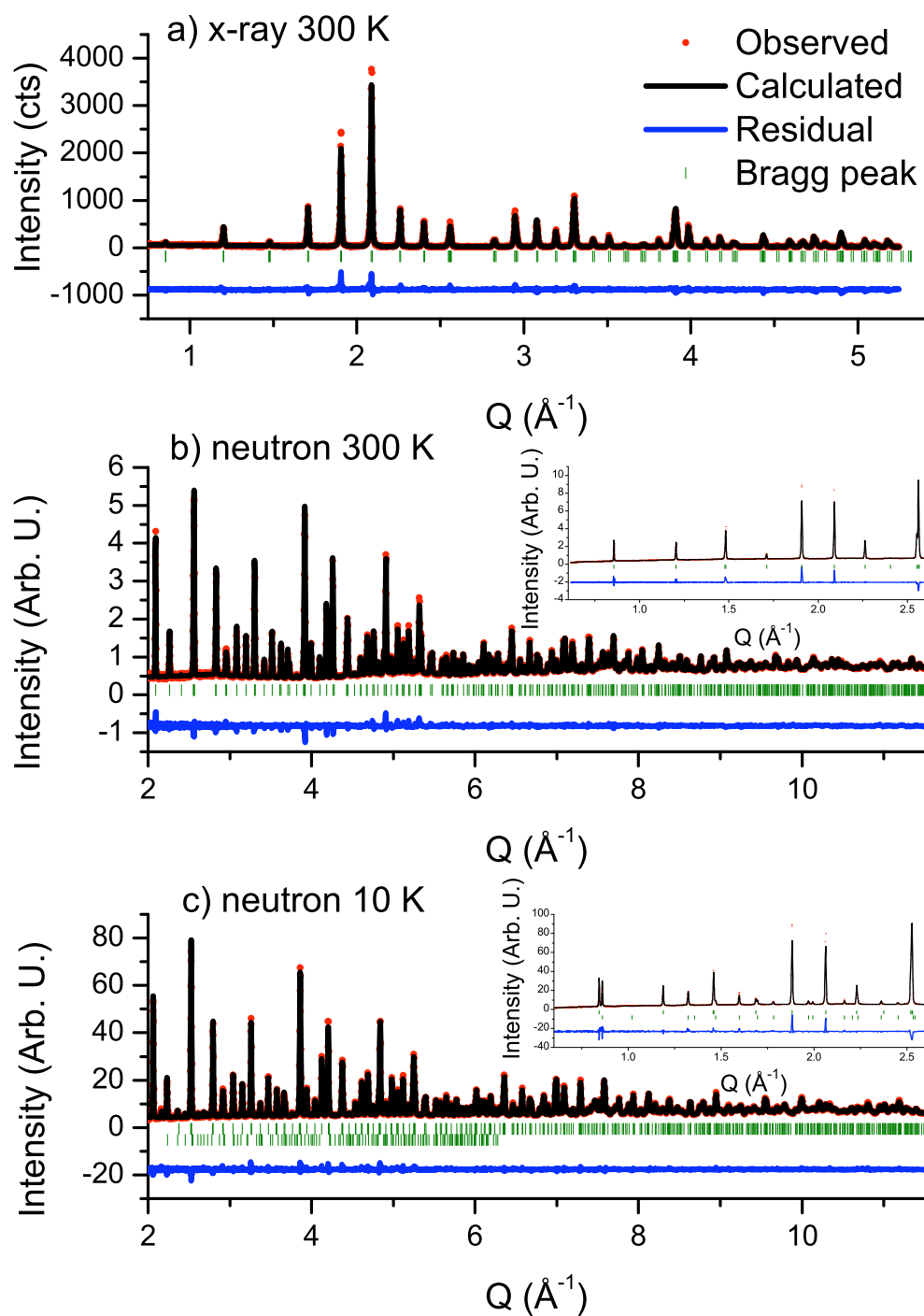


FIGURE 3.6: Joint x-ray/neutron refinement of  $Ba_3NbFe_3Si_2O_{14}$ . Room temperature x-ray and neutron data are shown in **a)** and **b)** respectively while neutron data at 10 K is shown in **c)**. Neutron bank 3 is shown in the outset while 7 is shown on the inset where relevant. For the 10 K data, magnetic reflections are labelled underneath nuclear reflections.

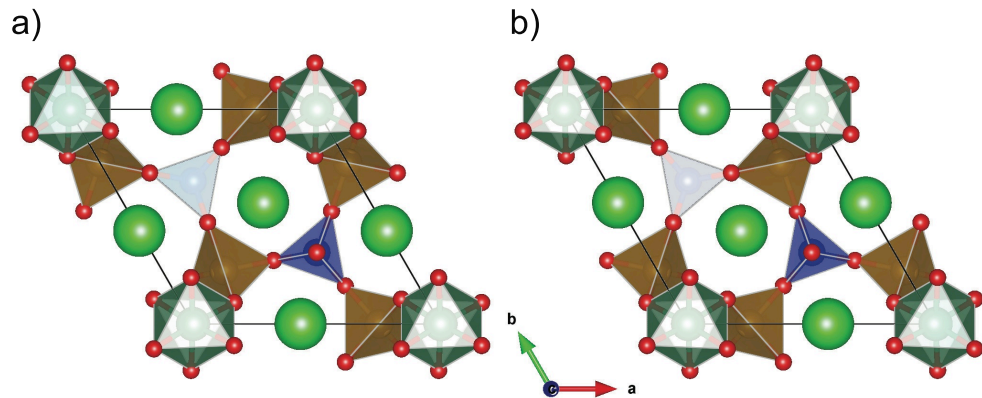


FIGURE 3.7: The **a**) right-handed (refined) and **b**) left-handed crystal structures of  $Ba_3NbFe_3Si_2O_{14}$ . Both of these structures are energetically stable and equivalent. Powders are a mixture of these structures while single crystals are enantiopure either in one or the other [90].  $Ba^{2+}$  ions occupy the green spheres while  $Nb^{5+}$ ,  $Fe^{3+}$ , and  $Si^{4+}$  are represented by the green octahedra, gold tetrahedra, and blue tetrahedra respectively.  $O^{2-}$  are depicted by small red spheres.

having a value of  $1.58(2)$  Å and the other Si-O bonds (forming the base) having bond lengths of  $1.63(4)$  Å. The bond angles in the tetrahedra are  $106.0(3)^\circ$  between O-Si-O bonds in the tetrahedral base and  $112.7(4)^\circ$  between O-Si- $O_{apical}$ . Si was found to have a bond valence sum of  $3.98(1)$ , which is a considerable improvement over values previously reported in the literature for this material [90, 94]. This likely reflects the use of both x-rays and neutrons simultaneously here.

$Fe^{3+}$  sits in a distorted tetrahedral site corner-linked to two  $SiO_4$  tetrahedra (to the base) and two  $NbO_6$  octahedra. Bond distances range from  $1.84(4)$  to  $1.89(5)$  Å, giving  $Fe^{3+}$  a bond valence sum of 2.98, which leaves little doubt as to the valence state of Fe in this material.  $Ba^{2+}$  is positioned in the intersites forming distorted decahedra that are edge-sharing with other decahedra,  $NbO_6$  octahedra, and  $SiO_4$  tetrahedral bases but corner-linked to  $FeO_4$  tetrahedra and  $O_{apical}$ . Small tetrahedral holes are formed from these decahedra directly opposing the Si- $O_{apical}$  bond (Figure 3.8).

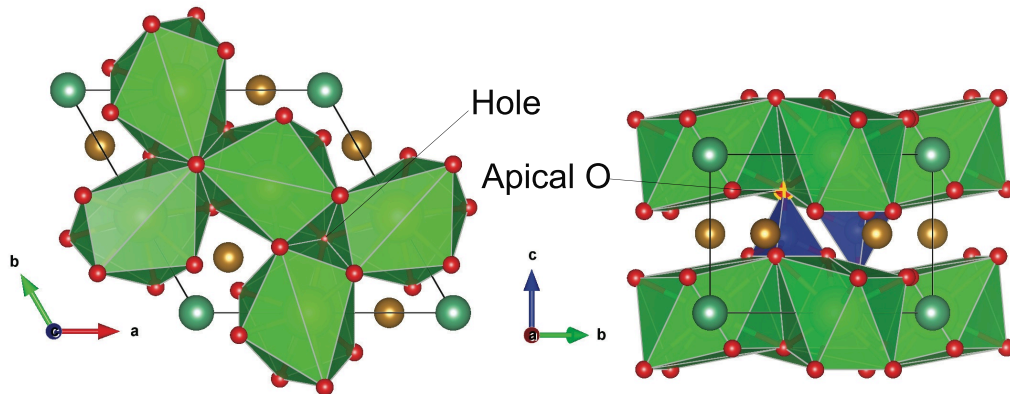


FIGURE 3.8: Holes are formed within the langasite structure.  $Ba^{2+}$  decahedra are labelled in green while  $Si^{4+}$  tetrahedra are labelled in blue. Gold and dark green ions are  $Fe^{3+}$  and  $Nb^{5+}$  respectively.

Although the decahedra are quite distorted, Ba still possesses a bond valence sum of 2.08. All isotropic thermal displacement parameters are positive with the general trend that the heavier elements have the smallest values. However, the refinement of the O3 isotropic thermal displacement parameter yielded an anomalously high value. For this atom, anisotropic thermal displacement parameters were tried in the refinement (not shown) and it was found that this atom preferentially displaces in a planar fashion along the  $y$ -axis.

### 3.4.2 Low-Temperature Refinement ( $T < T_N$ )

For this refinement, only neutron diffraction data was used. The atomic coordinates did not change within error although a reduction in the lattice constants was observed consistent with thermal expansion. The magnetic Bragg peaks could be fit using a propagation vector of  $\vec{k} = (0, 0, 0.142)$ , which is precisely the value reported previously in the literature [90]. An ordering of the  $Fe^{3+}$  moments can be well described by the irreducible representation (IR)  $\Gamma(1)$  of the little group  $G_x$  formed from the space group  $P321$  and the propagation vector  $\vec{k}$  restricted to the Hilbert space defined by the basis

vectors  $\Psi(1) = (1, 1, 1)$ ,  $\Psi(2) = (1, -1, 0)$ , and  $\Psi(3) = (1, 1, -2)$ , which all reduce to  $(1, 0, 0)$ ,  $(0, 1, 0)$ , and  $(0, 0, 1)$  respectively. The Fe moment refined to  $4.72(8) \mu_B$ , which is close to the expected value of  $5 \mu_B$  [8]. Restricting the view to a single displaced nuclear cell, the moments are oriented within the  $ab$  plane in  $120^\circ$  fashion (Figure 3.9). It is noted that the global triangular chirality (i.e. the absolute orientation of the moments within each trimer) cannot be solved even with the use of a single crystal and polarized neutrons [90, 116].

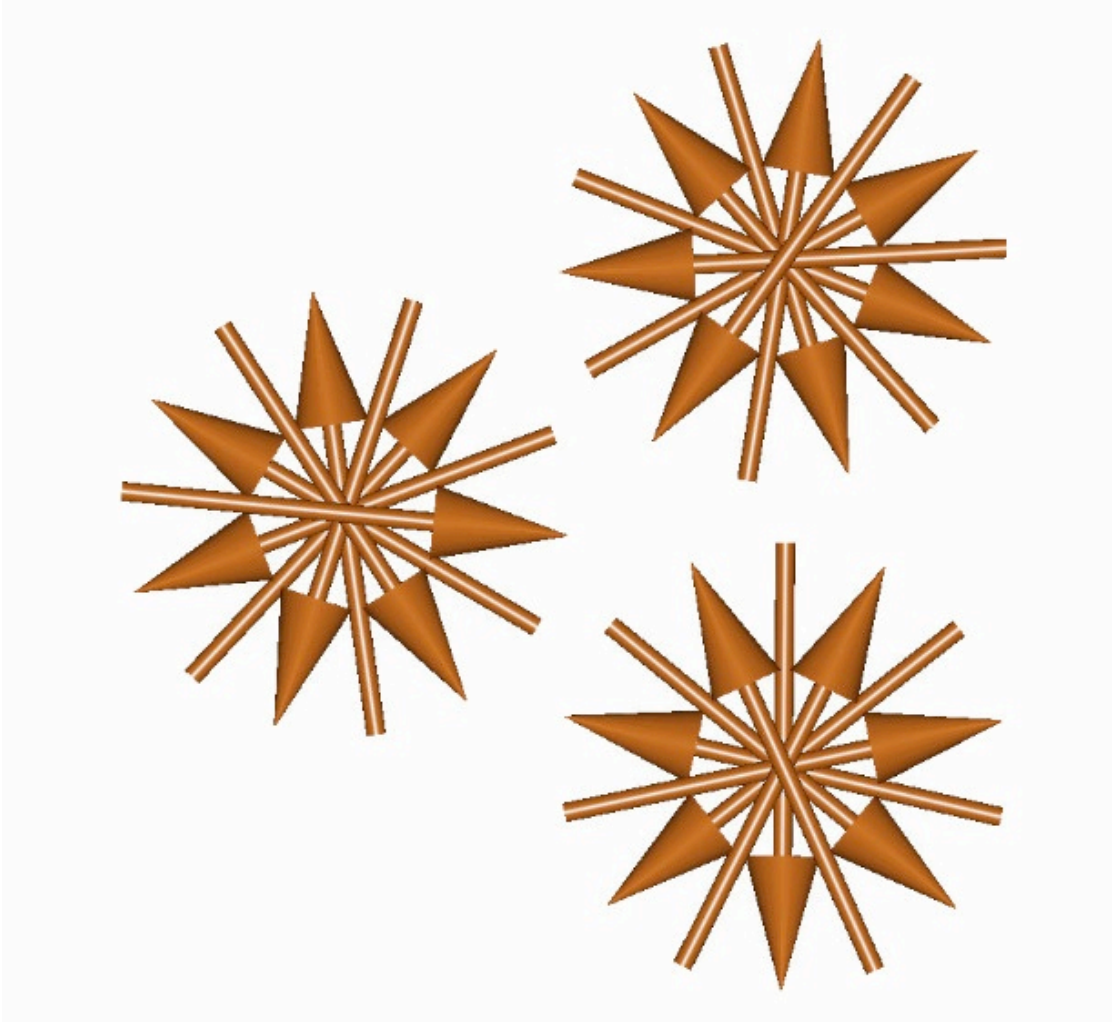


FIGURE 3.9: Schematic of the magnetic unit cell found in  $Ba_3NbFe_3Si_2O_{14}$  below  $T_N = 26$  K. Since the refinement is performed on powders using unpolarized neutrons the chirality and helical nature of the moments cannot be outright confirmed.

The phasing within the plane is completely arbitrary, implying that the moments propagate helically along the  $c$ -axis, also agreeing with previous results [90]. There are

problems associated with peak-widths, particularly in bank 7 (Figure 3.6c), although whether or not this is an instrumentation issue or indicative of a minor symmetry loss beyond the resolution of POWGEN is undetermined at this point in time (addressed in the next section). It is noted that small intricacies in the magnetic structure beyond the resolution of diffraction have been detected recently [117].

## 3.5 Discussion and Current Literature Review

### 3.5.1 Magnetic Structure

It was recognized almost a decade ago that  $Ba_3NbFe_3Si_2O_{14}$  is an ideal candidate to explore single-domain chiral magnetic states emerging either from competing exchange or from complex spin arrangements. This is because  $Ba_3NbFe_3Si_2O_{14}$  has a noncentrosymmetric crystal structure meaning that a single magnetic domain could exist in the absence of an external perturbing force in an enantiopure crystal. In practice this usually does not occur for most materials since centres of symmetry or sample inhomogeneities equally populate both chiral domains in a single sample, since both magnetic enantiomers are energetically equivalent.  $Ba_3NbFe_3Si_2O_{14}$  is quite interesting because of the isolated nature of the trimers, which seldom exists in other strictly inorganic materials (although there are some notable exceptions [118]), and the nonequivalence of the interplanar exchange pathways for each structural enantiomer. Furthermore, the langasite structure is quite robust: the nearly rigid state of  $NbO_6$  and  $SiO_4$  are expected to reduce the probability of oxygen nonstoichiometry. Additionally, each cation within  $Ba_3NbFe_3Si_2O_{14}$  has a different charge/volume ratio, meaning that site-mixing within these materials is negligible. This has been confirmed here in the joint x-ray/neutron diffraction refinement with accurate bond valence sums and thermal parameters using ideal site occupancies.

There are five relevant exchange pathways (Figure 3.10).  $J_2$  through  $J_5$  are thought to be mediated through Fe-O-O-Fe bonds (super-superexchange) but the nature of the

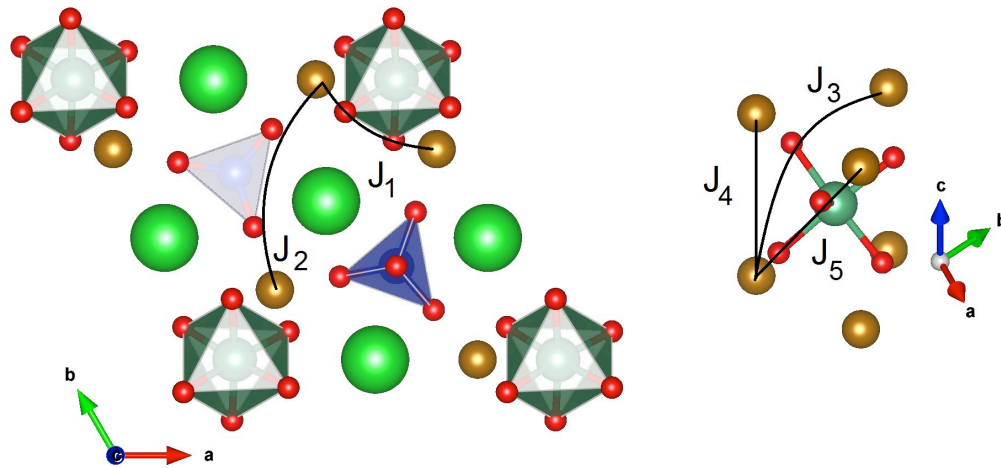


FIGURE 3.10: The exchange pathways of  $Ba_3NbFe_3Si_2O_{14}$ . The true nature of these pathways is still being debated in the literature.

$J_1$  exchange constant is currently under debate. Marty *et al.* believe that exchange is through an asymmetric Fe-O-Fe bond with lengths of approximately 1.73(2) and 2.93(2) Å and a bond angle of 100.1(9)° [90, 111, 119].  $Fe^{3+}$  ions are situated 3.67(7) Å away from each other within each trimer, making them likely too far apart to exchange directly. Marty *et al.* reasoned that due to the pathways for  $J_2$  through  $J_5$  being mediated through two oxygens as compared to just one, intertrimer exchange must be considerably weaker than intratrimer exchange. While this argument makes intuitive sense, one might reason that this effect would be quite dramatic resulting in a considerably simpler 120° structure as opposed to a chiral-helical one (in fact, a calculation using only antiferromagnetic  $J_1$  and  $J_2$  yields precisely this result [90]). Although one work reports the magnitude of  $J_2$  equating to roughly one quarter of  $J_1$  [120], it was later shown that  $J_2$  is quite strong compared to  $J_1$  [81, 82].

Stock *et al.* reason that  $J_1$  must also be a super-superexchange pathway due to the lack of a clear Fe-O-Fe pathway [82]: one of the Fe-O distances in such a pathway is much longer than what would be expected for a typical Fe-O bond. The differences in the strengths of the exchange interactions can be understood in the context of the Fe-Fe



and O-O distances (in addition to the dihedral angles for the helical exchange pathways along  $c$ ) in each super-superexchange pathway. Spin dimer calculations using  $Fe_2O_8^{10-}$  units were performed and the exchange energies (normalized by  $J_4$ ) were found to be 6.8, 4.2, 0, 1, and 3.6 from  $J_1$  through  $J_5$  [82], the magnitudes of which are in stark contrast to those reported by Lee *et al.* using density functional theory and mapping analysis for different on-site repulsion strengths [120] although the general pattern (such as having a weak  $J_3$ ) is the same. This is most likely due to Lee *et al.* assuming a metallic bridge to mediate exchange through the oxygen anions. Orbital overlap is required in order for exchange to occur: a quick look at bond distances between oxygens within each super-superexchange pathway yields values far beyond those of molecules with true O-O orbital overlap such as peroxides. However, this does not necessarily mean that metallic bridging must occur within these materials since they are extended inorganic solids and are expected to have larger bond distances. A more interesting scenario is the notion of either molecular  $Fe_3NbO_{12}^{10-}$  units or molecular Fe-trimer units that can delocalize electrons and make predicting their exchange pathways much more challenging (this has recently been observed in  $LiZnMo_3O_8$  [118] which has isolated Mo-trimers behaving as molecular units). A full theoretical examination of the nature of the exchange within this system is paramount to being able to understand the properties. Each potential scenario should be carefully examined using a variety of theoretical methods and compared to experimental data. In any case, the mean-field average strength of the interactions found through the Curie-Weiss law is reported to be between  $\theta_{CW} = -170$  and  $-190$  K [81, 82, 90, 94, 111, 116, 117, 119–128], which assigns  $Ba_3NbFe_3Si_2O_{14}$  a frustration index (defined as the the absolute value of  $\theta_{CW}$  over the ordering temperature),  $f = 7$ .

Marty *et al.* were able to grow single crystals of  $Ba_3NbFe_3Si_2O_{14}$  using the floating zone method [90]. They used some of those crystals to perform anomalous x-ray diffraction in order to obtain information regarding the chirality of the material. It was found that all single crystals in this study were enantiopure and left-handed; the exchange pathways along the  $c$ -axis twist in a left-handed fashion. Similarly, the single-domain helicity and

chirality of the magnetic structure can also be observed using single crystals as opposed to powders. A helical magnetic structure on a triangular lattice can be represented by the following [90]

$$\vec{m}_i(\vec{R}_n) = m \cos(\vec{k} \cdot \vec{R}_n + \epsilon_T \Phi_i) \vec{u} + \epsilon_H m \sin(\vec{k} \cdot \vec{R}_n + \epsilon_T \Phi_i) \vec{v} \quad (3.2)$$

where  $m$  denotes the magnitude of the orthogonal cosine and sine components of the helix oriented along orthonormal vectors  $\vec{u}$  and  $\vec{v}$  in the  $ab$  plane (the refinements are constrained to have a circular helix wherein both components are equal),  $\vec{k}$  is the propagation vector of the magnetic structure with form  $\vec{k} = (0, 0, \tau)$ ,  $\Phi_i$  is the phase of the  $i^{th} = 1, 2, 3$  atom in the trimer, and  $\epsilon_H$  and  $\epsilon_T$  determine the helicity through

$$\vec{m}_i(\vec{R}_n) \wedge \vec{m}_i(\vec{R}_n + \vec{c}) = m^2 \sin(\tau) \epsilon_H \frac{\vec{c}}{\|\vec{c}\|}; \epsilon_H = \pm 1 \quad (3.3)$$

and triangular chirality through

$$\sum_i \vec{m}_i(\vec{R}_n) \wedge \vec{m}_{i+1}(\vec{R}_n) = \left(\frac{3\sqrt{2}}{2}\right) m^2 \epsilon_H \epsilon_T \frac{\vec{c}}{\|\vec{c}\|}; \epsilon_H \epsilon_T = \pm 1. \quad (3.4)$$

Unpolarized neutrons cannot distinguish between  $(\epsilon_H, \epsilon_H \epsilon_T) = (1, -1)$  and  $(-1, 1)$  or  $(1, 1)$  and  $(-1, -1)$  pairs, that is, it is insensitive to triangular chirality. On the other hand, polarized neutron diffraction can distinguish between  $\epsilon_H = -1, +1$ , which was used to determine that the system selects only a single  $(\epsilon_H, \epsilon_H \epsilon_T)$  pair on comparison with the unpolarized data. These experiments were eventually repeated with a right-handed single crystal of the same material where a change in the helicity was found but the triangular chirality remained invariant [116].

A variety of  $Fe^{3+}$ -containing langasite systems derived from  $Ba_3NbFe_3Si_2O_{14}$  display similar ordering including many langasites such as  $Ba_3SbFe_3Si_2O_{14}$  ( $T_N = 35$  K),  $Sr_3NbFe_3Si_2O_{14}$  ( $T_N = 26$  K), and  $Sr_3SbFe_3Si_2O_{14}$  ( $T_N = 36$  K) [111]. Neutron scattering on those powders was performed in order to observe the magnetic structure dependence on Ba and

Nb substitution. It was found that Ba substitution for smaller Sr had a dramatic impact on the size of the crystal lattice, but little impact on the transition temperature or periodicity of the magnetic structure. On the other hand, Nb substitution for the slightly smaller Sb ion raised  $T_N$  by 38% and raised the helical propagation periodicity from approximately  $1/7$  to  $1/5$ . Although the authors were unable to explain this, one could reason that this is a direct consequence of the nature of the super-superexchange pathways:  $J_1$  super-superexchange is actually mediated through the covalent O-Nb-O bonds for  $J_1$  and  $J_3$  through  $J_5$ , as noted in [120]. Although substituting Nb for Sb does not dramatically change the bond distances and angles, it does change the electronic environment associated with four of the five exchange pathways, as opposed to substituting Ba for Sr which is not involved in any exchange pathway. Whether it is the difference in electronegativity or electronic configuration that is responsible for the change is still unknown [111]. This also explains why  $J_2$  is strong despite having the largest Fe-Fe distance.  $J_2$  is mediated through a smaller and straighter O-Si-O bridge: when the entire Fe-O-Si-O-Fe pathway is considered, the total bonding distance is actually smaller than the  $J_1$  Fe-O-Nb-O-Fe pathway. However, substituting Si for another ion such as Ge is not expected to yield much of a change as Si is only involved with one relevant exchange pathway as opposed to four. Experimental evidence thus far appears to support this theory [111]. For a while, unanswered questions remained regarding the magnetic structure. In particular, why a single chiral domain is chosen over another and why the *ab*-plane is selected as the easy-plane cannot be explained through the means discussed thus far. An experimental investigation of the moment dynamics and interactions are therefore of paramount importance in order to find these answers.

### 3.5.2 Moment Dynamics

The first experimental study of the inelastic behaviour of the  $Fe^{3+}$  moments was by Zhou *et al.* [81], where time-of-flight neutron scattering was performed on the DSC instrument at NIST. Elastic diffuse scattering was previously observed occurring as the temperature was lowered towards  $T_N$  followed by its disappearance by 5 K [81, 111].

However, an odd peak in the formation of this diffuse scattering occurs near 40 K, well above  $T_N$  [81] and occurs nearly commensurate with nuclear Bragg peaks. The diffuse scattering is ascribed to a gapless (or nearly gapless) excitation, since it extends into the inelastic region up to  $E = 5$  meV. Below  $T_N$ , the inelastic excitation develops into well-defined spin waves along  $[H,0,0]$ , integrated over  $K = [-0.1, 0.1]$ , that can be modelled quite nicely using a two-neighbour exchange Heisenberg Hamiltonian. Overall, this data suggests that the moments are ordering into regions of short-range clusters that eventually manifest into the long-range structure at  $T_N$ . This is not a complete description, however, since the crystal was aligned only within the  $[H,K,0]$  plane. By virtue of the interaction of the neutron with the magnetic moment, only the perpendicular component of the moment to the scattering vector is observable. Also, higher resolution studies are required to determine the true nature of the spin gap (or lack thereof) and account for the out-of-plane spin interactions.

Stock *et al.* performed similar experiments using a triple-axis spectrometer on a single crystal aligned within the  $[H,0,L]$  plane [82] as well as polarized elastic measurements. It was noted that all diffuse scattering was observed within the spin-flip channel indicating that it was magnetic. Additionally, correlations developed at  $\vec{q}_0 = (0, 0, 0.142)$  off from Brillouin zone centres which sharpened as the temperature was lowered from 100 K to 30 K. An anisotropic peak shape was observed that stretches over the  $[H00]$  direction. This implies that correlations do get stronger and become more long-range as the temperature is lowered in addition to the importance of out-of-plane exchange interactions, which were not accounted for previously. Data of higher resolution than Zhou *et al.* [81] was taken above and beneath the transition providing a clearer picture of a gap that opens up below  $T_N$  that is approximately 3 meV in size but softens near  $\vec{q}_0 = (1, 0, 0.142)$ . Upon closer inspection, it was shown that these excitations are actually composed of two broad modes occurring at 4.5 meV and 3 meV in addition to two branched modes emanating from a magnetic Bragg reflection, one gapless and one with a gap of

0.35 meV. Cuts were performed along energy over magnetic Bragg peaks in order to extract the inelastic peak width, which is proportional to the inverse magnetic correlation length. This was then compared to  $k_B T$ . It was found that the transition is second order and that there is no orbital contribution, which is not surprising given the electronic configuration of  $Fe^{3+}$ . However, this is in contrast to calculations performed by Lee *et al.* [120] and Mössbauer spectroscopy performed by other groups [105, 111, 119, 129].

Although spin waves were observed propagating beneath  $T_N$ , unlike Zhou *et al.* [81], Stock *et al.* attempted to use an XY Hamiltonian to model them following their analysis of the critical behaviour found using neutron scattering [82]. Spin waves were detected both along  $[H, 0, \frac{6}{7}]$ , which is sensitive to intraplanar exchange and  $[2, 0, L]$ , which is sensitive to interplanar exchange. Their analysis failed using the Dzyaloshinskii-Moriya interaction with an XY Hamiltonian (a planar spin model) yielding unphysical results. Instead, they turned their attention back to the Heisenberg model (fully three dimensional spin model) and were able to not only fit the spin waves, but could also reproduce the incommensurate wave vector using the extracted exchange energies of 1.3, 1, and 3.3 ( $J_3$  through  $J_5$  normalized by  $J_4$ ), which are also in much closer agreement to those proposed in reference [120]. It was determined that although the Dzyaloshinskii-Moriya interaction is present due to the low crystal symmetry, it is not required to select a particular magnetic chirality given an absolute structural chirality (its role in the latter is still not entirely known). Instead, the authors believe that single-ion anisotropy may play a role in selecting the ground state. Fitting the spin waves along the  $ab$ -plane yielded exchange constants of 16 and 3.1 for  $J_1$  and  $J_2$  (again normalized by  $J_4$ ) and again in good agreement with Lee *et al.* [120], perhaps implying that exchange may be mediated directly through the Nb or Si rigid body centres. The Curie-Weiss temperature,  $\theta_{CW}$ , can be found using

$$k_B \theta_{CW} = \frac{1}{3} S(S+1) \sum_n J_n, \quad (3.5)$$

where  $k_B$  is the Boltzmann constant and  $S$  is the spin momentum number. Using the

extracted exchange constants,  $\theta_{CW}$  is found to be -170 K, which is in good agreement with the experimentally reported values. It is noted that the Heisenberg Hamiltonian maps onto an effective XY model when considering only interplane interactions, which may be related to why the system appears to follow XY critical behaviour experimentally.

What was not addressed in either study of the spin dynamics is the extension of the chirality into the inelastic domain. Before addressing this topic any further, it should be noted that spin dynamics are usually chiral insofar that they must break time-reversal symmetry upon the application of a magnetic field. Loire *et al.* [121] were able to observe, for the first time in zero-field in any material, completely chiral spin dynamics over the entire measured energy range owing to this material's single-domain enantiopure magnetic structure. Even using unpolarized neutrons there is a strict difference in the spin wave excitations emanating from magnetic Bragg peaks with  $+\vec{k}$  and  $-\vec{k}$ . Using polarized neutrons, the amplitude of the chiral component of the magnetic scatter was equal to the full magnetic signal, indicating no chirality mixing. Spin-waves along  $c^*$  were found to be achiral while spin waves with a component perpendicular to it were chiral along the entire energy spectrum providing a unique way to identify the magnetic enantiomer in the ground state in the unpolarized limit for future studies. This was explained mainly using a mean-field model wherein the relative strengths of  $J_3$  and  $J_5$ , which oppositely twist around the interplanar trimers, dictate which chirality is stabilized (the other interactions determine the periodicity) and imply that the choice of structural chirality entails the choice of magnetic chirality. Indeed, this has been confirmed experimentally as well [116, 122]. Now using the out-of-plane Dzyaloshinskii-Moriya interaction with a Heisenberg Hamiltonian, Loire *et al.* beautifully model the observed excitations [121], which is at direct odds with the results from Stock *et al.* [82] who downplay the role of this interaction.

But as Jensen [122] pointed out, by comparing the differences in intensities between excitations from  $(H,0,L) + \vec{k}$  and  $(H,0,L) - \vec{k}$  from the data from Stock *et al.* and Loire

*et al.*, each had a single crystal with opposing structural chirality. This could result in the discrepancies between their respective theoretical calculations. Furthermore using a mean-field trimer cluster and by grounding the theoretical calculation of the exchange constants to the experimental magnetic susceptibility, Jensen is able to determine that the helicity is a consequence of the non-zero Dzyaloshinskii-Moriya interaction coupled to the structural chirality. The sign of this interaction is responsible for the triangular chirality. This is further corroborated from results using electron spin resonance by Zorko *et al.* [123] where it was shown that the out-of-plane Dzyaloshinskii-Moriya interaction, rather than single-ion anisotropy, better fits the resonances detected at low temperatures. Recent soft x-ray magnetic diffraction studies have highlighted the influence of the Dzyaloshinskii-Moriya interaction on the form of the magnetic ground state itself excluding chirality, where a small modulating out-of-plane moment component was found to exist that is not observable using neutron scattering [127]. Further questions still exist regarding the nature of the helices, particularly whether they are circular or elliptical. The presence of more than one Fe site that may be indicative of a structural symmetry loss [105, 117, 127, 129–132], the observed superparamagnetic phenomena [125], or how the out-of-plane Dzyaloshinskii-Moriya interaction, calculated to be only 45 mK [123], can account for the magnetic chirality given that chiral correlations have been detected above 100 K, also remain unanswered.

### 3.5.3 Multiferroic Behaviour

It has been shown both theoretically [91–93] and experimentally [17] that materials with chiral spiral magnetic structures can be ferroelectric even with a centrosymmetric lattice. However, such polarization does not strictly manifest solely due to the ordering of the moments themselves. For example, a sinusoidal spin density wave will not result in an electric polarization by itself [93]. In  $Ba_3NbFe_3Si_2O_{14}$ , if each trimer within the plane were to have a slightly different orientation to that of its neighbour, electric polarization can manifest perpendicular to the direction of propagation, but still within the plane [130]. Due to the Dzyaloshinskii-Moriya interaction, moments are predicted

to have a slight-spin canting out of the plane that is predicted to yield a small ferromagnetic moment perpendicular to the electric polarization (such an out-of-plane spin canting is outside of the resolution of neutron diffraction but may be detected using magnetometry). Such a small spin-twist within the plane has not been directly observed in  $Ba_3NbFe_3Si_2O_{14}$ , although this is later addressed in much more detail in the next chapter. Magnetoelastic distortions are also an important mechanism for multiferroicity in langasites especially due to their piezoelectric properties, but both electric and magnetic components are expected to be oriented within the plane [130]. These can both be directed out of the plane if an accompanying symmetry lowering occurs to either  $P3$  or  $C2$  [117, 127, 130]. Alternatively, strain gradients may be coupled with the polarization in langasites, a phenomenon known as the flexoelectric effect, which can augment the effects of the in-plane Dzyaloshinskii-Moriya interaction and/or magnetoelectric coupling (it is noted that strain gradients can occur in materials with *any* symmetry, so flexoelectricity is not restricted to materials within a particular set of space groups) [131, 132].

$Ba_3NbFe_3Si_2O_{14}$  exhibits an anomaly in the dielectric constant [94, 111, 124, 128] at the onset of magnetic order as well as a polarization when the electric field is applied along the  $c$ -axis [94]. Here, the polarization behaviour above the transition appears linear while the polarization beneath the transition appears as it would for a lossy dielectric [78, 133]. Lossy dielectrics occur due to the presence of charge impurities such as mixed valence cations and oxygen vacancies. Because of the electrical contacts put on the sample during such measurements, charge is made to physically flow through the material unlike in magnetometry. Inhomogeneous charge storage due to the current injection may occur on these defect sites that can lead to “ferroelectric-like” polarization curves [78]. However, this does not imply that  $Ba_3NbFe_3Si_2O_{14}$  is not ferroelectric as there is no reason to suspect a material “transitioning” from a standard to a lossy dielectric accompanying the onset of magnetic order. All refinements at all temperatures were shown to have no observable site-mixing or oxygen vacancies in the long-range limit.



Zhou *et al.* [94] postulate that  $NbO_6$  octahedral tilting outside of the resolution of diffraction are responsible for the polarization. Alternatively, it is possible that electron hopping between O  $2p$  and empty  $Nb^{5+}$   $4d$  orbitals could result in a small displacement of the cation from the octahedron centre, in a similar mechanism to that observed in  $BaTiO_3$  [134]. From the preceding section, it is clear that the Dzyaloshinskii-Moriya interaction plays a large role in the magnetic structure. The same can be said for the electric polarization. Considering that an electric field polarization-hysteresis loop has been observed in this material, it must be possible to switch the direction of the polarized domain from one noncentrosymmetric structure into its enantiomer [120]. Since this is not possible structurally, charge redistribution must be achieved magnetically through the inverse Dzyaloshinskii-Moriya interaction.

Lee *et al.* used Berry phase calculations to determine the nature of the polarization and while they found that the magnitude generally agreed with experiment, the direction of the polarization lay within the plane as opposed to what was found experimentally [120]. Mössbauer spectroscopy may point to another mechanism wherein a small structural distortion from  $P321$  to either  $P3$  or  $C2$  could also yield the polarization [105, 111, 119, 129], although the latter also implies polarization along the wrong axis. But THz spectroscopy has shown that excitations existing up to 110 K are observable when the directions of the electric field component of light are made either parallel or perpendicular to  $c$  with the magnetic component being held perpendicular to  $c$  (although not when the magnetic component is parallel to  $c$ ) [127]. In order to observe such excitations, a static polarization perpendicular to  $c$  must exist which can only be observed following the loss of the 3-fold axis along that direction (i.e.  $P321$  to  $C2$ ). Recently, more thorough investigations were performed on the ferroelectric nature of  $Ba_3NbFe_3Si_2O_{14}$  [128]. It was found that weak polarization exists along  $c$  and  $b^*$  while strong nonlinear polarization exists along  $a$  under zero magnetic field, which can explain previous results [94]. The most striking observation here is that no poling dependence of the ferroelectricity is observed, which is unique to single domain magnetically driven

ferroelectrics. Because the ferroelectricity normally observed in these improper multiferroics is quite weak (owing to the distributed domains of chiral magnetic structures), a material must be cooled under field to induce a single domain to maximize the desired effect. This need not occur with  $Ba_3NbFe_3Si_2O_{14}$  since the chiral magnetic structure is already single domain. Remarkable control over the electric polarization was demonstrated using a magnetic field along any of the three orthogonal directions with negligible hysteresis in each.

### 3.6 Conclusion

$Ba_3NbFe_3Si_2O_{14}$  and its associated Fe-containing structural analogues represent a clear and unique opportunity to study single-domain chirality in helical magnetic structures and associated chiral dynamics, even under zero-field. These single domain chiral structures also manifest in the electric properties of this material. Not only does  $Ba_3NbFe_3Si_2O_{14}$  show a spontaneous uniform polarization below  $T_N$ , but it is shown to change its polarization in highly nonlinear fashion with magnetic field and have no observed poling dependence upon cooling in an electric field [128].

Still unanswered questions remain regarding the fascinating physics observed here. The true nature of the magnetic structure and its influence on the multiferroic properties are not quite fully understood especially concerning small helical distortions of the moments within the plane (which by nature would change the magnetic propagation vector). Furthermore, while it is clear that the application of a magnetic field can dramatically alter the electrical properties of  $Ba_3NbFe_3Si_2O_{14}$ , no study exists exploring the mechanism behind such a phenomenon. For example, while it is generally agreed that the magnetic structure is the driving force behind the observed ferroelectric behaviour, how the magnetic structure itself changes as a function of field has never been explored. The role of the Dzyaloshinskii-Moriya interaction is still puzzling due to its small calculated magnitude. Theoretical calculations regarding the role of chirality, spin-orbit coupling, the magnetoelectric, and flexoelectric effects are still inconclusive, most likely because the

---

nature of the exchange pathways is still poorly understood. Finally, while many studies have surfaced showing the similarities between Fe-containing langasites, few have discussed the possibility of substituting Fe for other transition metal ions, which would alter the magnetic and electric properties more profoundly than any substitution attempted thus far. This last question is the main motivation behind this thesis, and is the subject of all of the remaining chapters.

## Chapter 4

# Complex nuclear and magnetic superstructures in the $S=5/2$ multiferroic candidate

## $\text{Pb}_3\text{TeMn}_3\text{P}_2\text{O}_{14}$

### 4.1 Introduction

Following the successful preparation of  $\text{Ba}_3\text{NbFe}_3\text{Si}_2\text{O}_{14}$ , there have been many studies that have focused on how its unique magnetic properties change as a function of chemical substitution [105, 111, 130, 131]. However, while all of these studies have managed to substitute Ba, Nb, and Si, none have managed to substitute Fe for another  $3d$  transition metal ion. On one hand, the approach taken thus far is a great way to examine the effects of perturbing the exchange pathways and lattice size on the multiferroic properties of  $\text{Ba}_3\text{NbFe}_3\text{Si}_2\text{O}_{14}$  without, potentially, changing the magnetic ground state. But on the other hand, perhaps a more interesting question is *how much can* the magnetic properties of these langasites be changed?

In the langasites, there are two sites that compete for  $3d$  transition metal ion occupation:

the  $1a$  site and the  $3f$  site that coordinate with oxygen in octahedral and tetrahedral fashions, respectively. Generally, the larger  $d$ - and  $p$ -block cations prefer to occupy the octahedral site, which presents a problem when trying to chemically substitute out Fe. Perfect co-occupation of both of these sites would dramatically alter the exchange pathways (Figure 4.1).

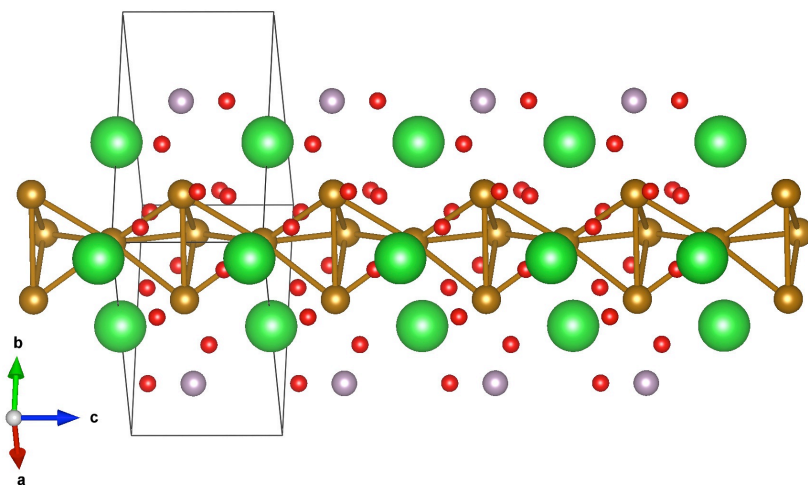


FIGURE 4.1: Co-occupation of the  $1a$  and  $3f$  site of the langasite by the metal cation could dramatically alter the frustrated sublattice and associated exchange interactions. The  $3e$ ,  $2d$  and oxygens are coloured green, white, and red respectively while the  $1a$  and  $3f$  sites are coloured gold.

While this would present researchers with an opportunity to study a novel type of geometrically frustrated sublattice and potentially explore new magnetic ground states, this has never been achieved in practice using a magnetic ion. More often the structural integrity of the langasite collapses resulting in multiple phases.

In 1978, a natural mineral was discovered in Arizona that is isostructural to the langasites [135]. This mineral was found in single crystal form and has the chemical formula  $Pb_3TeZn_3As_2O_{14}$  (with traces of other ions). The mineral is exceedingly rare in its natural form due to the inclusion of Te in its 6+ valence state, and was thus named “Dugganite” after the chemist Marjorie Duggan who spent her career studying Te. Dugganites are a Te-containing subgroup of the langasite family. An in-depth elemental analysis, single

crystal x-ray refinement, and Fourier analysis have been used to show that  $PbO_8$  decahedra are fairly regular indicating no stereochemically activated lone pairs, negligible site-mixing, and full site occupancies [75, 136]. This was the first time that a langasite was found to have a divalent  $3d$  transition metal cation occupying the  $3f$  site. In the 1990s, other members of the dugganite family were discovered including Cheremnykhite ( $Pb_3TeZn_3V_2O_{14}$ , Eastern-Siberian Region, Russia), Kuksite ( $Pb_3TeZn_3P_2O_{14}$ , Eastern-Siberian Region, Russia), and Joëlbruggerite ( $Pb_3Zn_3(Sb^{5+}, Te^{6+})As_2O_{13}(OH, O)$ , Montana) in 2009 [137, 138].

The major key to the dugganite structure is the inclusion of  $Te^{6+}$ , which is empirically known to only coordinate with oxygen octahedrally. This is believed to effectively force the  $3d$  ion solely into the  $3f$  site. In 2009, B. V. Mill reported the preparation of dozens of new dugganites including cations such as  $Co^{2+}$ ,  $Fe^{3+}$ ,  $Mn^{2+}$ ,  $Cu^{2+}$ , and  $Ni^{2+}$ , ranging in phase purity from 80 to nearly 100% [106, 108]. However, the only properties to be reported in that study were lattice constants, melting temperature, density, and material colour; no refinements were presented to offer any evidence of proper identification of the new phases or their purity, no magnetic measurements were reported, and the electric properties were not examined.

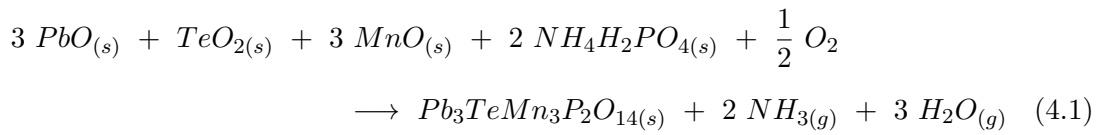
$Pb_3TeMn_3P_2O_{14}$  was among those dugganites first prepared by B. V. Mill [108]. Lattice constants for this material were given as 8.465(2) and 5.326(1) Å for  $a$  and  $c$  respectively. The stability of this material was thought to be dependent on the stability of  $Mn_2O_3$  between 700 and 900°C. Another study by Ivanov *et al.* [139] showed that  $Pb_3TeMn_3P_2O_{14}$  has an antiferromagnetic transition at  $T_N = 7.5(1.0)$  K with  $\theta = -20(2)$  K and  $\mu_{eff} = 5.9(1) \mu_B$  using DC susceptibility. Unlike the Fe-containing langasites, no remnant magnetization is observed for this material below  $T_N$ . No in-depth structural study, heat capacity, or neutron scattering experiments were reported for this material. Here, the findings from these measurements are detailed.

## 4.2 Methods

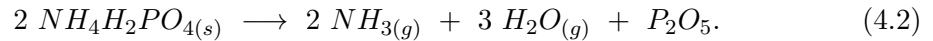
### 4.2.1 Preparation

Unlike  $Ba_3NbFe_3Si_2O_{14}$  where signs that the reaction had occurred were almost immediate, the best samples of  $Pb_3TeMn_3P_2O_{14}$  were prepared using a pre-reaction step. Stoichiometric amounts of  $PbO$ ,  $TeO_2$ ,  $MnO$ , and  $NH_4H_2PO_4$  of 99.9% purity or greater were ground by hand for 15 minutes for every gram of sample. The reactants were loaded into an alumina crucible inside a tube furnace in the form of a loose powder and slowly heated to 400 °C over 24 hrs (any faster resulted in the decomposition of the reactants). At this stage, the product appeared light grey in colour. The pre-reacted product was then ground by hand, pelleted under a pressure of 40 MPa, and heated to 550 °C for 24 hrs, taking on a darker grey appearance. The mixture was reground and repelleted under the same conditions, fired at 625 °C for 24 hrs, and fired once more at 825 °C. An annealing step was implemented for 180 hrs with intermittent grindings.  $Pb_3TeMn_3P_2O_{14}$  appears lilac-grey in colour, agreeing with previous results [108].

The overall reaction equation is believed to be as follows:



where  $NH_4H_2PO_4$  decomposes into  $P_2O_5$  at about 300°C:



The overall reaction was tried both in air and under oxygen, but this resulted in no observable change in the lattice parameters, suggesting that the uptake of oxygen from air occurs quite readily, although this is only speculative. It would be interesting to try

a reaction under an inert gas such as  $Ar_{(g)}$  in order to see how the reaction would proceed so as to identify the role of oxygen in the reaction (it is noted that Joëlbruggerite, like most dugganites, naturally occurs with a Pb:O:OH ratio of 3:13:1). It has also been reported that both  $P_2O_5$  and  $TeO_2$  readily react with divalent metal oxides at high temperatures [108] such that no stoichiometric excesses are required.  $TeO_2$  has a melting temperature of 733 °C; the pre-reaction step is thought to “lock”  $TeO_2$  into the main structure, allowing the reaction to proceed at 825 °C without issue. Adding excess  $TeO_2$  and  $NH_4H_2PO_4$  only resulted in the appearance of impurities.  $Pb_3TeZn_3P_2O_{14}$  and  $Pb_3TeMn_{1.5}Zn_{1.5}P_2O_{14}$  were also prepared for use as lattice standards for the heat capacity measurements. The reaction procedure for each was the same except MnO was replaced by ZnO as required. The lattice standards were white in colour, which is expected for insulating solid transition metal oxides.

One of the most frustrating issues for solid-state chemists is how challenging it is, in general, to gain insight into the mechanism of formation of the final product. This is in stark contrast to other disciplines such as organic chemistry, where the complete deduction of a reaction mechanism, while no doubt still challenging, is nevertheless common practice. The solution of such a reaction mechanism quite commonly relies on the ability to form metastable intermediates that might hint at the underlying formation processes. However, the formation of such reaction intermediates in the solid-state are reported far less frequently, most likely due to the over-reliance on high temperature ceramic synthesis techniques that encourage thermodynamic reaction products rather than kinetic ones. Knowledge of the reaction mechanism (or stated differently, how the reactants traverse the free energy landscape to get to the final product [140]) is vital to the rational design of new materials.

The story is not as bleak as one might think. For example, many *in situ* experimental techniques have been used to peer into the underlying chemical processes that result in the desired product. In this study on  $Pb_3TeMn_3P_2O_{14}$ , *ex situ* x-ray diffraction was



performed on the sample before the reaction and after every 24 hr heating interval until the reaction was stopped. These x-ray diffraction measurements were performed using a Siemens D5000 x-ray diffractometer using a Cu  $K\alpha$  anode in Bragg-Brentano ( $\theta/\theta$ ) geometry with 0.2; 0.6; 0.6; 1 mm slits. In the following discussion, Rietveld refinements could not be performed due to the low crystallinity of the sample, leading to peak shapes that could not be well modelled. Instead, profile matching was used to identify the phases. From 0 to 48 hrs the reactants appear to thermally degrade, but by 72 hrs at 550 °C, a clear new phase had formed that was different from any of the reactants or the final product (Figure 4.2).

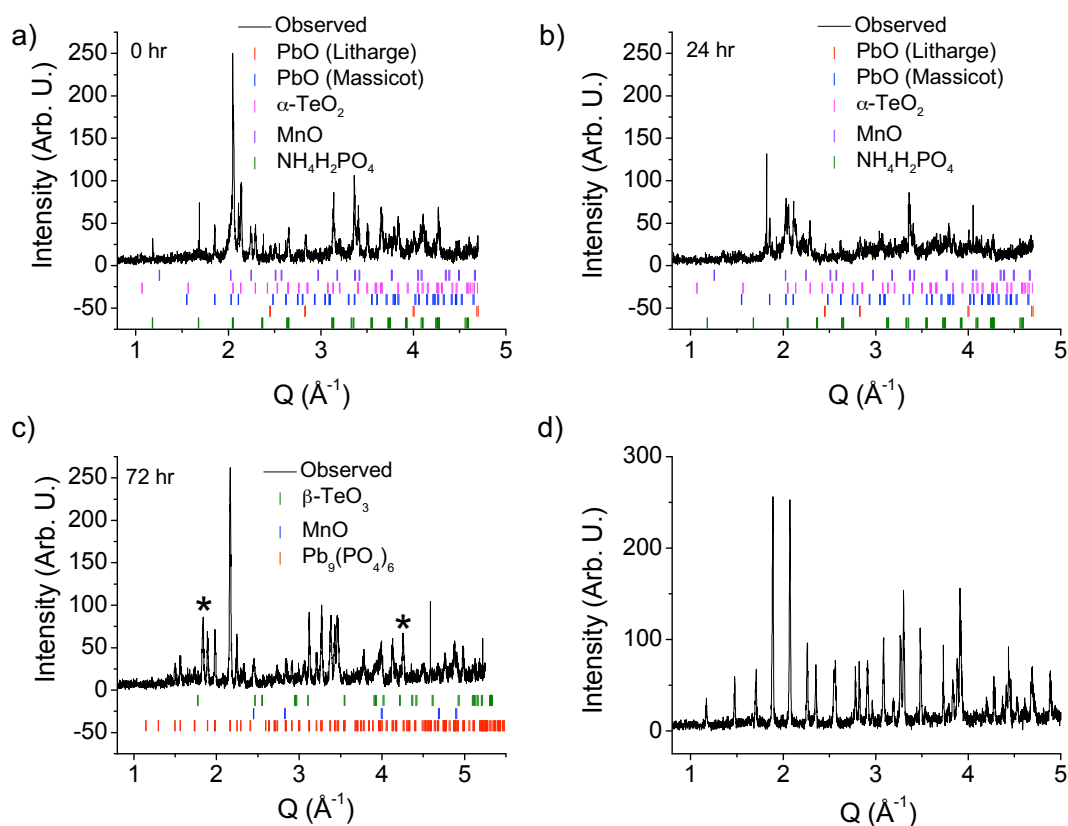


FIGURE 4.2: X-ray diffraction was performed at various stages during the reaction of  $Pb_3TeMn_3P_2O_{14}$ . By 72 hours, a clear intermediate was formed identified as  $Pb_9(PO_4)_6$ . Unidentified peaks are marked with an asterisk.

The phase was identified as the Pb-apatite material having the chemical formula  $Pb_9(PO_4)_6$  along with some other intense peaks that could not be identified, but probably belong to another Pb- $PO_4$  phase. These peaks could possibly be related to a small impurity found

in the final phase that could not be identified (addressed later). Further heating resulted in the complete elimination of the identified intermediate phase within the resolution of the 11-BM line at the Advanced Photon Source (APS, Argonne, IL) (details of these measurements to follow in the next section).

There are many identified Pb-PO<sub>4</sub> phases with countless different structures. The apatites are a broad group made of mainly phosphates and arsenates with hexagonal or pseudohexagonal symmetry. The chemical formula is A<sub>5</sub>(XO<sub>4</sub>)Z (A = divalent cation; X = pentavalent cation; Z = monovalent anion) that serves as the basic building block for the group. Pb<sub>9</sub>(PO<sub>4</sub>)<sub>6</sub> crystallizes with the hexagonal space group P6<sub>3</sub>/m and is a defect apatite [141]. It is believed that a sort of epitactic mechanism is responsible for the formation of the final product: MnO, β-TeO<sub>3</sub>, and Pb<sub>9</sub>(PO<sub>4</sub>)<sub>6</sub> each share common trigonal symmetry elements along at least one of their faces (Figure 4.3) (although the final phase appears quite distinct from these three intermediates at first glance).

This perhaps aids in the formation of the final product, which also has trigonal symmetry. Epitactic and topotactic mechanisms are quite common for PO<sub>4</sub> containing materials because the highly covalent and rigid PO<sub>4</sub> unit can act as chemical scaffolding agents: arguably the most well-known example is the role of the “phosphate backbone” in deoxyribonucleic acid [142]. Although many dugganites can be formed, the majority of those that can be made phase pure contain PO<sub>4</sub> units. Perhaps it is no surprise that materials such as Pb<sub>3</sub>TeMn<sub>3</sub>P<sub>2</sub>O<sub>14</sub>, Pb<sub>3</sub>TeCo<sub>3</sub>P<sub>2</sub>O<sub>14</sub>, and Ba<sub>3</sub>TeCo<sub>3</sub>P<sub>2</sub>O<sub>14</sub> can be readily made phase pure using a relatively low-temperature heating routine with simple oxide precursors [108, 143, 144]. Further credence to this mechanism is given when the same preparation method is used to make Pb<sub>3</sub>TeMn<sub>3</sub>V<sub>2</sub>O<sub>14</sub>. For this reaction, the materials phase separate into mixtures of Pb<sub>3</sub>V<sub>2</sub>O<sub>8</sub>, Pb<sub>2</sub>V<sub>2</sub>O<sub>7</sub>, MnO and TeO<sub>2</sub>, the exact quantities being dependent on whether V<sub>2</sub>O<sub>5</sub> or NH<sub>4</sub>VO<sub>3</sub> is used in the reaction (however, Pb<sub>3</sub>TeCo<sub>3</sub>V<sub>2</sub>O<sub>14</sub> can be made this way and is discussed in great detail in Chapter 6 [99, 103, 108, 145]). It is reasoned that for these reactions, VO<sub>4</sub> units are slightly less rigid due to having more ionic and *d* character than the PO<sub>4</sub> units. Pb<sub>9</sub>(PO<sub>4</sub>)<sub>6</sub> can

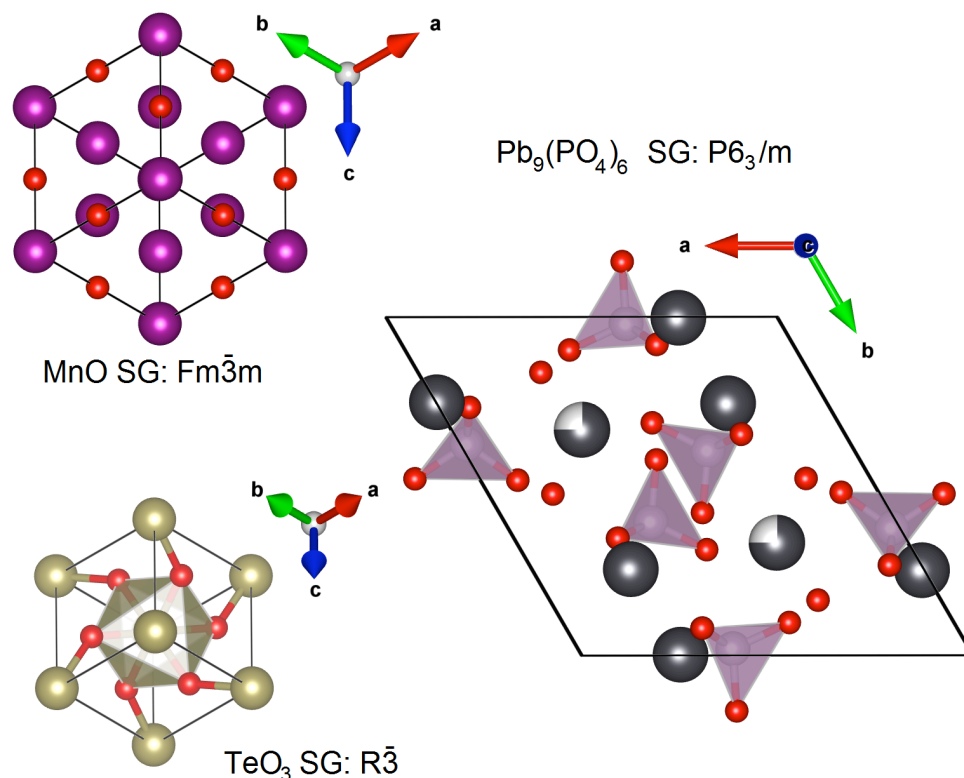


FIGURE 4.3: All three intermediates share trigonal symmetry elements normal to at least one of their faces.

be made using a wet-chemical technique at room temperature, but the analogous phase using  $V^{5+}$  instead of  $P^{5+}$  has not been reported to my knowledge [146]. That is not to say that vanadate apatites do not exist [147].

Added complexity to the reaction mechanism is apparent when trying to prepare another dugganite,  $Pb_3TeCu_3P_2O_{14}$ , which was reported in an earlier study although no x-ray diffraction patterns were provided to support the author's claims [108]. Using the methods outlined in that study, it was found that this material also phase separates into a monoclinic form of  $Pb_3(PO_4)_2$  and  $Cu_3TeO_6$ , the former of which may have a similar diffraction pattern to a distorted langasite at first glance (Figure 4.4). An attempt was made at synthesizing  $Pb_9(PO_4)_6$  and then combining it with stoichiometric amounts of CuO and  $TeO_2$ . However, only CuO and  $TeO_2$  ended up reacting to form  $Cu_3TeO_6$ . The

reaction was tried under a variety of conditions, including under high pressures up to 12 GPa at the Centre for Science at Extreme Conditions (CSEC, Edinburgh, UK), but this resulted in the same final products. This raises the question as to why  $Cu_3TeO_6$  would form whereas  $Mn_3TeO_6$  was not detected? It is speculated that the answer lies in the symmetry differences between the two known materials and the electronic differences between  $Mn^{2+}$  and  $Cu^{2+}$ , the latter being highly Jahn-Teller active.  $Mn_3TeO_6$  has a rhombohedral unit cell that is very similar in size to the ideal  $P321$  langasite unit cell with a doubled  $c$ -axis (Figure 4.5) [148]. On the other hand,  $Cu_3TeO_6$  crystallizes in a cubic unit cell that shares no structural motifs with the langasite [149]. It is speculated that how close the atomic geometries of these intermediate phases are to the final langasite phase is key in predicting whether or not a reaction will occur. Additionally,  $Cu^{2+}$  has six-fold coordination with oxygen, where the octahedra distort due to the Jahn-Teller effect. This arrangement may be more energetically favourable for  $Cu^{2+}$  than the large tetrahedral site offered by the langasite. Overall, dozens of dugganites can be made [106, 108] but the reaction mechanism, until now, has not been studied in detail. Since for many of the dugganites impurities have been observed, the insight offered here may aid in the preparation or purification of new dugganites. Further work on this problem using more sophisticated experimental *in situ* techniques is welcomed.

### 4.2.2 Diffraction

Diffraction experiments were carried out at a number of instruments and sources. Initial data was collected on the Siemens D5000 using the same procedure and setup as described earlier. Higher resolution data sets were collected using a Phillips X'Pert Pro diffractometer with a Cu  $K\alpha$  anode and a Ni filter over  $2\theta = [10^\circ, 120^\circ]$  using a step size of  $0.008^\circ$  counting for a total of 24 hrs. More data was collected at the 11-BM line [53] at the APS using a wavelength of  $0.413961 \text{ \AA}$  over  $2\theta = [2^\circ, 50^\circ]$  in transmission geometry. For this experiment, samples were loaded into a small Kapton capillary tube plugged with modelling clay. No explicit set-up procedures were used to reduce x-ray absorption by the sample. Neutron diffraction was collected using five grams of sample on

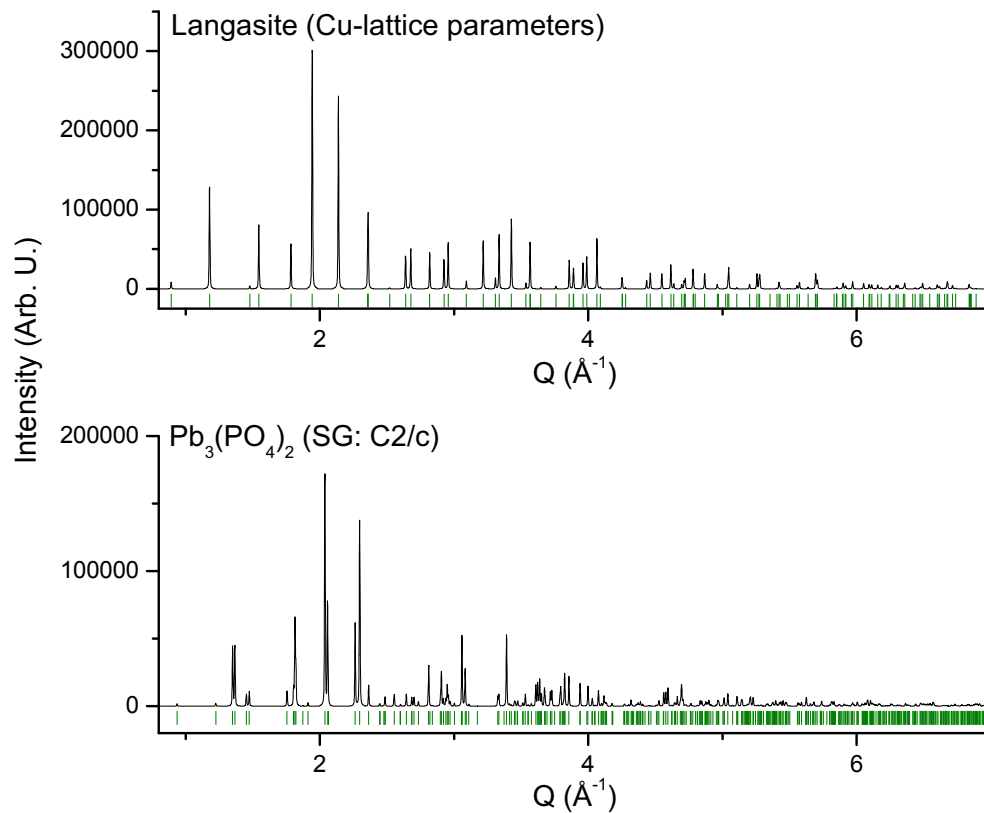


FIGURE 4.4: Calculated diffraction patterns of the Cu-langasite [108] and monoclinic  $Pb_3(PO_4)_2$ , which was the product found in this study. Both diffraction patterns share many features but become difficult to distinguish with an instrument with poor resolution as compared to current instrumental capabilities.

the C2 DUALSPEC instrument at the Canadian Neutron Beam Centre (CNBC, Chalk River, ON) over many temperatures ranging from 4.3 K to 300 K using a closed-cycle refrigerator. For the latter wavelength, a polygraphite filter was used to eliminate  $\lambda/2$  scattering. Neutron diffraction measurements on the same sample were also carried out using POWGEN at the SNS [115]. The sample was placed in a cylindrical vanadium sample can of diameter 8.0 mm and length 5.7 cm and carefully placed in the beam using a slit width of 10 mm and slit height of 35 mm so as to optimize the signal. For data collected at room temperature, the sample was placed in a He multi-chamber closed-cycle refrigerator to improve the background noise. Measurements were collected using a wavelength band centred at 1.066 and 3.731 Å that covers a d-spacing range of 0.3 to 8.24 Å. For all other temperatures, a standard ILL Orange Cryostat was used

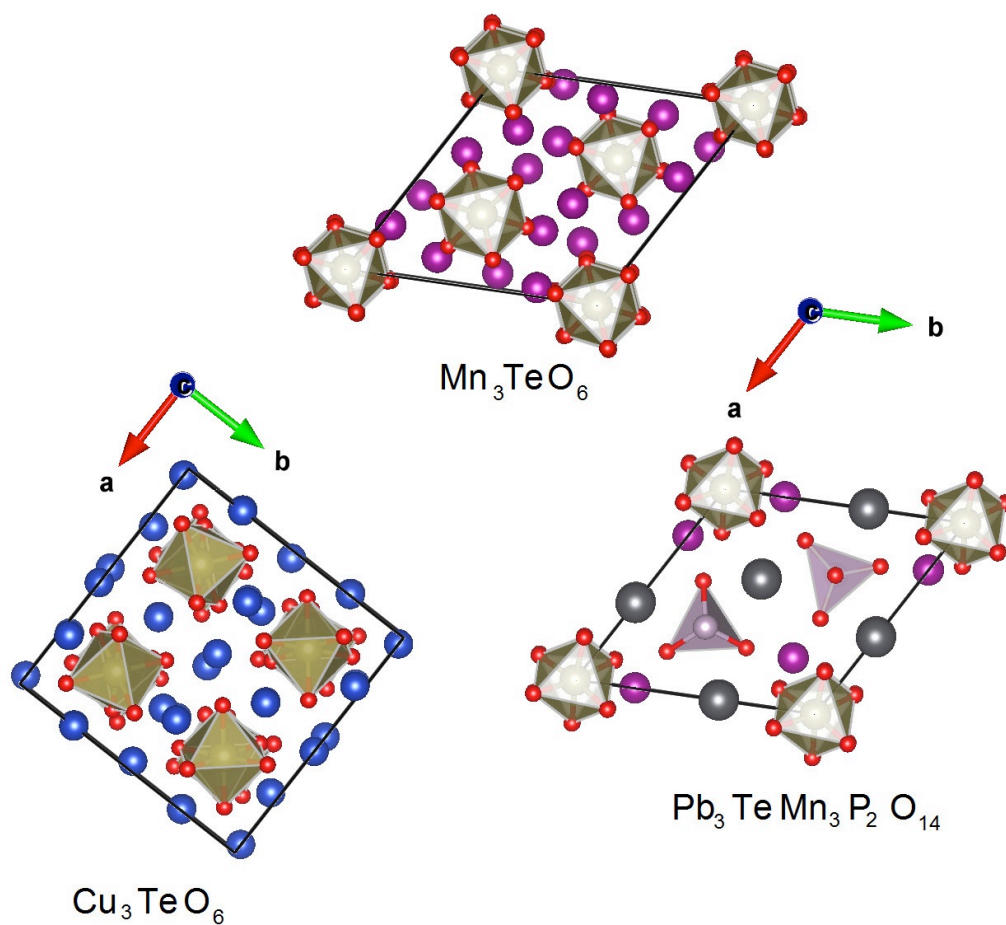


FIGURE 4.5: There is a large degree of similarity between  $Mn_3TeO_6$  and the ideal langasite unit cell. On the other hand,  $Cu_3TeO_6$  has a very different atomic structure. Pb, Te, Mn, P, Cu, and O are coloured dark grey, gold, purple, white, blue, and red.

with a wavelength band centred at 1.333 and 4.797 Å. The use of this cryostat made a significant contribution to the background noise that could not be relieved through an empty can subtraction or by rebinning the data. However, its use was necessary due to  $Pb_3TeMn_3P_2O_{14}$  having a Néel temperature at 6.6 K, which is below the accessible limit of the He multi-chamber closed-cycle refrigerator. These experiments were performed before the addition of a fine collimator that is now in operation.

### 4.2.3 Physical property measurements

Magnetization data was taken on a 49.6 mg sample of  $Pb_3TeMn_3P_2O_{14}$  using the vibrating sample magnetometer option on a 9 T DynaCool Physical Property Measurement System (Quantum Design). Magnetization versus temperature runs were performed between 2 and 300 K at 0.01 T, 0.1-0.5 T in 0.1 T steps, and 1 through 9 T in 1 T steps. A temperature ramp rate of 1 K/min was used. Measurements were done by first cooling in zero-field and again in fields to ensure that no unexpected glassy behaviour was observed, which might be indicative of an impurity. Magnetization measurements were performed at 2 K, 7 K, 15 K, and 85 K using a field ramp rate of 0.001 T/sec. Heat capacity measurements were performed by mounting a 10 mg sample onto a sample stage and analyzed using the two- $\tau$  method (Quantum Design).  $Pb_3TeZn_3P_2O_{14}$  and  $Pb_3TeMn_{1.5}Zn_{1.5}P_2O_{14}$  were used as lattice standards. All heat capacity measurements were performed under zero-field. High-field magnetization measurements up to 35 T were performed on the vibrating sample magnetometer at the National High Magnetic Field Laboratory (NHMFL, Tallahassee, FL) at 1.4 K using a 225 mg pelleted sample immersed in General Electric-7031 varnish. The dielectric constant was measured by creating electrical contacts on two opposite surfaces of a thin plate sample with Ag paste. An Anderson-Hagerling AH-2700A automated capacitance bridge was used. The capacitance was converted to the dielectric constant by approximating the sample as an infinite parallel capacitor, which assumes a uniform electric field distribution. The sample had an area of 5.527 mm<sup>2</sup> and thickness of 0.190 mm. These measurements were also done at the NHMFL. For all measurements, the sample was allowed to thermally equilibrate before the measurement was taken.

## 4.3 Refinement

### 4.3.1 Initial refinement

Le Bail fits of the data taken from the Siemens D5000 x-ray diffraction experiment indicated that  $Pb_3TeMn_3P_2O_{14}$  adopts a trigonal unit cell typified by a langasite. There

were small indications of impurity peaks on the order of 1%, which prompted work to be done using the Phillips X'Pert Pro system with higher resolution. A full Rietveld refinement was performed using the FullProf suite (Figure 4.6) [150]. A trigonal  $P321$  unit cell was used for the refinement, although this model was unable to account for tiny peaks that are not well resolved within the data. Some of these peaks could be accounted for using a monoclinic  $Mn_2P_2O_7$  phase, but the inclusion of this phase did not result in a large improvement of the fit. The refined parameters of the main phase are summarized in Table 4.1.

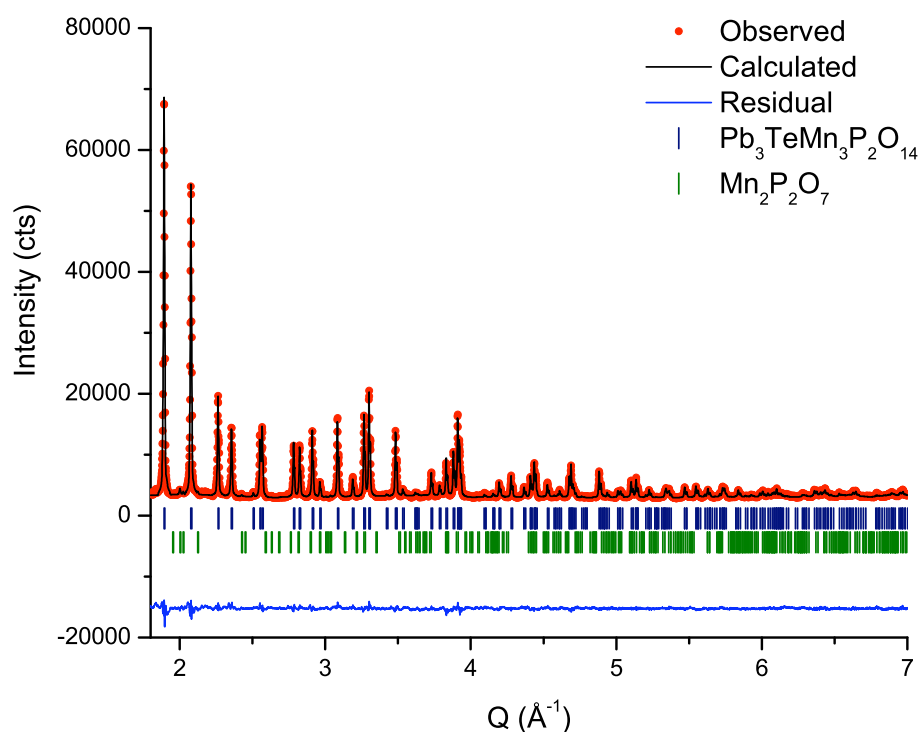


FIGURE 4.6: Refinement of  $Pb_3TeMn_3P_2O_{14}$  using only laboratory x-rays.

To get a better handle on the peaks that were unaccounted for and the atomic coordinates of oxygen atoms, data was collected at the 11-BM diffraction beam line at the APS and POWGEN at the SNS. Due to the high resolution of the data sets, the unaccounted for peaks become much more apparent (Figure 4.7). It was also immediately clear that many of these peaks were, in fact, satellite reflections as opposed to coming from an



TABLE 4.1: Refined atomic coordinates and thermal parameters for  $Pb_3TeMn_3P_2O_{14}$  in the  $P321$  unit cell with lattice constants  $a = 8.4745(1)$  Å and  $c = 5.33118(8)$  Å. The left-handed unit cell was chosen for this refinement. Final residuals were  $R_p = 3.16$ ,  $R_{wp} = 4.25$  and  $\chi^2 = 7.21$ . Only x-ray data was used in this refinement.

Ion	Site	x	y	z	$B_{iso}$ (Å <sup>2</sup> )
Pb1	3e	0.5974(1)	0	0	2.82(3)
Te1	1a	0	0	0	2.25(7)
Mn1	3f	0.2479(5)	0	$\frac{1}{2}$	3.0(1)
P1	2d	$\frac{1}{3}$	$\frac{2}{3}$	0.554(2)	1.6(3)
O1	2d	$\frac{1}{3}$	$\frac{2}{3}$	0.780(1)	2.2(1)
O2	6g	0.453(5)	0.191(4)	0.289(4)	7.1(7)
O3	6g	0.116(1)	0.207(2)	0.196(3)	2.2(4)

impurity. Many of these satellite peaks could be indexed using a propagation vector  $\vec{r} = (0.3775, 0.3775, 0)$  (see Figure 4.7 for a representative sample). A Le Bail fit [151] of the x-ray data was performed using the GSAS-II package [152] and a large metrically trigonal cell was found that was able to index nearly every observable peak with lattice constants  $a = 22.462$  Å and  $c = 5.3315$  Å. The Le Bail fit could be further improved by relaxing the trigonal constraint to allow for a slight monoclinic distortion (although by symmetry, the absence of a 2-fold axis would make this particular cell triclinic). At first, it was incorrectly believed that this large cell was not commensurate with the subcell [143]; this is understandable considering how large the new cell is, the overlapping nature of the reflections, the difficulty in obtaining the results from the Le Bail fit, the observation of numerous solutions that “almost” fit, and the lack of single crystals.

Unlike other dugganites (addressed in the remaining chapters of this thesis [99, 103, 145]), it was believed that  $Pb_3TeMn_3P_2O_{14}$  might retain the trigonal symmetry of the subcell in the larger supercell. This belief is founded on the lack of peak splitting observed in the synchrotron x-ray diffraction indicative of such a symmetry loss [143]. As such it was assumed that the  $P321$  unit cell might be a better fit for this particular

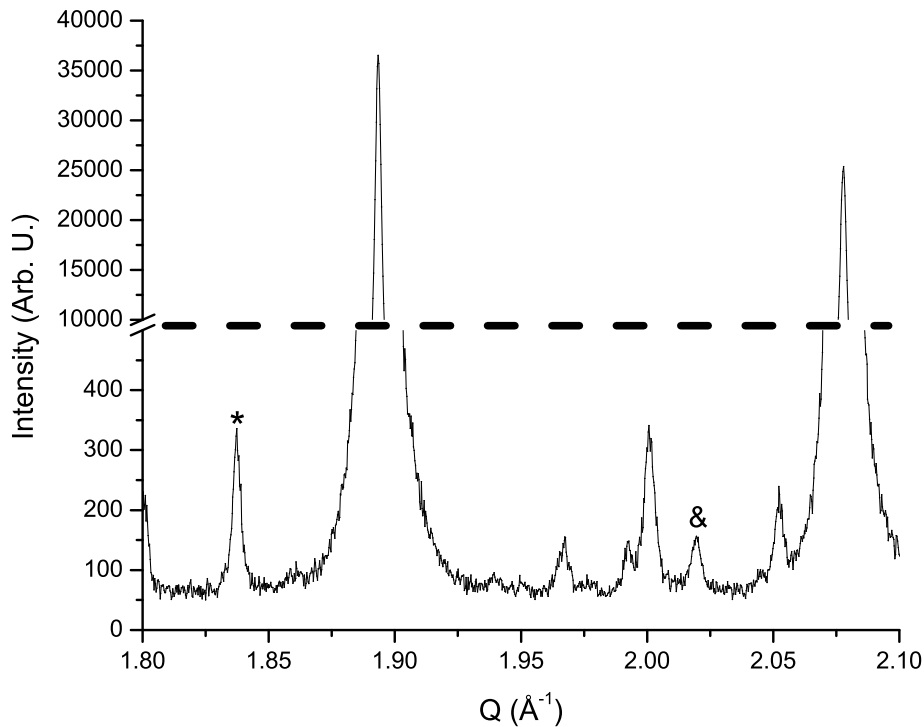


FIGURE 4.7: High resolution x-ray diffraction data taken at the APS at 300 K shows the presence of supercell peaks. Many peaks can be indexed using a propagation vector of  $\vec{r}$ , such as the  $(220-\vec{r})$  and the  $(110+\vec{r})$ , labelled as \* and & respectively.

dugganite than the others; the x-ray, C2, and POWGEN neutron data files were jointly refined in a similar procedure to what was done previously on  $Ba_3NbFe_3Si_2O_{14}$ . The results are summarized in Tables 4.2 and 4.3. It is unsurprising that the bond valence sums for  $Pb^{2+}$  and  $P^{5+}$  are incorrect since the  $P321$  cell is not the true unit cell of the material. However, this refinement yielded convergence statistics similar to those reported for the supercell refinements on other dugganites, indicating that the fit is still quite good [99, 143].

### 4.3.2 Supercell refinement

After further analysis, it was found that the large trigonal cell could be made commensurate with the nuclear cell following a rotation of  $19.11^\circ$  anticlockwise from the origin [144]. Rotating the cell by a non-multiple of three destroys the 2-fold rotation

TABLE 4.2: Refined atomic coordinates and thermal parameters for  $Pb_3TeMn_3P_2O_{14}$  at 300 K in the  $P321$  unit cell with lattice constants  $a = 8.47956(1)$  Å and  $c = 5.33153(1)$  Å. The refinement was carried out using joint high resolution synchrotron x-ray and neutron diffraction data. The left-handed unit cell was chosen for this refinement. Final residuals were  $R_p = 10.2$ ,  $R_{wp} = 14.3$  and  $\chi^2 = 3.87$  for the x-ray data (similar convergence statistics were achieved with the other data sets).

Ion	Site	x	y	z	$B_{iso}$ (Å <sup>2</sup> )
Pb1	3e	0.5978(1)	0	0	1.74(1)
Te1	1a	0	0	0	1.79(5)
Mn1	3f	0.2504(5)	0	$\frac{1}{2}$	1.47(7)
P1	2d	$\frac{1}{3}$	$\frac{2}{3}$	0.5512(14)	1.3(1)
O1	2d	$\frac{1}{3}$	$\frac{2}{3}$	0.265(2)	2.1(3)
O2	6g	0.4842(13)	0.2113(11)	0.3358(13)	4.6(3)
O3	6g	0.1271(8)	0.2134(8)	0.2074(13)	2.1(2)

TABLE 4.3: Selected bond distances and bond valence sums for  $Pb_3TeMn_3P_2O_{14}$  in the  $P321$  unit cell.

Ion	Bond valence sum	Coordination number	Ligand	Distance (Å)	Multiplicity
$Pb^{2+}$	1.22	8	O1	2.945(8)	2
			O2	2.727(5)	2
			O2	3.011(11)	2
			O3	2.344(5)	2
$Te^{6+}$	5.86	6	O3	1.926(7)	6
$Mn^{2+}$	2.01	4	O2	2.087(9)	2
			O3	2.008(7)	2
$P^{5+}$	5.48	4	O1	1.526(13)	1
			O2	1.492(10)	3

axes present in the  $ab$ -plane, which makes the space group of the supercell  $P3$  (and also explains why no trigonal peak-splitting was observed in this system as compared to the other dugganites [99]). The method used for the final refinement was similar to that reported for the structural solution of  $Pb_3TeCo_3P_2O_{14}$  [99] but with minor differences reflecting the different data collection methods. The refined  $P321$  subcell for  $Pb_3TeMn_3P_2O_{14}$  was transformed into the new unit cell.  $TeO_6$  and  $PO_4$  rigid bodies were defined and allowed to translate within the  $ab$ -plane using only the x-ray data (the cations were not allowed to move along the  $c$ -axis at this stage). Only a single overall thermal parameter was used at this point to help model the peak shapes. Next, the refinement was carried out using both x-ray and POWGEN neutron data (higher resolution than C2) using the same weighting scheme as described in Chapter 3 for  $Ba_3NbFe_3Si_2O_{14}$ .

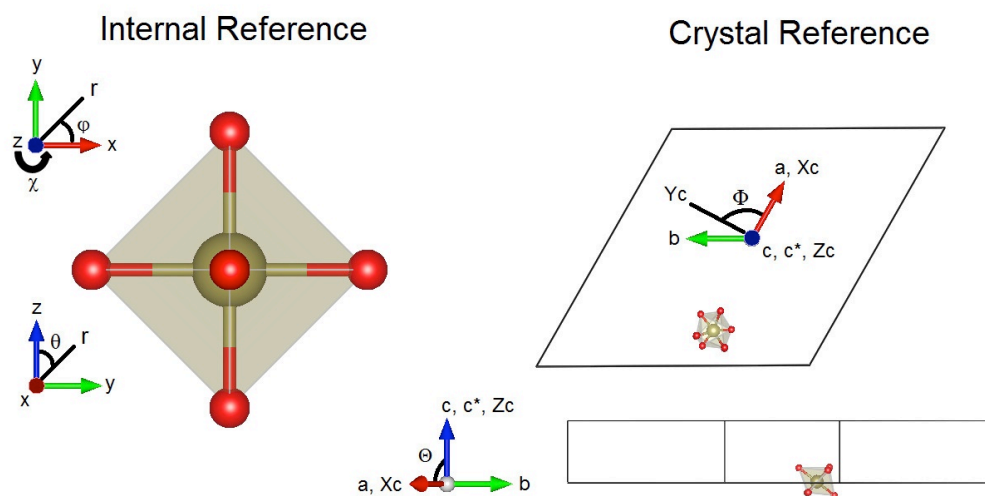


FIGURE 4.8: A rigid body is first defined using spherical coordinates  $r$ ,  $\theta$ , and  $\phi$  within an internal Cartesian coordinate system  $x$ ,  $y$ , and  $z$  (an ideal octahedron is shown on the left). The rigid body is then placed within the framework of the crystallographic unit cell (right). The rigid body coordinate system is then rotated within the crystallographic coordinate frame of reference using pseudo-Euler angles  $\Theta$  and  $\Phi$  (defined on the right for this system:  $X_c$ ,  $Y_c$ , and  $Z_c$  are the orthogonal crystallographic Cartesian coordinates while  $a$ ,  $b$ , and  $c$  ( $c^*$ ) are the directions of the real (reciprocal) lattice vectors). The rigid body frame of reference is then rotated about the internal  $z$ -axis by an angle  $\chi$ .

The rigid bodies were then defined with respect to an internal orthogonal spherical coordinate system  $(r, \phi, \theta)$  (Figure 4.8). Te-O lengths were fixed at 1.949 Å, in line with the expected distances determined from a refinement of the subcell and within a reasonable chemical limit [103, 143]. P-O lengths were defined according to the orthophosphates proper model [153] used for the structural solution of  $Pb_3TeCo_3P_2O_{14}$  [99]. The rigid bodies were placed within the framework of the crystallographic unit cell using additional spherical coordinates  $\Theta$  (angle from the  $c^*$ -axis),  $\Phi$  (angle from the  $a$ -axis), and  $\chi$  (rotation about the rigid body internal  $z$ -axis). Since there are only two degrees of freedom within the crystallographic coordinate system,  $\Theta$  and  $\Phi$  were refined keeping  $\chi$  dependent on those values. Extra attention was paid to rigid bodies on special sites, such as  $TeO_6$  located at the origin. After convergence was achieved, the rigid bodies were then allowed to translate along the  $c$ -axis. Finally, the rigid bodies were allowed to deform from their perfect defined shapes; this was done by refining internal orthogonal coordinates  $\phi$  and  $\theta$  ( $r$  was kept fixed at this point). After convergence, the rigid body option was disabled and the new atomic coordinates were used for all 57 unique atoms in the supercell. The following soft distance constraints were used in the refinement: apical P-O = 1.53(2) Å, base P-O = 1.53(2) Å, Te-O = 1.94(5) Å, and Mn-O = 2.00(12) Å. A larger tolerance was allowed on Mn-O due to the distorted nature of the  $P321\ 3f$  tetrahedron. For  $PO_4$  tetrahedra located on special sites, additional Pb-O soft constraints were implemented to prevent a continuous rotation of the base oxygens around the cation centre, which prevents convergence. The isotropic thermal displacement parameters were then refined with the constraint that all atoms of the same type must have the same displacement parameter. The refined parameters are summarized in Tables 4.4 through 4.6. Using soft distance constraints yields the expected bond valence sums after the refinement. The refinements are presented in Figure 4.9.

TABLE 4.4: Refined atomic coordinates and thermal parameters in  $Pb_3TeMn_3P_2O_{14}$  at 300 K in the  $P3$  supercell with lattice constants  $a = 22.43472(13)$  Å and  $c = 5.33154(4)$  Å. The refinement was carried out using joint high resolution synchrotron x-ray and neutron diffraction data. Final residuals were  $R_p = 7.60$ ,  $R_{wp} = 10.3$  and  $\chi^2 = 2.48$  for the x-ray data (similar convergence statistics were achieved with the other data sets).

Ion	Site	x	y	z	$B_{iso}$ (Å <sup>2</sup> )
Pb1	3d	0.1717(5)	0.9163(6)	0.039(3)	1.02(9)
Pb2	3d	0.3156(5)	0.3528(4)	0.036(3)	1.02(9)
Pb3	3d	0.4528(5)	0.7724(6)	0.010(5)	1.02(9)
Pb4	3d	0.5956(5)	0.1955(5)	-0.008(4)	1.02(9)
Pb5	3d	0.7499(4)	0.6323(5)	0.017(4)	1.02(9)
Pb6	3d	0.8842(5)	0.0587(5)	0.055(3)	1.02(9)
Pb7	3d	0.0278(5)	0.4773(5)	0.003(4)	1.02(9)
Te1	1a	0	0	0.032(5)	1.00(9)
O1	3d	0.060(2)	0.072(2)	0.242(8)	0.9(1)
O2	3d	0.0804(19)	0.033(2)	-0.166(8)	0.9(1)
Te2	3d	0.1509(6)	0.4263(7)	0.021(4)	1.00(9)
O3	3d	0.219(2)	0.506(2)	0.205(8)	0.9(1)
O4	3d	0.0856(19)	0.434(2)	0.251(7)	0.9(1)
O5	3d	0.153(2)	0.362(2)	0.242(8)	0.9(1)
O6	3d	0.2305(18)	0.440(2)	-0.152(7)	0.9(1)
O7	3d	0.127(2)	0.477(2)	-0.199(8)	0.9(1)
O8	3d	0.0758(19)	0.3484(18)	-0.155(8)	0.9(1)
Te3	3d	0.4257(7)	0.2897(7)	0.041(4)	1.00(9)
O9	3d	0.496(2)	0.363(2)	0.214(8)	0.9(1)
O10	3d	0.356(2)	0.286(2)	0.240(8)	0.9(1)
O11	3d	0.440(2)	0.224(2)	0.210(8)	0.9(1)
O12	3d	0.498(2)	0.316(2)	-0.224(7)	0.9(1)
O13	3d	0.399(2)	0.343(2)	-0.207(8)	0.9(1)
O14	3d	0.374(2)	0.208(2)	-0.184(8)	0.9(1)

TABLE 4.5: Continued...

Ion	Site	x	y	z	$B_{\text{iso}}$ ( $\text{\AA}^2$ )
Mn1	3d	0.0736(14)	0.9661(15)	0.539(5)	0.77(9)
Mn2	3d	0.2193(13)	0.3849(15)	0.529(6)	0.77(9)
Mn3	3d	0.3494(14)	0.8194(15)	0.501(5)	0.77(9)
Mn4	3d	0.5031(16)	0.2493(17)	0.510(6)	0.77(9)
Mn5	3d	0.6421(14)	0.6859(16)	0.519(6)	0.77(9)
Mn6	3d	0.7846(14)	0.1037(16)	0.521(6)	0.77(9)
Mn7	3d	0.926(2)	0.5319(14)	0.515(7)	0.77(9)
P1	3d	0.1849(8)	0.2326(8)	0.6010(19)	0.94(8)
O15	3d	0.2519(15)	0.233(2)	0.665(8)	0.9(1)
O16	3d	0.187(2)	0.2979(16)	0.710(8)	0.9(1)
O17	3d	0.131(2)	0.164(1)	0.725(8)	0.9(1)
O18	3d	0.168(2)	0.233(2)	0.321(3)	0.9(1)
P2	1b	$\frac{1}{3}$	$\frac{2}{3}$	0.5626(18)	0.94(8)
O19	3d	0.4036(14)	0.680(2)	0.665(8)	0.9(1)
O20	1b	$\frac{1}{3}$	$\frac{2}{3}$	0.2753(19)	0.9(1)
P3	3d	0.4723(8)	0.0948(8)	0.5798(17)	0.94(8)
O21	3d	0.5405(15)	0.101(2)	0.671(8)	0.9(1)
O22	3d	0.473(3)	0.1595(16)	0.689(8)	0.9(1)
O23	3d	0.4065(15)	0.0313(16)	0.687(8)	0.9(1)
O24	3d	0.473(2)	0.097(2)	0.2911(18)	0.9(1)
P4	3d	0.2433(8)	0.0469(8)	0.4619(17)	0.94(8)
O25	3d	0.296(2)	0.1195(12)	0.362(8)	0.9(1)
O26	3d	0.1686(11)	0.029(2)	0.397(8)	0.9(1)
O27	3d	0.264(2)	-0.0038(19)	0.345(9)	0.9(1)
O28	3d	0.251(2)	0.051(3)	0.750(2)	0.9(1)

TABLE 4.6: Continued...

Ion	Site	x	y	z	$B_{iso}$ ( $\text{\AA}^2$ )
P5	3d	0.3842(8)	0.4820(9)	0.5117(18)	0.94(8)
O29	3d	0.4072(18)	0.5548(12)	0.396(7)	0.9(1)
O30	3d	0.3174(15)	0.447(2)	0.350(7)	0.9(1)
O31	3d	0.4419(16)	0.472(2)	0.405(7)	0.9(1)
O32	3d	0.392(2)	0.495(2)	0.795(2)	0.9(1)
P6	1c	$\frac{2}{3}$	$\frac{1}{3}$	0.5329(18)	0.94(8)
O33	3d	0.665(2)	0.3989(13)	0.470(7)	0.9(1)
O34	1c	$\frac{2}{3}$	$\frac{1}{3}$	0.8207(19)	0.9(1)

Overall, 13 985 reflections were fitted in the refinement. Of all the observed peaks in the synchrotron x-ray data, only eight were unaccounted for. Only one peak was unaccounted for in either of the neutron data sets (this lone impurity peak remained constant in both position and intensity within the resolution of POWGEN at different temperatures between 300 and 2 K and also appears in the x-ray data). These peaks could not be indexed to a known phase. Since the integrated intensities of these peaks were less than 1% of the most intense peaks, the sample is approximated to be over 99% phase pure. The lone peak observable in all data sets was compared to the (140) reflection that is intense in both the x-ray and neutron data sets. It is estimated that these impurity peaks are from a  $Pb-PO_4$  phase on the bases that  $Pb_9(PO_4)_6$  is a known intermediate in the reaction and that the only peak visible in all data sets is relatively more intense in the neutron data sets. Looking at the absorption cross sections for all of the elements used here, neutrons are absorbed by Mn and Te by a factor of at least 40 as compared to Pb, P, and O. Therefore, the impurity is expected to be diamagnetic and should be small enough so as not to interfere with the bulk magnetic properties of the main phase too greatly. Hereafter, the impurity is not considered any further for the discussion of the magnetic properties.



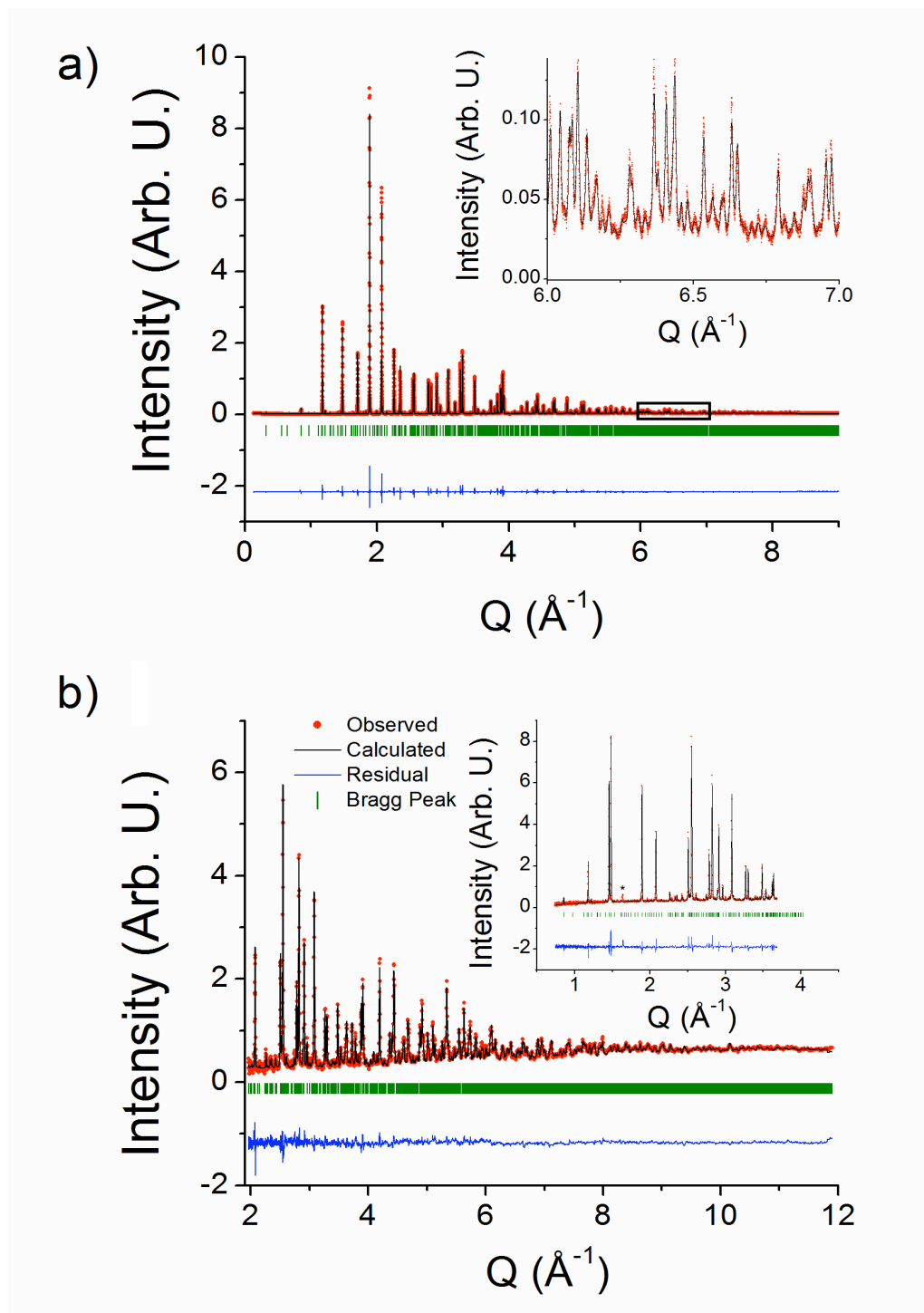


FIGURE 4.9: Final refinements using (top) synchrotron x-ray and (bottom) neutron diffraction data at 300 K. Both outset figures were weighted 45% in the refinement while the inset of (bottom) was weighted 10%. The region shown in the inset is marked in the outset; **Insets:** (top) No peak splitting was observed in the high-Q region of the synchrotron x-ray diffraction data; (bottom) 4.797 Å bank of the neutron diffraction data with the lone impurity marked using an asterisk.

Low temperature refinements were performed on neutron data alone using data from POWGEN and C2; C2 has a better signal-to-noise ratio but much lower Q-resolution as compared to POWGEN. Both data sets were refined in order to confirm findings from both instruments. Only the lattice constants and thermal parameters were refined, which resulted in excellent convergence to the data. The magnetic unit cell refinement will be discussed later in this chapter.

## 4.4 Results and Discussion

### 4.4.1 Crystal structure

Langasites are typified by their noncentrosymmetric  $P321$  unit cell based on the  $Ca_3Ga_2Ge_4O_{14}$  structure. However, many langasites have been reported to undergo phase transitions away from this symmetry with varying temperature and pressure, including  $Ba_3NbFe_3Si_2O_{14}$  [96, 154]. One study [110] suggests that the most likely transition observed in a langasite is either to a  $P3$  or a centred monoclinic unit cell. However, very few langasites have been reported to adopt alternate symmetry at ambient temperature and pressure. The dugganite subgroup is the exception; many of these materials contain  $Pb^{2+}$  lone pairs which are thought to distort the symmetry away from  $P321$  [99, 143–145]. In fact, this often occurs in natural minerals containing  $Pb^{2+}$ , where the distortions are so small that they cannot be observed using typical laboratory diffractometers.  $Pb_3TeCo_3V_2O_{14}$  (Chapter 6),  $Pb_3TeCo_3P_2O_{14}$  (Chapter 5), and artificial  $Pb_3TeZn_3P_2O_{14}$  are known to adopt a  $P2$  supercell [99]. However, this is not representative of the entire story. Natural dugganite,  $Pb_3TeZn_3As_2O_{14}$  single crystals, do not distort away from the prototypical langasite cell, nor do the  $PbO_8$  decahedra appear distorted as they do in other dugganites [75, 136]. An argument can be made that this is due to a lack of resolution in the data. But the same cannot be said for  $La_3SbZn_3Si_2O_{14}$  and  $La_3SbZn_3Ge_2O_{14}$ , which until 2009 were the only langasites prepared with a divalent cation on the  $3f$  site [96, 108]. Both of these systems distort away from  $P321$  symmetry which stresses the role that the ion occupying the  $3f$  site plays in the distortion. Mill [108] argues that the

larger divalent cation introduces stresses on the smaller  $P321$  lattice of the La-containing langasites than those of the larger Pb and Ba-containing langasites. Taking all of the current evidence into account, this theory makes sense;  $Fe^{3+}$  has a low crystal radius of  $0.63 \text{ \AA}$  while Zn and Mn have crystal radii of  $0.74$  and  $0.8 \text{ \AA}$  respectively [95]. However, the differences in sizes between La, Pb, and Ba are  $1.3$ ,  $1.43$ , and  $1.56 \text{ \AA}$  respectively. The coupled effect of a larger  $3f$  ion and a smaller  $3e$  ion should result in distortions in the Pb-containing materials while Ba-containing materials should be left in their  $P321$  state. Indeed,  $Ba_3TeCo_3P_2O_{14}$  was found to possess the typical langasite unit cell at all temperatures measured within the resolution of the 11-BM line at the APS and the HB-2A line [155] at the High Flux Isotope Reactor (HFIR, Oak Ridge, TN) [99]. However, peak shape anomalies were found that may indicate slight atomic positional disorder.

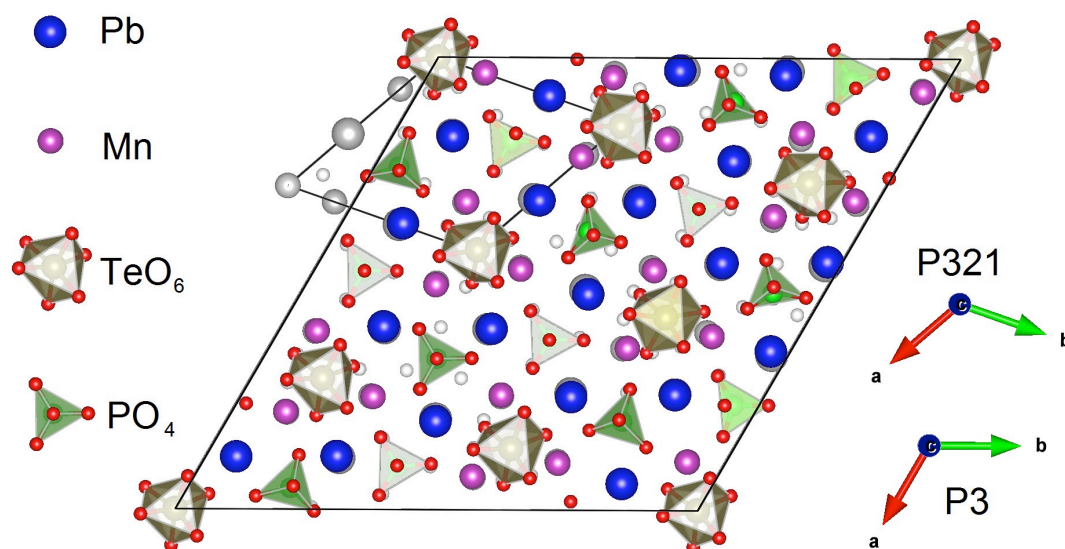


FIGURE 4.10: The supercell shown in relation to the subcell. Colourless spheres represent the ideal atomic coordinates of the subcell within the supercell framework. The supercell has lattice constants  $a = 22.4347(3) \text{ \AA}$  and  $c = 5.33154(9) \text{ \AA}$  and has  $P3$  symmetry.

Nevertheless,  $Pb_3TeMn_3P_2O_{14}$  adopts a  $P3$  unit cell that is unique in the langasite family, shown in Figure 4.10. Replacing  $Mn^{2+}$  for  $Co^{2+}$  completely changes the symmetry of the unit cell despite the latter ion being smaller than the former by only  $0.02 \text{ \AA}$ . It is

speculated that the role of the  $3f$  ion may be highlighted by the relative lack of translational motion of  $Pb^{2+}$  ions as compared to the Co-containing dugganites.  $Mn^{2+}$  is slightly larger than  $Co^{2+}$ , which might limit the motion of  $Pb^{2+}$  ions, and consequently,  $Pb^{2+}$  active lone pairs. In fact, the supercell for  $Pb_3TeMn_3P_2O_{14}$  is almost entirely due to  $PO_4$  tetrahedral rotations and distortions. Still it is surprising that the identity of the  $3f$  ion should play such a large role in the supercell formation since the size differences are so small. However, large effects stemming from substitutions such as this are a common occurrence in the dugganites (this is extensively discussed in later chapters).

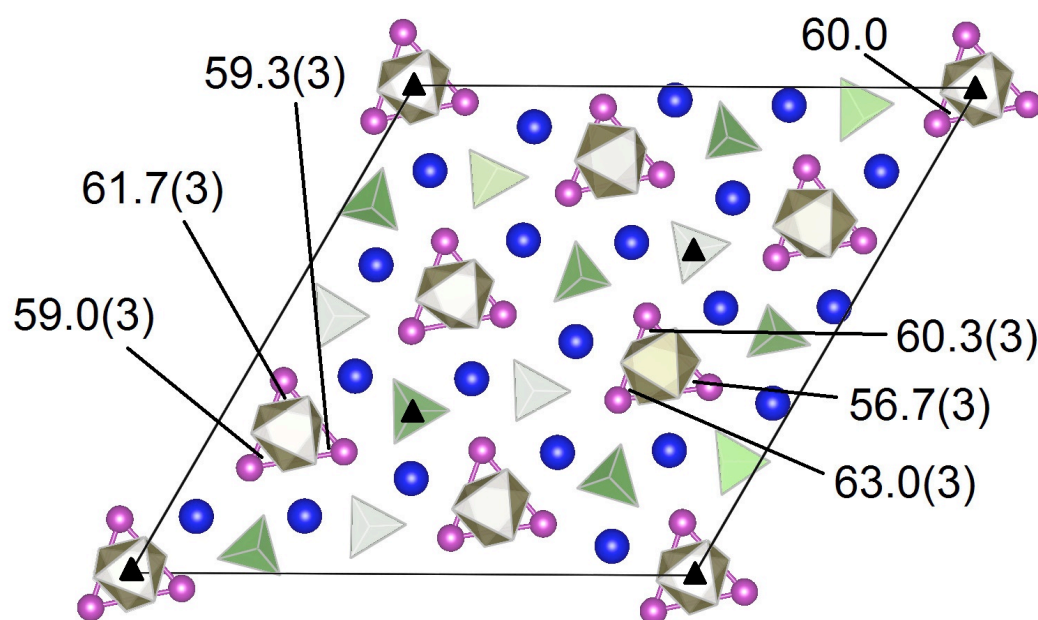


FIGURE 4.11: Mn ions are arranged in isolated nearly equilateral trimers. The symmetry elements of the unit cell are labelled with black triangles, indicating three-fold rotation axes perpendicular to the page. All angles are labelled in degrees.

For the purposes of exploring the magnetism within  $Pb_3TeMn_3P_2O_{14}$ , it is important to describe the nature of the  $Mn^{2+}$  trimers within the supercell (Figure 4.11). The volume of the supercell is seven times larger than the subcell, which itself contains the equivalent of one equilateral trimer. Therefore there are now seven  $Mn^{2+}$  trimers in the supercell, with only one having perfectly equilateral symmetry (surrounding the three-fold axis at the origin). The other six trimer units are divided into two groups of *nearly* equilateral

planar trimers as a result of the inner three-fold rotation axes in the cell. Obviously, this complicates any analysis of the exchange interactions; a thorough study of the exchange pathways is left for future work.

#### 4.4.2 Physical property measurements

DC susceptibility measurements up to 9 T were taken on a Physical Property Measurement System. A single transition was observed at 6.6 K, agreeing with previous reports (Figure 4.12) [139, 143, 144]. A bump in the susceptibility was observed in one study near 45 K using a field of 0.1 T [143] and was attributed to the potential onset of diffuse scattering. While diffuse scattering was observed in the neutron data, it is rather weak and the bump was not reproducible across all of the samples tested, pointing either to air in the sample chamber or to an artifact of the instrumental setup as likely culprits behind the feature.

The transition temperature is tracked as a function of field in Figure 4.13. It is worth noting two distinct features of the susceptibility curves: **1)** The peak maximum appears to have nonlinear field dependence and **2)** the peak shape and curve after the peak both change as a function of field as well, indicating a possible phase transition. Both features of the susceptibility can be simultaneously explored by plotting the peak maximum and minimum (where there is one). The results are graphed in Figure 4.14, where the peak maximum is also plotted with temperature in the inset of the latter. The peak at first appears to suppress with increasing field and then increases in intensity after the crossover at 3 T. This may indicate an increase in the ferromagnetic component to the spin structure as the field is increased to 3 T, followed by suppression (but with a plateau in the susceptibility) at still higher fields. Each data set was fit to the Curie-Weiss law between 75 and 300 K, and yielded an effective moment of  $5.7(2) \mu_B$  (within error of the  $Mn^{2+}$  free spin moment [8]) and Weiss temperature  $\theta_{CW} = -15(4)$  K. Here, the errors were found by fitting each data set using a variety of temperature ranges, the lowest temperature in the range being 70 K. There is no obvious field dependence to

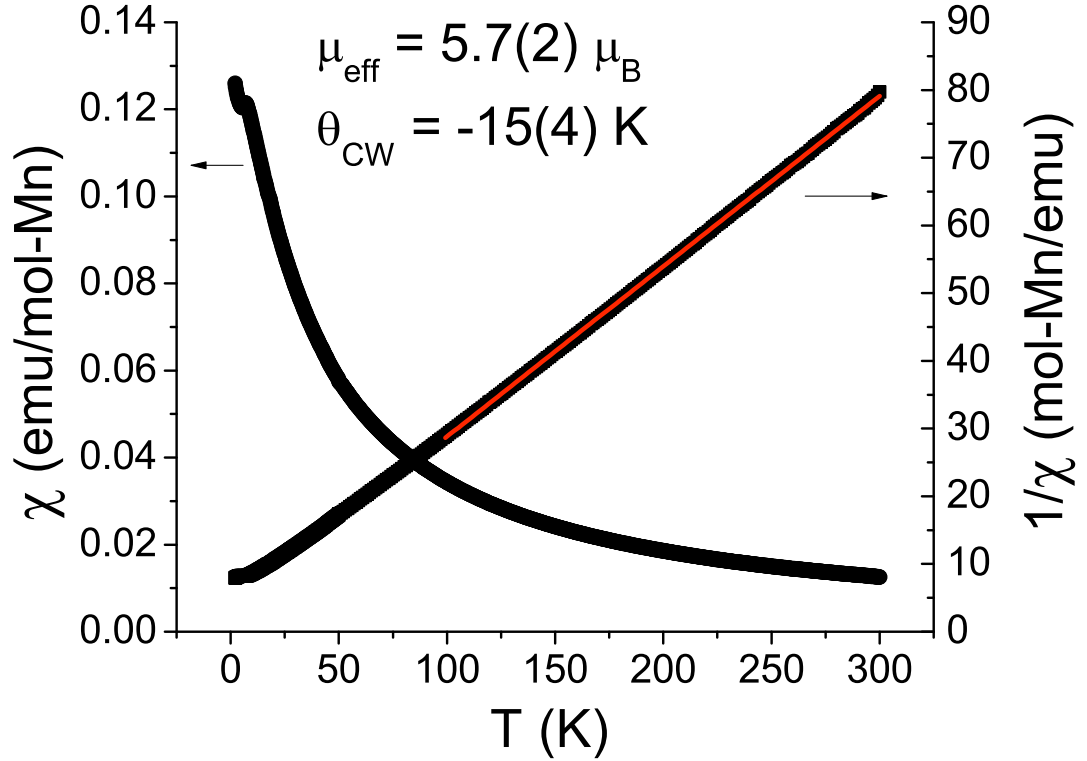


FIGURE 4.12: DC magnetic susceptibility and inverse as a function of temperature. The red line is a fit to the Curie-Weiss law.

either the effective moment or  $\theta_{CW}$ , although both agree with previously reported values [139, 143, 144]. High-field measurements up to 35 T were made at the NHMFL and plotted in Figure 4.15. Unlike  $Pb_3TeCo_3V_2O_{14}$ , which displays complex behaviour in field [156], no anomalies were detected in the magnetization data throughout the entire tested field range. Rather, the moment saturates at 25 T at a value of  $5.0(5) \mu_B$ , which is approximately the expected value for  $Mn^{2+}$ .

The temperature dependences of the zero-field heat capacities of  $Pb_3TeMn_3P_2O_{14}$  and  $Pb_3TeZn_3P_2O_{14}$  are shown in Figure 4.16 along with the residual heat capacity of  $Pb_3TeMn_3P_2O_{14}$  found by approximating  $Pb_3TeZn_3P_2O_{14}$  as a lattice standard. This residual heat capacity is largely assumed to be due to the differences in the magnetic behaviours between these samples.  $Pb_3TeZn_3P_2O_{14}$  heat capacity was scaled for this

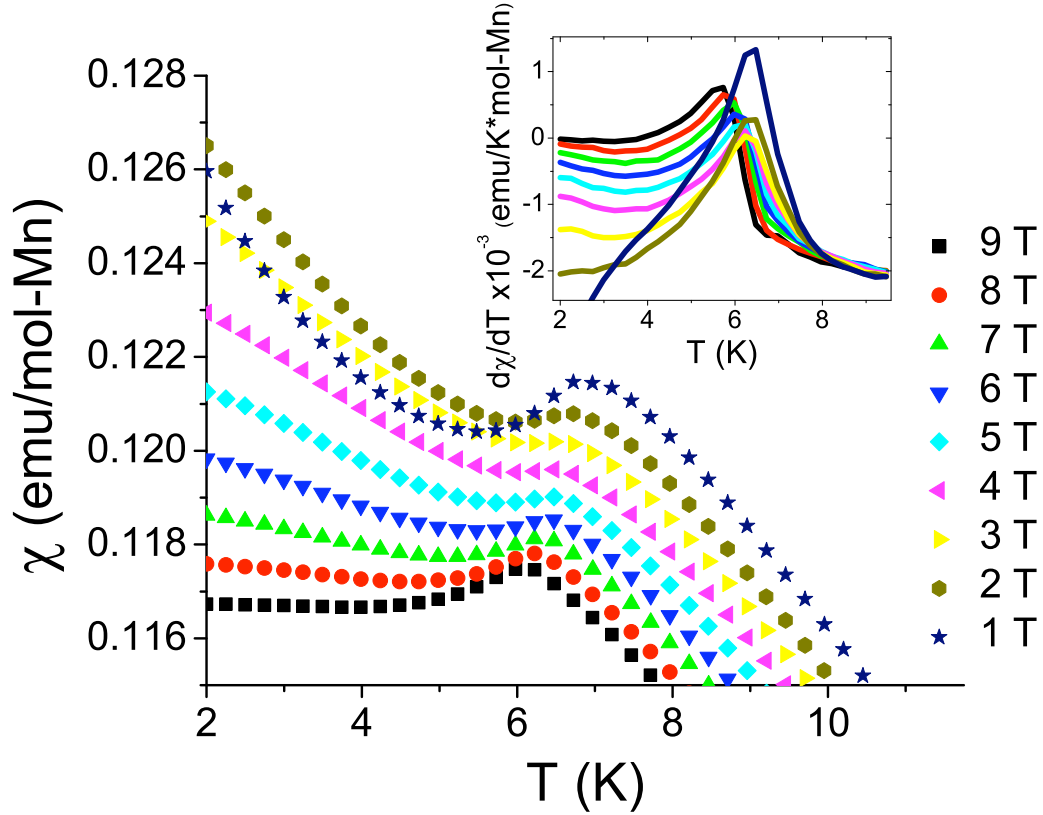


FIGURE 4.13: The transition temperature was tracked as a function of field (outset) as was the derivative of the curves (inset). All susceptibility data was linearly interpolated to evenly space the points (the total number of points per curve was not changed).

analysis. A peak in the heat capacity is observed at 6.6 K that is consistent with the transition observed in the magnetic susceptibility. The entropy, found by integrating  $C_{res}/T$ , is then an approximation of the magnetic entropy and was calculated to be 16.9 J/Kmol-Mn over the entire range. The theoretical value is  $\Delta S_{mag} = R \ln(2S+1) = 14.89$  J/Kmol-Mn, which is 113% of the theoretical value around 30 K (Figure 4.16). Clearly, this is unphysical and is a result of the slight lattice mismatch between  $Pb_3TeZn_3P_2O_{14}$ , which adopts either an orthorhombic or monoclinic supercell structure as compared to the large trigonal supercell of  $Pb_3TeMn_3P_2O_{14}$  (although both have the same subcell).  $Pb_3TeCo_3V_2O_{14}$  has a reported Debye temperature of 350 K [157]; an attempt was made to fit the heat capacity of  $Pb_3TeMn_3P_2O_{14}$  to the Debye function. This yielded a Debye temperature in the vicinity of 300 K, but the fits themselves were quite poor, as expected due to the lack of cubic symmetry. In fact, the heat capacities of langasites

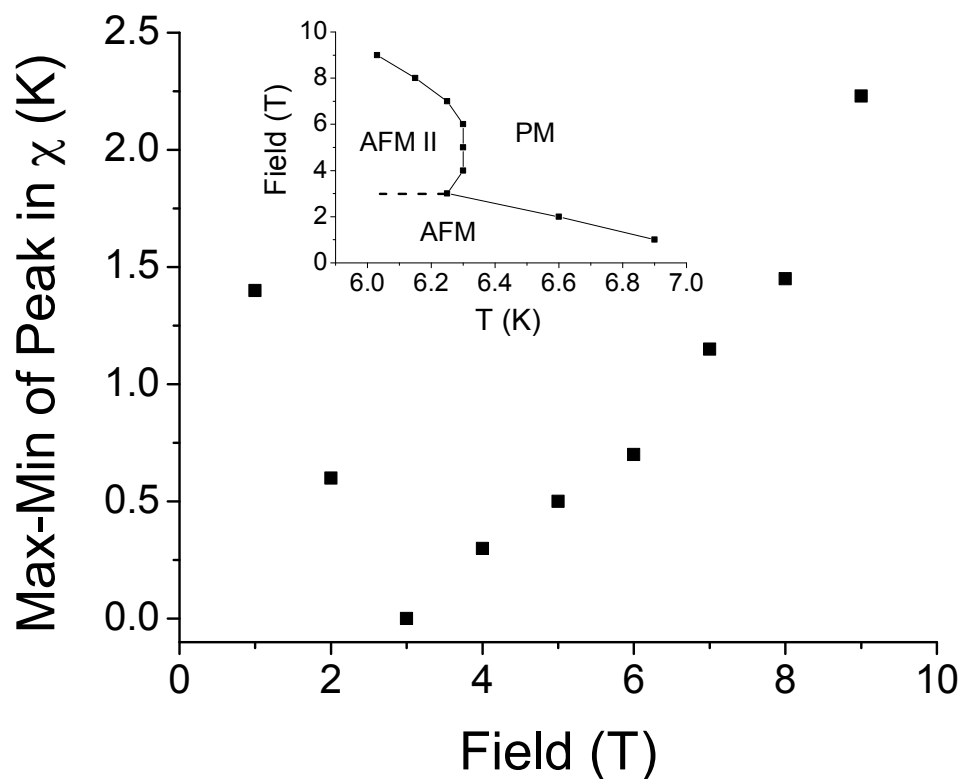


FIGURE 4.14: The peak maximum and minimum (points where the derivative is zero) are tracked as a function of field; **Inset:** The position of the peak maximum is tracked as a function of field. There is an abrupt change at 3 T possibly indicating a phase transition.

in general are seldom fit to the Debye function; a lattice standard is often used instead as a better approximation of the phonon contribution. Finally, an attempt was made to fit the lattice contribution of the heat capacity to that of  $Pb_3TeMn_{1.5}Zn_{1.5}P_2O_{14}$  in the hope that dampened magnetic interactions on a better lattice match could yield a more reasonable result, as was the case for  $Ba_3NbFe_3Si_2O_{14}$  [94]. The calculated entropy was 15.6 J/mol-K which is in much better agreement with the theoretical value, however caution must be taken in interpreting the final result;  $Pb_3TeMn_{1.5}Zn_{1.5}P_2O_{14}$  appears single phase with broadened peaks within the limits of the D5000 diffractometer, but microscopy reveals the presence of two types of distinctly coloured granules within the product, indicating phase separation (Figure 4.17).



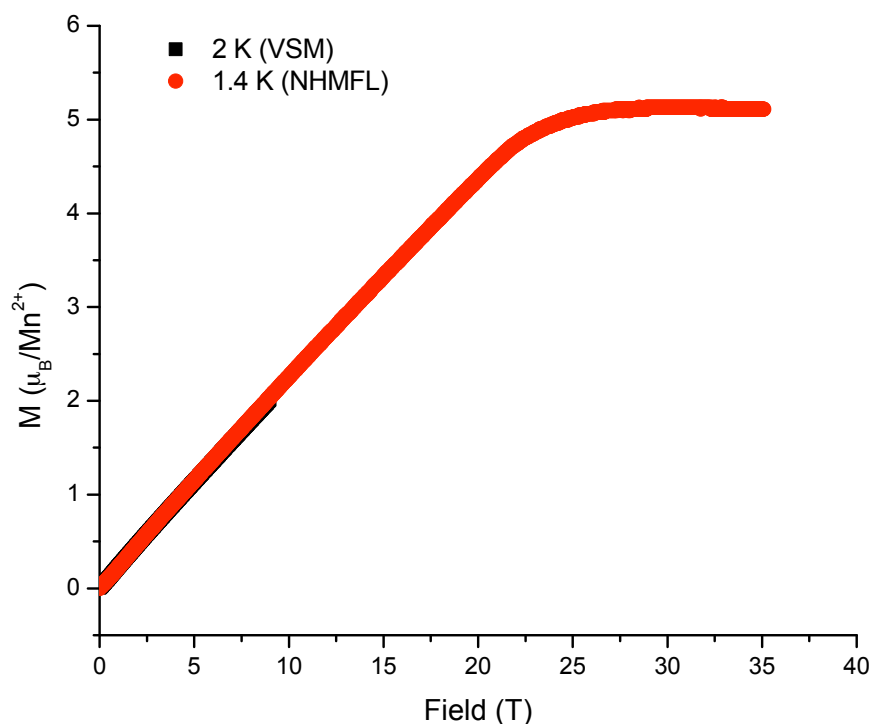


FIGURE 4.15: DC magnetic susceptibility up to 35 T taken at the NHMFL. The  $Mn^{2+}$  moment is saturated by 25 T at 1.4 K at a value of  $5.0(5) \mu_B$ . While the statistical error in each measurement is smaller than the symbols used, the error in the final moment is much larger due to friction within the sample chamber that is not recorded. Data from the NHMFL has been scaled by a factor of 1.12 to match the slope of the data taken using a vibrating sample magnetometer on a standard Physical Property Measurement System (Quantum Design).

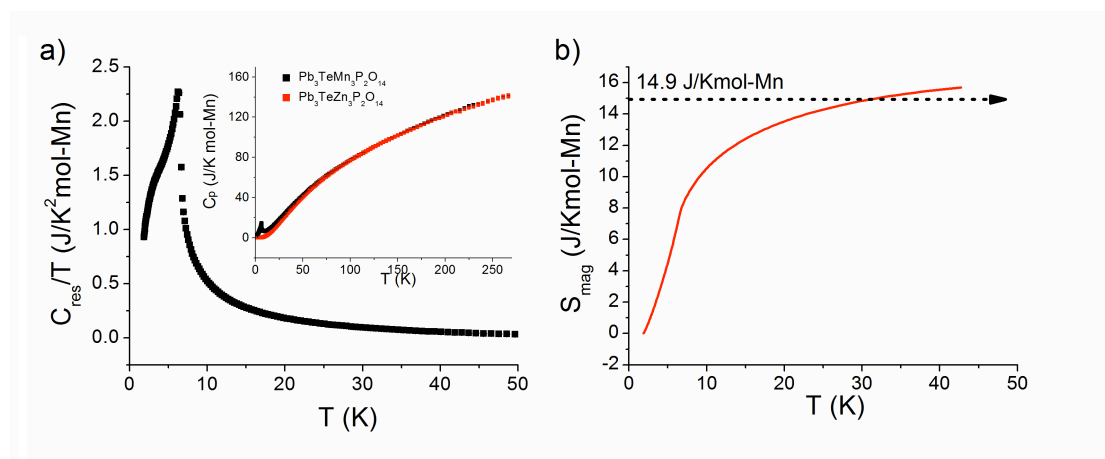


FIGURE 4.16: **Left**) A transition at 6.6 K is observed in the residual heat capacity found by subtracting off the heat capacity of  $Pb_3TeZn_3P_2O_{14}$  from  $Pb_3TeMn_3P_2O_{14}$  (Inset); **Right**) The magnetic entropy (red) and theoretical entropy (black dashed line).

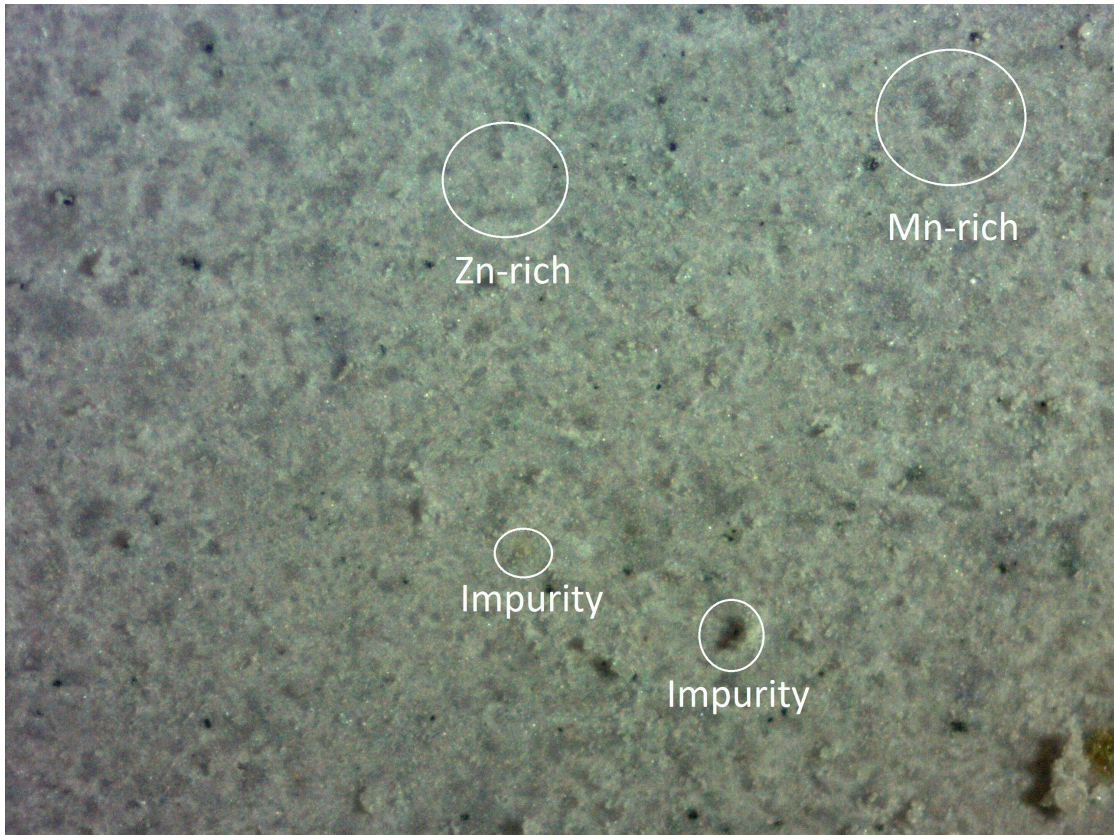


FIGURE 4.17: Although the diffractogram showed only a single  $Pb_3TeMn_{1.5}Zn_{1.5}P_2O_{14}$  phase, the peaks were significantly broadened hinting at phase separation. Phase separation is directly observed using microscopy. Zn-rich and Mn-rich regions are circled in white, along with impurities. These regions were determined solely by colour difference.

Finally, the temperature dependence of the dielectric constant is measured and presented in Figure 4.18. Indeed, the dielectric constant does decrease with frequency (Figure 4.19), and a weak peak can be observed after a background subtraction at  $T_N$  in Figure 4.18. The peak centre shifts slightly with field towards higher temperature until  $3T$  when it begins to shift back towards lower temperatures, which is consistent with the proposed phase diagram from magnetic susceptibility (it is noted that while weak magnetoelectric coupling exists, the magnetic and electric transition temperatures can differ slightly, as they do in  $Ba_3NbFe_3Si_2O_{14}$  [124, 126]). The overall shapes of the dielectric constant and dielectric loss curves are also consistent with previous findings on  $Ba_3NbFe_3Si_2O_{14}$  [124]. However, these features are quite weak in the present case as compared to Rathore *et al.* [124]. Strictly speaking, a direct comparison of the

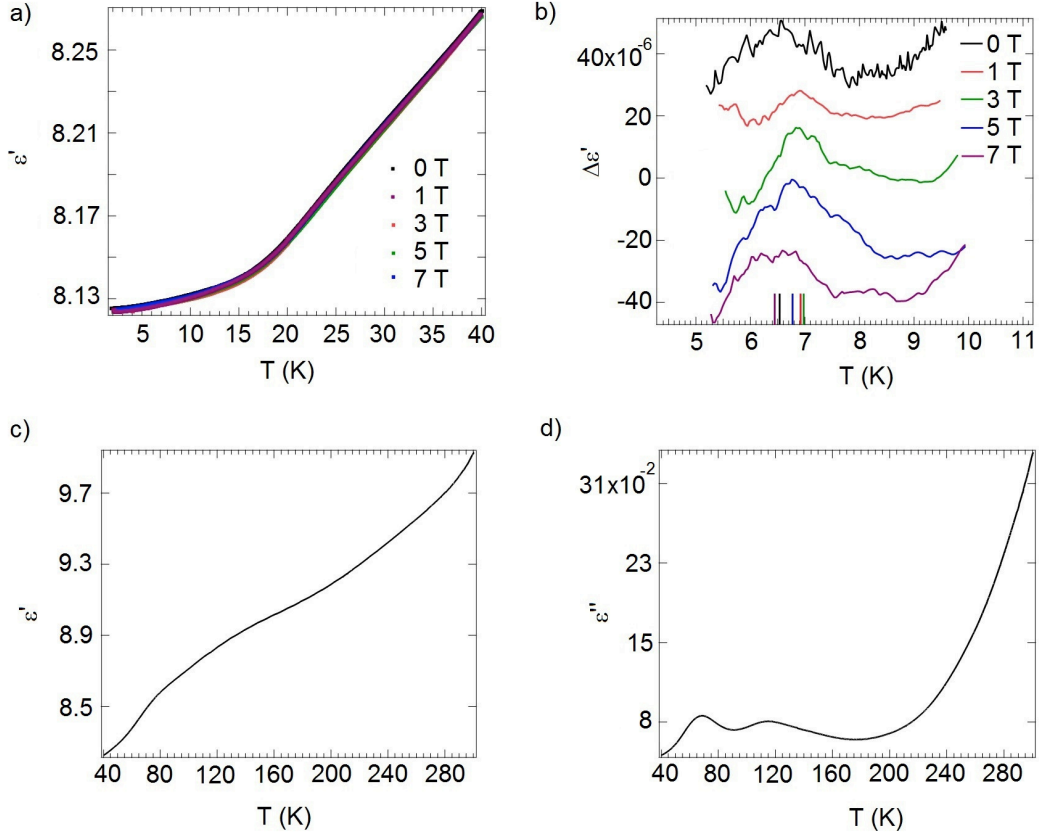


FIGURE 4.18: **a)** The temperature and field dependence of the dielectric constant,  $\epsilon'$ ; **b)** Background-subtracted low temperature dielectric constant (peak centres are marked at the bottom of the panel for clarity); **c)** High-temperature dielectric constant; **d)** Dielectric loss  $\epsilon''$ . All measurements are in arbitrary units with a frequency of 20 kHz using an electric field magnitude of 79 kV/m.

magnitudes of the features between the systems is not possible with the given data due to differences in the calibration of each of the instruments, but a background subtraction was required to observe the feature in  $Pb_3TeMn_3P_2O_{14}$ . Perhaps this is not so surprising: the magnetic interactions in  $Pb_3TeMn_3P_2O_{14}$  ( $\theta_{CW} = -15$  K) are approximately 10% of that found in  $Ba_3NbFe_3Si_2O_{14}$  ( $\theta_{CW} = -190$  K) [82, 94, 120]; it is reasonable to expect magnetoelectric coupling would scale with the Weiss temperature.

#### 4.4.3 Magnetic structure

$Ba_3NbFe_3Si_2O_{14}$  has a doubly chiral magnetic structure that is highly dependent on the chirality of the crystal structure. Although substituting Ba, Nb, and Si with other ions

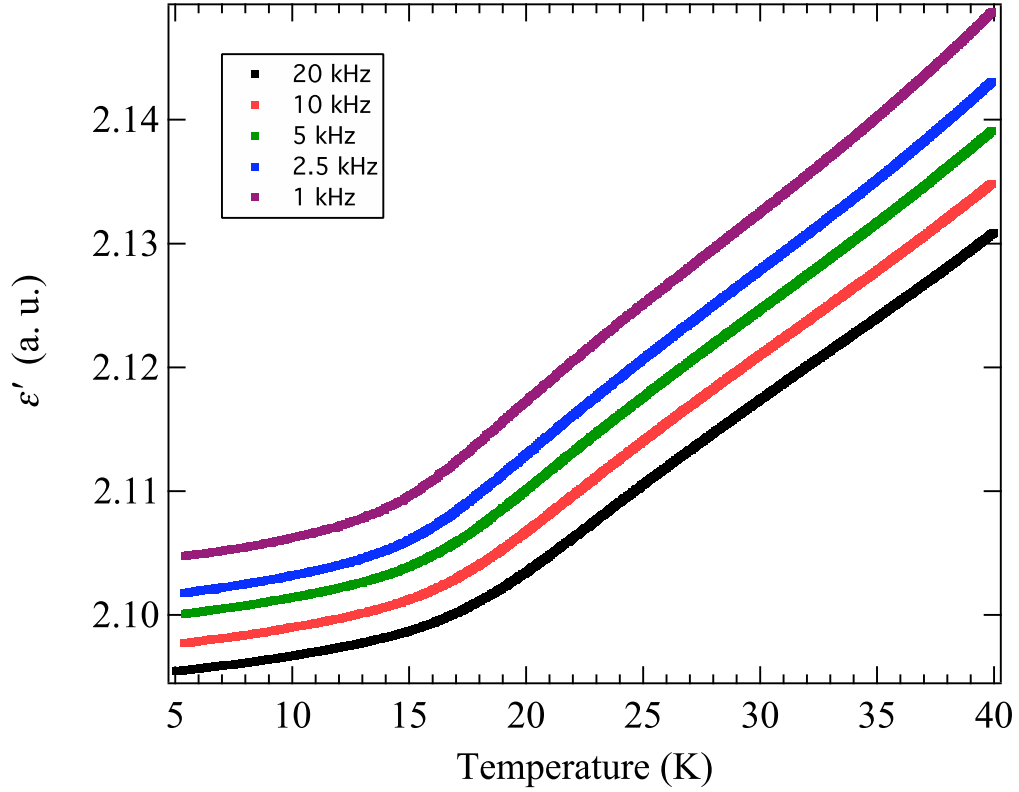


FIGURE 4.19: The frequency dependence of the dielectric constant.

all have little effect on the integrity of the magnetic structure, it is of great interest to observe how the structure might change by substituting  $Fe^{3+}$  for isoelectronic  $Mn^{2+}$ . Furthermore, the slight distortions away from  $P321$  symmetry may also affect the magnetism since there are now seven inequivalent Mn-trimers per cell, only one of them being strictly equilateral.

In addition to the evidence provided here, it was shown in previous studies that  $Pb_3TeMn_3P_2O_{14}$  has a single antiferromagnetic transition at  $T_N = 6.6$  K [139, 143, 144]. Low temperature refinements were performed on neutron diffraction data taken using the C2 diffractometer (Figure 4.20). The propagation vector was found to be  $\vec{k} = (0, 0, 0.189)$ , although it was later determined that  $\vec{k} = (u, 0, 0.189)$ , where  $u = 0.017$ , using higher resolution data from POWGEN. The symmetry of the magnetic cell can be represented by a single irreducible representation (IR)  $\Gamma_1$  of the little group  $G_x$  formed from the space group

$P3$  and the propagation vector, restricted to the Hilbert space defined by basis vectors  $\psi(1) = (1, 0, 0)$ ,  $\psi(2) = (0, 1, 0)$ , and  $\psi(3) = (0, 0, 1)$ . However, the general form of this propagation vector results in the Mn atoms splitting into three “orbits” each; that is, the act of three fold rotation to create three Mn atoms per site within the nuclear cell no longer applies in the magnetic unit cell, resulting in 21 individual moment position coordinates and 63 refineable parameters (three basis vectors per orbit). Since the material is of polycrystalline nature, approximations must be made in studying the magnetic structure. The first and most obvious of these is to consider a more symmetric propagation vector  $\vec{k}' = (0, 0, 0.189)$  where  $u = 0.017 \approx 0$ . Here,  $\vec{k}'$  is of the same form found in  $Ba_3NbFe_3Si_2O_{14}$ . Using this approximation, a magnetic structure refinement was made using IR  $\Gamma_1$  with  $\vec{k}'$  where all of the moments were constrained to point within the  $ab$ -plane. IRs  $\Gamma_2$  and  $\Gamma_3$  were tried but could not account for the proper intensities of the experimentally observed peaks. It is interesting to note that while the positions of the magnetic peaks could be modelled well, the widths of these peaks are anomalously large as compared to the nuclear phase peaks. After performing measurements on POWGEN, the cause of the anomalous peak widths became quite clear: the magnetic peaks have begun to split (Figure 4.20). The propagation vector  $\vec{k}'$  is able to account for the positions of every magnetic peak and magnetic peak doublet, but it cannot account for the peak splitting (Figure 4.21).

While the true magnetic structure is quite complex, an instructive approach would be to explore the magnetic unit cell with respect to the crystal subcell. This can be done for two reasons: **1)** The direction of propagation in  $\vec{k}'$  along the  $c$ -axis is invariant with respect to the subcell-supercell transformation, and **2)** the Mn ions sit on the 2-fold rotation axes present in the subcell, which eliminates the additional symmetry element imposed by the change of space group. Using this approach, a second approximation is then made; the Mn ions do not translate much from their ideal subcell positions which is evidenced by the nearly equilateral Mn trimers mentioned previously. After implementing these simple approximations, from the perspective of the Mn ions, there is no

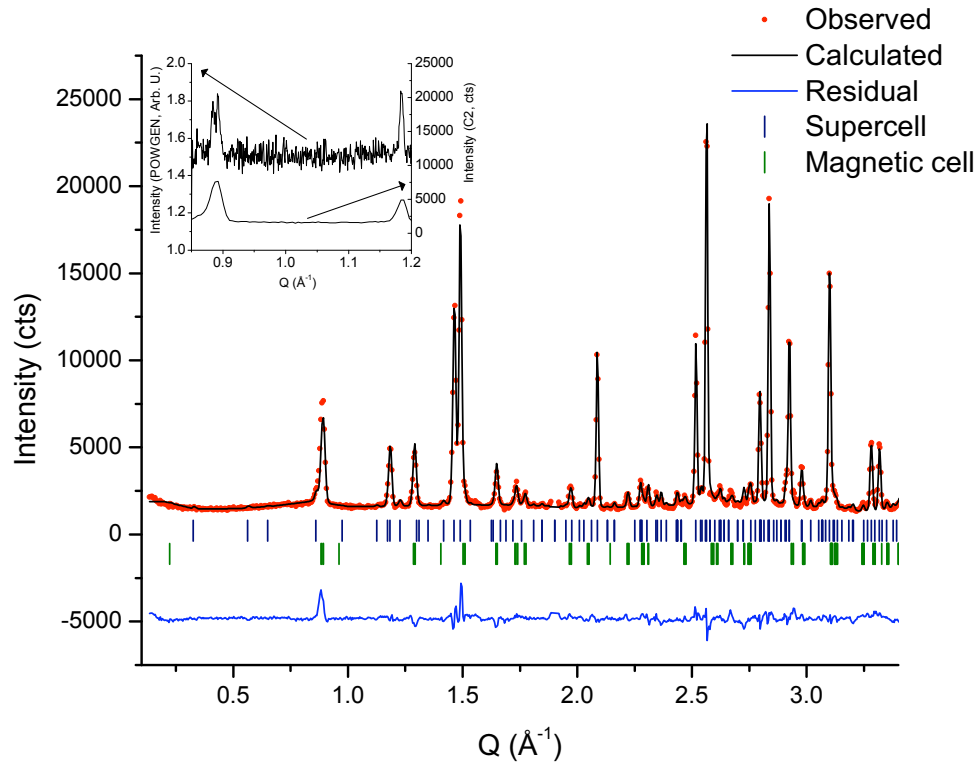


FIGURE 4.20: Refinement of the supercell and magnetic cell (subcell coordinates, read text for details) using neutron diffraction data taken with the C2 DUALSPEC instrument. The inset shows the increase in resolution and background noise of POWGEN data relative to C2. An excluded region was used at  $1.8 \text{ \AA}^{-1}$  to mask a dead detector that falls incident on a Bragg peak.

difference between the  $P321$  and  $P3$  space groups: only the size of the unit cell changes. For this refinement, a single ideal subcell Mn atomic position was used with  $\Gamma_1$  and  $\vec{k}'$ . This new refinement was checked against the previous one for consistency (again it was found that only  $\Gamma_1$  yields the proper intensities). Finally,  $\vec{k}'$  was relaxed to the general form  $\vec{k}$  ( $u$  was modified in accordance with the smaller crystallographic cell) and since there are now only three Mn atoms per unit cell, the refineable parameters become more manageable. To make the refinement easier, the moments were approximated such that the coefficients of the basis vectors reflect their symmetry from the converged refinement with  $\vec{k}'$ , although this is no longer strictly required. The result is shown in Figure 4.22. For completeness, a final set of magnetic structure calculations were performed on fictitious supercells that retained  $P321$  symmetry. The subcell was extended by factors

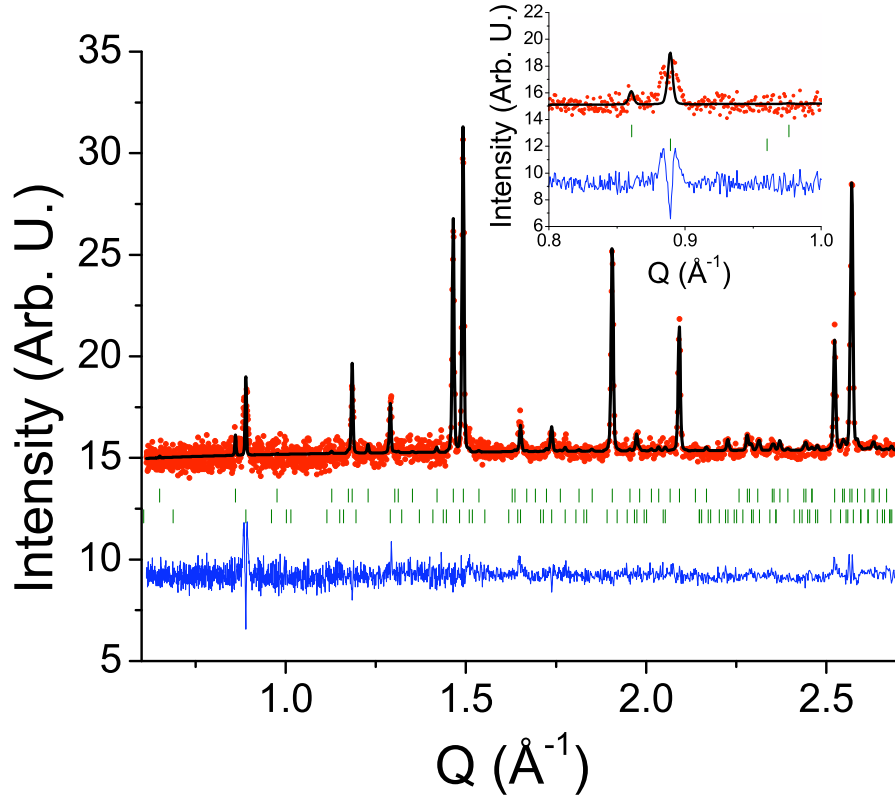


FIGURE 4.21: Magnetic structure refinement of  $Pb_3TeMn_3P_2O_{14}$  at 2 K using the supercell coordinate with reduced propagation vector  $\vec{k}' = (0, 0, 0.189)$ . This model cannot account for the peak splitting (one of the peak doublets is shown in the inset) observed on some of the magnetic Bragg reflections, but it can account for the general positions of all the observed magnetic reflections. Upper green tick marks indicate the positions of the nuclear reflections while the lower green tick marks indicate the positions of the magnetic reflections.

of two, three, and four along both the  $a$  and  $b$  directions. For the case of the two-fold extension, the single inequivalent Mn atom of the subcell becomes three inequivalent Mn atoms. Using  $\vec{k}'$ , it is possible to show that the peak splitting is not simply due to the enlargement of the cell, but the exact nature of the relationship between  $\vec{k}$  and the symmetry loss observed here remains to be seen. It is noted that like  $Ba_3NbFe_3Si_2O_{14}$ , the phasing of the moments within each trimer in the  $ab$ -plane is arbitrary, even with single crystals.

The magnetic structure presented here is quite robust in the sense that the propagation

vector  $\vec{k}$  restricts the possible IRs available for this space group to one but ambiguities nevertheless exist simply due to the powder nature of the sample. The magnetic unit cell of  $Pb_3TeMn_3P_2O_{14}$  can be compared to the highly studied structure of  $Ba_3NbFe_3Si_2O_{14}$ , except with the latter system, physicists have the luxury of large high quality single crystals and a less ambiguous magnetic structure solution. From the perspective of neutron scattering using enantiopure single crystals, it was determined that the moments lie within the  $ab$ -plane and propagate in a circular helix along the  $c$ -axis with propagation vector  $\vec{l} = (0, 0, 0.142)$  [90]. Using resonant x-ray scattering it was found that there is an additional small  $c$ -axis component that modulates with a sine curve along  $\vec{l}$ , but this effect is too small to be observed with neutron scattering [117]. Partly due to the chiral nature of the  $P321$  space group, the magnetic structure in  $Ba_3NbFe_3Si_2O_{14}$  exhibits single domain helicity and triangular chirality. While the same effects would likely occur in nearly isostructural  $Pb_3TeMn_3P_2O_{14}$  enantiopure single crystals, it is impossible to distinguish between these enantiomers using powders. This raises another issue: it is odd that  $\Gamma(3)$  of  $\vec{k}'$  does not model the magnetic Bragg reflection intensities as well as  $\Gamma(1)$  considering that they are equivalent chiral enantiomers of the magnetic structure within the resolution of powder diffraction. Perhaps this is due to the background noise or is a result of the approximations made in modelling the magnetic structure.

#### 4.4.4 Discussion

Aside from the most obvious questions concerning the chirality of the magnetic structure and interactions, a potentially more interesting issue presents itself in  $Pb_3TeMn_3P_2O_{14}$ : how does the electric behaviour follow from the magnetic behaviour and crystal structure? A number of theories have come to light, especially with respect to the discovery of multiferroicity in  $Ba_3NbFe_3Si_2O_{14}$ . In one theory, multiferroicity forms from the helicoidal twisting of the magnetic moments along the  $c$ -axis, which has been found to break symmetry in other materials resulting in an electric polarization normal to the direction of propagation [93]. In noncentrosymmetric materials however, helicoidal twisting is always predicted at any finite moment value below  $T_N$  strictly on the basis of free



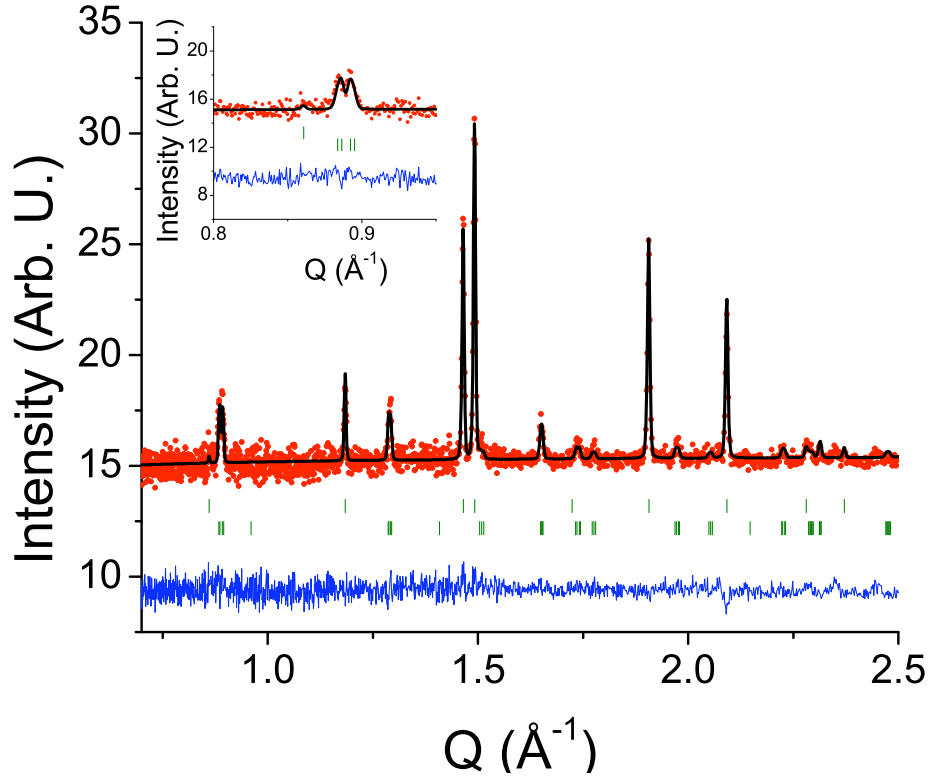


FIGURE 4.22: The positions, intensities, and peak splitting (inset) can all be accounted for using the subcell model described in the main text. Upper green tick marks indicate the positions of the nuclear subcell reflections while the lower green tick marks indicate the positions of the magnetic reflections.

energy calculations [130]. Furthermore, in triangular magnetic lattices where the planar components of the intratrimer moments sum to zero, electric polarization will not result by itself even with a finite magnetization directed along the out-of-plane axis (cause by moments canting out of the plane) [130].

Now suppose that each neighbouring trimer within the plane has a total planar moment of zero, but the orientations of the moments were allowed to differ slightly from one neighbouring trimer to the next as shown in Figure 4.24. The moments in every trimer are allowed to cant out of the plane in identical fashion, inducing a weak but net ferromagnetic moment along  $c$ . An electric polarization will develop along some axis within the plane perpendicular to  $c$  [130], resulting in a multiferroic state. Such an electric

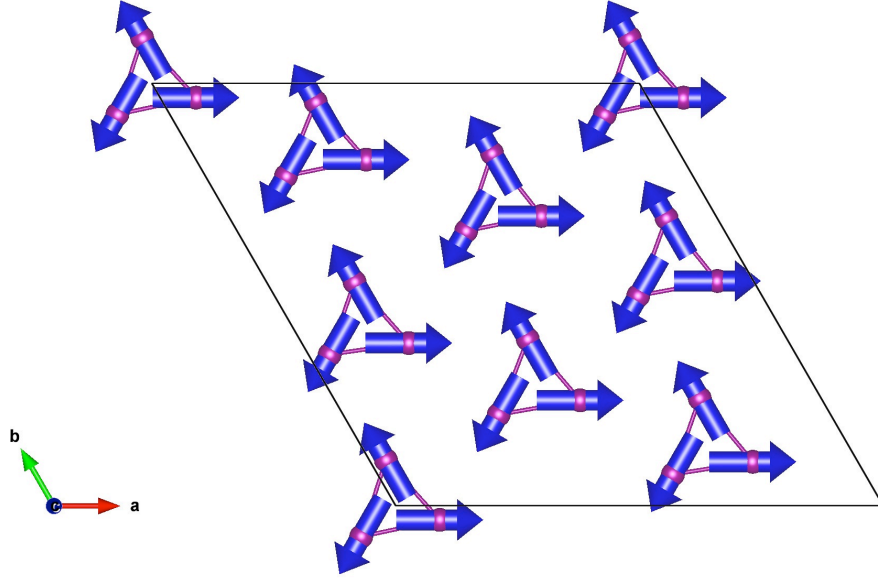


FIGURE 4.23: The magnetic unit cell of  $Pb_3TeMn_3P_2O_{14}$  viewed along the  $ab$ -plane.

polarization has already been realized in  $Ba_3NbFe_3Si_2O_{14}$  with an accompanying weak magnetic hysteresis below  $T_N$  in the magnetization measurements [94, 126, 128]. However, no evidence exists for such a twisting of the trimer moments within the  $ab$ -plane. In fact, some researchers believe instead that a phase transition occurs from  $P321$  to  $C2$  beyond the resolution of synchrotron diffraction [105, 117, 127]. In  $Pb_3TeMn_3P_2O_{14}$ , there is now direct evidence of such trimer moment twisting along an axis in the  $ab$ -plane;  $\vec{k} = (0.017, 0, 0.189)$  shows that the moments undergo an incommensurate helicoidal twist over approximately 59 supercells (149 subcells) in the  $ab$ -plane, in addition to the propagation along  $c$ . A weak anomaly was observed in the dielectric constant followed by a drop below  $T_N$  that would be expected for a material that exhibits an electric polarization. However, since no single crystals exist it is difficult to estimate the true strength of this interaction here (or even the true form of the magnetic structure). Although this route to multiferroicity may not be true for all langasites, it is shown quite clearly here that it is indeed experimentally viable. The question now is to show the cause of such a clear planar propagation in  $Pb_3TeMn_3P_2O_{14}$  as compared to  $Ba_3NbFe_3Si_2O_{14}$ . Is the multiferroicity due to the additional exchange interactions within each trimer that

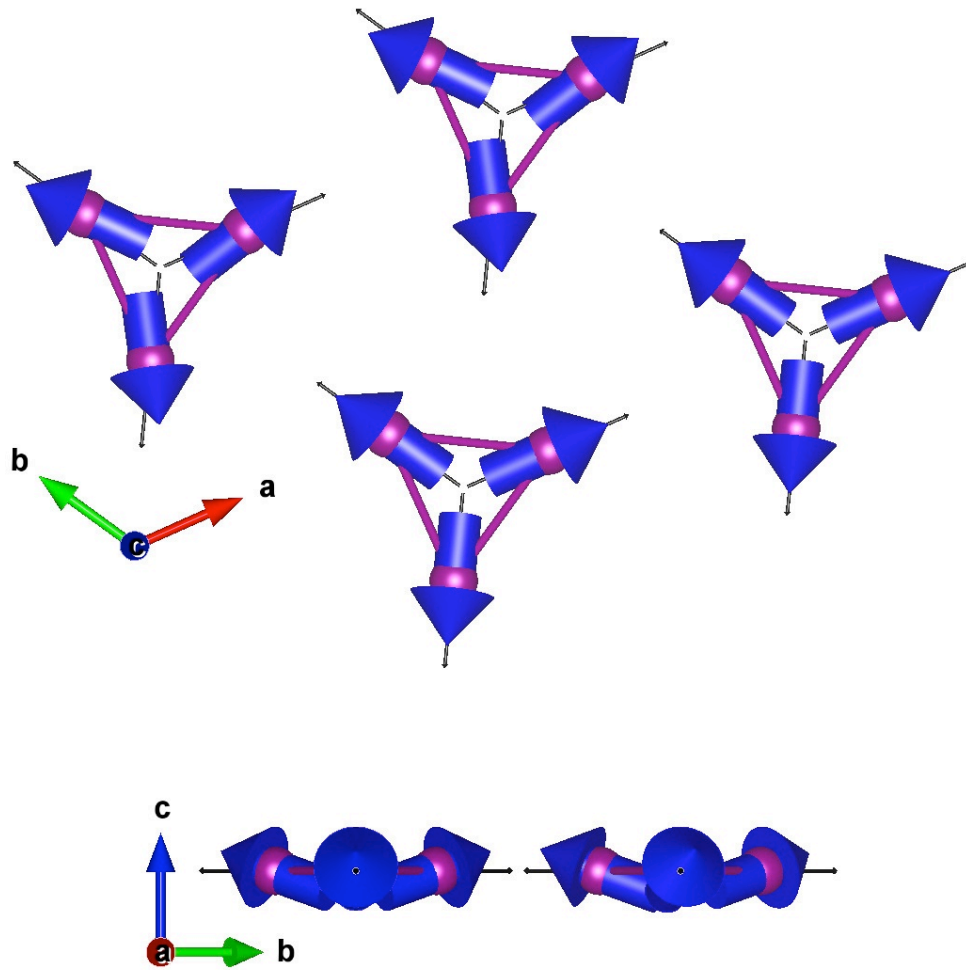


FIGURE 4.24: A possible mechanism for multiferroicity can result from a slight torsion of the trimer moments between neighbouring trimers along one direction within the plane (chosen as the  $b$ -axis here). Moment canting out of the plane would result in a ferromagnetic component along the  $c$ -axis. These can all be induced by the Dzyaloshinskii-Moriya interaction, which is known to heavily influence the magnetic structures in other langasites.

arises from the nonequivalence of the Mn atoms within each trimer in the supercell? Or perhaps it is due to the altering of the exchange pathways through the substitution of  $Nb^{5+}$  and  $Si^{4+}$  for  $Te^{6+}$  and  $P^{5+}$ . It is also possible that a more exotic mechanism of trimer-molecular orbital interactions could alter the propagation vector, on account of the nonequivalence of the trimers themselves within the supercell (seven as opposed to one in the subcell).

Finally, it was mentioned in Chapter 3 that the langasites are good piezoelectrics: that is, an electric polarization can arise in response to an applied mechanical stress resulting from a deformation of its noncentrosymmetric crystal structure. For trigonal crystal structures, a deformation along  $a$ -axis will lead to polarization that can be directed along either the  $a$  or  $c$ -axes [130]. This polarization can be further enhanced by the so-called “flexoelectric” effect where strain gradients can induce (or flip) polarization in an already ferroelectric material (the flexoelectric effect can occur in materials with any symmetry, but the study of flexoelectricity is a relatively new avenue of research in general) [130–132, 158]. It is not difficult to imagine such mechanisms at play in  $Pb_3TeMn_3P_2O_{14}$  considering the already enormous impact of  $Pb^{2+}$  lone pairs and the divalent  $3f$  cation on the crystal structure; the Dzyaloshinskii-Moriya interaction may induce further stresses within this material that could also be responsible for the observed effects. It would be interesting to conduct experiments to probe the local structure, such as pair distribution function analysis or NMR, that might indicate such effect on the structure below  $T_N$ .  $^{93}Nb$  NMR on  $Ba_3NbFe_3Si_2O_{14}$  already shows a broad distribution of environments developing below  $T_N$ , but this could easily be due to the onset of magnetic order rather than structural deformations [94].

## 4.5 Conclusion

$Pb_3TeMn_3P_2O_{14}$  powder was prepared via a standard solid state reaction. A new and previously unsolved supercell was reported for this material that appears to be unique

within the langasite family and lends some insight into the mechanism behind such supercell distortions present in other dugganites [99, 145]. DC susceptibility was performed at fields up to 35 T and it was found that a possible phase transition occurs at 3 T near 6.25 K. This finding is consistent with the temperature and field dependence of the peak in the dielectric constant, indicating weak magnetoelectric coupling in this material. The low temperature magnetic structure was solved with respect to both the supercell and subcell. Finally, the mechanism for potential multiferroicity in this material was discussed with reference to other multiferroic langasites such as  $Ba_3NbFe_3Si_2O_{14}$ .

## Chapter 5

# Magnetic phase diagram and spin dynamics in $\text{Pb}_3\text{TeCo}_3\text{P}_2\text{O}_{14}$

### 5.1 Introduction

So far, this work has focused only on langasites with  $S=5/2$  magnetic ions occupying the  $3f$  site. For a long time, replacing  $\text{Fe}^{3+}$  with another paramagnetic  $3d$  cation was not thought possible; until 2009 langasites had only been prepared using diamagnetic or  $\text{Fe}^{3+}$  ions on the  $3f$  site. B. V. Mill [108] reported the preparation of dozens of other Te-containing langasites wherein other paramagnetic ions such as divalent Co, Cu, Ni, and Mn could be placed in the trimer site with negligible site mixing. In the previous chapter,  $\text{Pb}_3\text{TeMn}_3\text{P}_2\text{O}_{14}$  was extensively discussed. In particular, it was found that a large  $P3$  supercell results from active  $\text{Pb}^{2+}$  lone pairs and strains imposed by the large  $\text{Mn}^{2+}$  cation. Despite this, the magnetism is largely consistent with  $\text{Ba}_3\text{NbFe}_3\text{Si}_2\text{O}_{14}$  with weaker exchange: magnetoelectric coupling and a large magnetic incommensurate spiral structure propagating predominately along  $c$  are observed in both.

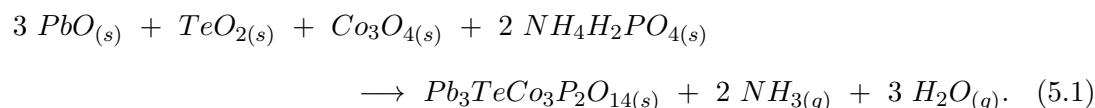
In this chapter the following question is asked: what happens to the system when  $S$  is no longer equal to  $5/2$ ?  $\text{Co}^{2+}$  is only  $0.02 \text{ \AA}$  smaller than  $\text{Mn}^{2+}$  in tetrahedral coordination [95] and, like the  $S=5/2$  ion, should not be subject to strong Jahn-Teller distortions

in this environment. And yet, it is shown that the superstructure and magnetic unit cells observed here are remarkably different than  $Pb_3TeMn_3P_2O_{14}$ . In particular, the magnetic unit cell becomes commensurate with the supercell and does not propagate in a helical spiral. The  $Co^{2+}$  dugganites have received comparatively more attention in the literature than the other dugganites most likely because they are the easiest of the magnetic species to prepare phase pure. Here, the preparation, physical property measurements, refinements and inelastic neutron scattering spectra are presented on powder  $Pb_3TeCo_3P_2O_{14}$ .

## 5.2 Methods

### 5.2.1 Preparation

Just as with the other langasites, this material was prepared via standard solid-state reaction. Stoichiometric amounts of  $PbO$ ,  $TeO_2$ ,  $Co_3O_4$ , and  $NH_4H_2PO_4$  were combined and ground for 15 min by hand for every gram of sample. The powder was then pelleted using a hydrostatic rod press at 40 MPa, placed in an alumina crucible with a lid, and reacted in  $O_2$  at 650 °C for 12 hrs. The final powder product appears immediately with the presence of some minor unidentified impurities. An annealing step was performed at 600 °C for over 240 hrs with intermittent mixing and pelleting following the initial sintering step. The overall reaction equation is:



Unlike  $Pb_3TeMn_3P_2O_{14}$ , a pre-reaction step is not strictly required (a pre-reaction step was introduced for other batches where loose powder was reacted at 400 °C for 6 hrs, but this did little to help the phase purity of the final product). In fact, the Co-dugganite main phase forms much more quickly and at much lower temperatures than

most dugganites and langasites. Perhaps this is not surprising; while it is thought that  $Te^{6+}$  plays a large role in effectively forcing other cations to occupy the tetrahedral  $3f$  site as opposed to the octahedral  $1a$  site, the electronic configuration of  $Co^{2+}$  may actually make the  $3f$  site *more* stable anyway due to the absence of a competing low-spin structure (Figure 5.1). For  $Mn^{2+}$  there is no immediately apparent advantage for selecting the distorted tetrahedral site over the octahedral site when considering Jahn-Teller distortion effects. It would be interesting to see if  $Te^{6+}$  can be substituted for another hexavalent *and* similarly sized ion such as  $Mo^{6+}$ . However, unlike  $Te^{6+}$ ,  $Mo^{6+}$  can be found in tetrahedral coordination with oxygen empirically in extended solids such as  $Rb_2Cu_2(MoO_4)_3$  [159], and even more commonly as an oxoanion  $MoO_4^{2-}$ .

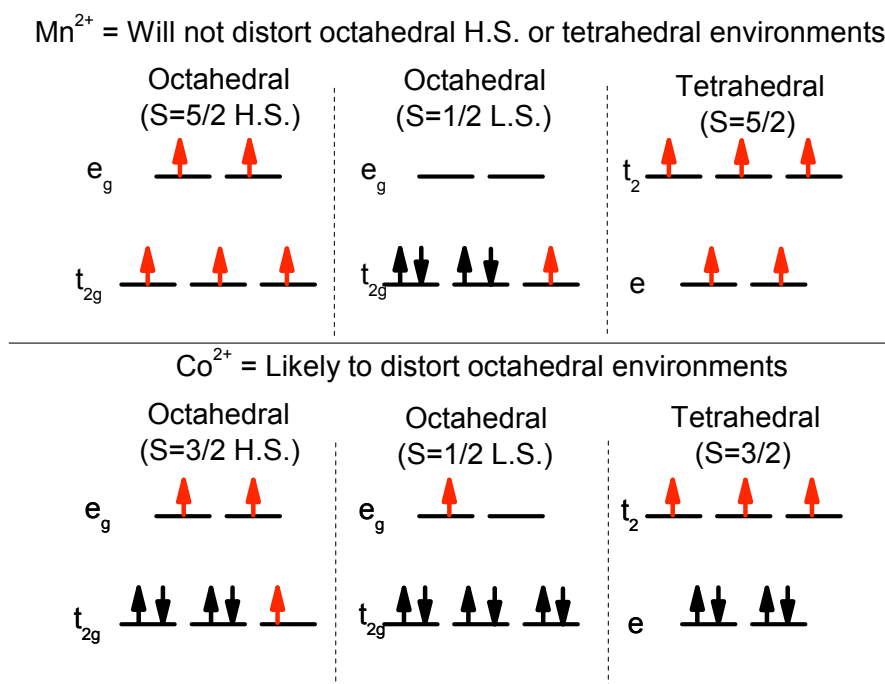


FIGURE 5.1: Different possible electronic environments for  $Co^{2+}$  and  $Mn^{2+}$  within the langasite unit cell. Red arrows are unpaired electrons while black arrows are paired. Note that these are for “ideal” polyhedra. In the langasite the octahedral site is quite ideal while the tetrahedral site is more distorted.



### 5.2.2 Diffraction

Phase purity was checked using a Siemens D5000 diffractometer with Cu  $K\alpha$  anode in Bragg-Brentano geometry with 0.2; 0.6; 0.6; 1 mm slits. Within the resolution of this instrument, the material appears phase pure with no supercell peaks or impurities. Neutron diffraction was performed using the POWGEN instrument (SNS, Oak Ridge, TN) using six grams of sample loaded into a vanadium sample can with dimensions 8 mm diameter by 5.7 cm height. The slit height was set at 35 mm while the width was set at 10 mm so as to optimize the signal at the detector. Banks with centring wavelengths of 1.333 and 4.797 Å were used, which covers a d-space range of approximately 0.8 to 13 Å. Measurements were taken at  $T = [2, 20]$  K in 2 K steps followed by measurements at 40, 80, 150, 200, and 250 K using a standard ILL Orange Cryostat. All measurements were taken upon warming from base temperature and the sample was allowed to equilibrate with the temperature before taking each measurement. Data was collected for one hour at each temperature per detector bank. High resolution diffraction measurements were performed on the 11-BM line [53] at the APS (Argonne, IL) using the same procedure mentioned previously in Chapter 4. Finally, neutron diffraction measurements were performed on the WISH diffractometer (ISIS, Oxford, UK) [160] using the same sample measured with POWGEN. WISH is a diffractometer optimized to collect unpolarized magnetic powder diffraction data in the large d-space region where the magnetic form factor is highest (up to  $d = [0.7, 50]$  Å with the option for high resolution up to 17 Å). For this experiment, five banks of data covering the entire d-spacing range were collected, counting for two hours at each temperature (sample temperature used POWGEN) using a He closed-cycle refrigerator. All measurements were taken on a warming cycle.

### 5.2.3 Physical property measurements

DC susceptibility was measured using the Vibrating Sample Magnetometer (VSM) option on a Physical Property Measurement System (Quantum Design) on a 36 mg sample of pelleted polycrystalline  $Pb_3TeCo_3P_2O_{14}$ . Measurements were performed between 0.1 and 1 T over 0.25 T intervals, and from 1 through 9 T in 1 T intervals. High-field

DC magnetization up to 35 T was performed on an in-house VSM equipped with a He cryostat at the NHMFL (Tallahassee, FL) using a 155 mg sample at 1.5, 3, 4, 5.5, 7, 8.5, 10, 11.5, 12, 12.5, 13, 13.5, 14, 20, 50, 100 and 200 K using a ramp-rate of 0.01 T/second. Only positive fields were used at each temperature. Heat capacity was performed placing an 11.4 mg sample on a sample stage and fixed in place using Apiezon-N grease (sample stage is part of a puck fixture from Quantum Design). The heat capacities of the grease and sample stage were measured before the sample. Heat capacity was measured between 2 and 30 K under zero-field and fields of 0.05, 0.1, 0.5, 1, 3, 4, 5, 7, and 9 T.  $Pb_3TeZn_3P_2O_{14}$  was used as a lattice standard and was prepared using the same method reported in Chapter 3.

#### 5.2.4 Refinement

Before describing the refinement process, it must be noted that these diffraction experiments were performed in conjunction with those of  $Pb_3TeMn_3P_2O_{14}$  and  $Pb_3TeCo_3V_2O_{14}$  before the discovery of any supercell. Refinements were first performed using joint x-ray diffraction and POWGEN neutron diffraction at room temperature using the  $P321$  subcell and the FullProf Suite [150]. Additional measurements were performed using neutrons only at low temperatures in an effort to find the magnetic structure. However, unlike  $Pb_3TeCo_3V_2O_{14}$  and  $Pb_3TeMn_3P_2O_{14}$  where the magnetic structures can be mostly described using the subcell, the magnetic peaks in  $Pb_3TeCo_3P_2O_{14}$  could not be indexed to any one propagation vector (a symmetry-allowed exhaustive search was performed using SARAh Representational Analysis and SARAh Refine [67–70] as shown in Figure 5.2). This prompted an investigation using the WISH diffractometer at ISIS. It became immediately clear that the  $P321$  structure was the wrong model because many magnetic peaks began to form on top of what were, at first, thought to be impurities.

High resolution synchrotron x-ray diffraction was employed to resolve these superlattice peaks in an effort to index the supercell. The GSAS-II program was implemented for

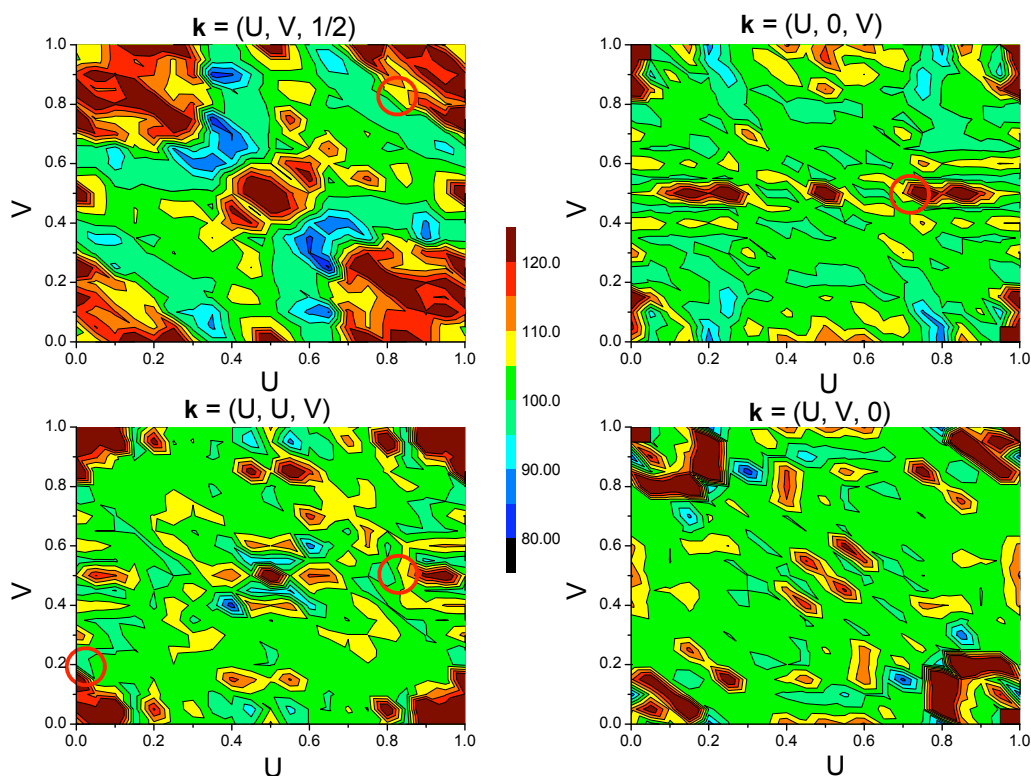


FIGURE 5.2: These contour plot shows the results of a symmetry exhaustive search of the magnetic propagation vector using FullProf and SARAh Refine. The colour represents  $\chi^2$  of the individual refinements. The lower the  $\chi^2$ , the more likely the propagation vector is correct. Regions circled in red represent known propagation vectors for other langasites with respect to the same  $P321$  space group.

this purpose as it was designed specifically (but not exclusively) for use with data collected at 11-BM [152]. The refinement began by indexing the cell to a large monoclinic, but metrically orthorhombic supercell. The subcell atomic coordinates  $(x, y, z)$  were transformed to their supercell coordinates  $(x', y', z')$  using the transformation matrix  $(1, 3, 0) (-1, 3, 0) (0, 0, 1)$ . At this point, it has been suggested that the most probable space group for a phase transformation out of the langasite subcell is to either the  $P3$  or  $C2$  space group [110]. However, the systematic absences for  $C2$  are not consistent with the observed intensities in the x-ray data (Figure 5.3). Next, in a process similar to that reported by Krizan *et al.* [99] and in Chapter 4, rigid bodies were defined for  $TeO_6$  and  $PO_4$  isolated polyhedra. Te-O distances were kept fixed to their subcell value found

through a joint x-ray/neutron refinement (about 1.92 Å) while P-O distances were defined in accordance with the phosphates proper model [153]. Using only the x-ray data, the positions of the cations were first allowed to refine in order to place some intensity on the superlattice reflections. Like any Rietveld refinement program, FullProf cannot refine the lattice parameters of the supercell effectively without first placing intensity on some of the satellite reflections. The lattice parameters were allowed to refine which helped to reach convergence. The final lattice parameters are  $a = 14.4885(11)$  Å,  $b = 25.10414(18)$  Å,  $c = 5.22052(1)$  Å and  $\beta = 90.013(1)^\circ$  which agrees well with other reported values [99]. Rather than being due to oxygen deficiencies, the small disagreement with these values and those reported in the literature is likely due to the different temperatures at which both refinements were performed.

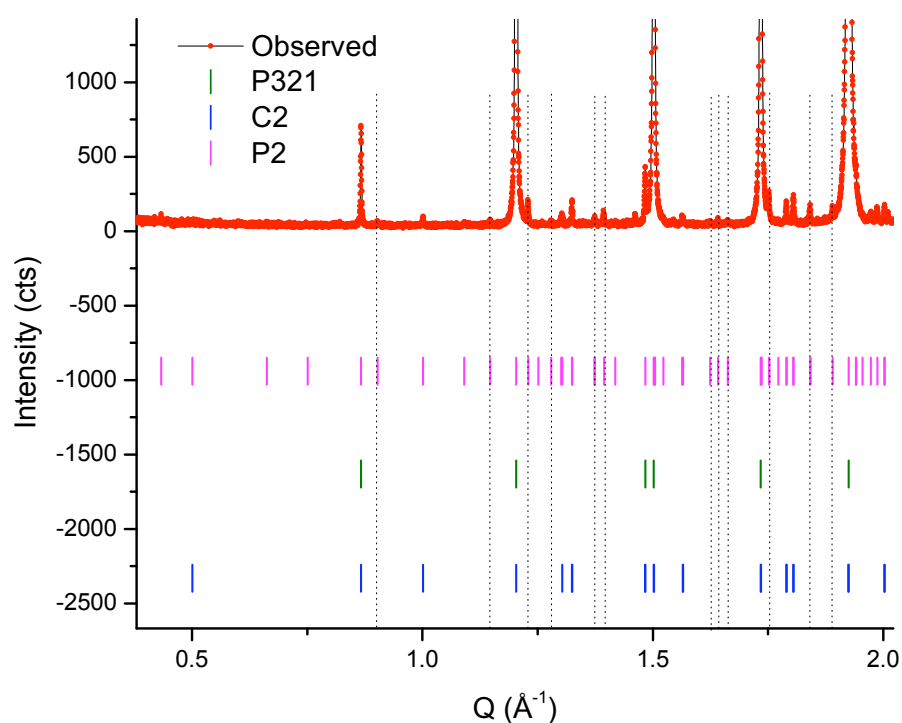


FIGURE 5.3:  $P2$  can account for all of the observed reflections. Dotted lines are guides to the eye.

Next, the model was co-refined against the x-ray and neutron data from POWGEN. The 12 rigid bodies were all allowed to rotate within their defined positions (phosphate rigid body groups were allowed to displace since both P and O have large coherent scattering and low incoherent and absorption cross sections). Once converged, the rigid body option was shut off and all atomic coordinates, lattice parameters, peak shape parameters, and background coefficients were allowed to refine. Soft distance constraints were used to force the refinement of the atomic coordinates along certain directions: P-O and Te-O distances were constrained to be near the value used for the rigid body refinement while Co-O distances were constrained to be  $2.0(1)$  Å. Additional constraints for Pb6 and Pb5 were used as extra assurance. The final refinement is shown in Figure 5.4 with the atomic coordinates listed in Tables 5.1 through 5.3.

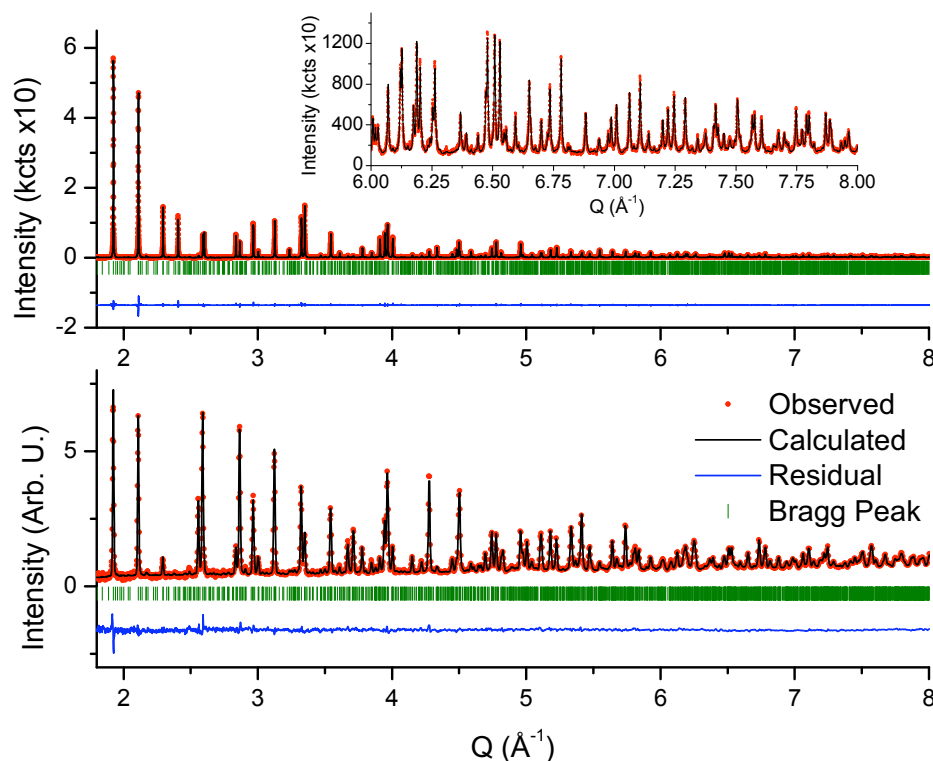


FIGURE 5.4: Final refinement of  $Pb_3TeCo_3P_2O_{14}$  using both x-ray (top) and neutron diffraction data (bottom) at 300 K. The inset shows the x-ray high  $Q$  data in more detail.

TABLE 5.1: Refined atomic coordinates for  $Pb_3TeCo_3P_2O_{14}$  in the  $P2$  supercell with lattice constants  $a = 14.48885(11)$  Å,  $b = 25.10414(18)$  Å,  $c = 5.22052(1)$  Å, and  $\beta = 90.013(1)^\circ$  at 300 K. A single overall isotropic thermal parameter ( $B_{iso} = 0.72$  Å<sup>2</sup>) was used in the refinement as it lead to more stable and reliable atomic coordinates. Final residuals were  $R_p = 8.27$ ,  $R_{wp} = 11.4$  and  $\chi^2 = 2.73$  for the x-ray pattern and  $R_p = 11.6$ ,  $R_{wp} = 7.39$  and  $\chi^2 = 4.01$  for neutron data (agreement factors corrected for background counts).

Ion	Site	x	y	z
Pb1	2e	0.2937(7)	0.0967(3)	-0.002(2)
Pb2	2e	0.8103(3)	0.2601(3)	-0.002(2)
Pb3	2e	0.2950(5)	0.4226(4)	-0.020(1)
Pb4	2e	0.8007(6)	0.5955(3)	0.000(2)
Pb5	2e	0.2959(5)	0.7599(4)	-0.002(2)
Pb6	2e	0.7839(3)	0.9286(4)	0.000(1)
Pb7	1a	0	0.1294(4)	0
Pb8	1c	$\frac{1}{2}$	0.3025(5)	0
Pb9	1a	0	0.4655(5)	0
Pb10	1c	$\frac{1}{2}$	0.6281(4)	0
Pb11	1a	0	0.8016(5)	0
Pb12	1c	$\frac{1}{2}$	0.9676(5)	0
Te1	1a	0	0.9930(4)	0
O1	2e	0.101(2)	0.980(1)	0.235(5)
O2	2e	0.962(2)	0.049(1)	0.231(6)
O3	2e	0.935(2)	0.943(1)	0.218(6)
Te2	1c	$\frac{1}{2}$	0.1660(5)	0
O4	2e	0.611(2)	0.166(2)	0.208(6)
O5	2e	0.458(2)	0.224(1)	0.211(6)
O6	2e	0.436(2)	0.120(2)	0.228(6)
Te3	1a	0	0.3362(5)	0
O7	2e	0.106(2)	0.325(1)	0.219(6)
O8	2e	-0.059(2)	0.392(1)	0.192(5)
O9	2e	-0.066(2)	0.286(1)	0.216(6)
Te4	1c	$\frac{1}{2}$	0.4905(4)	0
O10	2e	0.615(2)	0.491(2)	0.200(6)
O11	2e	0.442(2)	0.5504(9)	0.175(5)
O12	2e	0.428(2)	0.437(1)	0.189(5)

TABLE 5.2: Continued....

Ion	Site	x	y	z
Te5	1a	0	0.6695(5)	0
O13	2e	0.105(2)	0.654(1)	0.219(6)
O14	2e	-0.048(2)	0.725(1)	0.221(6)
O15	2e	-0.061(2)	0.617(1)	0.220(7)
Te6	1c	$\frac{1}{2}$	0.8309(5)	0
O16	2e	0.608(2)	0.828(2)	0.207(6)
O17	2e	0.449(2)	0.888(1)	0.199(6)
O18	2e	0.440(2)	0.781(1)	0.217(6)
Co1	2e	0.1251(9)	0.0322(6)	0.493(4)
Co2	2e	0.625(1)	0.2064(4)	0.515(3)
Co3	2e	0.1385(9)	0.3733(6)	0.512(4)
Co4	2e	0.6184(9)	0.5379(6)	0.500(4)
Co5	2e	0.1300(9)	0.7023(6)	0.502(4)
Co6	2e	0.6234(6)	0.8727(6)	0.503(4)
Co7	1b	0	0.2498(9)	$\frac{1}{2}$
Co8	1d	$\frac{1}{2}$	0.4223(8)	$\frac{1}{2}$
Co9	1b	0	0.5754(9)	$\frac{1}{2}$
Co10	1d	$\frac{1}{2}$	0.7498(9)	$\frac{1}{2}$
Co11	1b	0	0.9076(9)	$\frac{1}{2}$
Co12	1d	$\frac{1}{2}$	0.0874(8)	$\frac{1}{2}$
P1	2e	0.168(1)	0.1616(6)	0.463(2)
O19	2e	0.262(2)	0.173(2)	0.343(6)
O20	2e	0.099(2)	0.203(1)	0.345(6)
O21	2e	0.140(3)	0.1058(7)	0.363(6)
O22	2e	0.168(3)	0.164(2)	0.757(2)
P2	2e	0.658(1)	0.3276(6)	0.458(2)
O23	2e	0.754(2)	0.335(2)	0.316(5)
O24	2e	0.599(2)	0.375(1)	0.345(6)
O25	2e	0.622(3)	0.2752(8)	0.335(6)
O26	2e	0.658(2)	0.335(2)	0.751(2)

TABLE 5.3: Continued....

Ion	Site	x	y	z
P3	2e	0.174(1)	0.4954(6)	0.449(2)
O27	2e	0.266(1)	0.5142(15)	0.317(5)
O28	2e	0.118(2)	0.546(1)	0.368(7)
O29	2e	0.131(2)	0.4450(8)	0.330(6)
O30	2e	0.171(3)	0.499(2)	0.744(2)
P4	2e	0.659(1)	0.6648(6)	0.449(2)
O31	2e	0.759(1)	0.671(2)	0.338(7)
O32	2e	0.600(2)	0.708(1)	0.326(6)
O33	2e	0.631(3)	0.6095(8)	0.349(7)
O34	2e	0.660(3)	0.665(2)	0.743(2)
P5	2e	0.1733(8)	0.8285(3)	0.466(2)
O35	2e	0.2426(7)	0.8742(7)	0.417(6)
O36	2e	0.120(2)	0.876(1)	0.365(6)
O37	2e	0.173(2)	0.7723(5)	0.348(5)
O38	2e	0.146(2)	0.821(2)	0.748(3)
P6	2e	0.658(1)	-0.0019(5)	0.476(2)
O39	2e	0.738(1)	0.039(1)	0.412(6)
O40	2e	0.609(2)	0.046(1)	0.352(6)
O41	2e	0.648(2)	-0.0562(7)	0.345(6)
O42	6g	0.665(3)	0.000(2)	0.769(2)

Low temperature refinements of the crystal and magnetic structure were carried out over four of the five banks available on WISH at 20 K (the unused bank is the long wavelength bank and had only three visible reflections at such low values of Q). Two lone peaks were visible at all temperatures that could not be indexed to the supercell and were not visible in either the POWGEN or 11-BM data. Even though it is likely that these peaks are instrumental, efforts were still taken to investigate their origin. In one study, it was suggested that  $PO_4$  rattling within the framework of the rest of the structure is present as disorder that could actually represent an even larger supercell



[99]. These peaks are less likely to be observed using x-rays and may have been missed in the POWGEN data because they appear at such low  $Q$  (0.72 and 0.77  $\text{\AA}^{-1}$ ). A refinement of the cell devoid of any symmetry ( $P1$  space group) was tried to see if these peaks could be indexed. A Le Bail fit [151] also failed to index the peaks. Initially, only the lattice parameters and peak shapes were refined, which already fit the data quite well. The atomic coordinates were assumed to be mostly unchanged. They were checked against the atomic coordinates found by Krizan *et al.* [99] since those were found using a thermal average of data sets at lower temperatures (although their atomic coordinates are for a supercell with opposite chirality). Both sets visually agree quite well as shown in Figure 5.5. Some  $TeO_6$  and  $PO_4$  polyhedra look considerably more distorted in the model found here, but these distortions noticeably improved the quality of fit and are still within reasonable chemical constraints. The differences between the models most likely stem from how the data sets were collected and treated.

Magnetic reflections were observed below 12.5 K and increase in intensity until around 7 K where they reach a maximum. All the magnetic reflections could be indexed using the little group  $G_x$  formed by the propagation vector  $\vec{k} = (\frac{1}{2}, 0, -\frac{1}{2})$  and the space group  $P2$ . This results in two IRs that are described in Table 5.4. Both IRs fit the data nicely; if one were to consider the ideal subcell atomic coordinates, both magnetic structures are degenerate and differ by a displacement of 0.5 along the supercell  $a$ -axis. The real atomic coordinates may lift this degeneracy though (more on this later). Without single crystals, it cannot be determined which IR is correct since their powder diffraction patterns are identical. The magnetic structures will be discussed in more detail in the results section.

### 5.2.5 Inelastic neutron scattering

Inelastic neutron scattering was performed on SEQUOIA [79, 80] at the SNS using 6.5 g of powder  $Pb_3TeCo_3P_2O_{14}$  loaded onto an aluminum flat plate empty sample can, wrapped in aluminum foil, and sealed with indium wire. Helium exchange gas was loaded

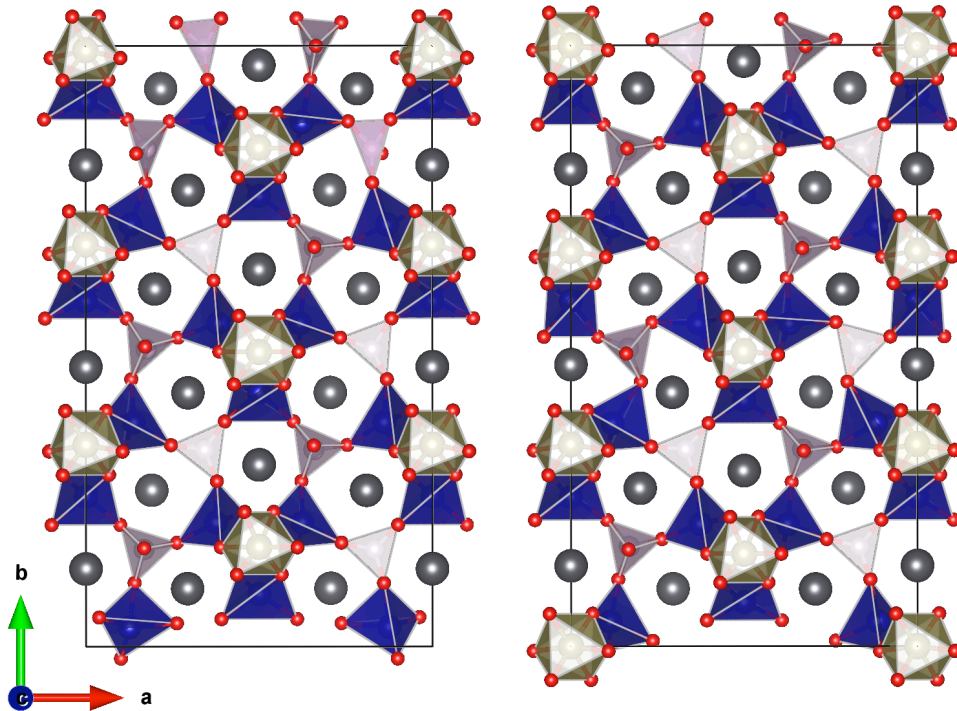


FIGURE 5.5: A comparison of the supercell found here (left) and the one found by Krizan *et al.* [99] (right) visually shows good agreement. Pb,  $TeO_6$ ,  $CoO_4$ ,  $PO_4$  are represented by grey spheres, gold octahedra, blue tetrahedra, and lilac tetrahedra respectively. A transformation of the cell found here was performed such that both structures are shown in the same enantiomer.

into the can. A standard ILL Orange cryostat was used to observe excitations at low energies (although SEQUOIA is typically designed for observing magnetic excitations that are higher in energy, it is capable of reaching 8 meV reliably within a resolution limit of about 4% of the incident energy (0.24 meV)).

## 5.3 Results and Discussion

### 5.3.1 Crystal structure

$Pb_3TeCo_3P_2O_{14}$  and  $Pb_3TeMn_3P_2O_{14}$  both share the same langasite subcell except the Co-dugganite is compressed along its  $c$ -axis compared to the Mn-dugganite. However, the supercell distortion is vastly different between these materials (Figure 5.6). Whereas

TABLE 5.4: Refined magnetic structures of  $Pb_3TeCo_3P_2O_{14}$  using the two IRs belonging to the little group  $G_x$  defined by the space group and propagation vector  $\vec{k} = (\frac{1}{2}, 0, -\frac{1}{2})$ . Refinement details are described in the text. For Co ions in general sites, magnetic symmetry operators for sites 1 (x, y, z) and 2 (-x, y, -z) are (U, V, W) and (-U, V, -W) for  $\Gamma(1)$ , and (U, V, W) and (U, -V, W) for  $\Gamma(2)$  respectively.

Ion	$\Gamma(1)$				$\Gamma(2)$			
	$\psi(1)$	$\psi(2)$	$\psi(3)$	m ( $\mu_B$ )	$\psi(1)$	$\psi(2)$	$\psi(3)$	m ( $\mu_B$ )
Co1	(1, 0, 0)	(0, 1, 0)	(0, 0, 1)	3.0	(1, 0, 0)	(0, 1, 0)	(0, 0, 1)	2.90(4)
Co2	(1, 0, 0)	(0, 1, 0)	(0, 0, 1)	2.90(2)	(1, 0, 0)	(0, 1, 0)	(0, 0, 1)	2.94(2)
Co3	(1, 0, 0)	(0, 1, 0)	(0, 0, 1)	3.0	(1, 0, 0)	(0, 1, 0)	(0, 0, 1)	2.90(4)
Co4	(1, 0, 0)	(0, 1, 0)	(0, 0, 1)	2.90(2)	(1, 0, 0)	(0, 1, 0)	(0, 0, 1)	2.94(2)
Co5	(1, 0, 0)	(0, 1, 0)	(0, 0, 1)	3.0	(1, 0, 0)	(0, 1, 0)	(0, 0, 1)	2.90(4)
Co6	(1, 0, 0)	(0, 1, 0)	(0, 0, 1)	2.90(2)	(1, 0, 0)	(0, 1, 0)	(0, 0, 1)	2.94(2)
Co7	(2, 0, 0)	(0, 0, 2)		3.0	(0, 2, 0)			2.90(1)
Co8	(0, 2, 0)			2.90(4)	(2, 0, 0)	(0, 0, 2)		2.91(3)
Co9	(2, 0, 0)	(0, 0, 2)		3.0	(0, 2, 0)			2.90(1)
Co10	(0, 2, 0)			2.90(4)	(2, 0, 0)	(0, 0, 2)		2.91(3)
Co11	(2, 0, 0)	(0, 0, 2)		3.0	(0, 2, 0)			2.90(1)
Co12	(0, 2, 0)			2.90(4)	(2, 0, 0)	(0, 0, 2)		2.91(3)

the Mn-dugganite loses its 2-fold symmetry and retains its 3-fold symmetry, the Co-dugganite does exactly the opposite, distorting into a large monoclinic (almost metrically orthorhombic) supercell that has approximately six times the volume of the subcell. Despite being a smaller cell, the space group here is almost devoid of any symmetry; there are now 78 unique atomic sites within the supercell. This distortion is quite striking considering that Mn and Co only differ in size by 0.02 Å, suggesting that the distortion may in fact be due to electronic differences between the ions.

The supercell is characterized mainly by Pb translation and  $PO_4$  rigid body rotations. However, distortions were found near the middle of the unit cell for  $Te_4O_6$  and  $P_3O_4$  rigid bodies (the rigid bodies of the fourth Te and third P). What is most important here is how the shape of the Co trimers changes from perfectly equilateral symmetry to

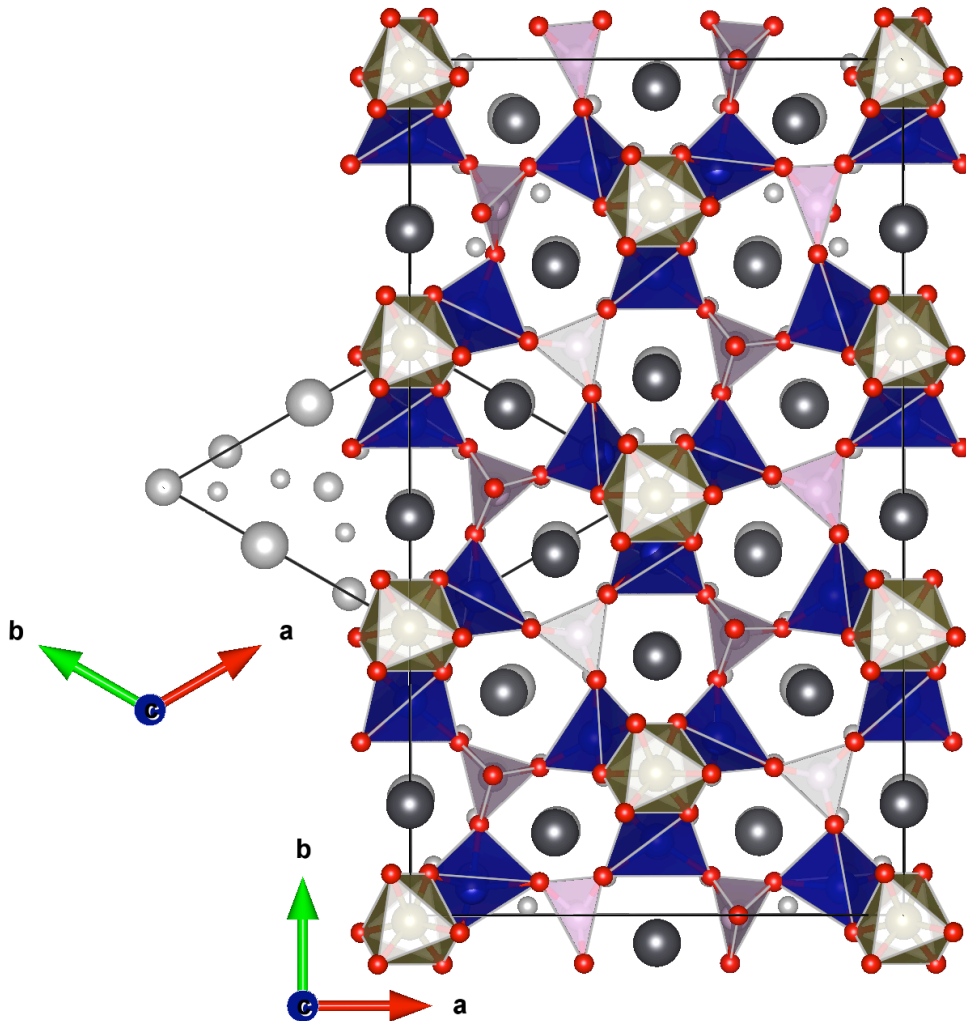


FIGURE 5.6: The relationship between the  $P321$  subcell and  $P2$  supercell. This figure has been adapted from [99] and the colour scheme is the same as in Figure 5.5. The ideal langasite atomic coordinates have been shaded grey as a guide to the eye.

isosceles symmetry [145] (Figure 5.7). This can have immensely important consequences on the behaviour of the magnetism within this system; unlike  $Pb_3TeMn_3P_2O_{14}$  where all of the trimers were nearly equilateral and mostly unchanged from their subcell form, trimers with isosceles symmetry split the intratrimer exchange interaction into single and doubly degenerate interactions  $J$  and  $2J' = 2\alpha J$ . A full investigation of the exchange pathways in this material is beyond the scope of this thesis, but would be welcomed in the future.

Krizan *et al.* solved independently the supercell of  $Pb_3TeCo_3P_2O_{14}$  using both x-ray

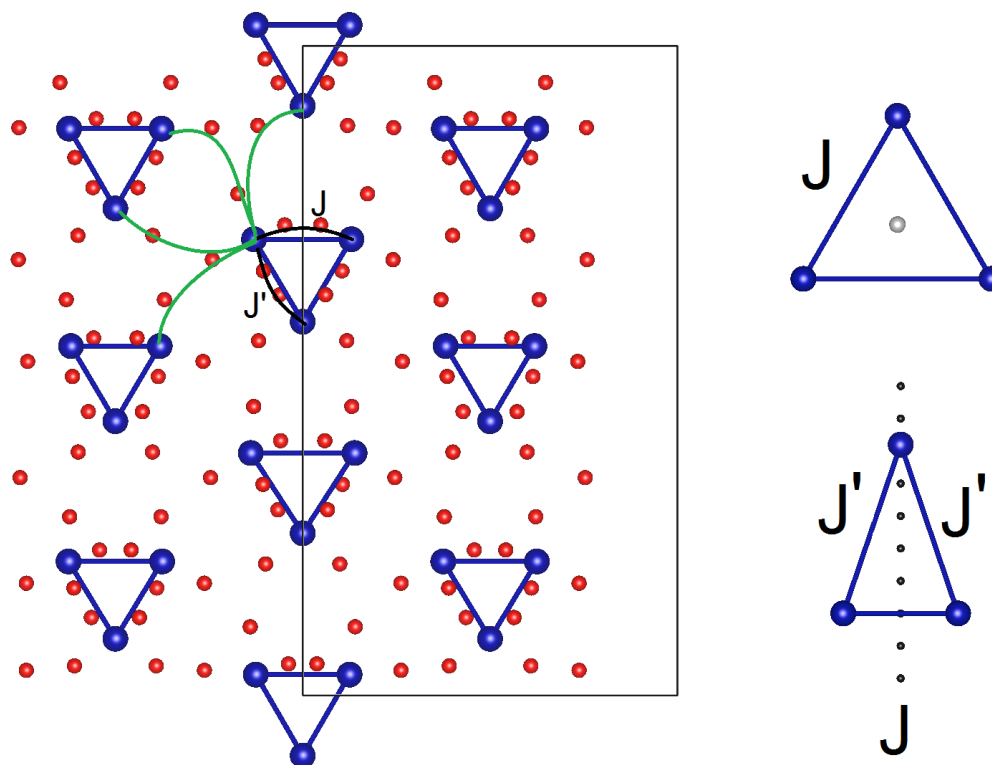


FIGURE 5.7:  $P2$  makes all of the trimers isosceles instead of equilateral. This introduces an extra intratrimer exchange term that is absent in the ideal subcell. The exchange pathways are labelled in black (intratrimer) and green (planar next nearest neighbour). Three additional exchange interactions also exist between Co ions in out-of-plane trimers that are not shown. Trimers on the right are ideal equilateral (upper) and isosceles (lower) with the relevant symmetries required to create them (a three-fold axis oriented out of the page and a two-fold axis of symmetry respectively).

and neutron data taken at 100 K, and additional neutron data taken at 4 K [99]. Their solution is a thermal average of what was found between these temperatures adjusting only the lattice constants. Their supercell was compared to the one found here in Figure 5.5 (a transformation into the right-handed chiral structure was made on the cell found here such that they match). Overall, the super cells are largely similar except the rigid bodies at the top and bottom of the unit cell were found to distort in opposite fashion. The reasons why this may be are unknown, but probably reflect different data collection and treatment protocols. A very nice and thorough analysis was done on  $PbO_8$  decahedra compared to  $BaO_8$  decahedra in  $Ba_3TeCo_3P_2O_{14}$ , which does not distort away from  $P321$  symmetry within instrumental resolution [99]. The main findings were that

$PbO_8$  are more distorted, as expected due to the higher polarizability of  $Pb^{2+}$  with its active lone pair. It was then theorized that  $Pb^{2+}$  lone pairs are responsible for imposing a small displacement and torque on the  $PO_4$  rigid bodies, which ultimately puts  $Pb_3TeCo_3P_2O_{14}$  over a tipping point and alters the structure. However, this cannot be the entire picture since the manner of the distortion is also highly dependent on the identity of the atom sitting in the  $3f$  site.

### 5.3.2 Physical property measurements

DC susceptibility was performed on  $Pb_3TeCo_3P_2O_{14}$ . After the first measurements which were done at 0.1 T, a sharp peak was observed near 13 K followed by a broad peak in the susceptibility at 7 K (Figure 5.8). This is in direct agreement with measurements performed by Krizan *et al.* [99] on the same material and with previous work [103, 145] on a similar material  $Pb_3TeCo_3V_2O_{14}$ . As such, it was fully expected that like  $Pb_3TeCo_3V_2O_{14}$ , this material would exhibit two antiferromagnetic transition temperatures. However, this is not the case; only the peak at 13 K resulted in magnetic order with no detectable changes occurring at 7 K (discussed in the next section). Since the broad peak was measured using three different instruments using three separate samples (the third measurement was made using a Superconducting Quantum Interference Device (SQUID) at the NHMFL and is not shown here), instrumental artefacts can be ruled out. DC susceptibility was then carried out over fields as low as 0.01 T (inset of Figure 5.8). The broad peak becomes quite sharp at low fields, broadens as the field is increased to 0.1 T, and disappears by 0.5 T. The field was then increased in 1 T steps all the way to 9 T. The peak at 13 K moves out to lower temperatures as the field is increased, but by 6 T, the peak significantly broadens and moves to lower temperatures more quickly with increasing field, indicating a possible phase transition (Figure 5.8). Figure 5.9 shows the inverse susceptibility taken at 1 T fit to the Curie-Weiss law. The effective moment was found to be  $4.45(1) \mu_B$  at all fields, which is constant with the theoretical  $Co^{2+}$  with a partially quenched orbital contribution. The Weiss temperature was found to be  $-16(4)$  K for all fits between the fields of 0.1 to 9 T. Other reported

values are closer to -30 K [99, 139], and this is likely due to differing fitting regions or small differences between sample compositions and morphologies outside of the resolution of conventional diffraction.

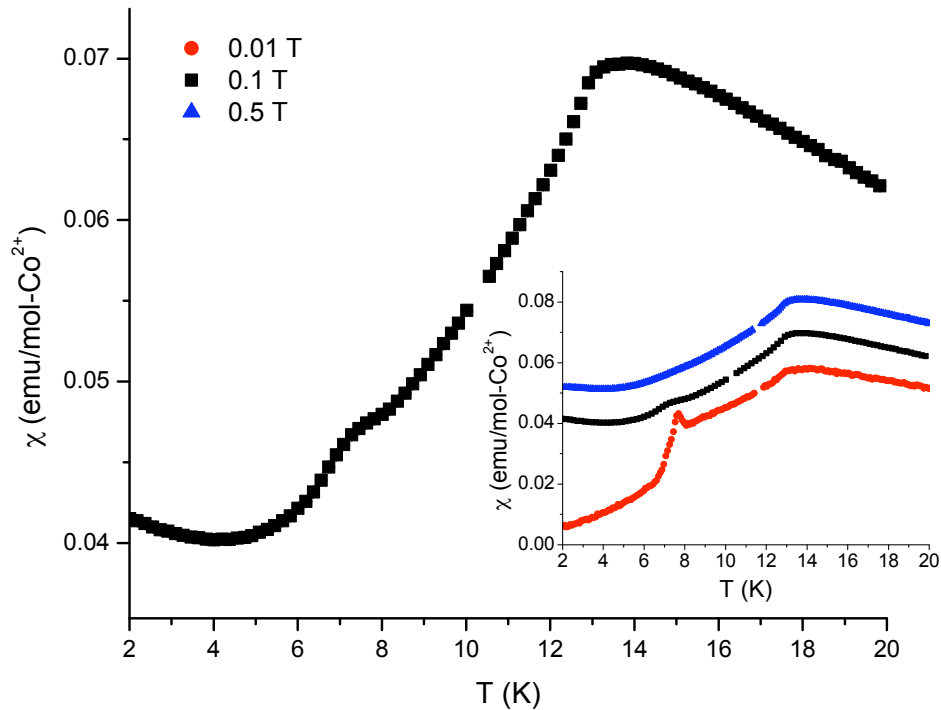


FIGURE 5.8: DC susceptibility of  $Pb_3TeCo_3P_2O_{14}$  shows two transitions near 13 and 7 K at low fields. The transition at 7 K disappears at fields above 0.5 T (inset). Measurements at different fields are offset for clarity.

Magnetization measurements up to 16 T were previously reported [99]. A phase transition was observed at 10 K around 9 T characterized by an upturn in the magnetization with accompanying hysteresis. Using the 9 T Physical Property Measurement System, the upturn is just visible at 5 K and 2 K. The magnetization curves are accompanied by weak hysteresis throughout the curve with a maximum field coercivity of nearly 10 Oe, which could be trapped flux in the 9 T magnet (Figure 5.10). But weak hysteresis of this sort has been observed in  $Ba_3NbFe_3Si_2O_{14}$  (but not isostructural  $Sr_3NbFe_3Si_2O_{14}$ ) and has been explained as being due to either grain boundaries or

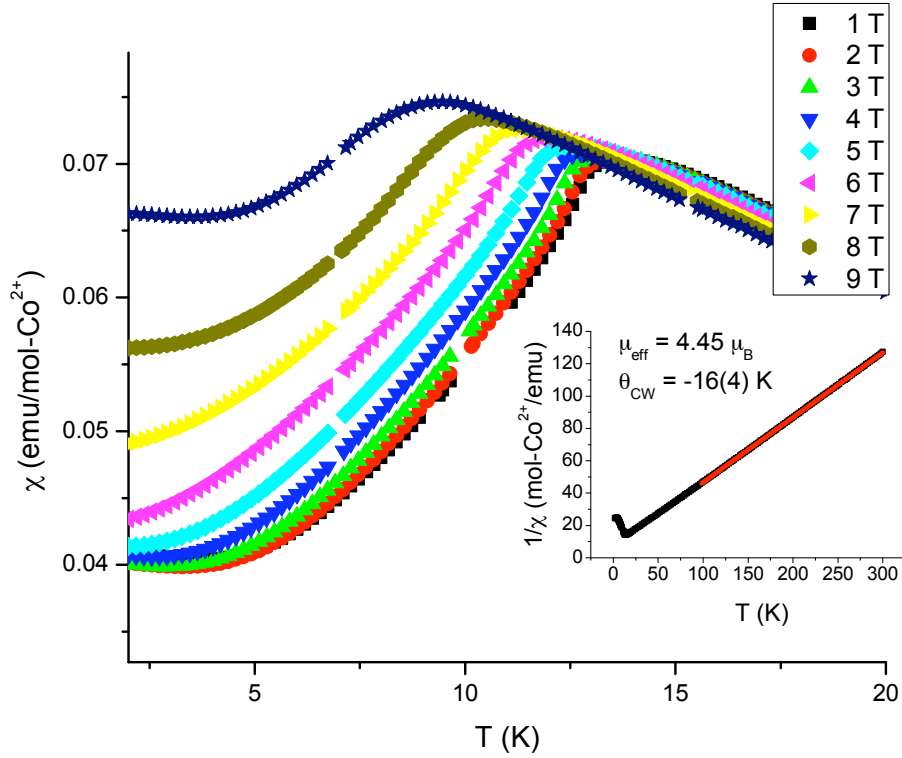


FIGURE 5.9:  $T_N$  moves out to lower temperatures as the field is increased to 9 T.  
**Inset:** Data taken at 1 T is fit to the Curie-Weiss law (red curve).

anti-site defects between Nb and Fe leading to the formation of clustered mixed magnetic states [161]. However, while anti-site defects between Nb and Fe are possible in the Fe-langasites, it is unclear why they would occur in the Ba langasite but not the Sr langasite. Furthermore, Te and Co anti-site defects are far less likely to occur since Te is only known to coordinate octahedrally with oxygen. Taking the derivative of this curve at 2 and 5 K yields two peaks indicated by local maxima near 7 and 9 T (Figure 5.11). High field magnetization measurements taken at the NHMFL found a weak temperature-dependent feature at 3 T and 2 K that was not reproducible on any other instrument. It is thought that this feature stems from the boiling of liquid He, which disrupts the VSM motor and ultimately alters the signal, although this is not known for certain. At 1.2 K, the signal appears to tend to saturation near  $3.0(5) \mu_B/\text{Co}^{2+}$  (Figure 5.12) with no other anomalies occurring beyond the phase transition at 9 T. This agrees



well with the appearance of a third magnetic phase in isostructural  $Pb_3TeCo_3V_2O_{14}$ .

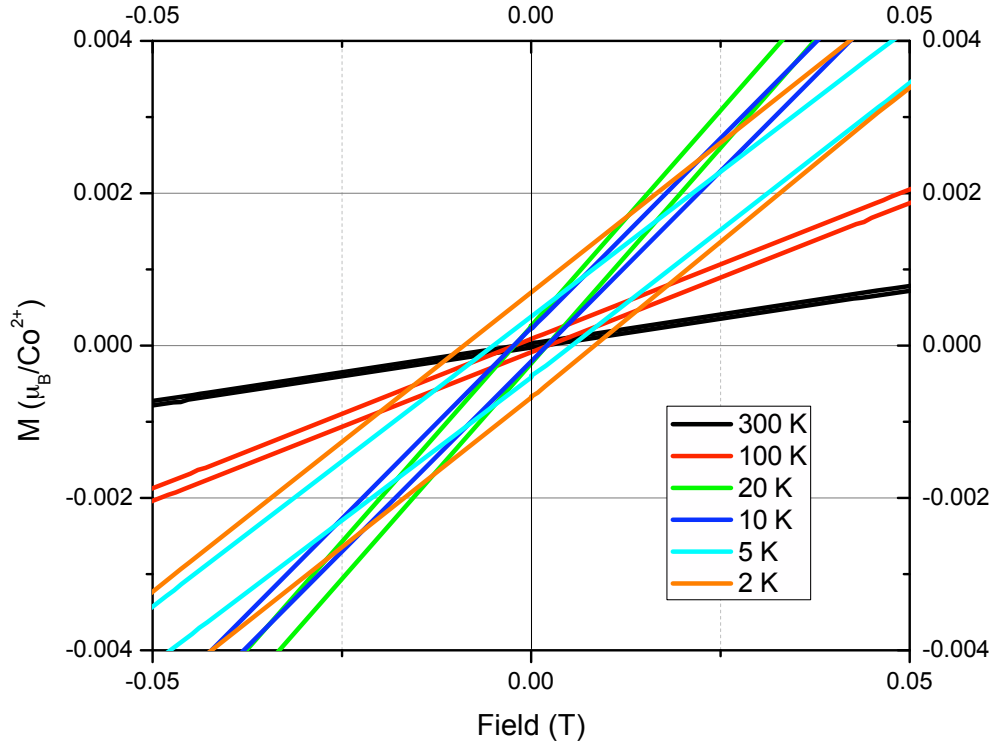


FIGURE 5.10: Low field magnetization shows small field-dependent hysteresis developing near  $T_N$  but increasing by 5 K as the temperature is lowered.

Heat capacity measurements were made to confirm the presence of these phase transitions. Unlike DC susceptibility, only one peak is observable in the heat capacity at zero-field or at 0.05 T (Figure 5.13); whatever the cause of the peak at 6 K, it contributes very little to the entropy released by this system as the temperature is lowered (Figure 5.13 right inset) although it is visible in  $C_{Res}/T$ . The entropy released by this system is 10.1 J/mol- $Co^{2+}$  at 300 K, which is 88% of the theoretical spin-only expected value and is consistent with other reported values [99]. The Fisher heat capacity,  $C_F$ , [162, 163] is defined by:

$$C_F = \frac{d(\chi T)}{dT} \quad (5.2)$$

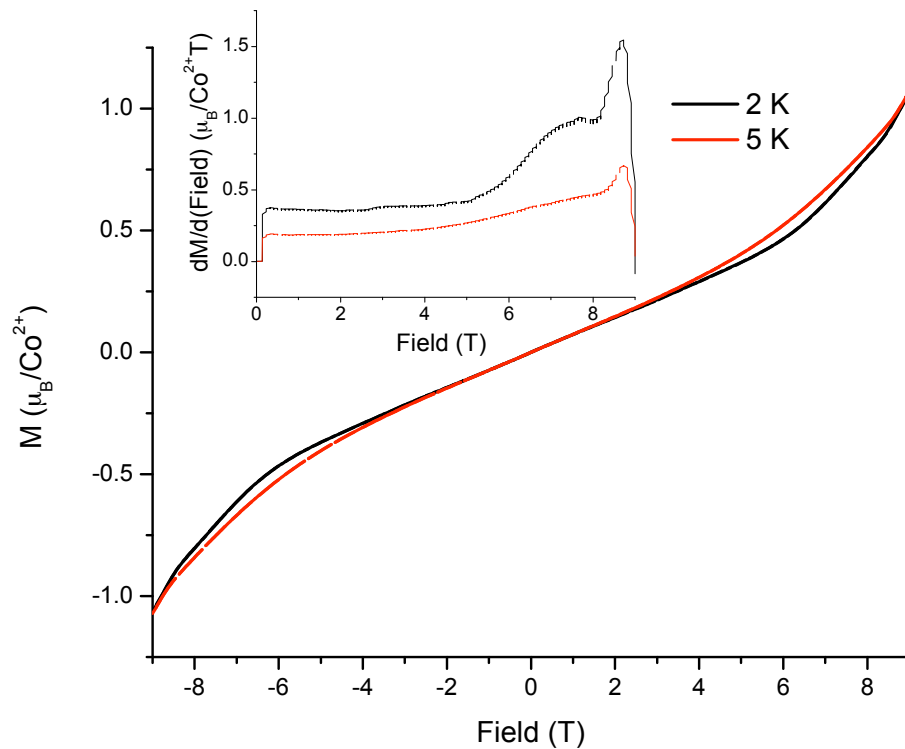


FIGURE 5.11: An upturn in the magnetization occurs near 6 T at temperatures below 5 K. **Inset:** The derivative of the magnetization shows the transition more clearly.

and can be calculated using the magnetic susceptibility.  $C_F$  looks very much like the real heat capacity after a lattice subtraction of the heat capacity of  $Pb_3TeZn_3P_2O_{14}$ , approximated to be the magnetic contribution (Figure 5.13 left inset). However, the anomaly at 6 K is quite visible in the Fisher heat capacity (left inset of Figure 5.13) while it is nearly absent in  $C_P$ . Turning to higher fields, the peak in the heat capacity also moves to lower temperatures as the field is increased (Figure 5.14). In addition to this, the peak appears to broaden around 7 T, which may indicate peak splitting. Altogether, the heat capacity, magnetic susceptibility and magnetization measurements can all be used to construct a phase diagram (Figure 5.15) that closely resembles that of  $Pb_3TeCo_3V_2O_{14}$  [156]. The nature of these phases remains largely unknown although at all phases there is finite magnetization that could imply complex magnetic states with a mixture of ferro- and antiferromagnetic moment interactions. Also, the phase

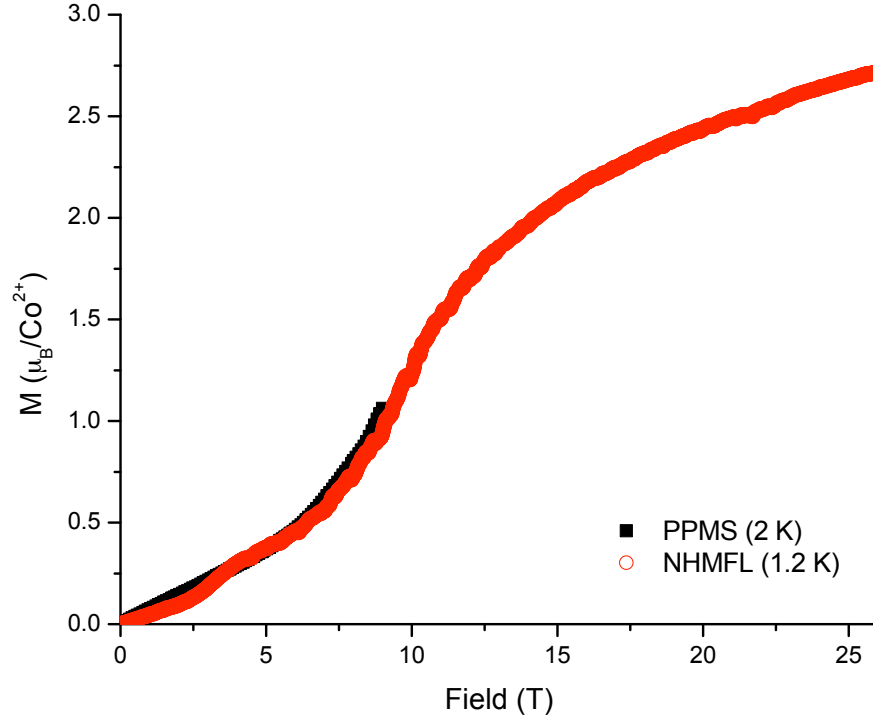


FIGURE 5.12: The magnetization is near saturation by 26 T at 1.2 K. Data from the NHMFL is quite noisy due to issues with the cryostat. The small instrumental feature at 2.5 T in the NHMFL data can be observed as a kink in the red curve.

boundaries are also up for debate but are close to what is shown in Figure 5.15; hysteresis in the field-dependent magnetization has been observed beginning near 9 T in [99] and persisting up until at least 14 T, but no anomalies signifying a transition out of this phase was observed up until at least 35 T here, although the data is quite noisy. The finite magnetization increases by over 50% as the field increases to 9 T. Neutron scattering shows that the magnetic structure is already quite complex at zero-field. It is difficult to resolve where this magnetization actually comes from in the magnetic structure.

### 5.3.3 Magnetic phases

At first glance  $Pb_3TeCo_3P_2O_{14}$  is both structurally and electronically similar to  $Pb_3TeCo_3V_2O_{14}$ : both not only have the same subcell, but also the same supercell. The only difference between them is the electronic nature of the diamagnetic ions  $V^{5+}$  and  $P^{5+}$ . Both ions

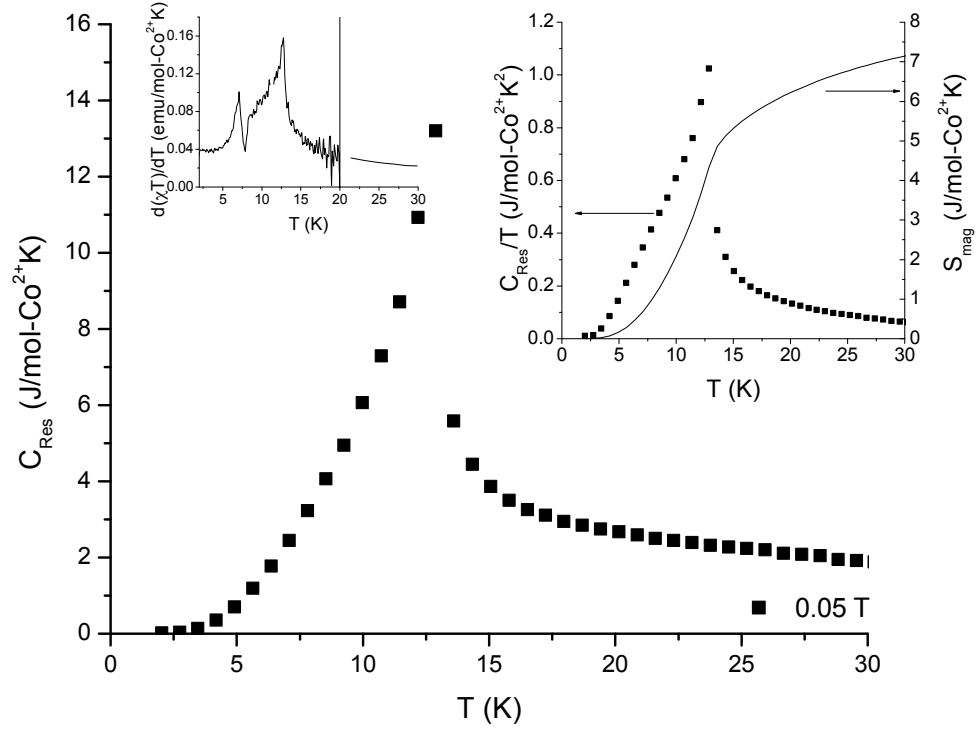


FIGURE 5.13: **Outset:** The residual heat capacity of  $Pb_3TeCo_3P_2O_{14}$  taken at 0.05 T found by subtracting off the lattice component. The heat capacity at 0.05 T was approximated to be nearly the same as that at 0 T (validated in Figure 5.14). **Left Inset:** The Fisher heat capacity at 0.05 T clearly shows the 7 K transition that appears absent from the heat capacity. **Right Inset:** The feature at 7 K appears as a broad hump in  $C_{Res}/T$ , which is consistent with the literature [99]. The magnetic entropy is approximated by integrating under this curve and is also consistent with reported values in the literature [99].

have noble gas configurations although  $V^{5+}$  has empty  $3d$  orbitals that are much more accessible than  $P^{5+}$ , which not only opens up more electronic states in  $Pb_3TeCo_3V_2O_{14}$  than in  $Pb_3TeCo_3P_2O_{14}$  due to  $V^{5+}$   $3d$  hybridization with  $O^{2-}$   $2p$  orbitals [156], but also make the former slightly larger than the latter [95, 145]. Despite this, the differences in the magnetic behaviour between these materials are striking, especially given that ionic substitution in other langasites does not dramatically change the magnetic phases, magnetic structures, or even the transition temperatures [111]. The most remarkable difference is the complete absence of a second antiferromagnetic transition at 6 K in zero-field, as observed using neutron scattering in  $Pb_3TeCo_3P_2O_{14}$ , despite

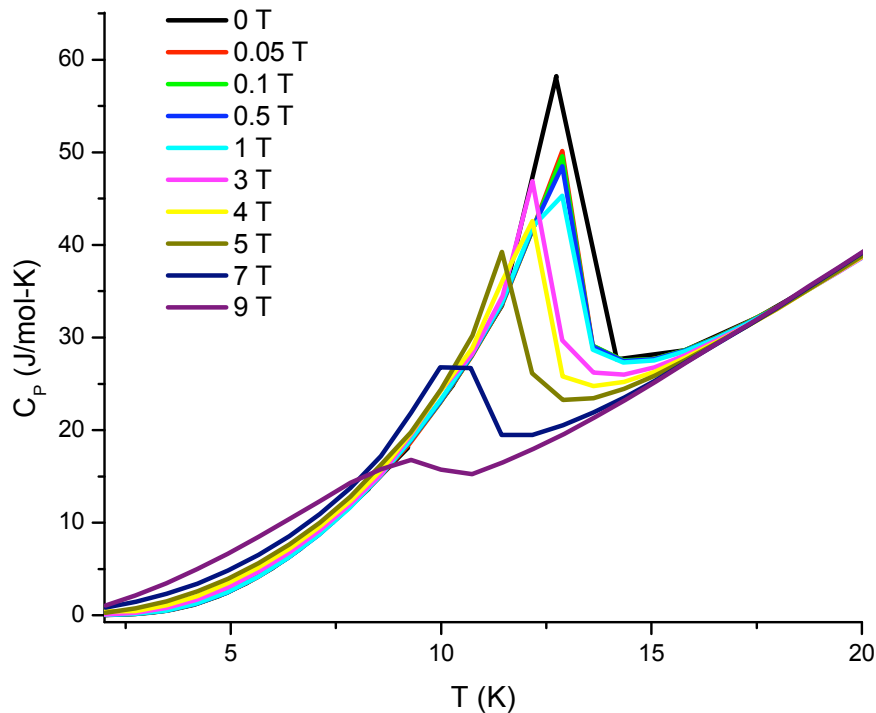


FIGURE 5.14: The heat capacity of  $Pb_3TeCo_3P_2O_{14}$  taken at various fields. Note that the units are per mole of  $Pb_3TeCo_3P_2O_{14}$  and that the data has not been corrected for the lattice component. Due to issues during puck calibration, this data should be viewed from a qualitative standpoint rather than a quantitative one. The entropy released as a function of field is left for a future study.

the anomaly in the susceptibility. Also unlike  $Pb_3TeCo_3V_2O_{14}$ , the magnetic phase in  $Pb_3TeCo_3P_2O_{14}$  cannot be modelled using the subcell [103, 145].

Magnetic structure refinements with this material are quite challenging due to there being 12 inequivalent magnetic ions in the supercell. A number of solutions were obtained that could fit the data quite nicely: some of these magnetic structure were physical while other were not. Before discussing the best magnetic structure solutions, it is best to point out some of the challenges of magnetic structure refinement in general. It is easy to adjust intensities and peak widths of magnetic structures by changing the magnetic moment to unphysical values, just as it is easy to do the same using unphysical negative

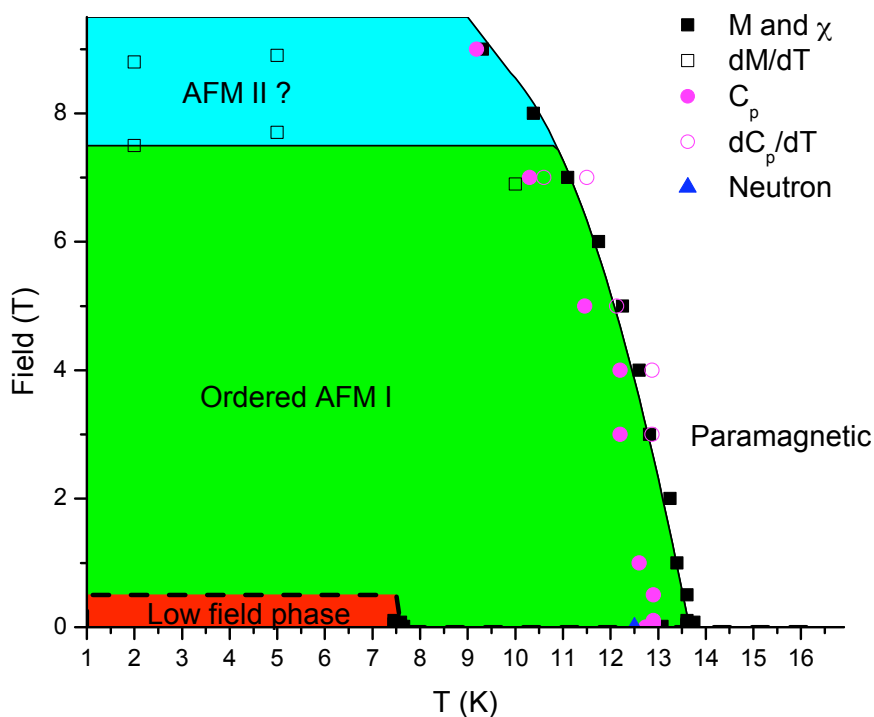


FIGURE 5.15: Proposed magnetic phase diagram using all of the data described within this chapter. Maxima in the derivative, rather than minima are marked on the figure as the minima did not agree with real transitions found in the data. Phase boundaries are approximate; more data is required to determine them precisely.

isotropic thermal parameters in the nuclear structure. However, magnetic structure determination using powders is always ambiguous. In general, one must be careful not to treat FullProf as a so-called “black-box” so as to obtain physically meaningful results. But using such unphysical values can still aid in understanding these magnetic structures strictly with respect to the orientation of the moments. This has been done numerous times using langasites. For example, in  $Ba_3NbFe_3Si_2O_{14}$ , a “magnetic isotropic thermal parameter” was introduced in order to account for intensity issues resulting in an artificially lowered magnetic moment from the saturated value [111]. Marty *et al.* [111] reasoned that partial spin transfer from the  $Fe^{3+}$  centre to the oxygen  $2p$  orbitals results in an alteration of the magnetic form factor, rectifying these issues (that is, there is still

a physical basis through which this parameter can be introduced). But in that particular example, it is also possible that the propagation vector could be “losing symmetry”, similar to what occurs in  $Pb_3TeMn_3P_2O_{14}$ , instead resulting in broadened peaks and altered intensities. For  $Pb_3TeCo_3V_2O_{14}$ , the maximum magnetic moment found in the subcell magnetic structure refinement was  $3.1 \mu_B/Co^{2+}$ , which is slightly above the saturated value of  $3 \mu_B/Co^{2+}$  [103]. However, such small deviations from the saturated moment are not uncommon and occur when FullProf tries to compensate for intensity errors in overlapping nuclear structures [164]. This is especially true for this case since the subcell cannot account for many of the reflections originally observed using neutron data. One of the possible magnetic structures of  $Pb_3TeCo_3P_2O_{14}$  was first reported by Krizan *et al.* [99] where  $Co^{2+}$  moments ranged between 2.42 and  $4.9 \mu_B$ . The maximum magnetic moment is nearly 2/3 higher than the saturated value and is likely unphysical considering the saturation plateau in the high-field magnetization, yet the orientations of the moments are what are more important here. A similar magnetic structure was reported previously [145] with better, but still unphysical moment values reaching a maximum of  $3.3 \mu_B$ . These structures are now discussed in detail.

The magnetic structure reported by Krizan *et al.* [99] depicts peculiar clustering behaviour of the magnetic moments wherein  $Co^{2+}$  trimers located in the centre of the crystal unit cell have moments oriented in a  $120^\circ$  orientation with zero net trimer moment. These trimers were constrained to behave this way to make the refinement easier. The trimers centred on and along the  $b$ -axis of the supercell have their moments aligned directly along the  $c$ -axis: all of the moments within each trimer point along the same direction (either parallel or antiparallel to  $c$ ), wherein the moment value varies in magnitude. A depiction of this magnetic structure will be provided later in Figure 5.17 as it is similar to the refined structures found here. Alternatively in another work [145], the supercell centre trimer moments were refined to point only along the  $b$ -axis resulting in a net trimer moment oriented along that axis (Figure 5.16). This produced a noticeably better fit to the data. The magnetic moments pointing along the  $c$ -axis were also refined

and found to vary between 2.3 and 3.3  $\mu_B$  [145]. In both studies, the magnetic structure was refined using  $\Gamma(1)$  with propagation vector  $\vec{k} = (\frac{1}{2}, 0, -\frac{1}{2})$ .

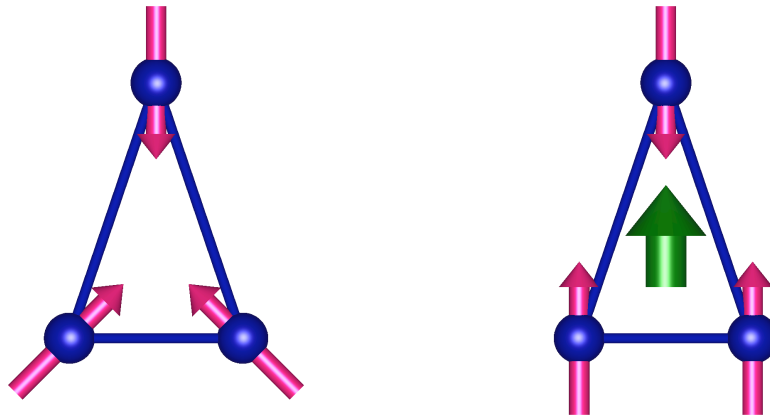


FIGURE 5.16: Net moments were put on the trimers located in the unit cell in [99]. This considerably improved the fit.

Here, magnetic refinements were performed using both  $\Gamma(1)$  and  $\Gamma(2)$  using the same  $G_x$ . The refinements were done first placing severe soft constraints on the moment sizes to  $2.90(2) \mu_B/\text{Co}^{2+}$ . This resulted in magnetic structures shown in Figure 5.17, which is similar to the structure reported earlier. For  $\Gamma(1)$ ,  $\text{Co}^{2+}$  moments directed along the  $c$ -axis were constrained to be exactly  $3.0 \mu_B$ . It is possible to cant the moments directed along the  $c$ -axis towards the  $a$ -axis for  $\text{Co}^{2+}$  ions situated on special sites in both  $\Gamma(1)$  and  $\Gamma(2)$ . The canting slightly improves the fit, but neutron powder diffraction is not very sensitive to it. The fits to the data are shown in Figure 5.18. Lifting the soft constraints noticeably improves the fit but results in unphysical moment magnitudes. Also, the unconstrained moment canting becomes more dramatic, with preferential canting taking place in the structure found using  $\Gamma(2)$  over  $\Gamma(1)$ . The moment increases with decreasing temperature in a predictable fashion (Figure 5.19). Because a spallation source was used to collect the diffraction pattern, tracking how a magnetic peak evolves with temperature is more challenging than it is using non-time-of-flight instruments (for example, in [165] the authors used POWGEN data in conjunction with data collected



on the HB-1A triple axis instrument at the High Flux Isotope Reactor (HFIR, Oak Ridge, TN) to track the order parameter). On top of this, the magnetic moment could not be found at each temperature due to the ambiguities associated with the magnetic structures in the refinements. Instead, the  $(0\bar{1}1)$ ;  $(011)$ ;  $(\bar{1}\bar{1}1)$ ;  $(\bar{1}11)$  magnetic reflection was fit to a Gaussian and the integrated intensity was tracked with temperature.

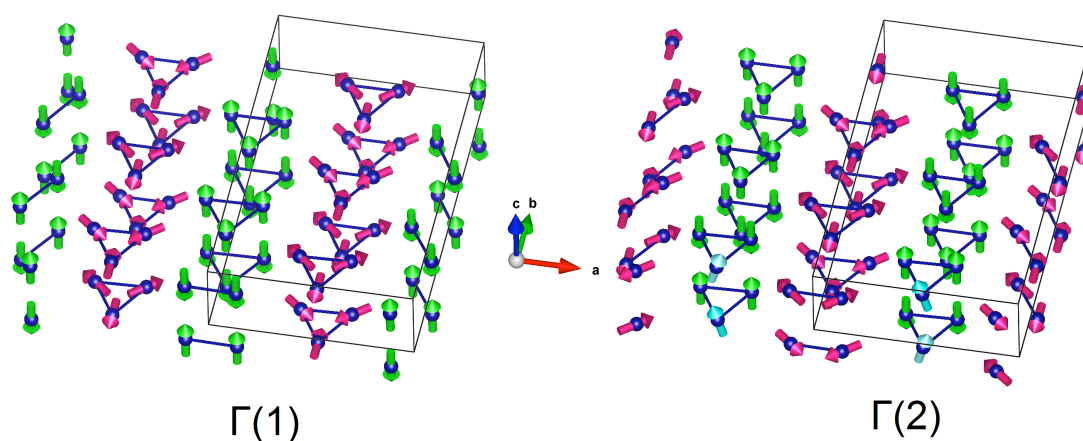


FIGURE 5.17: The full magnetic unit cells of  $Pb_3TeCo_3P_2O_{14}$  as found by neutron diffraction and drawn to scale. The groups of trimers referred to in the text are coloured green and magenta for clarity. A blue vector in  $\Gamma(2)$  denotes a small  $a$ -axis component that appeared to improve the fit, but did not do the same when tried in  $\Gamma(1)$ . It is noted that small  $c$  and  $a$ -axis components to some of the moments are allowed in magenta and green trimers respectively that neutrons are not very sensitive to.

A small but finite magnetization was detected in the magnetic susceptibility at low temperatures. It is quite difficult to reconcile the refined magnetic structures with the finite magnetization. In these magnetic structures the propagation vector almost acts as a pseudo-centre of symmetry by exactly counterbalancing any observed moment in the neighbouring nuclear unit cell (although this is strictly on average and does not influence local fluctuations). One possible way to reconcile the data sets with each other is to imagine magnetic domains. Using this propagation vector, it is possible to obtain net moments oriented along the  $b$ -axis. In order for these moments to exactly cancel, a magnetic domain would have to have equal amounts of parallel and antiparallel oriented moments. Grain boundaries and local disorder could be responsible for perturbing the

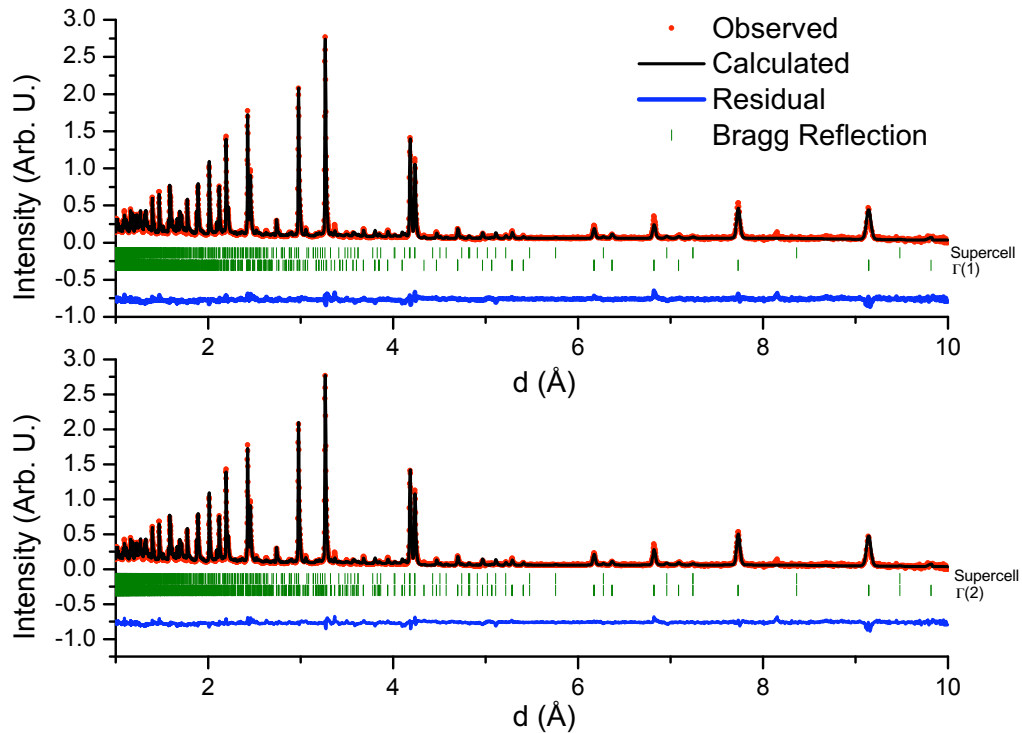


FIGURE 5.18: The final refinement of the magnetic unit cell using data taken from WISH.

system away from this ideal state, thereby inducing a finite magnetization. Alternatively, moments near magnetic domains can have ferromagnetic interactions dependent on the size of the domain, resulting in small hysteresis in the magnetization data in antiferromagnets [161]. AC susceptibility could yield some insight into this issue.

From the magnetic structure, it is quite difficult to predict which axis would be the easy axis: Half the of the trimers have moments oriented along the  $b$ -axis while the other half have moments oriented along the  $c$ -axis. For incommensurate magnetic structures in langasites, the  $c$ -axis is the easy axis [81, 82, 90, 94, 111, 119–123]. The Dzyaloshinskii-Moriya interaction is believed to play a large role in  $Pb_3TeCo_3P_2O_{14}$ , yet helical ordering of the magnetic moments does not occur. Krizan *et al.* [99] theorized that superexchange between  $Co^{2+}$  within a trimer should indicate a net ferromagnetic interaction

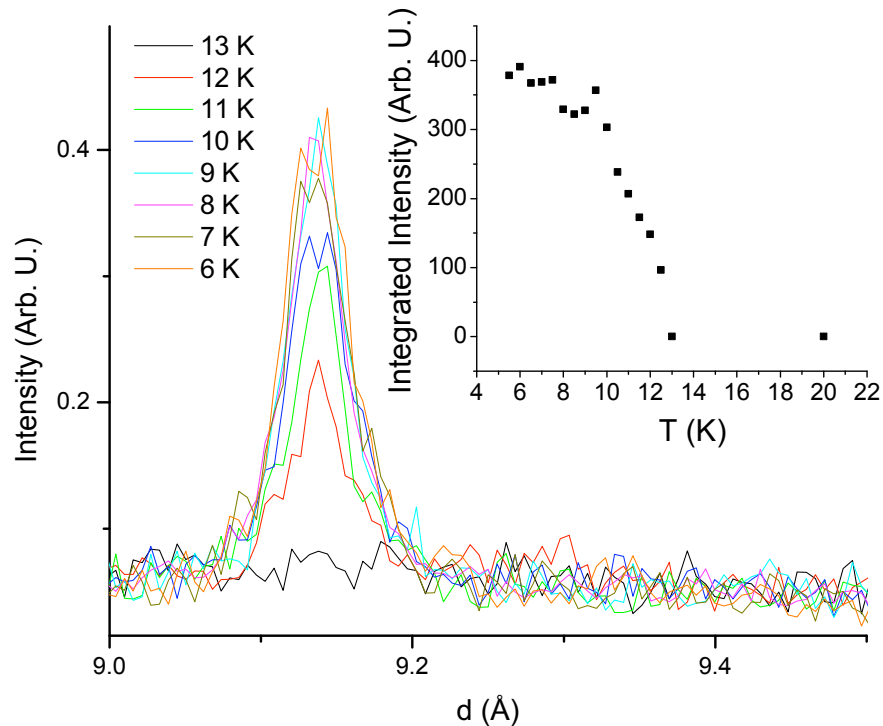


FIGURE 5.19: The evolution of the  $(0\bar{1}1)$ ;  $(011)$ ;  $(\bar{1}\bar{1}1)$ ;  $(\bar{1}11)$  magnetic reflection as a function of temperature. **Inset:** The peak was fit to a Gaussian function and the integrated area is plotted.

while super-superexchange between Co-trimers within the same plane would lead to anti-ferromagnetic interactions. The interactions are likely much more complex since half the trimers appear to have ferromagnetic intratrimer interactions while the other half have a structure predicted by the canonical geometrically frustrated antiferromagnetic trimer [26]. Furthermore,  $Pb_3TeCo_3V_2O_{14}$  has vastly different magnetic structures, highlighting the importance of orbital hybridization in these materials.

One interesting aspect of these magnetic structures is the relationship to the 6 K anomaly in the susceptibility observed at low fields. It is possible that this is another effect induced by the chirality of the structure. Both magnetic irreducible representations yield effectively equivalent magnetic structures which cannot be distinguished using powder neutron diffraction. The layout of the oxygen sublattice changes with each structural

enantiomer, altering the Dzyaloshinskii-Moriya interaction, and therefore selecting one of the magnetic irreducible representations (this mechanism is responsible for selecting out a single out of two otherwise equivalent irreducible representations in enantiopure  $Ba_3NbFe_3Si_2O_{14}$  single crystals). Consider a single structural enantiomer: it is possible that between 12.5 K and 6.0 K, both magnetic structures are equivalent and are equally populated. However by 6.0 K, the system selects only one of the magnetic structures. This would lead to no changes in the diffraction pattern and very little change in the heat capacity since both magnetic structures are roughly equivalent, but can be detected through a change in the magnetization. Driving this transition is the structural chirality. This picture becomes even more muddled in powders; both structural enantiomers exist so it is expected that both irreducible representations exist as well. Between 6.0 and 12.5 K, both structural enantiomers contain both magnetic structures but below 6.0 K, each structural enantiomer contains only one magnetic structure such that both magnetic structures are still present at all temperatures in powders. Alternatively, it is also possible that only one of the magnetic structures is selected out in both enantiomers below 6 K, such that only one exists in both single crystals *and* powders. Because of the supercell, there are now six Co-trimer clusters which are nearly, but not quite equivalent. These distortions lift the degeneracy in the magnetic structures selecting out one with slightly lower energy at low temperatures, where the system can no longer overcome the energy barrier of the other magnetic structure. For example, simply due to local distortions around the trimers, it may be energetically more favourable for the trimers in the centre of the unit cell to have their moments directed along the  $c$ -axis than those trimers on the unit cell edge. If this is the case, an experiment exploring the local magnetic structure, such as muon spin rotation ( $\mu$ SR), could be useful.

### 5.3.4 Inelastic excitations

Like x-rays, neutrons can also scatter from samples inelastically, which results in a change of the incident neutron's velocity dependent on whether energy is transferred to or from the sample. Inelastic neutron scattering was performed on  $Pb_3TeCo_3P_2O_{14}$

powder on the SEQUOIA time-of-flight spectrometer at the SNS using incident energies of 8, 50, 200, and 1 000 meV. Because no excitations could be uniquely distinguished above 10 meV (although a weak signal is still observed), the discussion will be limited to the excitations observed below 10 meV.

A slice of the neutron data set at 6 K is shown in Figure 5.20. Here, data taken at 25 K was subtracted from data taken at 6 K in order to isolate the magnetic signal (background empty can data sets have also been subtracted from the set). Very broad dispersionless (within the resolution of SEQUOIA) modes are observed between 2 and 4 meV and between 4.6 and 7 meV. These low-energy dispersionless modes are quite unusual for an extended solid with a  $3d$  transition metal ion and a well-ordered magnetic structure: normally one would expect to observe spin waves as in [123]. On the other hand, dispersionless modes are often observed for molecular magnet systems where spin waves do not exist in the conventional sense [166, 167]. The broad magnetic background implies the development of short-range interactions as the temperature is lowered followed by the formation of better-defined excitations. At 6 K, the excitations were fit to Gaussians in order to extract their energy centres (Figure 5.21). The first four excitations were found to occur at 2.041(9), 2.35(1), 2.903(5), and 3.515(6) meV. The latter two excitations are quite broad and occur at 4.81(4) and 6.32(6) meV. However, these excitations appear to be composed of many smaller ones that could not be resolved. They are all magnetic in origin and can be fit to the spin-only form factor of  $Co^{2+}$  reasonably well.

The detailed structural analysis of Co-trimers in this dugganite shows a deviation away from equilateral symmetry to isosceles symmetry. This has important consequences for the magnetism, namely that each trimer now has two intratrimer exchange energies  $J$  and  $J'$ . A thorough analysis of the neutron scattering and magnetic observable of  $S=1/2$  spin clusters and molecular magnets found through first-principles are outlined by Haraldsen, Barnes, and Musfeldt [168]. In particular an isosceles trimer will split the degeneracy in the  $S=1/2$  ground state, which can produce three observable excitations

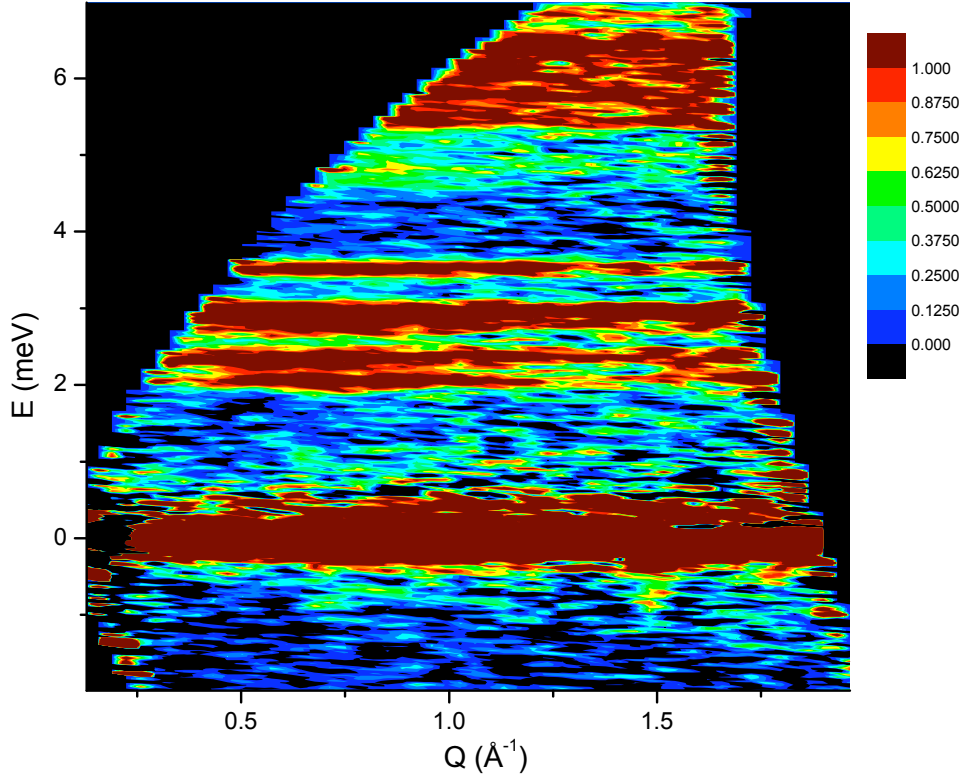


FIGURE 5.20: A slice of the excitations as a function of both energy and  $Q$  in  $Pb_3TeCo_3P_2O_{14}$  powder. The y-axis is energy transferred from the incident neutron (with energy  $E_i = 8$  meV). Therefore, diffraction information is located in the band at 0 meV running across  $Q$  indicating elastic processes. Intensity is in arbitrary units and only positive intensity is shown for clarity. Step size for energy is 0.02 meV while step size for  $Q$  is  $0.01 \text{ \AA}^{-1}$ .

within the inelastic neutron scattering selection rules (Figure 5.22). These Co-trimers can be approximated as non-interacting effective  $S=1/2$  molecular spin clusters. Although there are six inequivalent Co-trimers in the unit cell, they can also be roughly separated into two groups of three roughly equivalent trimers. This approximation is validated when one considers the magnetic structure; one row of trimers contains moments oriented within the plane while the other row of trimers contains moments directed perpendicular to it (whether or not moments in neighbouring trimers lie parallel or antiparallel to each other is assumed to be due to the weak interactions between trimers, which are not considered in this phenomenological and primitive model). Denoting  $J_i$  and  $\alpha_i$  as the exchange energy and isosceles perturbation of the  $i^{th}$  group of trimers, the

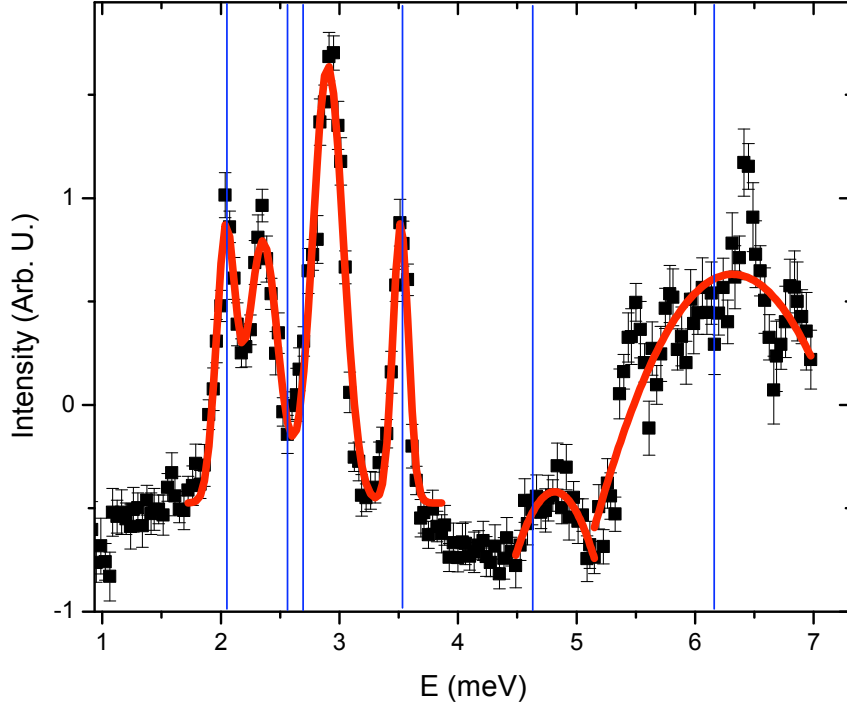


FIGURE 5.21: A cut was made along energy in Figure 5.20 integrating over all Q. Excitations were fit to Gaussians in order to extract their centres. Blue lines are calculated positions of the excitations based on the exchange model described in the main text.

peak centres in the inelastic neutron scattering data were best fit using the values  $J_1 = 3.75(20)$  meV,  $J_2 = 5.0(2)$  meV,  $\alpha_1 = 0.45(5)$ , and  $\alpha_2 = 0.47(5)$ . These fits were not performed using a rigorous least-squares fitting regimen since this yielded unphysical results. Instead the fits were approximated using trial and error. The positions of the expected inelastic excitations are marked in blue in Figure 5.21.

In order to verify the agreement of these values, the magnetic susceptibility taken using a field of 0.1 T was fit to a modified model by Haraldsen *et al.* [168]:

$$\frac{\chi}{(g\mu_B)^2} = \frac{1}{4}\beta \left( \frac{10 + e^{\frac{3}{2}\alpha\beta J_1} + e^{(1+\frac{1}{2}\alpha)\beta J_1}}{2 + e^{\frac{3}{2}\alpha\beta J_1} + e^{(1+\frac{1}{2}\alpha)\beta J_1}} + \frac{10 + e^{\frac{3}{2}\alpha\beta J_2} + e^{(1+\frac{1}{2}\alpha)\beta J_2}}{2 + e^{\frac{3}{2}\alpha\beta J_2} + e^{(1+\frac{1}{2}\alpha)\beta J_2}} \right) + W \quad (5.3)$$

where  $\chi$  is the magnetic susceptibility,  $\alpha$  is an exchange damping parameter due to

the distortion,  $g$  is the electron g-factor,  $\mu_B$  is the Bohr Magnetron,  $J_i$  is the exchange constant of the  $i^{th}$  trimer,  $W$  includes extra terms such as the diamagnetic contribution to the susceptibility, and  $\beta$  is  $1/k_B T$ , where  $k_B$  is the Boltzmann constant and  $T$  is the temperature. The agreement with the susceptibility is shown in Figure 5.22 where the only parameter allowed to vary was a scaling constant (not shown in the equation), which was found to be 0.73(5). The scaling constant mostly represents the fact that we do not have an  $S=1/2$  system (the effective moment is  $4.46 \mu_B$ ) since the orbital moment is only partially quenched. Already, the fit is quite good considering that so many approximations have been made: the fact that these equations were solved for an  $S=1/2$  system, the neglect of orbital magnetism in the neutron excitation spectra, six inequivalent trimers were approximated as two groups of inequivalent trimers, and that all intertrimer and magnetoelastic coupling interactions were excluded. The value obtained here agree well with those reported for  $Pb_3TeCo_3V_2O_{14}$  [145]. Still, unanswered questions remain such as why  $\alpha$  is so small considering that deviations from equilateral trimer symmetry are only slight, or where the broadness of the higher energy excitations actually come from (although some insight is given in the next chapter as this same problem relates to  $Pb_3TeCo_3V_2O_{14}$ ). However, one interesting explanation may come from an expansion of the subcell. If each trimer is to be approximated as roughly equilateral, then one may connect each trimer to form a triangular lattice of connected trimer clusters as in Figure 5.23 (this was proposed for  $Ba_3TeCo_3P_2O_{14}$  [99] although no effects resultant from such a model were proposed). Although it is not clear how such a triangular arrangement would impact the Haraldsen *et al.* [168] trimer model, this would explain how the two exchange energies differ so dramatically: the larger exchange energy represents exchange within a Co-cluster while the smaller exchange energy represents the interplanar trimer exchange, which was also shown to be half the former value in Fe-langasites [82, 120, 122]. Furthermore, classical Heisenberg triangular lattice antiferromagnets have phase diagrams that closely resemble the one constructed here [169] and which have also been recently observed in low spin  $Co^{2+}$  systems [170, 171]. A kink in the magnetization is even observed at  $1 \mu_B$  (Figure 5.12), which is  $1/3$  of the



magnetization, that is expected for an  $S=1/2$  triangular lattice antiferromagnet [171]. But it is important to keep in mind that the lattice is only perfect in the subcell limit and that  $Co^{2+}$  is in its  $3/2$  state. This example is very primitive, and at this point, is only mainly meant to show that the complexity of the supercell and magnetic structures should not limit how these systems are to be understood in the future. More calculations and better neutron data are required to draw certain and more quantitative conclusions.

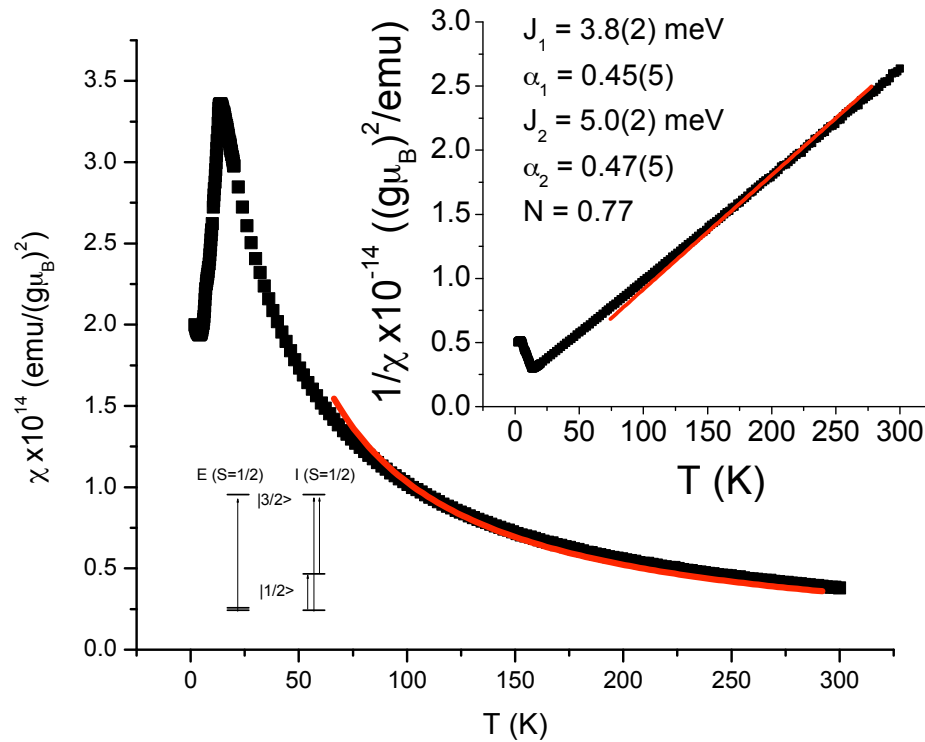


FIGURE 5.22: The DC susceptibility was fit to the equation described in the text (red). The inset displays the inverse in order to better show deviations from the fit. A schematic of the neutron scattering selection rules for equilateral (E (S=1/2)) and isosceles (I (S=1/2)) effective S=1/2 trimers is shown in the inset, derived in [169] (note that for the equilateral case, the S=1/2 state is a doublet that results in only one excitation).

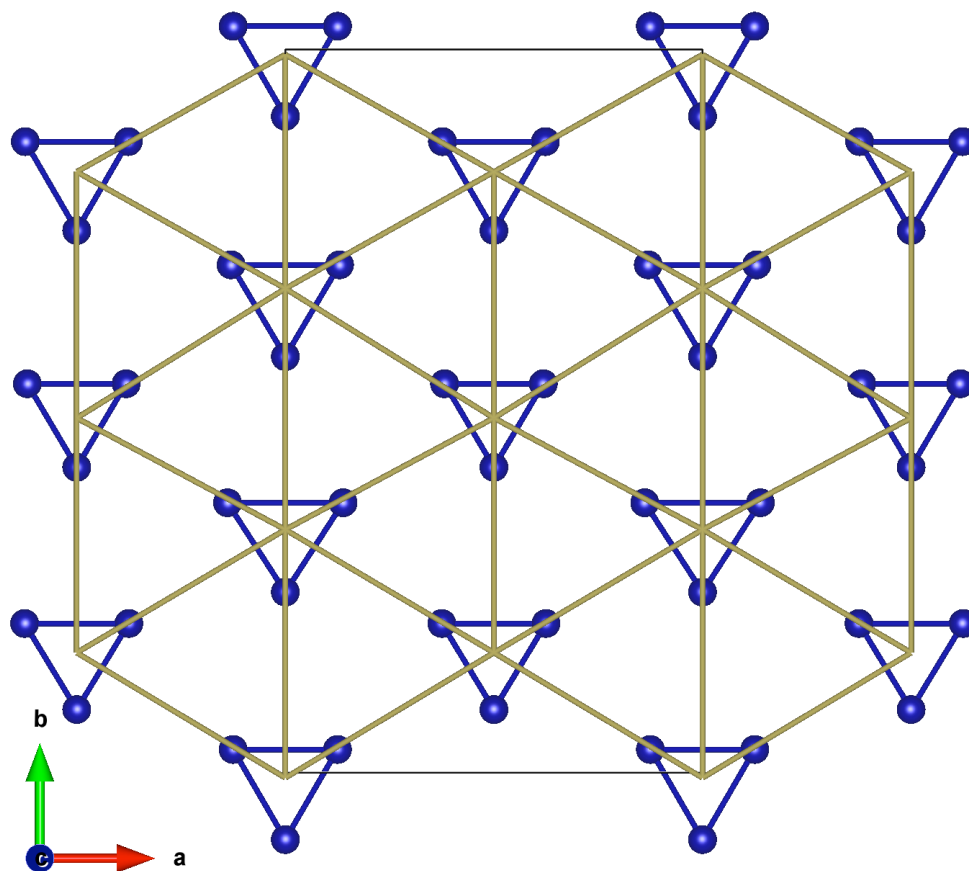


FIGURE 5.23: One theory proposed to explain the observed phenomena in  $Pb_3TeCo_3P_2O_{14}$  is the triangular lattice of connected trimer clusters.

## 5.4 Conclusion

$Pb_3TeCo_3P_2O_{14}$  was prepared using a standard solid-state reaction. Unlike  $Pb_3TeMn_3P_2O_{14}$ , a large  $P2$  supercell was found resulting in six inequivalent Co-trimers centred along the 2-fold rotation axes. Although magnetic susceptibility yields two transitions at 12.5 and 6.0 K at low fields, only the transition at 12.5 K was observable in the heat capacity and using neutron scattering. A phase diagram up to 35 T was constructed using magnetic susceptibility, heat capacity and neutron scattering, indicating a high-field phase beginning near 7 T below 12.5 K. Magnetization measurements show weak hysteresis below the antiferromagnetic transition temperatures, which is likely caused by domain effects. The magnetic unit cell was solved using both IRs belonging to the little group  $G_x$  formed from the space group and propagation vector  $\vec{k} = (\frac{1}{2}, 0, -\frac{1}{2})$ . It was theorized that the second magnetic transition could be the result of the system selecting one magnetic structure either by chirality or due to the supercell distortions. Finally, inelastic neutron scattering was used to show that individual Co-trimer clusters behave nearly independently and can be approximated using an  $S=1/2$  isosceles trimer cluster model. Rough approximations of the intratrimer exchange energies were found by fitting both the excitations and the magnetic susceptibility. More work will be required to learn about the system dynamics and energy scale in more detail. What is very clear is that substituting an  $S=5/2$  ion for a similarly sized  $S=3/2$  ion in these systems has profound implications on not only the magnetism, but even the nuclear structure, further showing tight coupling between the two.

## Chapter 6

# Two magnetic transitions in the multiferroic candidate

## $\text{Pb}_3\text{TeCo}_3\text{V}_2\text{O}_{14}$

### 6.1 Preamble

This chapter focuses on  $\text{Pb}_3\text{TeCo}_3\text{V}_2\text{O}_{14}$ . Although this thesis packages the work differently, experimental work first began with this material following the successful preparation of  $\text{Ba}_3\text{NbFe}_3\text{Si}_2\text{O}_{14}$ . The original intent of the project was to raise the langasite multiferroic transition temperature by substituting  $\text{Fe}^{3+}$  for another transition metal ion. While I was not able to do so using this approach, instead I found a dramatic departure from the magnetism found in  $\text{Ba}_3\text{NbFe}_3\text{Si}_2\text{O}_{14}$ . What was most striking was that this material has not one, but two antiferromagnetic transition temperatures despite having the same atomic arrangement. It was not until later that we discovered a large supercell in  $\text{Pb}_3\text{TeCo}_3\text{V}_2\text{O}_{14}$ . The work described in this chapter was first published in *Chemistry of Materials* in 2012 [103], followed by another publication in the *Journal of Physics: Condensed Matter* in 2013 [145]. In this chapter, the data is presented in the order of discovery. My results pertaining to the subcell are presented first followed by those pertaining to the supercell.

## 6.2 Introduction

$Pb_3TeCo_3P_2O_{14}$  magnetism exhibits a dramatic departure from the chiral statics and dynamics observed in most paramagnetic langasites, and possibly  $Pb_3TeMn_3P_2O_{14}$  as well. In the previous chapter, it was shown that simply substituting  $Mn^{2+}$  for  $Co^{2+}$  not only completely changes the nature of the nuclear supercell distortions, but also the low temperature magnetic structure. This is quite unlike the effects observed when ionic substitutions are made for  $Ba_3NbFe_3Si_2O_{14}$  (other than  $Fe^{3+}$ ); substituting Ba, Nb, and/or Si has little effect on the magnetic properties [111]. Even when  $Fe^{3+}$  is swapped for another isoelectronic  $S=5/2$  ion  $Mn^{2+}$  along with all of the other cations in the cell, the low temperature magnetic properties still remain quite similar [143, 144].

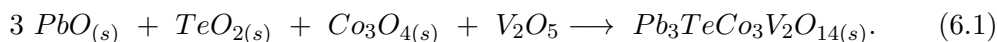
In this chapter,  $P^{5+}$  is substituted for  $V^{5+}$  to make  $Pb_3TeCo_3V_2O_{14}$ . Electronically, the only difference between these materials is that diamagnetic  $P^{5+}$  has the same electronic configuration as the noble gas Ne while  $V^{5+}$  has the electron configuration of the noble gas Ar. In terms of size,  $P^{5+}$  has a crystal radius of 0.31 Å while  $V^{5+}$  is much larger at 0.495 Å in tetrahedral coordination [95], but still within the tolerable limit of the  $2d$  special site in the langasite unit cell.  $V^{5+}$  also has easier access to empty  $3d$  orbitals than  $P^{5+}$ . Despite this,  $Pb_3TeCo_3V_2O_{14}$  has dramatically different magnetism than  $Pb_3TeCo_3P_2O_{14}$ . In this chapter, the preparation, subcell and supercell structure, magnetic and dielectric properties, low temperature magnetic structures, and magnetic dynamics are all introduced and explored.

## 6.3 Methods

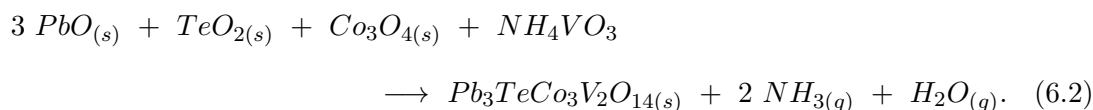
### 6.3.1 Preparation

Polycrystalline  $Pb_3TeCo_3V_2O_{14}$  was prepared using a standard solid-state reaction. Stoichiometric amounts of  $PbO$ ,  $TeO_2$ ,  $Co_3O_4$ , and  $V_2O_5$  were ground together and pressed into one centimetre diameter pellets under 10 MPa of pressure. The pellets were sintered in air between 650 °C and 800 °C for 15-24 hrs. Samples were annealed at 600 °C for

up to 72 hrs with intermittent grindings. All oxides were of high purity (99.99%) and purchased from Sigma-Aldrich. The overall reaction equation is:



Before the discovery of the supercell, this reaction method was first reported by Mill [108] to yield approximately 1% impurities on the basis of powder diffraction plots. Although it is now known that these “impurity peaks” are supercell reflections, at the time other preparative methods were attempted in order to make the material “phase pure”. This includes using  $NH_4VO_3$  in place of  $V_2O_5$  in the following reaction:



In addition to this,  $PbO_2$ ,  $CoO$ , and  $TeO_3$  (laboratory prepared) were also used as starting reagents. Depending on the reaction, a variety of atmospheres were used as well including air, Ar, and  $N_2$ . Alumina crucibles (99.8%) and platinum crucibles were both used and reactions were attempted both with and without crucible lids to control volatilization of  $PbO$  and  $TeO_3$ . Many intermediates were isolated over the course of the reaction including  $Pb_3V_2O_8$  and  $Pb_2V_2O_7$ , the quantities of which heavily depended on the choice of reactants used. Overall, the best results were found using the first method.

### 6.3.2 Diffraction

Room temperature powder x-ray diffraction (XRD) data were collected on a PANalytical X’pert Pro System with a Cu  $K\alpha$  anode equipped with a diffracted beam Ni-filter and an X’Celerator detector. Using a zero background sample holder, the angular range  $[10^\circ, 120^\circ]$  was measured in  $0.0083^\circ$  steps over 24 hrs. High resolution synchrotron x-ray diffraction (SXRD) was carried out at the 11-BM line [53] at the APS through the mail-in program.  $Pb_3TeCo_3V_2O_{14}$  was loaded into a Kapton capillary tube plugged

with clay and kept at 295 K for the measurement. A wavelength of 0.413961 Å was used in transmission mode. Neutron powder diffraction (NPD) was collected at two different sources. NPD measurements were first performed using the C2 diffractometer at the CNBC. Measurements were made using two sets of conditions. For the first set, a wavelength of 1.33 Å was used at 298 and 4.3 K using both the low and high angle detector banks to obtain a full diffraction pattern counting for two hours each. The second set of conditions used a wavelength of 2.37 Å over a temperature range of 4.3 to 10.25 K in 0.25 K steps. Additional measurements were taken at 15, 20, 25, and 40 K. These wavelengths were selected using a Si monochromator. A pyrolytic graphite filter was used for all measurements at 2.37 Å to exclude  $\lambda/2$  reflections. NPD data were also collected using the WISH time-of-flight diffractometer (Didcot, Oxfordshire, UK) as previously described in Chapter 5. All samples were cooled using either a He CCR or a standard ILL Orange cryostat designed to reach temperatures as low as 1.8 K. Six grams of sample were used for each neutron experiment.

### 6.3.3 Physical property measurements

DC susceptibility measurements were first carried out using a SQUID magnetometer purchased from Quantum Design using an applied field of 0.1 T. Following these results, further susceptibility and magnetometry measurements were made using the VSM attachment of a Physical Property Measurement System (PPMS, Quantum Design) between 1.8 and 300 K using fields at 0.1, 0.25, 0.5, 0.75, and 1 through 9 T (in 1 T steps) on a 36.0 mg sample. High-field magnetization measurements were carried out at the NHMFL up to 35 T on an in-house-designed VSM instrument at temperatures between 1.2 and 50 K. Specific heat measurements were made using a PPMS (Quantum Design) in zero-field.  $Pb_3TeZn_3P_2O_{14}$  was prepared as a lattice standard as previously described in Chapter 4. Dielectric constant measurements were made by creating electric contacts on two opposite surfaces of a thin plate sample using Ag paste. An automated capacitance bridge (Andeen-Hagerling AH-2700A) operating at a frequency of 10 kHz was used. Capacitance was converted to the dielectric constant by approximating the sample as an



infinite parallel capacitor. With the exception of the susceptibility measurements taken using the VSM on the PPMS at the University of Winnipeg, all property measurements were performed at the NHMFL.

### 6.3.4 Refinement

Unlike the other materials discussed thus far, a refinement of the atomic structure of  $Pb_3TeCo_3V_2O_{14}$  presents a more formidable challenge, even with respect to the refinement of the subcell structure. This is because x-rays are quite sensitive to the cation positions but insensitive to O. However, V and Co are difficult to distinguish and refine using x-rays alone because they are quite close in electron count. Alternatively, neutron scattering can be used to identify the O positions, but an additional complication arises because of V: it has a very large incoherent scattering cross section (5.08 barns) compared to its coherent scattering cross section (0.0184 barns) [172]. This means that almost all of the diffracted neutrons from V nuclei will indicate nothing about their positions in the crystal structure. While this helps in distinguishing between V and Co, this makes refining V-O bond lengths quite difficult without the aid of expensive isotopically pure  $^{50}V$ , which is a great neutron absorber anyway. Very careful joint refinements were initially employed using the FullProf suite [150]. However, even with the joint refinement, realistic values for V-O1 distances, which are oriented directly on the 3-fold rotation axis normal to the *ab*-plane could not be determined. As a result, values were fixed to the As-O distances determined by Lam *et al.* [75, 136] for single crystal natural dugganite. A refinement of the subcell using both XRD and C2 NPD data at room temperature is shown in Figure 6.1. The agreement factors are  $R_p = 2.46$ ,  $R_{wp} = 3.36$  and  $\chi^2 = 4.16$  for the x-ray data and  $R_p = 5.50$ ,  $R_{wp} = 7.23$  and  $\chi^2 = 8.48$  using the short-wavelength neutron data. Over 100 impurities containing common elements and reflections with the unindexed peaks were initially tried [103]. Many of these peaks could be accounted for using  $Pb_2O_3$ ,  $TeO_3$ , and  $Co_3O_4$  impurities. The crystallographic parameters for the subcell are listed in Table 6.1.

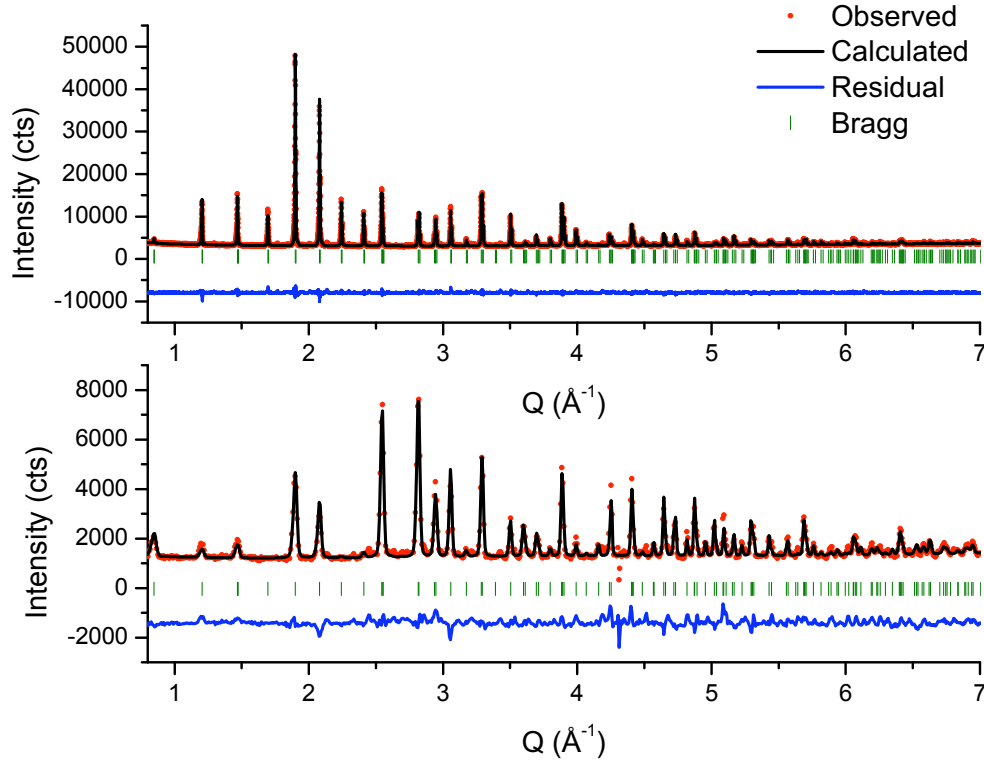


FIGURE 6.1: Refinement of  $Pb_3TeCo_3V_2O_{14}$  using laboratory x-ray diffraction data (upper) and neutron diffraction data taken from C2 (lower). A dead detector appears at  $4.34 \text{ \AA}^{-1}$  which was excluded in the refinement, but presented in the profile.

TABLE 6.1:  $Pb_3TeCo_3V_2O_{14}$  crystallographic parameters at room temperature with space group  $P321$  and lattice constants  $a = 8.5595(4) \text{ \AA}$  and  $c = 5.2167(3) \text{ \AA}$ . Oxygen  $B_{\text{iso}}$  values were refined together while the position of vanadium was fixed to the value found for  $As^{5+}$  in natural dugganite [75, 136]. Data published in [103].

Ion	Site	x	y	z	$B_{\text{iso}} (\text{\AA}^2)$
Pb1	$3e$	0.59984(11)	0	0	2.53(3)
Te1	$1a$	0	0	0	2.36(8)
Mn1	$3f$	0.2373(6)	0	$\frac{1}{2}$	2.9(1)
V1	$2d$	$\frac{1}{3}$	$\frac{2}{3}$	0.5294(6)	2.5(3)
O1	$2d$	$\frac{1}{3}$	$\frac{2}{3}$	0.239(4)	2.82(1)
O2	$6g$	0.4583(16)	0.1866(13)	0.3297(20)	2.82(1)
O3	$6g$	0.1261(12)	0.2127(13)	0.226(2)	2.82(1)

The supercell refinement for  $Pb_3TeCo_3V_2O_{14}$  was also performed using a similar procedure to that detailed earlier in Chapters 4 and 5. However, many complications arose not only due to the reasons mentioned earlier in this section, but because of the lower-quality room temperature neutron diffraction data taken before it was realized that this material had a supercell. The rigid body refinement was performed as earlier with the exception that the  $VO_4$  distances were changed to reflect typical experimental values [173, 174]. This resulted in adequate and realistic metal-oxygen bond distances, but the convergence parameters were not low enough for the neutron data. As such, three other models were refined to fit the data. In the first, WISH data taken at 20 K was used to find a thermal average of the supercell structure. The data obtained from WISH is of high quality and high resolution, but data could not be obtained at room temperature due to unforeseen issues relating to a stoppage in neutron flux from the source. It was assumed that the atomic coordinates remain unchanged at all temperatures: only the lattice parameters change with temperature. However, this refinement method did not result in better statistics at room temperature. Krizan *et al.* [99] did not use neutron data in their refinement and only estimated oxygen atomic coordinates from their 100 and 4 K thermal average refinement of the structure of  $Pb_3TeCo_3P_2O_{14}$ . The second refinement method involved refining the atomic coordinates reported in [99] using both x-ray and neutron data (it is also noted that rigid bodies appeared to only be allowed to rotate within the *ab*-plane in their model). This approach yielded results that better agree with the x-ray data, but had worse agreement with the neutron data, which is likely a natural consequence of those initial atomic coordinates having been solely derived from synchrotron x-ray data. The third method involved refining the atomic coordinates of the cations in  $Pb_3TeCo_3V_2O_{14}$  using only the x-ray data at 300 K found using the rigid body approximation. Following this, the atomic coordinates of the oxygens were refined using only the WISH data at 20 K keeping the atomic coordinates of the cations constant. Afterwards a joint refinement of the model was done using both the x-ray and C2 neutron data at 300 K and the obtained atomic coordinates. All of these methods resulted in similar agreement factors despite having atomic coordinates

that do not agree with each other within error. This could be due to the presence of correlated residuals [175] that raises the errors on the obtained values. Better quality room temperature neutron diffraction with higher resolution is required to make definitive conclusions about the metal-oxygen distances. In any case, the rigid body refinement profile is presented in Figure 6.2 with the atomic coordinates listed in Tables 6.2 through 6.4.

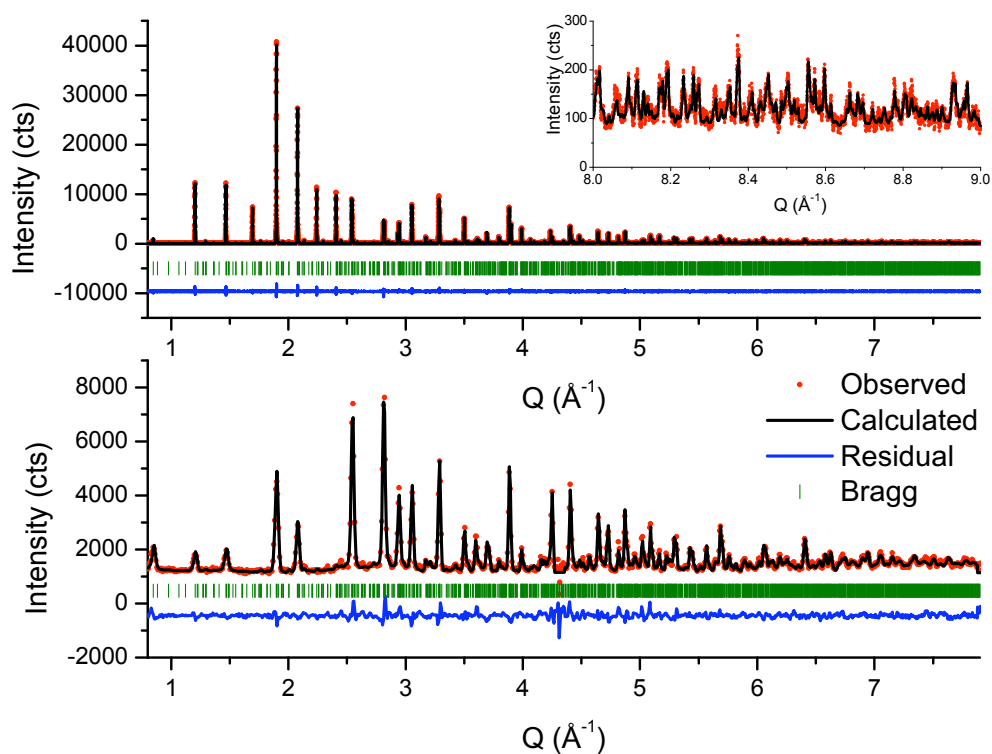


FIGURE 6.2: Refinement of  $Pb_3TeCo_3V_2O_{14}$  using synchrotron x-ray diffraction data (upper and inset) and neutron diffraction data taken from C2 (lower).

### 6.3.5 Inelastic neutron scattering

Inelastic neutron scattering was performed on SEQUOIA at the SNS using 6.0 g of powder  $Pb_3TeCo_3V_2O_{14}$  loaded onto an aluminum flat plate empty sample can, wrapped in aluminum foil, and sealed with indium wire. Helium exchange gas was loaded into the can. A standard ILL Orange cryostat was used to get down to temperatures as low as 1.8 K. An incident energy of 8 meV was used to observe excitations at low energies (although SEQUOIA is typically designed for observing magnetic excitations that are higher in energy, it is capable of reaching 8 meV reliably with a resolution limit of about 4% of the incident energy (0.24 meV). Incident neutron energies of 5 meV, 48 meV, 1 eV, and 2 eV were also used.

## 6.4 Results and Discussion

### 6.4.1 Crystal structure

The crystal structure of  $Pb_3TeCo_3V_2O_{14}$  is hypothesized to be similar to  $Pb_3TeCo_3P_2O_{14}$ , except that the larger size of  $V^{5+}$  would alter the metal-oxygen bond distances and slightly enlarge both the subcell and supercell [99, 108, 145]. It is important to note that due to the difficulty of this particular refinement and the lower quality of the room temperature neutron data, the following bond lengths (Tables 6.5 and 6.6) and resulting polyhedral shapes will be discussed on more of a qualitative level than a quantitative one. In this study, it was found that the obtained bond lengths are directly related to the manners in which the data were collected, treated, and the level of hard and soft constraints implemented in the refinement. Much stricter constraints had to be used here for the refinements to converge compared to those used for  $Pb_3TeCo_3P_2O_{14}$ . Despite this, general distortive trends were observed. The final structure is shown in Figure 6.3 and compared to  $Pb_3TeCo_3P_2O_{14}$ .

In the final stages of the refinement,  $TeO_6$  and  $VO_4$  rigid bodies were replaced with the following strict soft distance constraints:  $Te-O = 1.94 \pm 0.01 \text{ \AA}$ ,  $V-O_{\text{base}} = 1.75 \pm 0.01 \text{ \AA}$ ,

TABLE 6.2: Refined atomic coordinates for  $Pb_3TeCo_3V_2O_{14}$  in the  $P2$  supercell with lattice constants  $a = 14.83420(7)$  Å,  $b = 25.6861(1)$  Å,  $c = 5.21866(2)$  Å, and  $\beta = 90.04(1)^\circ$  at 300 K. A single overall isotropic thermal parameter ( $B_{iso} = 0.88(9)$  Å<sup>2</sup>) was used in the refinement as it lead to more stable and reliable atomic coordinates. Final residuals were  $R_p = 8.4$ ,  $R_{wp} = 12.3$  and  $\chi^2 = 2.78$  for the x-ray pattern and  $R_p = 4.01$ ,  $R_{wp} = 5.11$  and  $\chi^2 = 4.71$  for neutron data.

Ion	Site	x	y	z
Pb1	2e	0.3185(3)	0.1271(4)	-0.007(1)
Pb2	2e	0.8014(4)	0.2857(3)	-0.008(1)
Pb3	2e	0.2981(4)	0.4631(3)	-0.018(1)
Pb4	2e	0.8002(4)	0.6307(4)	0.013(1)
Pb5	2e	0.2806(3)	0.7928(3)	0.006(1)
Pb6	2e	0.7940(5)	0.9651(3)	0.002(1)
Pb7	1a	0	0.1540(4)	0
Pb8	1c	$\frac{1}{2}$	0.3317(4)	0
Pb9	1a	0	0.4884(4)	0
Pb10	1c	$\frac{1}{2}$	0.6583(4)	0
Pb11	1a	0	0.8343(4)	0
Pb12	1c	$\frac{1}{2}$	0.9907(4)	0
Te1	1a	0	0.0231(3)	0
O1	2e	0.098(3)	0.0119(16)	0.240(8)
O2	2e	-0.045(4)	0.0841(8)	0.180(9)
O3	2e	-0.075(2)	-0.023(2)	0.203(8)
Te2	1c	$\frac{1}{2}$	0.2055(3)	0
O4	2e	0.596(3)	0.189(2)	0.243(9)
O5	2e	0.456(3)	0.257(1)	0.243(9)
O6	2e	0.439(2)	0.115(2)	0.22(1)
Te3	1a	0	0.3544(3)	0
O7	2e	0.106(2)	0.325(2)	0.218(9)
O8	2e	-0.051(4)	0.4160(7)	0.160(7)
O9	2e	-0.078(2)	0.309(2)	0.199(7)
Te4	1c	$\frac{1}{2}$	0.5240(4)	0
O10	2e	0.620(1)	0.532(3)	0.147(7)
O11	2e	0.469(4)	0.580(1)	0.238(9)
O12	2e	0.447(3)	0.467(2)	0.192(9)

TABLE 6.3: Continued....

Ion	Site	x	y	z
Te5	1a	0	0.6998(3)	0
O13	2e	0.108(3)	0.687(2)	0.204(9)
O14	2e	-0.054(4)	0.7573(9)	0.186(7)
O15	2e	-0.055(3)	0.641(2)	0.168(7)
Te6	1c	$\frac{1}{2}$	0.8532(3)	0
O16	2e	0.607(3)	0.847(2)	0.213(9)
O17	2e	0.466(4)	0.910(1)	0.224(10)
O18	2e	0.433(2)	0.810(2)	0.237(9)
Co1	2e	0.118(1)	0.0677(6)	0.514(3)
Co2	2e	0.6470(9)	0.2364(6)	0.524(3)
Co3	2e	0.1102(9)	0.4048(5)	0.508(2)
Co4	2e	0.6215(9)	0.5630(6)	0.485(3)
Co5	2e	0.1170(9)	0.7375(6)	0.492(3)
Co6	2e	0.6299(9)	0.8958(5)	0.511(3)
Co7	1b	0	0.2940(8)	$\frac{1}{2}$
Co8	1d	$\frac{1}{2}$	0.4350(9)	$\frac{1}{2}$
Co9	1b	0	0.6254(9)	$\frac{1}{2}$
Co10	1d	$\frac{1}{2}$	0.7740(9)	$\frac{1}{2}$
Co11	1b	0	0.9599(8)	$\frac{1}{2}$
Co12	1d	$\frac{1}{2}$	0.1166(8)	$\frac{1}{2}$
V1	2e	0.1496(6)	0.1923(3)	0.497(1)
O19	2e	0.246(1)	0.203(2)	0.308(5)
O20	2e	0.079(3)	0.240(2)	0.359(6)
O21	2e	0.147(2)	0.1354(7)	0.310(5)
O22	2e	0.165(4)	0.206(3)	0.807(4)
V2	2e	0.6804(4)	0.3553(3)	0.481(2)
O23	2e	0.785(2)	0.369(3)	0.346(8)
O24	2e	0.618(3)	0.407(2)	0.35(1)
O25	2e	0.635(4)	0.3021(8)	0.313(7)
O26	2e	0.660(4)	0.358(3)	0.798(3)

TABLE 6.4: Continued....

Ion	Site	x	y	z
V3	2e	0.1560(6)	0.5305(5)	0.462(2)
O27	2e	0.2708(9)	0.526(6)	0.38(1)
O28	2e	0.092(3)	0.582(2)	0.340(7)
O29	2e	0.135(5)	0.4697(8)	0.322(6)
O30	2e	0.172(4)	0.527(3)	0.780(3)
V4	2e	0.6735(6)	0.6922(3)	0.446(2)
O31	2e	0.7752(13)	0.709(2)	0.299(5)
O32	2e	0.608(3)	0.744(2)	0.328(9)
O33	2e	0.678(4)	0.6275(6)	0.338(8)
O34	2e	0.626(6)	0.684(3)	0.736(5)
V5	2e	0.1545(6)	0.8632(2)	0.454(2)
O35	2e	0.260(2)	0.875(3)	0.311(6)
O36	2e	0.093(4)	0.916(2)	0.333(7)
O37	2e	0.184(3)	0.8001(5)	0.36(1)
O38	2e	0.173(4)	0.865(3)	0.770(3)
V6	2e	0.676(1)	0.0283(4)	0.491(3)
O39	2e	0.774(2)	0.043(2)	0.320(6)
O40	2e	0.582(2)	0.062(1)	0.366(7)
O41	2e	0.652(4)	-0.0338(8)	0.358(6)
O42	6g	0.664(5)	0.026(3)	0.814(2)

and  $V-O_{\text{apex}} = 1.67 \pm 0.01$  Å.  $TeO_6$  octahedra are slightly distorted and have an average bond valence sum of about 5.6. While the constraints forced under bonding in all  $Te^{6+}$  ions, lifting or even softening the constraint resulted in unrealistic metal-anion bond distances. In particular,  $Te4-O$  bond distances ranged from 1.75 to 2.23 Å, which is well beyond known empirical limits [75].  $VO_4$  tetrahedra are just slightly under bonded with an average bond valence sum of 4.82, but appear much more distorted. In particular,  $V5O_4$  and  $V1O_4$  tetrahedra are significantly more distorted than the other tetrahedra.  $V5-O37$  and  $V1-O40$  bonds result in edge sharing  $Pb$  polyhedra that are quite distorted



compared to the langasite ideal. Special attention was paid to these four atomic coordinates during the refinement. No matter what procedure or constraint mechanism was employed, altering the positions of these four atoms to more ideal locations significantly raised  $\chi^2$  by as much as 0.20 for any one atom. This implies that this particular distortion is not only real (relative to where the other cations are located), but also probably important in the formation of the supercell. It is likely due to the presence of  $Pb^{2+}$  lone pairs that push on one side of the  $VO_4$  tetrahedra (in this case, Pb11 and Pb1 lone pairs for the  $V5O_4$  and  $V1O_4$  tetrahedra respectively).

$Co^{2+}$  bond valence sums ranged between 1.61 and 1.97 due to the looser constraint used ( $1.98 \pm 0.03 \text{ \AA}$ ). This value was determined based on previous refinements of the subcell.  $Co^{2+}$  occupy distorted tetrahedral environments which results in a dark blue colour [174] and unambiguously shows that the magnetism in this material comes strictly from  $Co^{2+}$  rather than  $V^{5+}$  [99]. The  $Co^{2+}$  trimers are all nearly equilateral but are ultimately isosceles in nature; the most distorted trimer has angles that are  $54.6^\circ$  (x2) and  $70.7^\circ$ . Like  $Pb_3TeCo_3P_2O_{14}$ , the isosceles nature of the trimers has important consequences on the nature of the magnetism (discussed later).  $PbO_8$  decahedra are extremely distorted, as expected due to the  $Pb^{2+}$  active lone pairs. Bond valence sums for  $Pb^{2+}$  range between 1.6 and 2.5. No distance constraints were used for Pb polyhedra except in the case of Pb(5), Pb(11), Pb(12) and Pb(1) whose active lone pairs directly influenced the surrounding  $VO_4$  tetrahedra mentioned earlier. O40 is a common anion shared between Pb12 and Pb1. However, O40 strongly prefers to coordinate with Pb12 rather than Pb1, which results in almost 12- and 7-fold coordination rather than the conventional 8 and 8 (it is noted that 8-fold coordination of all Pb-O became much more apparent and “symmetrical” at lower temperatures). V6-O40 distance constraints were dramatically softened while Pb1-O40 was introduced. This resulted in better coordination polyhedra with only a small increase in the agreement factors, but did not shed light on the cause behind the coordinates of O40 or why its position has such a high influence on the goodness of fit in the refinement. The  $PbO_8$  decahedra are shown in Figure 6.4, with

the average Pb-O distances listed in Table 6.6.

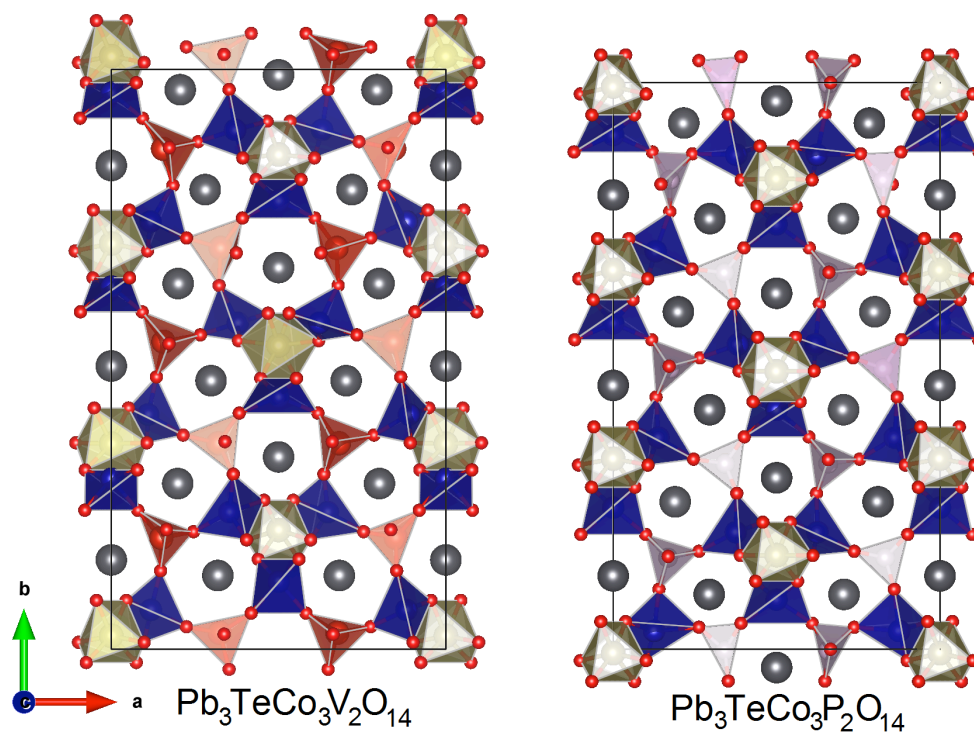


FIGURE 6.3: The final structure found from the joint refinement is presented on the left and compared to isostructural  $Pb_3TeCo_3P_2O_{14}$  on the right. Pb,  $TeO_6$ ,  $CoO_4$ ,  $VO_4$ , and  $PO_4$  are represented as grey spheres, gold octahedra, blue tetrahedra, red tetrahedra, and pink-grey tetrahedra respectively. Extra O atoms in the figure on the left appearing over some  $VO_4$  tetrahedra are actually located in the neighbouring unit cell.

TABLE 6.5: Observed bond lengths and bond valence sums in the  $Pb_3TeCo_3V_2O_{14}$  supercell. The constraints imposed on the refinement are tightly correlated with the values listed here. B. R., B. Avg., B. A. V., Q. E., and B. V. S. stand for bond length range, bond length average, bond angle variance, quadratic elongation, and bond valence sum. Bond angle variance and quadratic elongation are defined in [176, 177] for octahedra and tetrahedra only. Together they are indicators of the distortion of a rigid body taken with respect to the point symmetry of the polyhedron.

Atom	B. R. (Å)	B. Avg. (Å)	B. A. V. ( $^{\circ 2}$ )	Q. E.	B. V. S.
Te1	1.937 - 1.944	1.940	85.99	1.024	5.63
Te2	1.939 - 1.952	1.944	106.98	1.032	5.58
Te3	1.936 - 1.942	1.940	99.12	1.028	5.64
Te4	1.939 - 1.947	1.944	67.20	1.019	5.58
Te5	1.934 - 1.950	1.941	107.00	1.030	5.63
Te6	1.934 - 1.945	1.941	78.65	1.023	5.63
V1	1.673 - 1.758	1.735	335.82	1.090	4.82
V2	1.680 - 1.760	1.736	89.56	1.023	4.81
V3	1.680 - 1.86	1.760	72.69	1.019	4.56
V4	1.679 - 1.756	1.734	394.56	1.125	4.86
V5	1.674 - 1.758	1.733	373.83	1.122	4.85
V6	1.620 - 1.780	1.723	107.38	1.027	5.02
Co1	1.92 - 2.08	2.01	121.15	1.036	1.73
Co2	2.01 - 2.06	2.03	211.09	1.051	1.61
Co3	1.96 - 1.96	1.96	320.28	1.097	1.92
Co4	1.93 - 2.06	2.00	288.59	1.072	1.73
Co5	1.99 - 2.06	2.02	319.65	1.082	1.67
Co6	1.95 - 2.02	1.98	48.12	1.014	1.82
Co7	1.97 - 1.99	1.98	646.12	1.152	1.84
Co8	1.97 - 2.03	2.00	364.53	1.117	1.73
Co9	1.95 - 1.95	1.95	605.97	1.160	1.98
Co10	1.93 - 1.99	1.96	238.30	1.068	1.92
Co11	1.95 - 1.99	1.97	518.92	1.134	1.86
Co12	1.98 - 2.00	1.99	99.56	1.028	1.80

TABLE 6.6: Continued....

Atom	B. R. ( $\text{\AA}$ )	B. Avg. ( $\text{\AA}$ )	B. V. S.
Pb1	2.26 - 3.21	2.82	1.80
Pb2	2.18 - 3.01	2.68	2.36
Pb3	2.25 - 3.20	2.74	2.01
Pb4	2.29 - 3.25	2.69	2.33
Pb5	2.34 - 3.40	2.72	1.99
Pb6	2.23 - 2.93	2.66	2.25
Pb7	2.13 - 3.12	2.74	2.57
Pb8	2.39 - 3.20	2.74	1.88
Pb9	2.17 - 3.28	2.77	2.43
Pb10	2.42 - 3.27	2.83	1.94
Pb11	2.34 - 3.43	2.94	1.50
Pb12	2.43 - 3.00	2.78	1.60

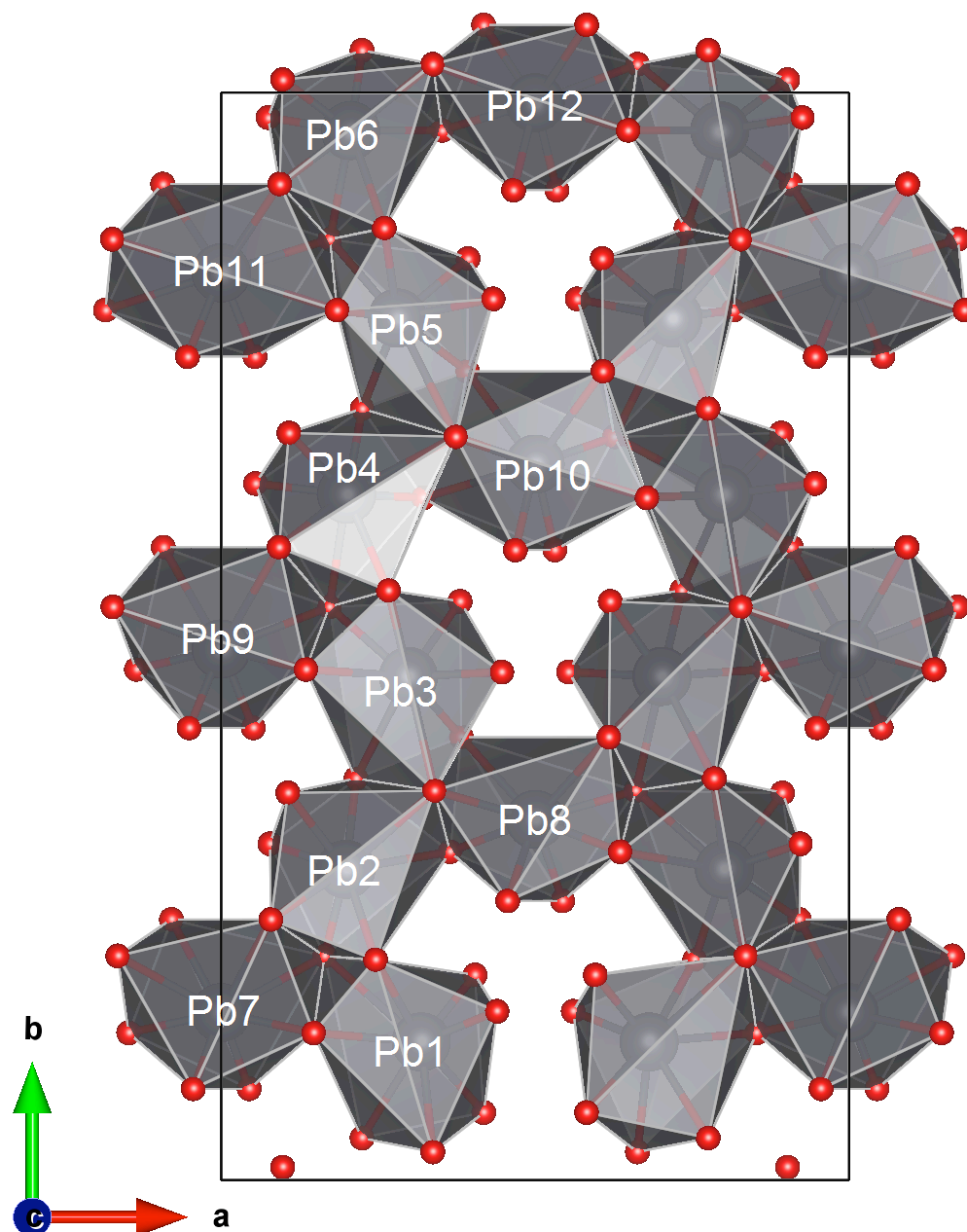


FIGURE 6.4: Pb-decahedra at 300 K.

It is also important to compare the results here to those found by Krizan *et al.* [99] and other works [145] in order to gauge whether or not these distortions have been found elsewhere. Due to a lack of neutron data, Krizan *et al.* [99] assumed that the rigid body orientations were conserved between  $Pb_3TeCo_3V_2O_{14}$  and  $Pb_3TeCo_3P_2O_{14}$  and only allowed for the translations of the cations. This resulted in  $TeO_6$  rotating strictly

within the  $ab$ -plane giving excellent agreement factors with the synchrotron x-ray data (even better than those found in this study) although the O positions were not refined. On the other hand, others [145] were able to refine the O sublattice proposed by Krizan *et al.* [99] using WISH data and found only slight disagreement between the converged values and those reported in [99]. Using the model by Krizan *et al.* [99] it was found that they resulted in better fits to the x-ray data, but poorer fits to the neutron data than the model used for the current description of the structure. Weighting the x-ray and neutron data differently resulted in similar agreement factors between both models. Using similar constraints, the same (by symmetry) V and O atoms began distorting in a similar fashion, but all other atomic positions remained invariant despite having different coordinates. This effectively places a data-driven limit on how well the distortions and bond distances can be tracked within the resolution of powder diffraction. The structure shown here and found by Krizan *et al.* are compared in Figure 6.5, where the true structure is likely some superposition between the two, since both are quite similar.

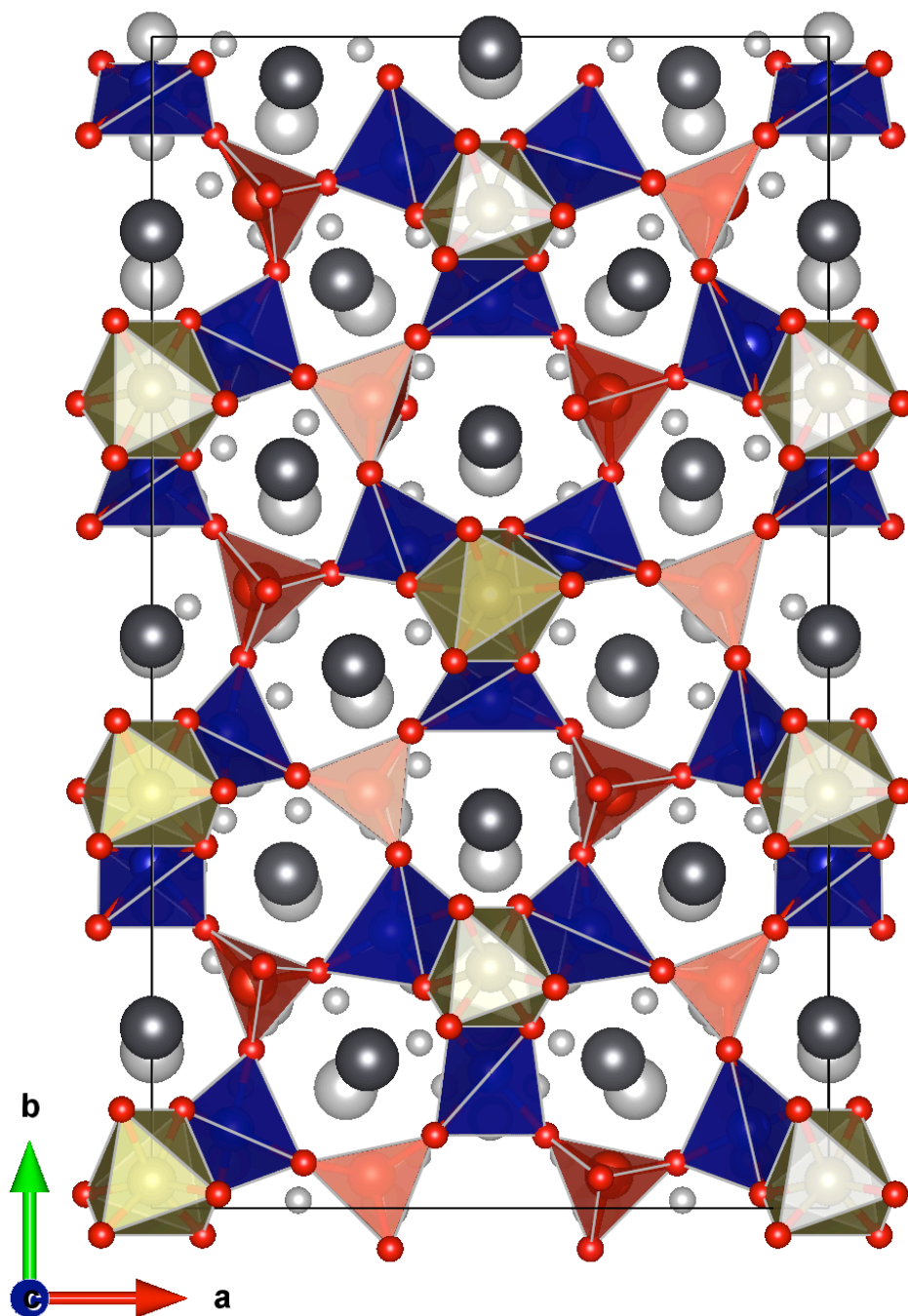


FIGURE 6.5: Comparison of the structure found here with that reported in [99] (greyscale). While the greyscale figure better agrees with x-ray data, the colour figure agrees better with neutron data, indicating that the true structure is likely some intermediate.

### 6.4.2 Physical property measurements

The physical properties of  $Pb_3TeCo_3V_2O_{14}$  have been measured more than any other dugganite [99, 103, 108, 139, 145, 156]. The first study to report physical property measurements came from Ivanov *et al.* where the magnetic susceptibility was measured. A single transition temperature at 11 K was reported with an effective moment of  $\mu_{\text{eff}} = 4.5 \mu_B$  and Weiss temperature of  $\theta_{\text{CW}} = -13$  K. Prior measurements [103] of the susceptibility, heat capacity (against a  $Pb_3TeZn_3V_2O_{14}$  lattice standard), and the temperature dependence of the dielectric constant yielded similarities between the effective moment and Weiss temperatures, but dramatically different transition temperatures. Many of these measurements are reproduced here in addition to susceptibility measurements taken at fields as high as 35 T.

The magnetic susceptibility curve looks qualitatively similar to that from Ivanov *et al.* [139] as shown in Figure 6.6. However, if one were to look at the derivative of the susceptibility, two sharp peaks occur at 8.6 and 6.0 K which are labelled  $T_{N1}$  and  $T_{N2}$  respectively. In fact, this situation is almost identical to that of  $Pb_3TeCo_3P_2O_{14}$  at fields less than 0.5 T. The inverse susceptibility was fit to the Curie-Weiss law yielding an effective moment of  $4.28(9) \mu_B$  and Weiss temperature of  $-22(5)$  K (these uncertainties reflect fitting at different fields and in different temperature regimes). Susceptibility measurements were made up to fields of 9 T. Unlike  $Pb_3TeCo_3P_2O_{14}$ , the transition at  $T_{N2}$  persists until about 5 T, where a finite magnetization remains. For magnetization measurements, strong features are observed at 3 T at every temperature, which are not reproducible on other instruments, is inconsistent with other reports [99], and are probably due to liquid helium boiling that disrupts the VSM motor. Other temperature dependent features appear near 5 T and have been used to construct a phase diagram (Figure 6.7) that agrees well with other reports [156]. Finally, a weak feature was observed near 23 T at low temperatures possibly indicating a fourth phase transition (Figure 6.8). This feature only appears upon ramping the field up (that is, there is weak hysteresis associated with this feature). The moment is almost fully saturated by 35 T



at 1.4 K, getting quite close within error.

But whereas the magnetic susceptibility is quite similar between both Co-containing dugganites, the heat capacities differ quite dramatically. In  $Pb_3TeCo_3V_2O_{14}$ , both  $T_{N1}$  and  $T_{N2}$  appear as sharp lambda-like features in the heat capacity (Figure 6.9), which is reproducible in every study reported thus far [99, 103, 156].  $Pb_3TeZn_3P_2O_{14}$  was used as a lattice standard; the residual heat capacity can be used to estimate the magnetic entropy released by the system (Figure 6.9). Approximately 93% of the theoretical entropy of an  $S=3/2$  system is released within 31% of that being released at temperatures above  $T_{N1}$ , indicating the possible building of short-ranged correlations. Heat capacity measurements under magnetic fields were recently performed by Markina *et al.* [156] and verify the phase diagram found using magnetic susceptibility and magnetization measurements. Turning to the dielectric constant, kinks can be observed at both  $T_{N1}$  and  $T_{N2}$  in Figure 6.10 (although the kink at  $T_{N2}$  is more pronounced), despite the powder nature of the sample. This indicates weak magnetoelectric coupling possibly driven by the Dzyaloshinskii-Moriya effect, which would make one or possibly both of these magnetic transitions first order.

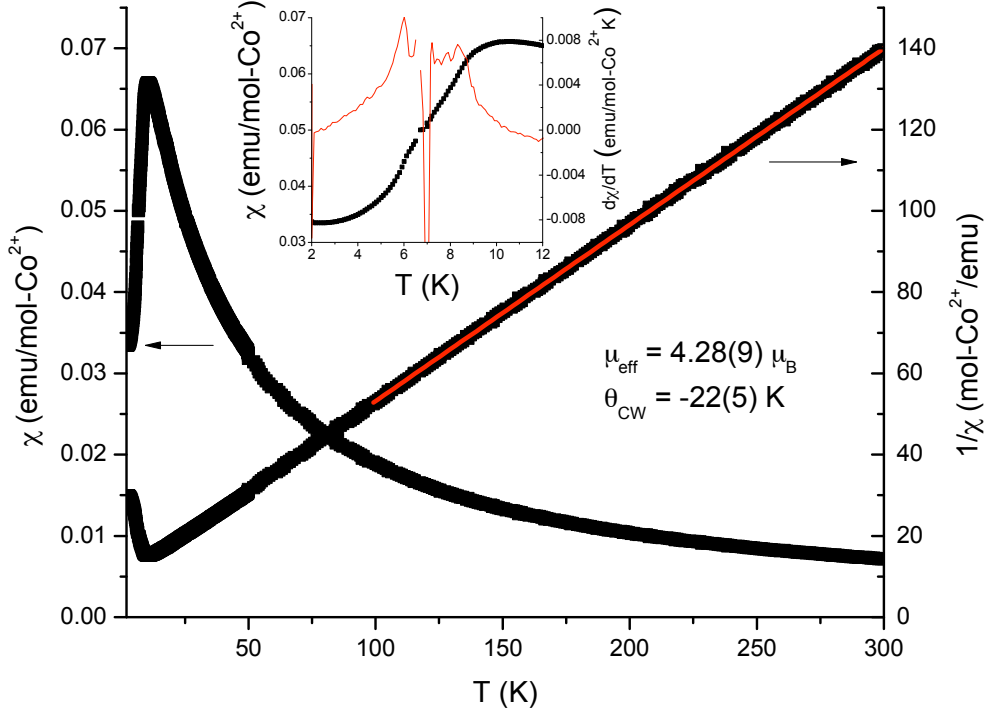


FIGURE 6.6: The magnetic susceptibility and inverse taken under a field of 0.1 T. The inverse susceptibility was fit to the Curie-Weiss law (errors reflect the error in the values associated with fitting different temperature regimes). **Inset:** A closer look at the transitions found in the susceptibility at  $T_{N1} = 8.6$  K and  $T_{N2} = 6.0$  K. The derivative in red shows the transitions more clearly.

### 6.4.3 Magnetic structures

The magnetic structures of  $Pb_3TeCo_3V_2O_{14}$  were first solved and reported in [103] before knowledge of the supercell. Both  $T_{N1}$  and  $T_{N2}$  result in detectable magnetic order using neutron diffraction (Figure 6.11), which is unlike  $Pb_3TeCo_3P_2O_{14}$  where only  $T_{N1}$  resulted in a change in the diffraction pattern. A model of the subcell magnetic structures was refined using data taken with the C2 and WISH diffractometers. It was found that most magnetic Bragg peaks below  $T_{N1}$  could be accounted for using the propagation vector  $\vec{k} = (0.752, 0, \frac{1}{2})$ , resulting in one IR splitting the  $Co^{2+}$  site into three orbits. The moments are allowed to point anywhere in space and the model yielded adequate agreement factors with a maximum moment of  $3.7 \mu_B$ . The real-space orientation of

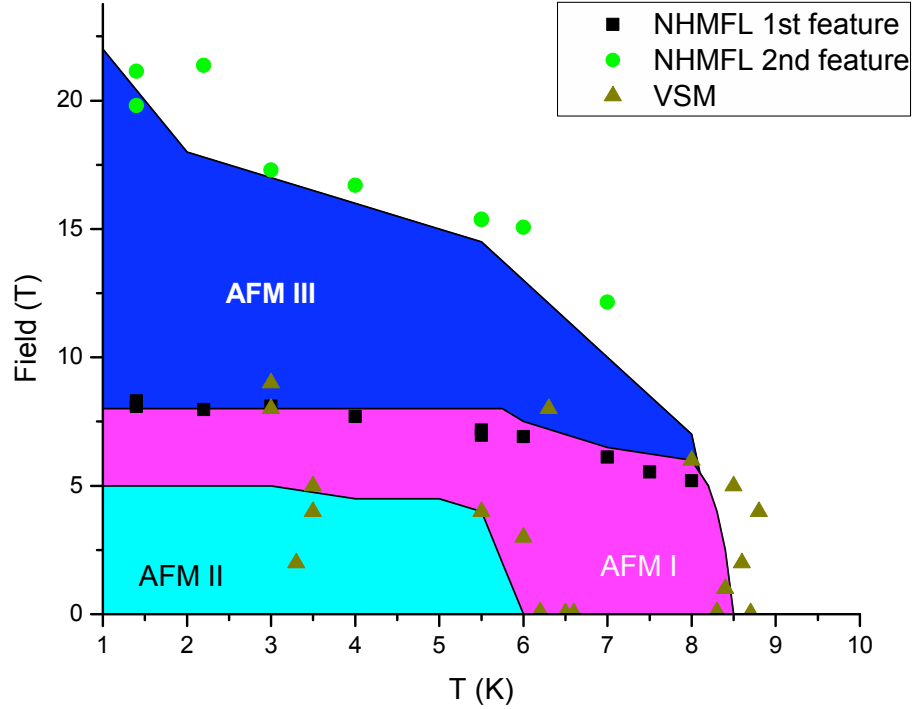


FIGURE 6.7: The magnetic phase diagram was constructed using two different sets of magnetization and magnetic susceptibility data. Heat capacity data was used in another study [156] to confirm the shape of the phase diagram.

the moments is depicted in Figure 6.11 and appears to be a partially ordered structure. Magnetic Bragg reflections below  $T_{N2}$  can be accounted for using a propagation vector of  $\vec{k} = (\frac{5}{6}, \frac{5}{6}, \frac{1}{2})$  and can be modelled using only the first irreducible representation. Again, the converged structure places an unphysical moment on  $Co^{2+}$ , but the structure appears fully ordered with a maximum moment of  $3.7 \mu_B$  (Figure 6.12). The moment magnitude varies in sinusoidal fashion as a result of the propagation vector. Unlike  $Ba_3NbFe_3Si_2O_{14}$ , the orientation of the moments within the trimers matter, implying the presence of a sine-like wave over the  $Co^{2+}$  atoms as opposed to a helix propagating within the  $ab$ -plane.

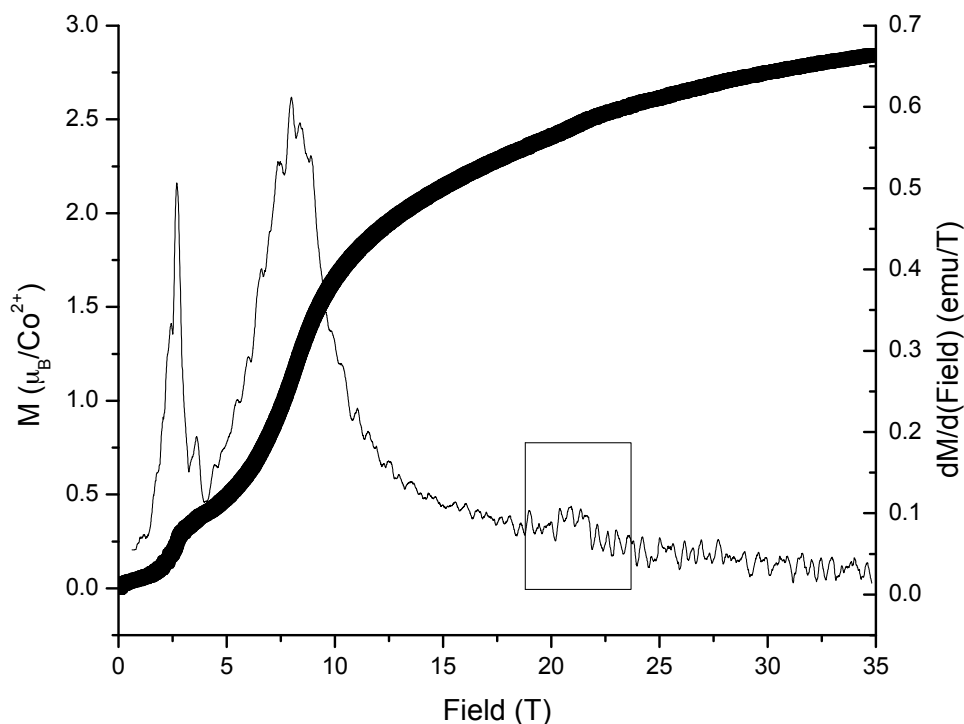


FIGURE 6.8: High-field magnetization and derivative up to 35 T at 1.4 K. A weak feature is observed at higher fields (boxed region on the derivative curve).

One of the first indications of the supercell was given as a result of the magnetic structural transitions within this material; such a spin-flop transition where a total reorientation of the moments occurring within a temperature range of 2.6 K is highly unlikely due to the energy requirement for such a transition. The magnetic structure below 8.6 K can be described using the same little group  $G_x$  as that of  $Pb_3TeCo_3P_2O_{14}$ , which means that the moments belong to the same Hilbert space. Again, like  $Pb_3TeCo_3P_2O_{14}$ , both irreducible representations result in degenerate magnetic structures that only differ by a  $(0, \frac{1}{2}, 0)$  displacement within the supercell. The refinements are shown in Figures 6.13 and 6.14 for both irreducible representations. Moments were soft-constrained to have a value of  $2.3(4) \mu_B$ . All trimer clusters centred along a single two-fold rotation axis were assumed to behave in the same fashion (relaxing this constraint did little to improve the fit). The real space orientation of the moments is pictured in Figure

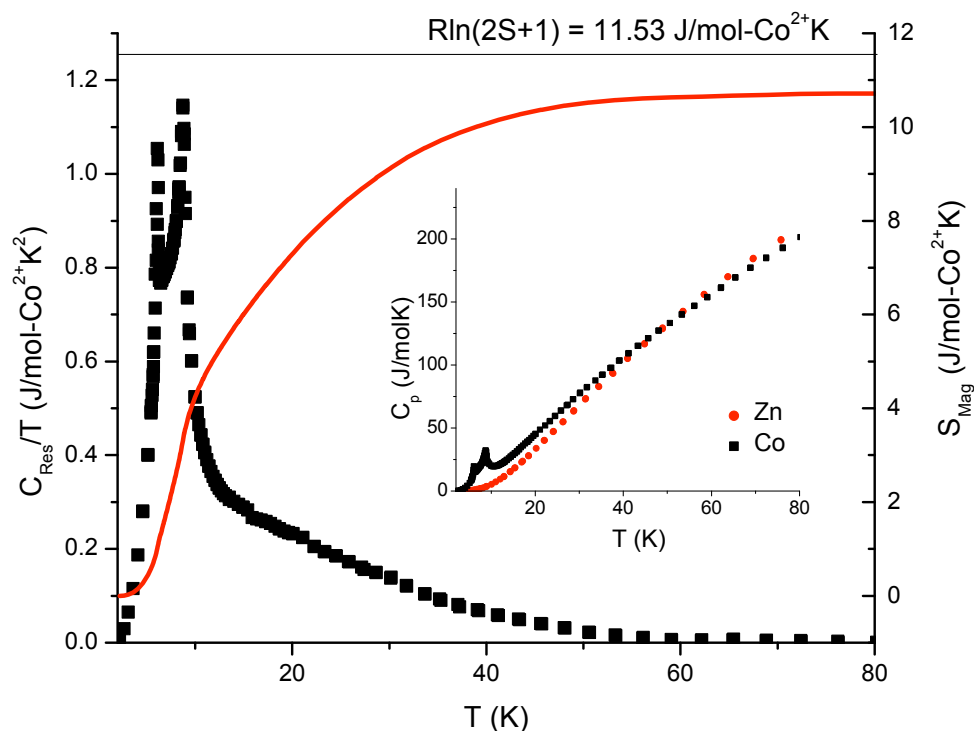


FIGURE 6.9: The lattice subtracted heat capacity divided by temperature as a function of temperature (black squares). Integrating this curve yields the magnetic entropy (red curve), which was found to be about 93% of the theoretical value. Any error from the theoretical value is likely rooted from an imperfect lattice subtraction. **Inset:** The raw heat capacities of the Co-V and Co-P dugganites.

6.15. Both irreducible representations yield similar results; one row of trimers contains moments that are roughly pointed in  $120^\circ$  arrangement within the  $ab$ -plane, while the other row contains trimers with one moment directed along the  $c$ -axis and the other two oriented along the same  $a$ -direction but opposite  $b$ -direction (no  $c$ -direction). For  $\Gamma(1)$ , the first set of trimers has two moments pointing along  $b$  and the other moment along  $-b$ , while in  $\Gamma(2)$ , all moments are directed along  $b$ . It is not yet clear why these differences manifest or whether components of the moments that are not situated on the two-fold axis have  $c$ -axis component to them. The general orientation of the moments are quite reliable while the moment magnitudes, including whether they align parallel or antiparallel within a single trimer, are much harder to determine with certainty. What is clear is that the majority of the moments are oriented in planar fashion; there are not

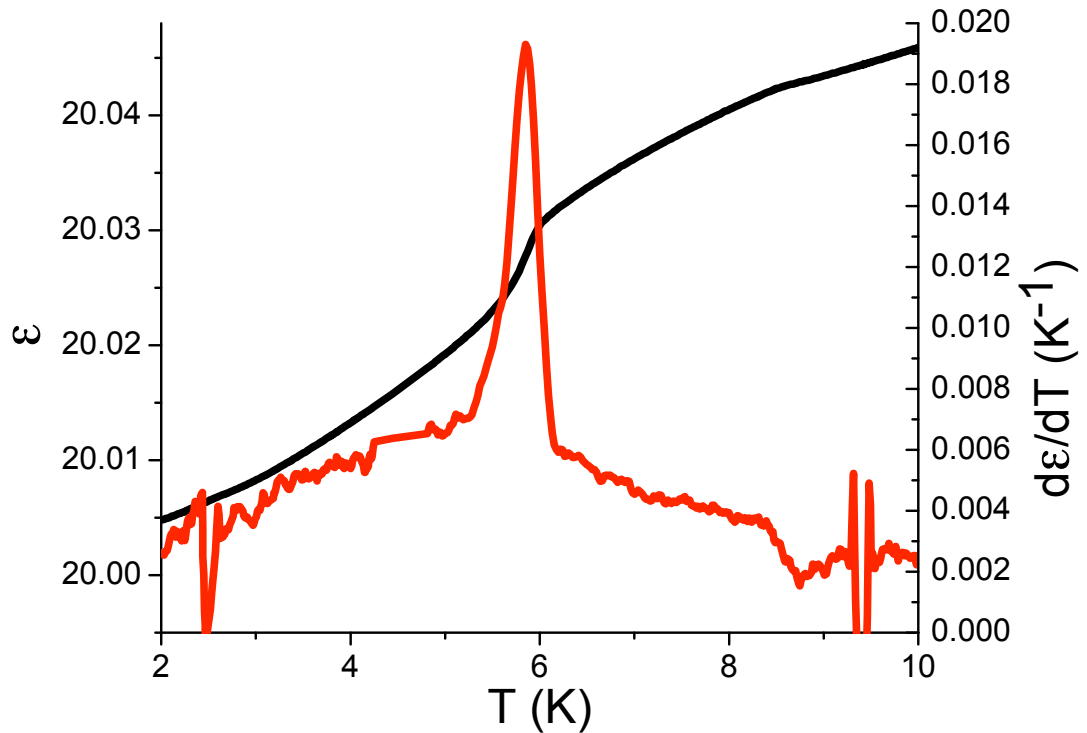


FIGURE 6.10: Two kinks are observable in the dielectric constant (black) at both transition temperatures. This is more clearly observed in the derivative of the curve (red).

two distinct groups of trimers as there are for  $Pb_3TeCo_3P_2O_{14}$ , and this has a direct consequence for the observed cluster excitations (discussed later). This is also probably related to the reason why the subcell could be used to model the magnetic excitations in  $Pb_3TeCo_3V_2O_{14}$ , but not  $Pb_3TeCo_3P_2O_{14}$ . It is also important to note that the moment magnitude increases with decreasing temperature as evidenced by the increase in the intensities of the magnetic Bragg peaks (Figure 6.16).

Unlike  $Pb_3TeCo_3P_2O_{14}$ , a spin reorientation develops at 6 K that is clearly visible with neutron scattering. Here, the magnetic structure can be described by either of two irreducible representations belonging to  $G_x$  defined by the space group and propagation vector  $\vec{k}' = (\frac{1}{2}, -\frac{1}{2}, -\frac{1}{2})$  (Figures 6.17 and 6.18). The basis vectors for the moments are invariant from the first magnetic structure. These magnetic structures appear very

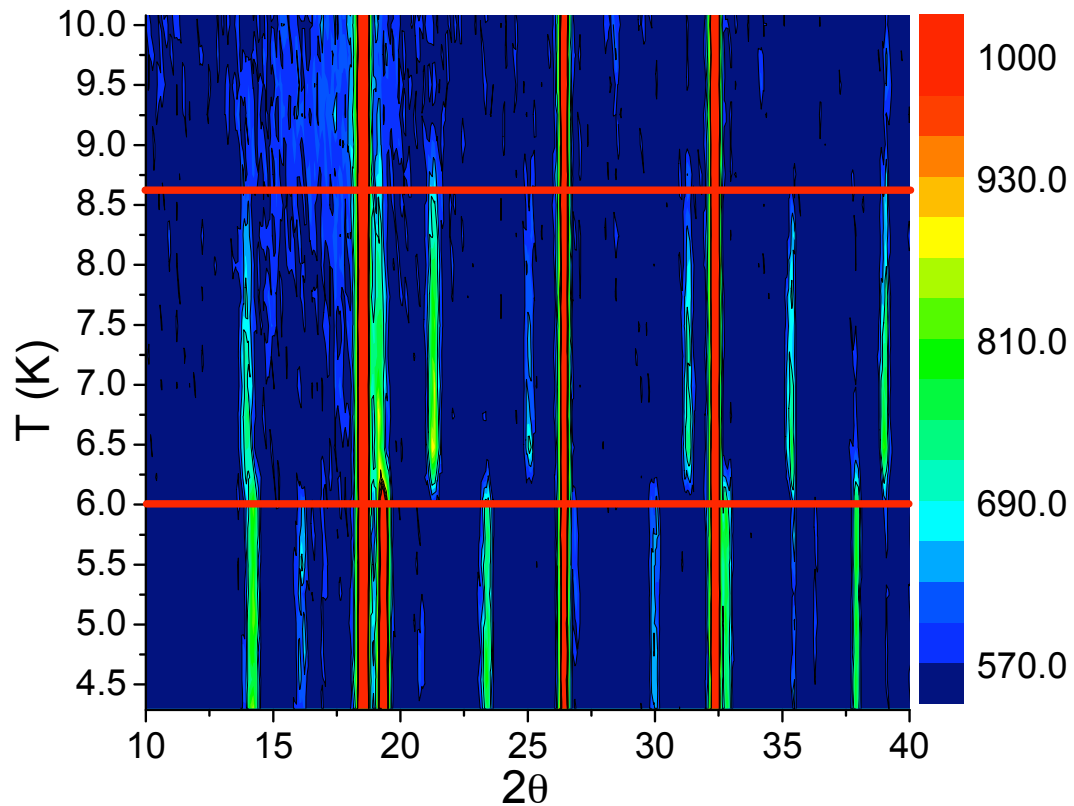


FIGURE 6.11: Contour plot depicting both magnetic transitions observed using the C2 diffractometer with a wavelength of 2.37 Å. The transitions are marked with red horizontal bars for clarity. Diffuse scattering beginning near 40 K (not shown) is observed as the first transition is approached from above.

similar to the earlier ones (Figure 6.19), the main difference being the addition of the moment propagation along the  $b$ -axis. This puts to rest the question of the peculiar spin reorientation raised in the magnetic subcell solutions. The moments on Co7, Co9 and Co11 in  $\Gamma(1)$  should be oriented in a similar fashion to the moments on Co8, Co10, and Co12 in  $\Gamma(2)$ , since they are defined by the same basis vectors. However, there is a significant component of the moment directed along the  $a$ -axis in  $\Gamma(2)$  that is absent in  $\Gamma(1)$ , and leaving it out severely decreases the quality of the fit. No clear explanation for this exists presently, but this may represent a route to eventually determining which IR is correct in single crystals. Another interesting feature is that both magnetic structures below  $T_{N1}$  and  $T_{N2}$  coexist at 6 K (Figure 6.20) with measurable hysteresis. There are many ways that this can be explained, including that the sample was not thermally

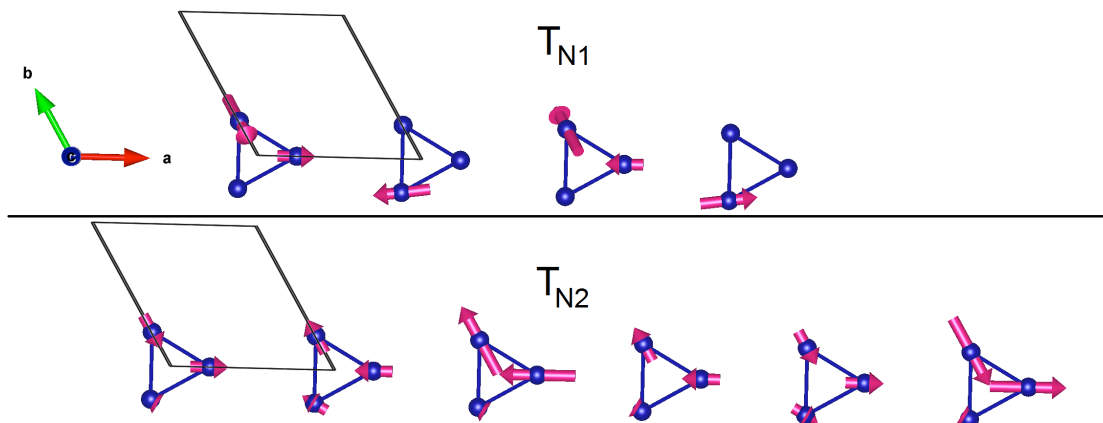


FIGURE 6.12: Real space schematic of the magnetic cells found through low temperature subcell refinements. For  $T_{N1}$ , the magnetic structure is shown without the additional propagation along  $c$  (out of the page). For  $T_{N2}$ , the magnetic structure is shown without the additional propagation along both  $b$  and  $c$ . Moments are drawn to scale.

equilibrated or that there are significant structural differences between powder grains altering  $T_{N2}$  (the latter scenario can be essentially ruled out from synchrotron x-ray diffraction data). In order to rule this out, the sample was allowed to sit for over six hours at 6 K: no change in the diffraction pattern was observed. This means that the magnetic transition at 6 K is first order.



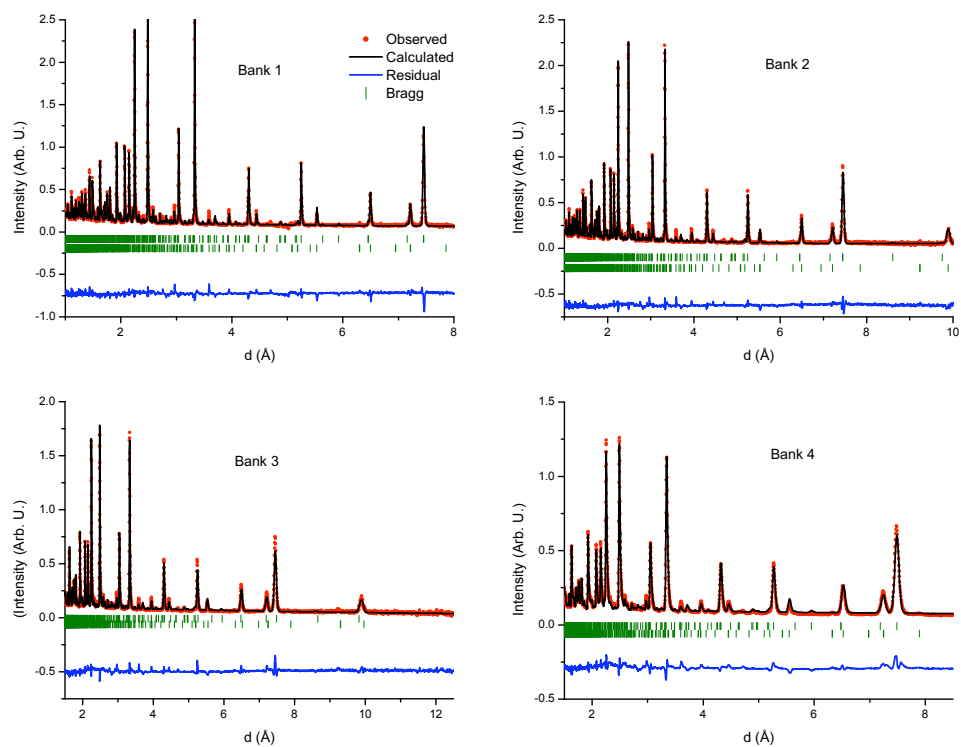


FIGURE 6.13: The refinement profile using four detector banks from the WISH diffractometer of the magnetic structure at  $T_{N1}$  using  $\Gamma(1)$ .

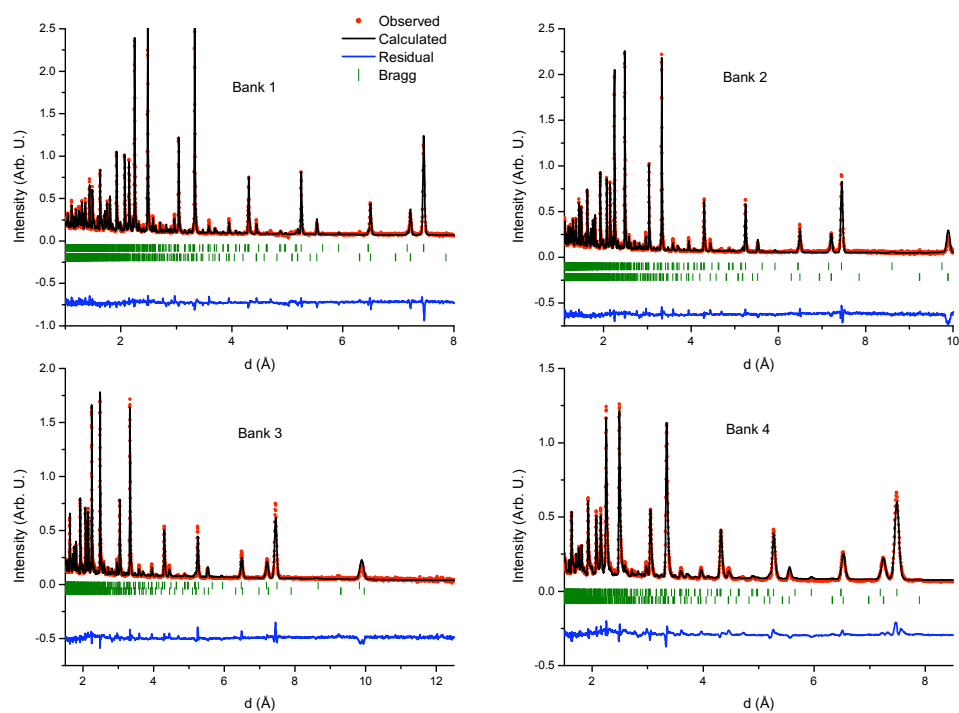


FIGURE 6.14: The refinement profile using four detector banks from the WISH diffractometer of the magnetic structure at  $T_{N1}$  using  $\Gamma(2)$ .

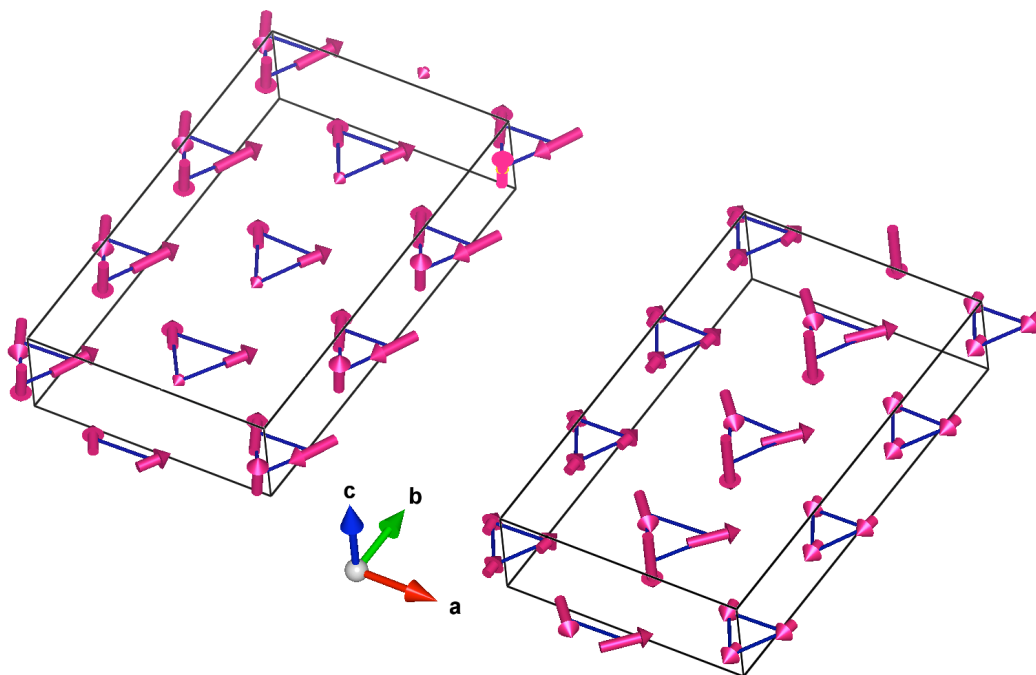


FIGURE 6.15: The magnetic structures found from the refinements. Only the crystal unit cell is shown in these figures for simplicity (the propagation of the moments occurs along the  $a$ - and  $c$ -axes similar to the full magnetic unit cell of  $Pb_3TeCo_3P_2O_{14}$ ). Moments are drawn to scale.

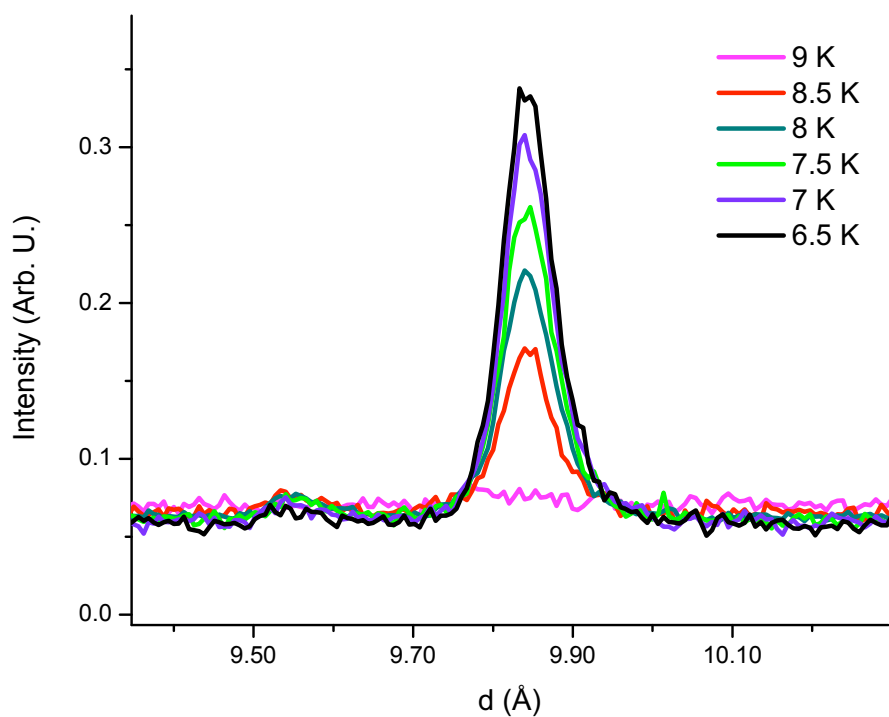


FIGURE 6.16: The intensity of this magnetic Bragg reflection increases with decreasing temperature. This is typical of all magnetic Bragg reflections found in this system for this phase.

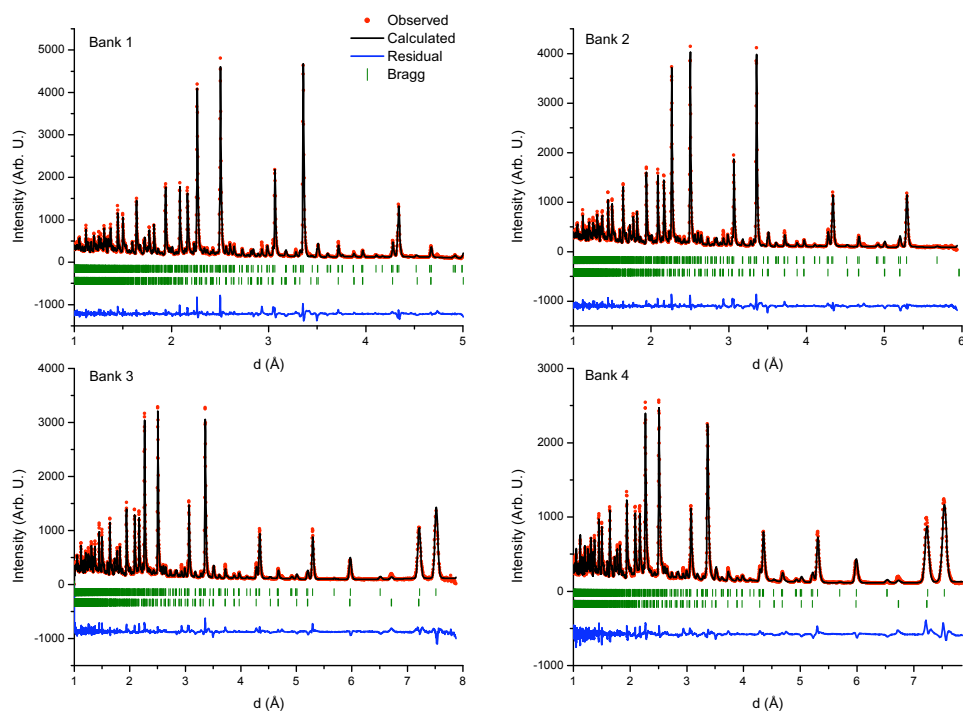


FIGURE 6.17: The refinement profile using four detector banks from the WISH diffractometer of the magnetic structure at  $T_{N2}$  using  $\Gamma(1)$ .

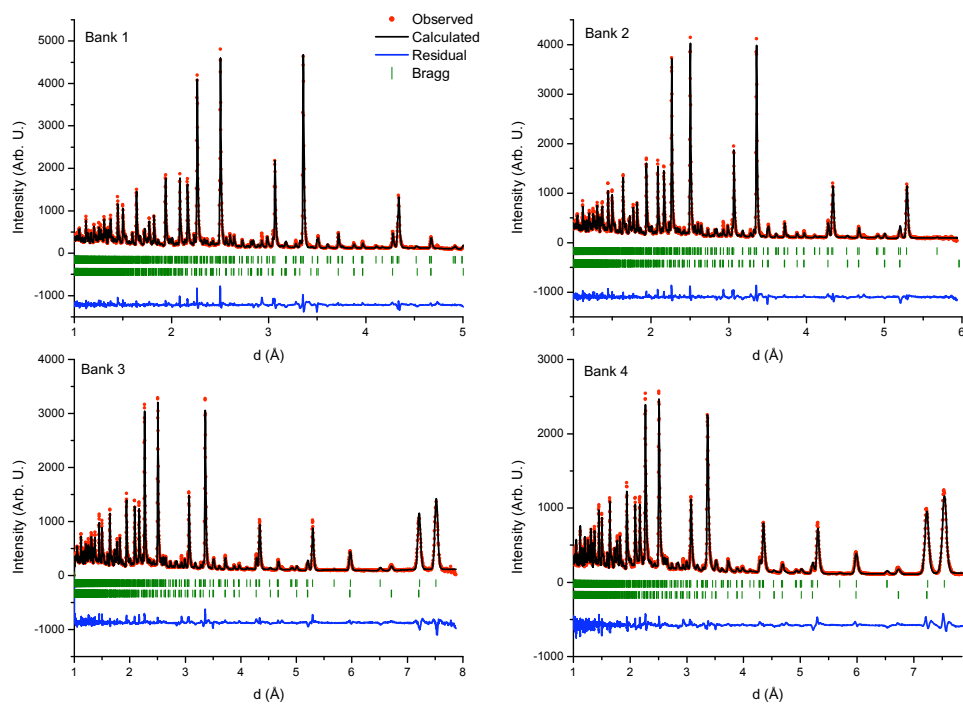


FIGURE 6.18: The refinement profile using four detector banks from the WISH diffractometer of the magnetic structure at  $T_{N2}$  using  $\Gamma(2)$ .

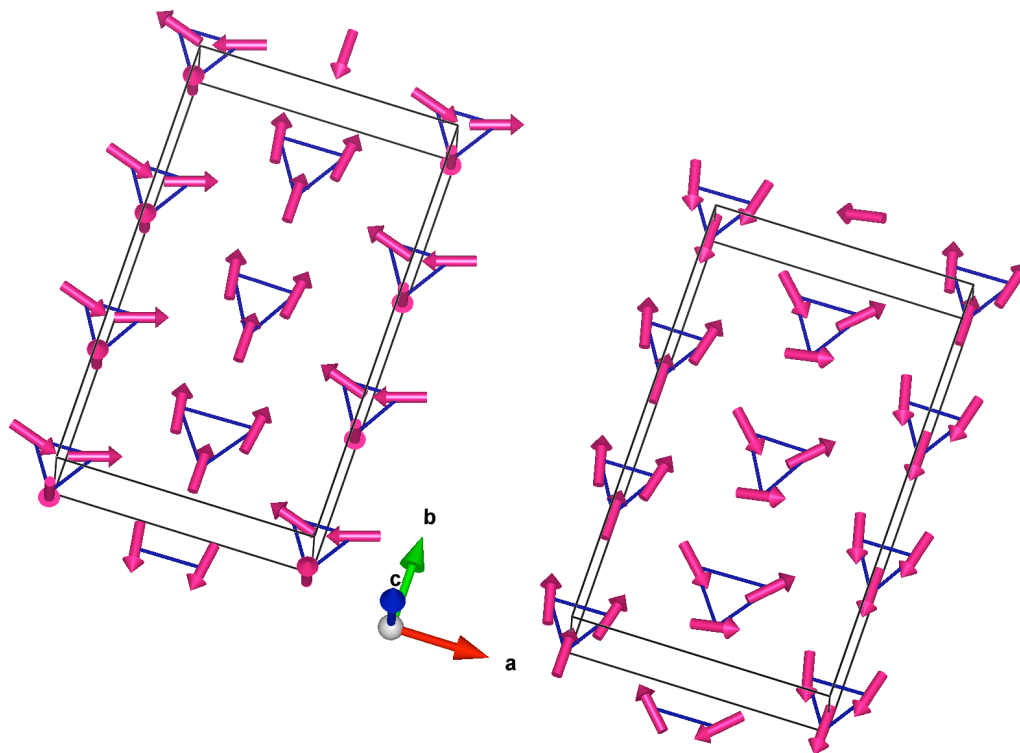


FIGURE 6.19: The magnetic structures found from the refinements. Only the crystal unit cell is shown in these figures for simplicity. The moments propagate along all three crystal axes. Moments are drawn to scale.

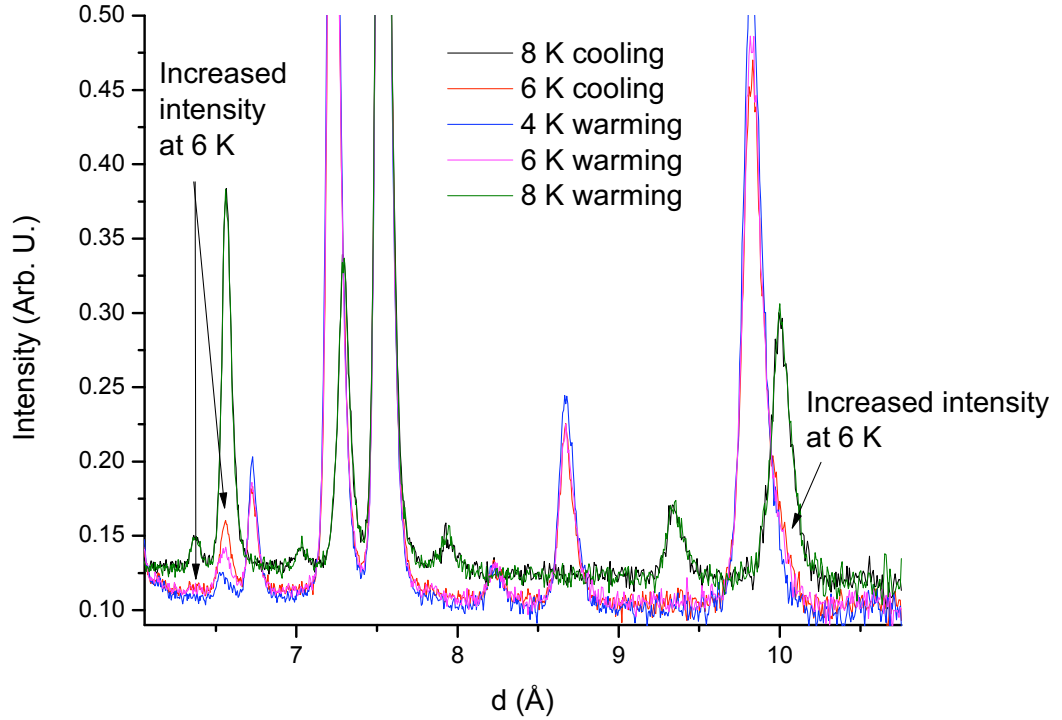


FIGURE 6.20: At 6 K one is able to observe remnants of the first magnetic structure with clear hysteresis with respect to temperature. The cryostat was allowed to sit at that temperature for hours before a final measurement was taken so that the sample temperature is well equilibrated with the environment.

#### 6.4.4 Inelastic excitations

The same trimer-cluster type excitations were observed in  $Pb_3TeCo_3V_2O_{14}$  that were observed in  $Pb_3TeCo_3P_2O_{14}$ . For the magnetic structure between 8.6 and 6 K, it is expected that the excitations would be largely similar due to the similarity of the magnetic structures that were observed. However, only two excitations were observed below 3 meV at 1.978(5) and 2.432(4) meV, while a single broad excitation was observed centred at 5.4 meV (Figure 6.21). Using the same phenomenological model as  $Pb_3TeCo_3P_2O_{14}$ , the magnetic susceptibility can be fit using one type of inelastic  $Co^{2+}$  trimer with an exchange energy of 3.2 meV and  $\alpha$  of 0.45 (Figure 6.21). This model should yield excitations at 1.6(1) meV, 2.4(1) meV, and 5.2(1) meV, which is in rough agreement with



the values shown here.

Below 6 K, the broad excitations become much more highly resolved (Figure 6.22a). SEQUOIA is a spectrometer optimized to detect magnetic excitations occurring above 10 meV. Using a neutron incident energy of 6 meV really pushes the instrument to its useable boundaries and sacrifices resolution as a fraction of the incident neutron energy. However, it is possible to resolve additional details regarding the low energy excitations of  $Pb_3TeCo_3V_2O_{14}$  using such low energy neutrons. In particular, it appears as if each of the excitations below 3 meV may be composed of even smaller excitations just outside of the resolution of SEQUOIA (Figure 6.22b). An experiment on the Cold Neutron Chopper Spectrometer (CNCS, Oak Ridge, TN) [178], which specializes in resolving low energy excitations, would greatly aid here. Unfortunately for now the low temperature spectrum is too complex to analyze quantitatively, but this does not mean that phenomenological conclusions cannot still be made. All of the excitations are magnetic, as denoted by the dispersionless feature obtained by dividing out the magnetic form factor squared (Figure 6.22c). An additional sinusoidal component is expected due to powder averaging of the trimer cluster excitations [167]. When this component is divided out, one finds that the data increases in intensity as  $Q$  tends towards 0 from above. Five excitations are observed at 4.746(9), 5.04(1), 5.59(1), 6.05(1), and 6.49(1) meV. The excitations at 5.59 meV appears to be composed of two peaks at 5.51(2) and 5.673(5) meV. This by itself is quite striking considering that this is an extended solid with a well-defined crystal lattice. Below  $T_{N1}$ , an argument can be made that the broad feature between 5 and 7 meV in  $Pb_3TeCo_3V_2O_{14}$  (and even  $Pb_3TeCo_3P_2O_{14}$ ) is indicative of local disorder in the magnetic structure, which can disrupt the formation of spin waves. However below  $T_{N2}$ , this broad feature is resolved into well-defined dispersionless (within the resolution of SEQUOIA) excitations: spin waves are still absent! In fact, no other features are observed in the data until around 300-500 meV, which only appear at high- $Q$  and are present at all temperatures. Therefore, these high energy excitations are either spurious features stemming from the sample can or are nonmagnetic features from

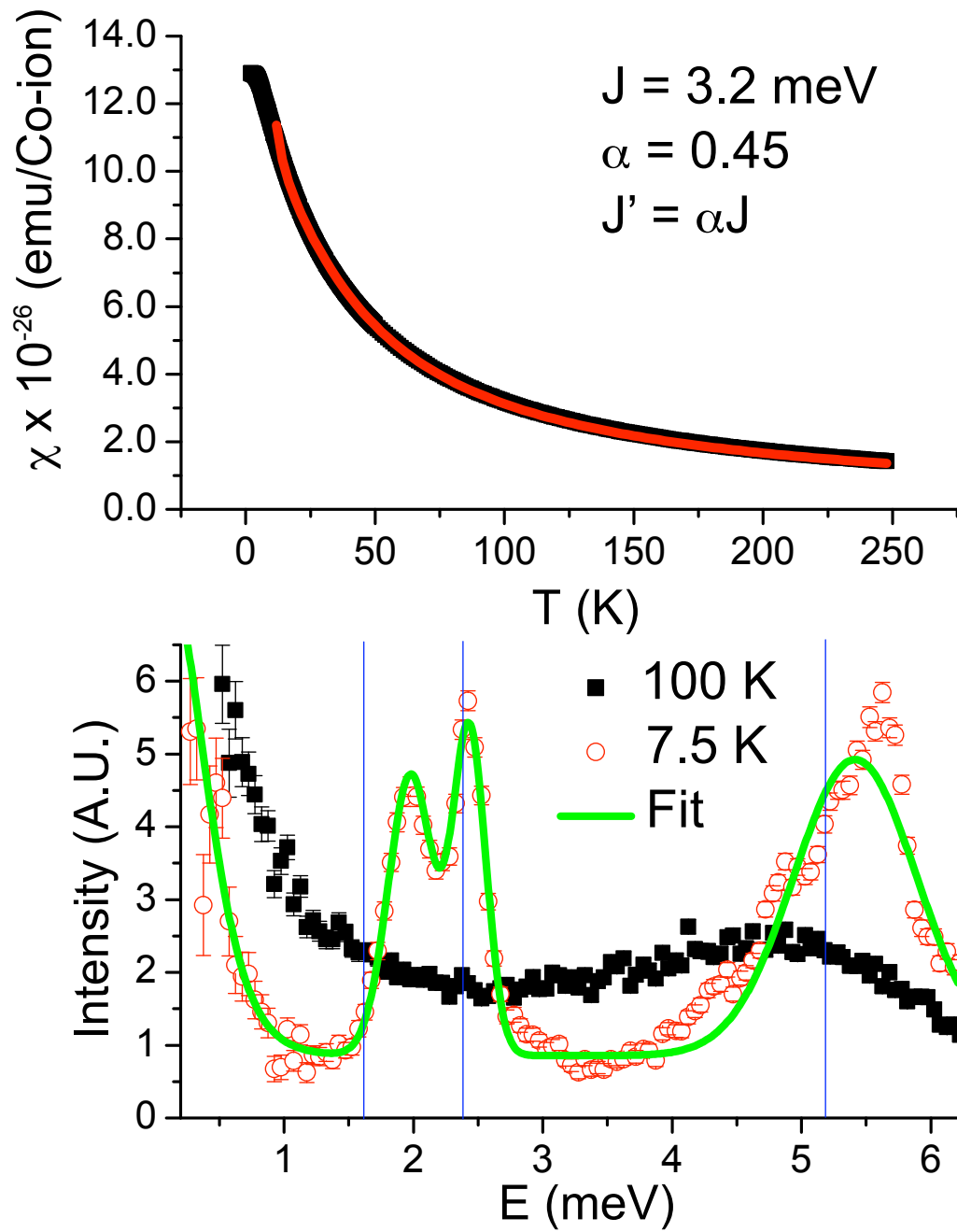


FIGURE 6.21: **Top:** The magnetic susceptibility (black) is fit to the trimer model described in Chapter 5 [168] (red) approximating only one group of isosceles trimers. **Bottom:** The inelastic excitations at 7.5 K were fit to Gaussians over a linear background in order to extract their centres. Blue lines are where the excitations are expected based on the fit of the magnetic susceptibility.

the sample. This really solidifies the idea that each trimer is acting as, more-or-less, an independent unit and that intertrimer exchange is quite weak, but still important in this system.

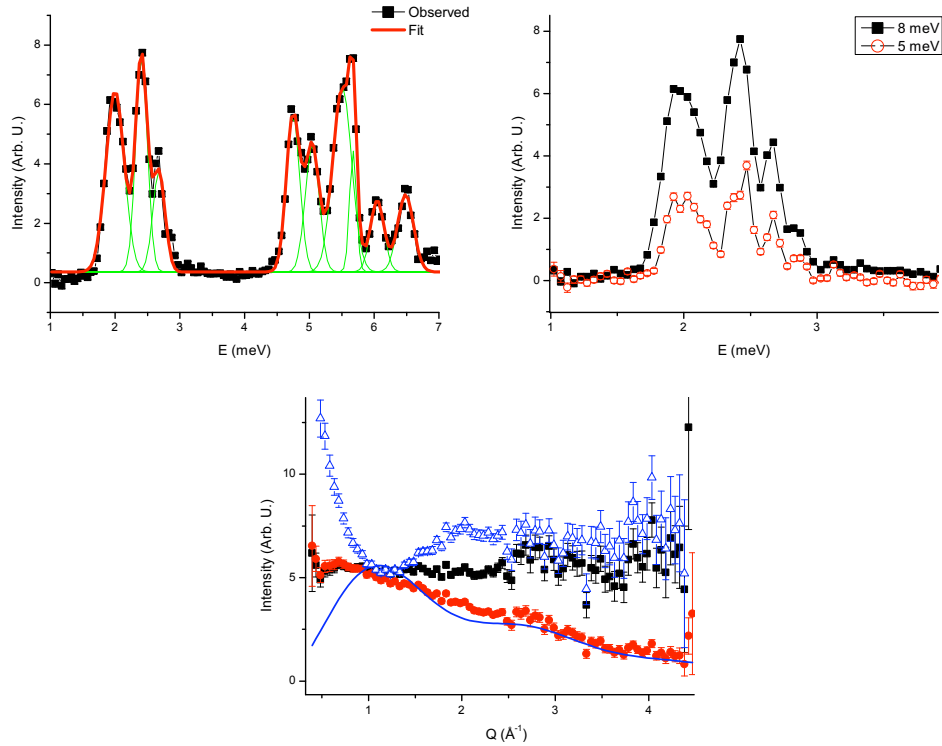


FIGURE 6.22: **a)** Inelastic excitations (black) were fit to nine Gaussians (green curves) over a linear background. The overall fit is coloured red. **b)** These excitations are likely composed of many smaller excitations outside of the resolution limit of SEQUOIA, as evidenced in the data taken with neutrons having an incident energy of 5 meV. **c)** The magnetic form factor squared was divided out of the data between 4 and 7 meV (red) to yield dispersion less excitations in  $Q$  (black): a signature of magnetic origin. However, an additional sinusoidal component to the excitations is expected to occur due to powder averaging of the trimer excitations [167]. This component is entirely dependent on the Co-Co nearest neighbour distance (taken to be an average of 3.75 Å), resulting in the blue curve. Although the error bars are large, the peak in the blue curve corresponds well with the hump in the form factor-subtracted data. When this curve is divided out, one obtains the signal denoted by blue open triangles.

So far, three things are known or can be assumed: 1. there are six trimers in the crystal unit cell, 2. they are isosceles, and 3. they act independently as trimer clusters. Considering the model by Haraldsen *et al.* [168] (Equation 5.3), one would expect 18

excitations for each of the trimers: 12 lower energy excitations and six higher energy ones. Indeed, it appears as if six higher energy excitations are observed between 4.5 and 7 meV. The lower energy modes below 3 meV are more puzzling since only three excitations are observed using an incident neutron energy of 8 meV. However, considering that each of these appears to be composed of smaller excitations at higher resolution, it is not a stretch to consider that there may be twelve closely spaced excitations composing the observed features. This is especially true since all of the trimers in the supercell are very similar in size and shape. The addition of a magnetic field is expected to increase the Zeeman splitting between energy levels and alter the positions of the observed excitations, perhaps even separating them in strong enough fields. Further neutron investigations are welcomed.

## 6.5 Conclusion

$Pb_3TeCo_3V_2O_{14}$  was prepared using a standard solid-state reaction. It was found that this material adopts a large  $P2$  supercell isostructural to  $Pb_3TeCo_3P_2O_{14}$ . However, the magnetic properties differ quite dramatically. There are two magnetic transitions at  $T_{N1} = 8.6$  K and  $T_{N2} = 6.0$  K observed using magnetic susceptibility, heat capacity, and neutron scattering. Two kinks in the temperature dependence of the dielectric constant are observed at both magnetic transition temperatures, indicating magneto-electric coupling and potential multiferroic behaviour. Both magnetic structures were solved with reference to the subcell and supercell, and at least one magnetic transition appears to be first order, although more work needs to be done on this matter. Inelastic neutron scattering spectra were obtained at temperatures below  $T_{N1}$  and  $T_{N2}$ . While a phenomenological quantitative model was implemented to explain the excitations observed below  $T_{N1}$ , only a qualitative explanation was proposed for the excitations below  $T_{N2}$ . More neutron scattering experiments are required to better resolve the observed excitations.

## Chapter 7

# Conclusions and Future

## Directions

There is no question that the langasites offer researchers the opportunity to study interesting and unique magnetic properties.  $\text{Ba}_3\text{NbFe}_3\text{Si}_2\text{O}_{14}$  not only exhibits multiferroic behaviour, but also truly unique chiral magnetism and magnetic dynamics. The magnetic structure, multiferroic, and chiral properties of  $\text{Ba}_3\text{NbFe}_3\text{Si}_2\text{O}_{14}$  are robust in the sense that replacing  $\text{Ba}^{2+}$ ,  $\text{Nb}^{5+}$ , and  $\text{Si}^{4+}$  do little to change the magnetic transition temperature or magnetic structure as evidenced thus far. Upon chemical substitution, the most profound changes came from substituting  $\text{Nb}^{5+}$  for  $\text{Sb}^{5+}$  (although very recent evidence suggests that this may not be the case after all [161]), suggesting that this ion may play a role in the exchange pathways between neighbouring  $\text{Fe}^{3+}$  ions. However, more recent works suggest that it is also possible to create  $\text{Fe}^{3+}$  containing dugganites, which are subclass of the langasite family containing  $\text{Te}^{6+}$  [109]. This area of future study is quite intriguing since only the influence of isovalent chemical substitutions on the magnetic properties of langasites have been studied thus far. It is expected that such substitutions will impact the magnetism modestly: more so than substituting  $\text{Nb}^{5+}$  with  $\text{Sb}^{5+}$ , but not enough to disrupt the chiral and multiferroic properties.

Naturally, the next question to be asked is what would happen if  $\text{Fe}^{3+}$  were replaced?

$Pb_3TeMn_3P_2O_{14}$  is ideally suited to this study since  $Mn^{2+}$  and  $Fe^{3+}$  are isoelectronic. Although  $Pb_3TeMn_3P_2O_{14}$  appears isostructural to the Fe-langasite at first glance, the larger size of  $Mn^{2+}$ ,  $Te^{6+}$ , and the presence of  $Pb^{2+}$  lone pairs distort this system away from the typical  $P321$  langasite symmetry into a large  $P3$  supercell. The supercell has consequences for the observed magnetism; the single equilateral trimer composed of  $3d$  ions are now split into seven trimers composed of two groups of three scalene, *nearly* equilateral trimers and one strictly equilateral trimer. Like  $Ba_3NbFe_3Si_2O_{14}$ ,  $Pb_3TeMn_3P_2O_{14}$  has a single antiferromagnetic transition with an accompanying helical incommensurate magnetic structure propagating along the  $c$ -axis. It is assumed that the magnetic structure also shares the same chiral properties observed in  $Ba_3NbFe_3Si_2O_{14}$ , however they cannot be observed without a single crystal. However, unlike  $Ba_3NbFe_3Si_2O_{14}$ , an additional propagation of the moments was observed along the crystal within the  $ab$ -plane that may be a direct indication of an effect similar to a flexoelectric phenomenon. This increases the size of the magnetic unit cell, relative to the crystal supercell, by many orders of magnitude into the realm of sizes accessible by techniques such as small angle neutron scattering. A dielectric anomaly was also observed at  $T_N$  in  $Pb_3TeMn_3P_2O_{14}$  indicating weak magneto electric coupling and possible multiferroicity within this material.

Next, the question regarding what would happen if the spin number was changed was asked.  $Mn^{2+}$  was replaced for  $Co^{2+}$  in  $Pb_3TeCo_3P_2O_{14}$ , which had a profound effect on both the crystal and magnetic properties in this system. A supercell was still observed, although the distortion was quite different; a  $P321$  to  $P2$  transition was found that turned the single equilateral magnetic trimers into six inequivalent isosceles magnetic trimers. The phase diagram of this material was partly solved through magnetic susceptibility, magnetization, and heat capacity measurements that indicated a high-field transition occurring around 6 T at 12.5 K. The magnetic structure is also quite different compared to the  $Fe^{3+}$  or  $Mn^{2+}$ -containing langasites. Here, one row of three  $Co^{2+}$  trimers had moments aligned in  $120^\circ$  orientation within the  $ab$  plane while the other row of three  $Co^{2+}$  trimers had moments aligned ferromagnetically parallel or antiparallel to

the  $c$ -axis. Inelastic neutron scattering yielded low energy dispersionless excitations between 1 and 8 meV. A phenomenological model based off of independent effective  $S=1/2$  isosceles trimer clusters was used to explain the excitations and yield exchange constants, which were then used to fit the magnetic susceptibility as a verification. There are still questions that remain to be answered. One primary question is why the intratrimer isosceles exchange constants are so different when the equilateral to isosceles distortion is so small?

Finally,  $\text{Pb}_3\text{TeCo}_3\text{V}_2\text{O}_{14}$  was prepared, where diamagnetic  $\text{P}^{5+}$  was substituted for diamagnetic  $\text{V}^{5+}$ . There are no indications of V magnetism in any of our measurements that may occur due to oxygen non-stoichiometry. Although substituting  $\text{Si}^{4+}$  for  $\text{Ge}^{4+}$  had little effect on the magnetic properties in  $\text{Ba}_3\text{NbFe}_3\text{Si}_2\text{O}_{14}$ , substituting  $\text{P}^{5+}$  for  $\text{V}^{5+}$  has an enormous effect here. In particular, a second magnetic transition is observed in  $\text{Pb}_3\text{TeCo}_3\text{V}_2\text{O}_{14}$  that is absent from  $\text{Pb}_3\text{TeCo}_3\text{P}_2\text{O}_{14}$ , in addition to a radically different inelastic excitation spectrum. This raises the question as to why  $\text{V}^{5+}$  has such a dramatic impact on the magnetic properties. It is hypothesized that orbital overlap and hybridization play a large role here:  $\text{V}^{5+}$  has easily accessible  $3d$  states that are absent in  $\text{P}^{5+}$  [156], which would alter the well-known Goodenough-Kanamori rules [12, 13]. Orbital hybridization has recently been shown to play a role in the magnetic phase diagram of  $\text{Cr}_2(\text{Te}_{1-x}\text{W}_x)\text{O}_6$  [179]. In-depth computational studies of the electronic and phononic structures are welcomed. Inelastic x-ray spectroscopy is also expected to shed some light on this issue. It appears as if this problem is even more complex: Previous work [145] reports that partial doping of  $\text{P}^{5+}$  into  $\text{Pb}_3\text{TeCo}_3\text{V}_2\text{O}_{14}$  suppresses the second magnetic transition at  $\text{P}^{5+}:\text{V}^{5+}$  ratios of 1:3, and results in a magnetic structure that is different from either of the end series-members. This only further solidifies the notion of delicate magnetism within these materials. Overall, the langasites offer truly fascinating and easily accessible magnetic phenomena for experimentalists to explore. Despite the real-world complexity of these systems, relatively simple models can be employed to gain some insight into the underlying processes that govern the behaviour in these systems.

# Bibliography

- [1] D. C. Mattis. *The Theory of Magnetism Made Simple*. World Scientific Publishing Co., 2008.
- [2] S. X. Wang, N. X. Sun, M. Yamaguchi, and S. Yabukami. *Nature*, 407:150–151, 2000.
- [3] W. Harneit. *Phys. Rev. A*, 65:032322, 2002.
- [4] J. G. Bednorz and K. A. Müller. *Z. Phys. B*, 64:189–193, 1986.
- [5] R. E. Cohen. *Nature*, 358:136–138, 1992.
- [6] J. Bohm, R. B. Heimann, M. Hengst, R. Roewer, and J. Schindler. *J. Cryst. Growth*, 204:128–136, 1999.
- [7] H. Qi, A. Wei, and D. Yuan. *Mater. Sci. Eng. B*, 117:143–145, 2005.
- [8] C. Kittel. *Introduction to solid state physics*. Wiley, 7 edition, 1996.
- [9] P. Atkins and J. de Paula. *Physical Chemistry*. W. H. Freeman and Company, 8th edition, 2006.
- [10] I. N. Levine. *Quantum Chemistry*. Prentice Hall, 6th edition, 2009.
- [11] A. M. Hallas. *ho<sub>2</sub>ge<sub>2</sub>o<sub>7</sub> and pr<sub>2</sub>zr<sub>2</sub>o<sub>7</sub>: A tale of two spin ices*. Master’s thesis, University of Manitoba, 2013.
- [12] J. B. Goodenough. *Phys. Rev.*, 100:564, 1955.



- 
- [13] J. Kanamori. *J. Phys. Chem. Solids*, 10:87, 1959.
- [14] A. M. Oleś, P. Horsch, L. F. Feiner, and G. Khaliullin. *Phys. Rev. Lett.*, 96:147205, 2006.
- [15] I. Dzyaloshinsky. *J. Phys. Chem. Solids*, 4:241–255, 1958.
- [16] T. Moriya. *Phys. Rev.*, 120:91–98, 1960.
- [17] S.-W. Cheong and M. Mostovoy. *Nat. Mater.*, 6:13–20, 2007.
- [18] C. R. Wiebe. *Studies of Magnetism in Rhenium and Manganese Based Perovskite Oxides*. PhD thesis, McMaster University, 2002.
- [19] P. Hofmann. *Solid State Physics*. Wiley-VCH, 1st edition, 2009.
- [20] K. A. Dill and S. Bromberg. *Molecular Driving Forces*. Garland Science, 2nd edition, 2011.
- [21] C. G. Shull and M. K. Wilkinson. *Rev. Mod. Phys.*, 25:100–107, 1953.
- [22] S. Geller and M. A. Gilleo. *J. Phys. Chem. Solids*, 3:30–36, 1957.
- [23] V. G. Veselago and L. I. Vinokurova. *The Magnetic and Electron Structure of Transition Metals and Alloys*, volume 3. Nova Publishers, 1988.
- [24] D. F. McMorrow, D. A. Jehan, R. A. Cowley, P. P. Swaddling, R. C. C. Ward, M. R. Wells, N. Hagmann, and K. N. Clausen. *Europhys. Lett.*, 23:523–528, 1993.
- [25] T. Eriksson, L. Bergqvist, T. Burket, S. Felton, R. Tellgren, P. Nordblad, O. Eriksson, and Y. Andersson. *Phys. Rev. B*, 71:174420, 2005.
- [26] J. E. Greedan. *J. Mater. Chem.*, 11:37–53, 2001.
- [27] P. W. Anderson. *Phys. Rev.*, 102:1008, 1956.
- [28] G. Toulouse. *Commun. Phys.*, 2:15, 1977.

- 
- [29] Y. Shimizu, K. Miyagawa, K. Kanoda, M. Maesato, and G. Saito. *Phys. Rev. Lett.*, 91:107001, 2003.
- [30] R. Coldea, D. A. Tennant, A. M. Tsvelik, and Z. Tylczynski. *Phys. Rev. Lett.*, 86:1335–1338, 2001.
- [31] Y. Okamoto, M. Nohara, H. Aruga-Katori, and H. Takagi. *Phys. Rev. Lett.*, 99:137207, 2007.
- [32] T.-H. Han, J. S. Helton, S. Chu, D. G. Nocera, J. A. Rodriguez-Rivera, C. Broholm, and Y. S. Lee. *Nature*, 492:406–410, 2012.
- [33] S. Nakatsuji, Y. Nambu, H. Tonomura, O. Sakai, S. Jonas, C. Broholm, H. Tsunetsugu, Y. Qiu, and Y. Maeno. *Science*, 9:1697–1700, 2005.
- [34] J. S. Helton, K. Matan, M. P. Shores, E. A. Nytko, B. M. Bartlett, Y. Yoshida, Y. Takano, A. Suslov, Y. Qiu, J.-H. Chung, D. G. Nocera, and Y. S. Lee. *Phys. Rev. Lett.*, 98:107204, 2007.
- [35] J. S. Gardner, M. J. P. Gingras, and J. E. Greedan. *Rev. Mod. Phys.*, 82:53, 2010.
- [36] R. A. McKinnon. Studies of new multiferroics. Master’s thesis, University of Warwick, 2011.
- [37] B. B. Van Aken, J.-P. Rivera, H. Schmid, and M. Fiebig. *Nature*, 449:702–705, 2007.
- [38] J. Wang, J. B. Neaton, H. Zheng, V. Nagarajan, S. B. Ogale, B. Liu, D. Viehland, V. Vaithyanathan, D. G. Schlom, U. V. Waghmare, N. A. Spaldin, K. M. Rabe, M. Wuttig, and R. Ramesh. *Science*, 299:1719–1722, 2003.
- [39] S. A. Sunshine, D. Kang, and J. A. Ibers. *J. Am. Chem. Soc.*, 109:6202–6204, 1987.
- [40] K. S. Park, J. T. Son, H. T. Chung, S. J. Kim, C. H. Lee, and H. G. Kim. *Electrochim. Commun.*, 5:839–842, 2003.

- [41] Z. R. Dai, Z. W. Pan, and Z. L. Wang. *Adv. Funct. Mater.*, 13:9–24, 2003.
- [42] J.-M. Ntep, S. S. Hassani, A. Lusson, A. Tromson-Carli, D. Ballutaud, G. Didier, and R. Triboulet. *J. Cryst. Growth*, 207:30–34, 1999.
- [43] Y. Ying, S.-S. Chang, C.-L. Lee, and C. R. C. Wang. *J. Phys. Cem. B*, 101:6661–6664, 1997.
- [44] L. E. Smart and E. A. Moore. *Solid State Chemistry*. CRC Press, 4th edition, 2012.
- [45] A. R. West. *Solid State Chemistry and its Applications*. Wiley, 1991.
- [46] E. M. Otto. *J. Electrochem. Soc.*, 112:367, 1965.
- [47] F. Shenouda and S. Aziz. *J. Appl. Chem.*, 17:258, 1967.
- [48] A. Guinier. *X-ray Diffraction in Crystals, Imperfect Crystals, and Amorphous Bodies*. Courier Corporation, 1994.
- [49] No. 3 1992 pp. 29-37 Neutron News, Vol. 3. URL <http://www.ncnr.nist.gov/resources/n-lengths/list.html>.
- [50] M. T. Dove. *Structure and Dynamics: An Atomic View of Materials*. Oxford University Press, 2002.
- [51] W. I. F. David, K. Shankland, L. B. McCusker, and Ch. Baerlocher, editors. *Structure Determination from Powder Diffraction Data*. Oxford University Press, 2006.
- [52] B. D. Cullity. *Elements of X-ray Diffraction*. Addison-Wesley Publishing Co., 1956.
- [53] J. Wang, B. H. Toby, P. L. Lee, L. Ribaud, S. M. Antao, C. Kurtz, M. Ramanathan, R. B. Von Dreele, and M. A. Beno. *Rev. Sci. Instrum.*, 79:085105, 2008.

- [54] P. L. Lee, D. Shu, M. Ramanathan, C. Preissner, J. Wang, M. A. Beno, R. B. Von Dreele, L. Ribaud, C. Kurtz, S. M. Antao, X. Jiao, and B. H. Toby. *J. Synchrotron Rad.*, 15:427–432, 2008.
- [55] B. H. Toby, Y. Huang, D. Dohan, D. Carroll, X. Jiao, L. Ribaud, J. A. Doebbler, M. R. Suchomel, J. Wang, C. Preissner, D. Kline, and T. M. Mooney. *J. Appl. Cryst.*, 42:990–933, 2009.
- [56] G. L. Squires. *Introduction to the Theory of Thermal Neutron Scattering*. Dover Publications Inc., 1996.
- [57] R. A. Young, editor. *The Rietveld Method*. Oxford University Press, 2006.
- [58] B. H. Toby. *Powder Diffr.*, 21:67–70, 2006.
- [59] M. De Graef and M. E. McHenry. *Structure of Materials: An Introduction to Crystallography, Diffraction and Symmetry*. Cambridge University Press, 2nd edition, 2012.
- [60] A. S. Wills. *Magnetic Structures and Their Determination Using Group Theory*. University College London, Department of Chemistry, 20 Gordon Street, London, WC1H 0AJ, Aug 2011.
- [61] A. M. Lesk. *Introduction to Symmetry and Group Theory for Chemists*. Springer, 2004.
- [62] E. F. Bertaut. *J. Appl. Phys.*, 33:1138, 1962.
- [63] E. F. Bertaut. *Acta. Cryst. A*, 24:217, 1968.
- [64] E. F. Bertaut. *J. de Physique Colloque C*, 1:462, 1971.
- [65] E. F. Bertaut. *J. Magn. Magn. Mater.*, 24:267, 1981.
- [66] A. S. Wills. *Appl. Phys. A*, 74:s856–s858, 2002.
- [67] O. V. Kovalev, H. T. Stokes, and D. M. Hatch. *Representations of the Crystallographic Space Groups*. Gordon and Breach, 2nd edition, 1993.

- [68] A. S. Wills. *Z. Kristallogr.*, 30:39–44, 2009.
- [69] A. S. Wills. *Physica B*, 276:680, 2000.
- [70] G. King, A. S. Wills, and P. M. Woodward. *Phys. Rev. B*, 79:224428, 2009.
- [71] E. R. Hovestreydt, M. I. Aroyo, and H. Wondratschek. *J. Appl. Cryst.*, 25:144, 1992.
- [72] L. Pauling. *The Nature of the Chemical Bond*. Cornell University Press, 2nd edition, 1945.
- [73] D. Altermatt and I. D. Brown. *Acta. Cryst. B*, 41:244–247, 1985.
- [74] I. D. Brown. *The Chemical Bond in Inorganic Chemistry: The Bond Valence Model*. Oxford University Press, 2006.
- [75] A. E. Lam. *An X-ray Crystallographic Study of the Crystal Structure of Four Tellurium Oxysalt Minerals: Dugganite, Choloaitite, Rodalquilarite, and Graemite*. PhD thesis, University of British Columbia, 1998.
- [76] *Dynacool Physical Property Measurement System Manual*. Quantum Design.
- [77] R. E. Hummel. *Electrical Properties of Materials*. Springer, 4th edition, 2011.
- [78] M. Maglione and M. A. Subramanian. *Appl. Phys. Lett.*, 93:032902, 2008.
- [79] G. E. Granroth, D. H. Vandergriff, and S. E. Nagler. *Physica B: Cond. Matter*, 385-386:1104–1106, 2006.
- [80] G. E. Granroth, A. I. Kolesnikov, T. E. Sherline, J. P. Clancy, K. A. Ross, J. P. C. Ruff, B. D. Gaulin, and S. E. Nagler. *J. Phys.: Conf. Ser.*, 251:012058, 2010.
- [81] H. D. Zhou, Y. Barlas, C. R. Wiebe, Y. Qiu, J. R. D. Copley, and J. S. Gardner. *Phys. Rev. B*, 82:132408, 2010.
- [82] C. Stock, L. C. Chapon, A. Schneidewind, Y. Su, P. G. Radaelli, D. F. McMorrow, A. Bombardi, N. Lee, and S.-W. Cheong. *Phys. Rev. B*, 83:104426, 2011.

- [83] V. N. Molchanov, B. A. Maksimov, A. F. Kondakov, T. S. Chernaya, Y. V. Pisarevskii, and V. I. Simonov. *J. Exp. Theor. Phys. Lett.*, 75:222–225., 2001.
- [84] D. Damjanovic. *Curr. Opin. Solid St. M.*, 3:469–473, 1998.
- [85] J. Robert, V. Simonet, B. Canals, R. Ballou, P. Bordet, P. Lejay, and A. Stunault. *Phys. Rev. Lett.*, 96:197205, 2006.
- [86] J. Robert, V. Simonet, B. Canals, R. Ballou, P. Bordet, and A. Stunault. *Phys. Rev. Lett.*, 97:259901, 2006.
- [87] H. D. Zhou, B. W. Vogt, J. A. Janik, Y. J. Jo, L. Balicas, Y. Qiu, J. R. D. Copley, J. S. Gardner, and C. R. Wiebe. *Phys. Rev. Lett.*, 99:236401, 2007.
- [88] A. Zorko, F. Bert, P. Mendels, P. Bordet, P. Lejay, and J. Robert. *Phys. Rev. Lett.*, 100:147201, 2008.
- [89] X. S. Xu, T. V. Brinzari, S. McGill, H. D. Zhou, C. R. Wiebe, and J. L. Musfeldt. *Phys. Rev. Lett.*, 103:267402, 2009.
- [90] K. Marty, V. Simonet, E. Ressouche, R. Ballou, P. Lejay, and P. Bordet. *Phys. Rev. Lett.*, 101:247201, 2008.
- [91] H. Katsura, N. Nagaosa, and A. V. Balatsky. *Phys. Rev. Lett.*, 95:057205, 2005.
- [92] M. Kenzelmann, G. Lawes, A. B. Harris, G. Gasparovic, C. Broholm, A. P. Ramirez, G. A. Jorge, M. Jaime, S. Park, Q. Huang, A. Ya. Shapiro, and L. A. Demianets. *Phys. Rev. Lett.*, 98:267205, 2007.
- [93] M. Mostovoy. *Phys. Rev. Lett.*, 96:067601, 2006.
- [94] H. D. Zhou, L. L. Lumata, P. L. Kuhns, A. P. Reyes, E. S. Choi, N. S. Dalal, J. Lu, Y. J. Jo, L. Balicas, and J. S. Brooks. *Chem. Mater.*, 21:156–159, 2009.
- [95] R. D. Shannon. *Acta. Cryst. A*, 32:751–767, 1976.
- [96] B. V. Mill and Y. V. Pisarevsky. *P. IEEE Int. Freq. Cont.*, (133-144), 2000.

- [97] T. Kudo, Y. Yokota, M. Sato, K. Tota, K. Onodera, S. Kurosawa, K. Kamada, and A. Yoshikawa. *J. Cryst. Growth*, 401:173–176, 2014.
- [98] K. Xiong, Y. Zheng, X. Tu, S. Zhang, H. Kong, and E. Shi. *J. Cryst. Growth*, 401:820–823, 2014.
- [99] J. W. Krizan, C. de la Cruz, N. H. Anderson, and R. J. Cava. *J. Solid State Chem*, 203:310–320, 2013.
- [100] M. Kitahara, Y. Yokota, Y. Futami, and S. A. Yoshikawa. *Ferroelectrics*, 451:107–112, 2013.
- [101] Y. Yokota, M. Sato, Y. Futami, K. Tota, K. Onodera, T. Yanagida, and A. Yoshikawa. *IEEE T. Ultrason. Ferr.*, 59:1864–1867, 2012.
- [102] Y. Yokota, A. Yoshikawa, Y. Futami, M. Sato, K. Tota, K. Onodera, and T. Yanagida. *IEEE T. Ultrason. Ferr.*, 59:1868–1871, 2012.
- [103] H. J. Silverstein, K. Cruz-Kan, A. M. Hallas, H. D. Zhou, R. L. Donaberger, B. C. Hernden, M. Bieringer, E. S. Choi, J. Hwang, A. S. Wills, and C. R. Wiebe. *Chem. Mater.*, 24:664–670, 2012.
- [104] G. M. Kuz'micheva, I. A. Kaurova, V. B. Rybakov, S. S. Khasanov, A. Cousson, O. Zaharko, E. N. Domoroschina, and A. B. Dubovsky. *2012*, 47:131–138, Cryst. Res. Technol.
- [105] I. S. Lyubutin, P. G. Naumov, B. V. Mill, K. V. Frolov, and E. I. Demikhov. *Phys. Rev. B*, 84:214425, 2011.
- [106] B. V. Mill. *Russ. J. Inorg. Chem.*, 55:1611–1616, 2010.
- [107] B. V. Mill, A. A. Klimenkova, B. A. Maksimov, V. N. Molchanov, and D. Yu. Pushcharovsky. *Crystallogr. Rep.*, 52:785–794, 2007.
- [108] B. V. Mill. *Russ. J. Inorg. Chem.*, 54:1205–1209, 2009.
- [109] B. V. Mill. *Russ. J. Inorg. Chem.*, 54:1425–1427, 2009.

- [110] B. V. Mill and M. V. Lomonosov. *P. IEEE Int. Freq. Cont.*, pages 255–262, 2001.
- [111] K. Marty, P. Bordet, V. Simonet, M. Loire, R. Ballou, C. Darie, J. Kljun, P. Bonville, O. Isnard, P. Lejay, B. Zawilski, and C. Simon. *Phys. Rev. B*, 81:054416, 2010.
- [112] A. P. Dudka, Yu. V. Pisarevsky, V. I. Simonov, and B. V. Mill. *Crystallogr. Rep.*, 55:748–752, 2010.
- [113] H. D. Zhou, C. R. Wiebe, Y. J. Jo, L. Balicas, R. R. Urbano, L. L. Lumata, J. S. Brooks, P. L. Kuhns, A. P. Reyes, Y. Qiu, J. R. D. Copley, and J. S. Gardner. *Phys. Rev. Lett.*, 102:067203, 2009.
- [114] A. Zorko, F. Bert, P. Mendels, A. Potočnik, A. Amato, C. Baines, K. Marty, P. Bordet, P. Lejay, E. Lhotel, V. Simonet, and R. Ballou, 2012. URL [arXiv.org/pdf/1210.8187.pdf](https://arxiv.org/pdf/1210.8187.pdf).
- [115] A. Huq, J. P. Hodges, O. Gourdon, and L. Heroux. *Z. Kristallogr. Proc.*, 1:127–135, 2011.
- [116] V. Simonet, M. Loire, and R. Ballou. *Eur. Phys. J. Spec. Top.*, 213:5–36, 2012.
- [117] V. Scagnoli, S. W. Huang, M. Garganourakis, R. A. de Souza, U. Staub, V. Simonet, P. Lejay, and R. Ballou. *Phys. Rev. B*, 88:104417, 2013.
- [118] J. P. Sheckelton, J. R. Neilson, D. G. Soltan, and T. M. McQueen. *Nat. Mater.*, 11:493–496, 2012.
- [119] K. Marty, V. Simonet, P. Bordet, R. Ballou, P. Lejay, O. Isnard, E. Ressouche, F. Bourdarot, and P. Bonville. *J. Magn. Magn. Mater.*, 321:1778–1781, 2009.
- [120] C. Lee, E. J. Kan, H. J. Xiang, and M. H. Whangbo. *Chem. Mater.*, 22:5290–5295, 2010.
- [121] M. Loire, V. Simonet, S. Petit, K. Marty, P. Bordet, P. Lejay, J. Ollivier, M. Enderle, P. Steffens, E. Ressouche, A. Zorko, and R. Ballou. *Phys. Rev. Lett.*, 106:207201, 2011.



- [122] J. Jensen. *Phys. Rev. B*, 84(104405), 2011.
- [123] A. Zorko, M. Pregelj, A. Potocnik, J. van Tol, A. Ozarowski, V. Simonet, P. Lejay, S. Petit, and R. Ballou. *Phys. Rev. Lett.*, 107:257203, 2011.
- [124] S. S. Rathore, S. K. Mishra, and S. Vitta. *J. Appl. Phys.*, 111:074103, 2012.
- [125] K. Y. Choi, Z. Wang, A. Ozarowski, J. van Tol, H. D. Zhou, C. R. Wiebe, Y. Skourski, and N. S. Dalal. *J. Phys. Condens. Matter*, 24:246001, 2012.
- [126] S. S. Rathore and S. Vitta. *IEEE T. Magn.*, 48:3529–3531, 2012.
- [127] L. Chaix, S. de Brion, F. Lévy-Bertrand, V. Simonet, R. Ballou, B. Canals, P. Lejay, J. B. Brubach, G. Creff, F. Willaert, P. Roy, and A. Cano. *Phys. Rev. Lett.*, 110:157208, 2013.
- [128] N. Lee, Y. J. Choi, and S.-W. Cheong. *Appl. Phys. Lett.*, 104:072904, 2014.
- [129] I. S. Lyubutin, P. G. Naumov, and B. V. Mill. *Europhys. Lett.*, 90:67005, 2010.
- [130] S. A. Pikin and I. S. Lyubutin. *Phys. Rev. B*, 86:064414, 2012.
- [131] S. A. Pikin and I. S. Lyubutin. *J. Exp. Theor. Phys. Lett.*, 96:240–244, 2012.
- [132] I. S. Lyubutin and S. A. Pikin. *J. Phys. Condens. Matter*, 25:236001, 2013.
- [133] J. F. Scott. *J. Phys. Condens. Matter*, 20:021001, 2008.
- [134] K. J. Choi, M. Biegalski, Y. L. Li, A. Sharan, J. Schubert, R. Uecker, P. Reiche, Y. B. Chen, X. Q. Pan, V. Gopalan, L.-Q. Chen, D. G. Schlom, and C. B. Eom. *Science*, 306:1005–1009, 2004.
- [135] S. A. Williams. *Amer. Mineral.*, 63:1016–1019, 1978.
- [136] A. E. Lam, L. A. Groat, and T. S. Ercit. *Can. Mineral.*, 36:823, 1998.
- [137] J. L. Jambor and D. A. Vanko. *Amer. Mineral.*, 77:446–452, 1992.

- [138] S. J. Mills, U. Kolitsch, R. Miyawaki, L. A. Groat, and G. Poirier. *Amer. Mineral.*, 94:1012–1017, 2009.
- [139] V. Yu. Ivanov, A. A. Mukhin, A. S. Prokhorov, and B. V. Mill. *Solid State Phenom.*, 152-153:299–302, 2009.
- [140] M. Jansen. *Angew. Chem. Int. Ed.*, 41:3746–3766, 2002.
- [141] A. S. Posner and A. Perloff. *J. Res. Nat. Bur. Stand.*, 58:279, 1957.
- [142] J. D. Watson and F. H. C. Crick. *Nature*, 171:737–738, 1953.
- [143] H. J. Silverstein, A. Z. Sharma, K. Cruz-Kan, H. D. Zhou, A. Huq, R. Flacau, and C. R. Wiebe. *J. Solid State Chem*, 204:102–107, 2013.
- [144] H. J. Silverstein, A. Huq, M. Lee, E. S. Choi, H. D. Zhou, and C. R. Wiebe. *J. Solid State Chem*, 221:216–223, 2015.
- [145] H. J. Silverstein, A. Z. Sharma, A. J. Stoller, K. Cruz-Kan, R. Flacau, R. L. Donaberger, H. D. Zhou, P. Manuel, A. Huq, A. I. Kolesnikov, and C. R. Wiebe. *J. Phys. Condens. Matter*, 25:246004, 2013.
- [146] Z. Xiu, M. Lü, F. Gu, S. Wang, D. Xu, and D. Yuan. *J. Cryst. Growth*, 264:468–471, 2004.
- [147] W. E. Baker. *Amer. Mineral.*, 51:1712–1721, 1966.
- [148] S. A. Ivanov, P. Nordblad, R. Mathieu, R. Tellgren, C. Ritter, N. V. Golubko, E. D. Politova, and M. Weil. *Mater. Res. Bull.*, 46:1870–1877, 2011.
- [149] L. Falck, O. Lindqvist, and J. Moret. *Acta. Cryst. B*, 34:896–897, 1978.
- [150] J. Rodriguez-Carvajal. *Physica B*, 192:55, 1993.
- [151] A. Le Bail, H. Duroy, and J. L. Fourquet. *Mater. Res. Bull.*, 23:447–452, 1988.
- [152] B. H. Toby and R. B. Von Dreele. *J. Appl. Cryst.*, 46:544–549, 2013.
- [153] W. H. Baur. *Acta. Cryst. B*, 30:1195, 1974.

- [154] A. G. Gavriiliuk, I. A. Trojan, I. S. Lyubutin, A. G. Ivanova, Yu. A. Davydova, S. S. Starchikov, and S. N. Aksenov. High-pressure structural properties of new multiferroics of the langasite family. Technical report, Deutsches Elektronen-Synchrotron, 2013.
- [155] V. O. Garlea, B. C. Chakoumakos, S. A. Moore, G. B. Taylor, T. Chae, R. G. Maples, R. A. Riedel, G. W. Lynn, and D. L. Selby. *Appl. Phys. A*, 99:531–535, 2010.
- [156] M. M. Markina, B. V. Mill, E. A. Zvereva, A. V. Ushakov, S. V. Streltsov, and A. N. Vasiliev. *Phys. Rev. B*, 89:104409, 2014.
- [157] B. V. Mill, A. N. Vasiliev, R. Klingeler, B. Buechner, and M. M. Markina. Thermodynamic properties of langasite family compounds  $\text{Pb}_3\text{TeCo}_3\text{V}_2\text{O}_{14}$  and  $\text{Pb}_3\text{TeMn}_3\text{As}_2\text{O}_{14}$ . In *Moscow International Symposium on Magnetism MISM*, 2011.
- [158] P. Zubko, G. Catalan, and A. K. Tagantsev. *Annu. Rev. Mater. Res.*, 43:387–421, 2013.
- [159] H. J. Koo and M. H. Whangbo. *Inorg. Chem.*, 45:4440–7, 2006.
- [160] L. C. Chapon, P. Manuel, P. G. Radaelli, C. Benson, L. Perrott, S. Ansell, N. J. Rhodes, D. Raspino, D. Duxbury, E. Spill, and J. Norris. *Neutron News*, 22:22–25, 2011.
- [161] S. S. Rathore and S. Vitta, 2014. URL [arXiv.org/ftp/arxiv/papers/1407/1407.2049.pdf](https://arxiv.org/ftp/arxiv/papers/1407/1407.2049.pdf).
- [162] T. Aharen, J. E. Greedan, F. Ning, T. Imai, V. Michaelis, S. Kroeker, H. D. Zhou, C. R. Wiebe, and L. M. D. Cranswick. *Phys. Rev. B*, 80:134423, 2009.
- [163] M. E. Fisher. *Philos. Mag.*, 7:1731, 1962.
- [164] J. Rodríguez-Carvajal, 2014. URL [neutrons.ornl.gov/conf/2014/magstr/docs/Tutorial\\_Magnetic\\_Structures.pdf](https://neutrons.ornl.gov/conf/2014/magstr/docs/Tutorial_Magnetic_Structures.pdf).

- [165] J. M. Allred, K. M. Taddei, D. E. Bugaris, S. Avci, D. Y. Chung, H. Claus, C. de la Cruz, M. G. Kanatzidis, S. Rosenkranz, R. Osborn, and O. Chmaissem. *Phys. Rev. B*, 90:104513, 2014.
- [166] A. Furrer and O. Waldmann. *Rev. Mod. Phys.*, 85:367–420, 2013.
- [167] M. B. Stone, F. Fernandez-Alonso, D. T. Adroja, N. S. Dalal, D. Villagrán, F. A. Cotton, and S. E. Nagler. *Phys. Rev. B*, 75:214427, 2007.
- [168] J. T. Haraldsen, T. Barnes, and J. L. Musfeldt. *Phys. Rev. B*, 71:064403, 2005.
- [169] L. Seabra, T. Momoi, P. Sindzingre, and N. Shannon. *Phys. Rev. B*, 84:214418, 2011.
- [170] H. D. Zhou, C. Xu, A. M. Hallas, H. J. Silverstein, C. R. Wiebe, I. Umegaki, J. Q. Yan, T. P. Murphy, J.-H. Park, Y. Qiu, J. R. D. Copley, J. S. Gardner, and Y. Takano. *Phys. Rev. Lett.*, 109:267206, 2012.
- [171] T. Susuki, N. Kurita, T. Tanaka, H. Nojiri, A. Matsuo, K. Kindo, and H. Tanaka. *Phys. Rev. Lett.*, 110:267201, 2013.
- [172] A.-J. Dianoux and G. Lander. Neutron data booklet. ILL OCP Science, 2003.
- [173] M. Schindler, F. C. Hawthorne, and W. H. Baur. *Chem. Mater.*, 12:1248–1259, 2000.
- [174] R. D. Shannon and C. Calvo. *J. Solid State Chem.*, 6:538, 1973.
- [175] R. J. Hill and H. D. Flack. *J. Appl. Cryst.*, 20:356–361, 1987.
- [176] K. Robinson, G. V. Gibbs, and P. H. Ribbe. *Science*, 172:567–570, 1971.
- [177] M. E. Fleet. *Mineral. Mag.*, 40:531–533, 1976.
- [178] G. Ehlers, A. Podlesnyak, J. L. Niedziela, and E. B. Iverson. *Rev. Sci. Instrum.*, 82:085108, 2011.
- [179] M. Zhu, D. Do, C. de la Cruz, Z. Dun, H. D. Zhou, S. D. Mahanti, and X. Ke. *Phys. Rev. Lett.*, 113:076406, 2014.